FORMULATION AND APPLICATIONS OF CONSISTENT SHELL AND BEAM ELEMENTS

By

Bradley Louis Koziey, B. Eng., M. Eng.

A Thesis

Submitted to the School of Graduate Studies

in Partial Fulfillment of the Requirements

for the Degree

Doctor of Philosophy

McMaster University

FORMULATION AND APPLICATIONS OF CONSISTENT SHELL AND BEAM ELEMENTS

To my wife, Suzanne, for

her love and support.

DOCTOR OF PHILOSOPHY (1993) McMASTER UNIVERSITY

(Civil Engineering) Hamilton, Ontario

TITLE: Formulation and Applications of Consistent Shell and Beam Elements

AUTHOR: Bradley Louis Koziey, B. Eng. (McMaster University)

M. Eng. (McMaster University)

SUPERVISOR: Dr. F. A. Mirza

NUMBER OF PAGES: xix, 215

ABSTRACT

A new shell element for the analysis of thin and thick plate and shell structures has been formulated along with the compatible beam element. The new elements are referred to as the consistent shell element and the consistent beam element. By combining the consistent shell element and the consistent beam element a finite element model for the analysis of reinforced concrete structures has been formulated. The scope of the study is broadened further through the modification of the new elements to allow for the analysis of laminated fiber-reinforced composite beams and shells.

Many of the currently available beam and shell elements exhibit spurious variations of the transverse shear stress(es). To obtain improved responses when thin beams or shells are analysed the reduced integration technique has typically been employed. This approach is not acceptable since the reduced integration technique cannot be applied with complete confidence. In the present study it is found that the unsatisfactory behaviour of these elements is due to an inconsistency in their formulation. In the formulation of the new elements a consistent formulation has been ensured. The new elements behave very well in the analysis of both thin and thick beams and shells and contain no spurious zero energy modes. In addition, they provide a quadratic variation of the transverse shear stress(es), and a cubic variation of the displacement(s) through their thicknesses. Therefore, the shear correction factor κ which is usually required to correct for the assumption of constant

transverse shear strain through the thickness is not required. Both elements include material non-linearity. Special attention has been given to the efficient implementation of the consistent shell element by employing a sub-matrix formulation in conjunction with a modified frontal solution algorithm. The numerical results show the new elements to be highly accurate and computationally efficient.

The reinforced concrete finite element model employs a rational elasto-plastic constitutive relationship for concrete, discrete bar elements for modelling of reinforcement, joint elements for bond slip between concrete and reinforcement, beam elements for supporting girders and shear connector elements along the concrete/girder interface. The numerical results show that the model accurately predicts the behaviour of reinforced concrete slabs, including punching shear failure under point loads. The constitutive model employed has been found to be reasonably objective with respect to refinement of the finite element mesh.

The consistent laminated beam element and the consistent laminated shell element, have been formulated for the analysis of laminated fiber-reinforced composites. Special attention has been given to the approximation of stresses through the thickness of the laminate because of their importance in predicting delamination failures. This has been achieved by allowing the transverse shear strain(s) to be discontinuous at the interface of two layers while still maintaining continuity of the global displacements across the interface. The numerical results show that the elements provide very accurate predictions of stresses through the thickness of both thin and thick laminates.

ACKNOWLEDGEMENTS

I wish to express my deep appreciation to my supervisor, Dr. F. A. Mirza, for his guidance, criticism and encouragement throughout the research and preparation of this thesis. The valuable advice of Drs. R. M. Korol and D. S. Weaver, members of my supervisory committee is also sincerely appreciated.

The financial support of the Natural Sciences and Engineering Research Council Post Graduate Scholarship, McMaster University Hooker Scholarship, Ontario Graduate Scholarship and the Department of Civil Engineering Graduate Assistantship are gratefully acknowledged.

Thanks also to my family and friends for their unending support and encouragement throughout the duration of this study.

TABLE OF CONTENTS

ABSTRACT iii

ACKNOWLEDGEMENTS v

TABLE OF CONTENTS vi

LIST OF FIGURES xi

LIST OF TABLES xvii

LIST OF SYMBOLS xviii

CHAPTER ONE INTRODUCTION

1.1 General Review 1

1.1.1 Plate and Shell Finite Elements 1

1.1.2 Finite Element Modelling of Reinforced Concrete Structures 4

1.1.3 Finite Element Analysis of Laminated Fiber Reinforced Composites 6

1.2 Objectives and Scope 8

CHAPTER TWO CONSISTENT BEAM ELEMENT FORMULATION AND APPLICATIONS

2.1 Introduction 11

2.2 Consistency of Formulation 12

2.3 Consistent Beam Element Formulation 18

2.3.1 Co-ordinate Systems and Geometry 18

2.3.2 Displacement Field 19
2.3.3 Strain-Displacement and Stress-Strain Relationships 21
2.3.4 Stiffness Matrix 24
2.4 Elasto-Plastic Formulation 26
2.4.1 Elasto-Plastic Constitutive Relationship 27
2.4.2 Nonlinear Finite Element Analysis Procedure 29
2.5 Numerical Examples 33
2.5.1 Elimination of Spurious Shear Stress Mode 34
2.5.2 Degeneration to Slender Beam Solution 34
2.5.3 Thick Beam Under Sinusoidal Transverse Loading 35
2.5.4 Thin Pinched Ring 36
2.5.5 Elasto-Plastic Analysis of a Thick Beam 37

CHAPTER THREE CONSISTENT SHELL ELEMENT FORMULATION AND APPLICATIONS

3.1 Introduction 51
3.2 Consistent Shell Element Formulation 52
3.2.1 Co-ordinate Systems and Geometry 52
3.2.2 Displacement Field 54
3.2.3 Strain-Displacement and Stress-Strain Relationships 55
3.2.4 Sub-Matrix Formulation of Elastic Stiffness Matrix 57

3.2.5 Assembly and Solution of Global Equilibrium Equations 65
3.3 Elasto-Plastic Formulation 67
3.3.1 Elasto-Plastic Constitutive Relationship 67
3.3.2 Elasto-Plastic Stiffness Matrix 69
3.4 Numerical Examples 71
3.4.1 Convergence to Thin Plate Solution 71
3.4.2 Cylindrical Panel 72
3.4.3 Hemispherical Shell Under Point Loads 74
3.4.4 Elasto-Plastic Thin Plate 76
3.4.5 Consistent Shell Element Convergence 77

CHAPTER FOUR FINITE ELEMENT MODEL FOR COMPOSITE STRUCTURES OF STEEL AND CONCRETE

4.1 Introduction 85
4.2 Finite Element Models 86
4.2.1 Reinforcement Element 86
4.2.2 Joint Element 90
4.2.3 Transformation of Boundary Degrees of Freedom 93
4.2.4 Girder Element 95
4.2.5 Shear Connector Element 102
4.2.6 Elasto-Plastic Constitutive Model For Concrete 105
4.3 Numerical Examples 113
4.3.1 Simply Supported Reinforced Concrete Slab 114

4.3.2 Multi-girder Prestressed Concrete Slab 115

4.3.3 Plain Concrete Tension Test 117

CHAPTER FIVE FORMULATIONS AND APPLICATIONS OF CONSISTENT LAMINATED BEAM AND CONSISTENT LAMINATED SHELL ELEMENTS

5.1 Introduction 135

5.2 Consistent Laminated Beam Element 136

5.2.1 Co-ordinate Systems and Geometry 136

5.2.2 Displacement Field 137

5.2.3 Strain-Displacement and Stress-Strain Relationships 140

5.2.4 Element Stiffness Matrix 141

5.3 Consistent Laminated Shell Element 143

5.3.1 Co-ordinate Systems and Geometry 143

5.3.2 Displacement Field 143

5.3.3 Strain-Displacement and Stress-Strain Relationships 146

5.3.4 Element Stiffness Matrix 149

5.4 Kinematic Constraints 150

5.5 Numerical Examples 152

5.5.1 Deep Laminated Composite Beam 152

5.5.2 Laminated Composite Plate 153

5.5.3 Thin Laminated Composite Cylindrical Shell 156

CHAPTER SIX CONCLUSIONS AND RECOMMENDATIONS

6.1 Introduction 169

6.2 Recommendations For Future Research 173

APPENDIX A FINITE ELEMENT INTERPOLATION FUNCTIONS

Appendix A1: Consistent Beam Element 176

Appendix A2: Consistent Shell Element 177

Appendix A3: Reinforcement Element 178

Appendix A4: Girder Element 179

APPENDIX B DERIVATION OF THROUGH THICKNESS INTERPOLATION FUNCTION M2 181

APPENDIX C CONSTRUCTION OF ORTHOGONAL BASIS 185

APPENDIX D CONSISTENT SHELL ELEMENT STIFFNESS SUB-MATRICES 187

APPENDIX E CONSISTENT SHELL ELEMENT STRAIN DISPLACEMENT MATRIX [B′] 197

APPENDIX F JOINT ELEMENT AND REINFORCEMENT ELEMENT BOUNDARY NODE TRANSFORMATION MATRICES 199

APPENDIX G DERIVATION OF LAMINA THROUGH THICKNESS INTERPOLATION FUNCTIONS M3, M4, M5 AND M6 201

APPENDIX H CONSISTENT LAMINATED BEAM ELEMENT STRAIN DISPLACEMENT MATRIX [B′] 205

APPENDIX I CONSISTENT LAMINATED SHELL ELEMENT STRAIN DISPLACEMENT MATRIX [B′] 207

REFERENCES 211

LIST OF FIGURES

CHAPTER TWO

2.1 Dimensions, loading and material properties of prismatic cantilever. 40

2.2 Average shear stress variation along the length of a prismatic cantilever subjected to a concentrated load at its free end. 40

2.3 Consistent beam element co-ordinate systems and degrees of freedom. 41

2.4 Cross-sectional deformation due to rotations α_i and ϕ_i. 41

2.5 Incremental load analysis with modified Newton-Raphson iterative procedure. 42

2.6 Dimensions, loading and material properties of fix-fix beam subjected to a U.D.L. 42

2.7 Normalized mid-span deflection versus length to thickness ratio for a fix-fix beam under a uniformly distributed load. 43

2.8 Dimensions, loading and material properties of simply supported thick beam. 43

2.9 Thick beam normal stress distribution at x = L/4. 44

2.10 Thick beam shear stress distribution at x = 0. 44

2.11 Geometry, loading and material properties of thin pinched ring. 45

2.12 Geometry, material properties and loading for fix-fix thick beam. 45

2.13 Applied load versus mid-span displacement for elasto-plastic analysis of thick fix-fix beam. 46

2.14 Normal stress and shear stress distributions at fixed end of beam for P = 3 MN. 47

2.15 Normal stress and shear stress distributions at fixed end of beam for P = 7 MN. 47

2.16 Normal stress and shear stress distributions 12 cm from fixed end of beam for P = 3 MN. 48

2.17 Normal stress and shear stress distributions 12 cm from fixed end of beam for P = 7 MN. 48

2.18 Effective stress contours for thick beam between fixed end and x = 30 cm for P = 3 MN. 49

2.19 Effective stress contours for thick beam between fixed end and x = 30 cm for P = 7 MN. 50

CHAPTER THREE

3.1 Consistent shell element co-ordinate systems and nodal degrees of freedom. 79

3.2 Consistent shell element nodal unit vectors. 79

3.3 Stiffness sub-matrix referencing using sub-variable location vectors. 80

3.4 Normalized center plate deflection versus width to thickness ratio for a simply supported square plate under uniform load q. 80

3.5 Cylindrical shell roof dimensions, loading and material properties. 81

3.6 Hemispherical shell geometry, loading and material properties. 81

3.7 Geometry, material properties and loading for simply supported thin square plate. 82

3.8 Total load versus center plate displacement for a simply supported square plate loaded by uniform load q. 82

3.9 Convergence of center plate deflection for a clamped thin square plate subjected to a u.d.l. 83

3.10 Convergence of center plate deflection for a clamped thick circular plate subjected to a u.d.l. 83

CHAPTER FOUR

4.1 Components of reinforced concrete finite element model. 120

4.2 Reinforcement element co-ordinate systems and nodal degrees of freedom. 121

4.3 Girder element co-ordinate systems and nodal degrees of freedom. 121

4.4	Failure surface in (a) principal stress space; (b) meridional plane; (c) deviatoric plane.	122
4.5	Plastic potential surfaces in meridional plane.	123
4.6	Geometry and reinforcement details for simply supported reinforced concrete slab (dimensions in mm).	124
4.7	Central deflection of simply supported reinforced concrete slab under a uniformly distributed load.	125
4.8	Geometry and cross-section of multigirder prestressed concrete slab (dimensions in mm).	126
4.9	Placement of reinforcement for multigirder prestressed concrete slab (dimensions in mm).	127
4.10	Detail of a typical shear connector.	128
4.11	Finite element mesh for multigirder prestressed concrete slab (dimensions in mm).	128
4.12	Load deflection curve for multigirder prestressed concrete slab at the loading point.	129
4.13	Cracking pattern around loading point at failure; P = 90 KN (0,1,2,3,4,5 denote the number of cracked integration points).	129
4.14	Geometry and material properties of notched plain concrete specimen (dimensions in mm).	130

4.15 Force versus displacement curves for variation of finite element mesh with $\mu = 1.0$. 131

4.16 Force versus displacement curves for variation of finite element mesh with $\mu = 3.0$. 131

4.17 Load versus displacement curves for variation of μ using a six element mesh. 132

4.18 Load versus displacement curves for variation of H using a six element mesh. 132

4.19 Load versus displacement curves for variation of residual strength using a six element mesh. 133

CHAPTER FIVE

5.1 Definition of principal material directions for fiber reinforced composite lamina. 157

5.2 Consistent laminated beam element co-ordinate systems and degrees of freedom. 157

5.3 Laminae degrees of freedom and co-ordinate t_L at the i^{th} node. 158

5.4 Consistent laminated shell element co-ordinate systems and nodal degrees of freedom. 159

5.5 Definition of fiber orientation with respect to local x′ axis. 159

5.6 Dimensions and material properties of laminated fiber reinforced composite beams. 160

5.7 Normal stress distribution at the mid-span of the (a) 2 ply laminate (b) 3 ply laminate. 161

5.8 Shear stress distribution at x = 0 for the (a) 2 ply laminate (b) 3 ply laminate. 162

5.9 Cross-sectional deformation at x = 0 for the (a) 2 ply laminate (b) 3 ply laminate. 163

5.10 Dimensions and material properties for laminated fiber reinforced composite plates. 164

5.11 Normal stress σ_{xx} through thickness of 9 ply laminate; (a) L/H = 4 (b) L/H = 10. 165

5.12 Shear stress τ_{xz} through thickness of 9 ply laminate; (a) L/H = 4 (b) L/H = 10. 166

5.13 Variation of inplane displacement u through thickness of 9 ply laminate; (a) L/H =4 (b) L/H = 10. 167

5.14 Dimensions and material properties of thin laminated fiber reinforced cylindrical shell. 168

5.15 Composite cylindrical shell shear stress $\tau_{y\theta}$ distribution at y = 0. 168

LIST OF TABLES

CHAPTER TWO

2.1 Thick beam normalized mid-span deflections. 36

2.2 Pinched ring normalized radial deflections. 37

CHAPTER THREE

3.1 Results of cylindrical panel analysis using the consistent thick shell element. 73

3.2 Results of cylindrical panel analysis using the nine node isoparametric shell element without reduced integration. 73

3.3 Results of hemispherical shell analysis using the consistent shell element. 75

3.4 Results of hemispherical shell analysis using the nine node isoparametric shell element.

CHAPTER FOUR

4.1 Reinforced concrete slab material properties. 114

4.2 Multi-girder concrete slab material properties. 116

CHAPTER FIVE

5.1 Mid-span deflections for laminated composite beams. 153

5.2 Deflections and inplane shear stresses for laminated composite plates. 155

LIST OF SYMBOLS

All symbols are defined at their first appearance. The principal symbols used are listed below:

α_i, β_i, ϕ_i, ψ_i	Rotational degrees of freedom.
b	Consistent beam element width.
[B′]	Strain matrix relating degrees of freedom to local strains.
$[C_i]$	Consistent shell element direction cosine cross product matrix.
CU_i, CW_i	Consistent beam element direction cosine cross product terms.
$CP1_i$, $CP2_i$	Girder element direction cosine cross product terms.
[D′]	Elasticity matrix in local co-ordinate system.
$d\phi^T_{i,L}$, $d\phi^B_{i,L}$, $d\psi^T_{i,L}$, $\psi^B_{i,L}$	Laminated element displacement degrees of freedom for the L^{th} layer.
E, G, ν, κ	Elastic modulus, shear modulus, Poisson's ratio and shear correction factor.
$\phi^T_{i,L}$, $\phi^B_{i,L}$, $\psi^T_{i,L}$, $\psi^B_{i,L}$	Laminated element rotational degrees of freedom for the L^{th} layer.
ζ, $\bar{\zeta}$	Reinforcement element non-dimensional and dimensional co-ordinates.

$\Lambda^g_1, \Lambda^g_2, \Lambda^g_3$	Girder element direction cosines relating local axis $\bar{\xi}$ to global axes x,y, and z.
γ_i	Angle between local and global co-ordinate systems for consistent beam element.
h_L, t_L	Layer thickness and non-dimensional co-ordinate.
H_i	Laminate thickness at i^{th} node.
H', E_T	Plastic modulus and tangent modulus.
$[k^{shear}], \{P^{shear}\}$	Shear element stiffness matrix, load vector and
$[N^{shear}]$	interpolation functions.
$[k^{joint}], \{P^{joint}\}$	Joint element stiffness matrix, load vector and
$[N^{joint}]$	interpolation functions.
$[k^r], \{P^r\}$	Reinforcement element stiffness matrix and load vector.
$l_i, m_i, n_i; i=1,3$	Direction cosines.
M_1,M_2,M_3,M_4,M_5,M_6	Through thickness interpolation functions.
$N_i, \bar{N}_i$	Quadratic and cubic interpolation functions.
$\lambda^r_1, \lambda^r_2, \lambda^r_3$	Reinforcement element direction cosines relating local axis $\bar{\xi}$ to global axes x, y, and z.
r, s, t	Curvilinear co-ordinates.
$\bar{\sigma}, \sigma_Y$, F	Effective stress, yield stress and yield function.
$[\theta]$	Transformation matrix relating local axes x′, y′ and z′ to global axes x, y, and z.
$[T_1],[T_4]$	Transformation matrices for joint and reinforcement element boundary degrees of freedom.
u_i, v_i, w_i	Displacement degrees of freedom.
$\hat{V}_{1i},\hat{V}_{2i},\hat{V}_{3i}$	Consistent shell element nodal unit vectors.

CHAPTER ONE

INTRODUCTION

1.1 General Review

1.1.1 Plate and Shell Finite Elements

Over the last three decades a considerable amount of work has gone into the development of plate and shell finite elements which can be used to model curved surfaces and boundaries, and be applied to the analysis of both thin and thick structures. This has led to the development of a popular group of elements generally referred to as 'degenerate elements', since they result from degeneration of three dimensional brick elements. Among the most popular of the 'degenerate elements' are the eight node isoparametric plate element (Ergatoudis et al. 1968) and the nine node isoparametric shell element (Ahmed et al. 1970). By employing Mindlin (1951) theory in the formulation of these elements the effects of transverse shear deformation are approximately accounted for. Thus, they are applicable to both thin and thick plates or shells. In addition, the elements employ an isoparametric formulation which allows them to be distorted into arbitrarily curved shapes.

Both the eight node isoparametric plate element and the nine node isoparametric shell element have been found to perform well in the analysis of moderately thick plates and shells. However, for thin plates and shells, overly

stiff solutions have been obtained and as such the results were deemed to be unreliable. This behaviour has commonly been referred to as 'locking'. Furthermore, the predicted transverse shear stresses were found to be erroneous for both thin and thick plate or shell structures. One of the earliest investigations of these problems was conducted by Zienkiewicz et al. (1971). In their work the elements were found to exhibit spurious variations of the transverse shear stresses when loaded in pure bending. According to Zienkiewicz et al. the application of a selective reduced integration scheme can improve responses for thin plates and shells. It was also found that the only reliable points for sampling of the transverse shear stresses are at the locations of the (2x2) reduced integration points. Despite the improved results obtained through application of the reduced integration technique they were unable to provide a detailed explanation as to why it works. Furthermore, beyond the elastic limit the ability to predict the spread of plasticity within the element is restricted by use of the reduced integration technique. Following their work many researchers worked to explain the reduced integration technique and also to determine its limitations. Even at the present time it is still a topic of investigation; see for example Kreja and Cywinski (1988) and Kamoulakos (1988).

Parisch (1979) found that application of the reduced integration technique leads to development of zero energy modes. These modes are not rigid body motions but deformation modes which actually produce zero strain energy. They occur when the stiffness matrix obtained using reduced integration is rank deficient. For certain boundary conditions the rank deficiency of the element may lead to singularity of the global stiffness matrix,

or to a solution which is obscured by the zero energy modes. For this reason use of the reduced integration technique is not desirable as it can not be applied with complete confidence to very general situations. This has lead to a considerable amount of research into the identification and suppression or stabilization of such zero energy modes, Briassoulis (1988), Belytschko et al. (1989) and Vu-Quoc and Mora (1989). While some of the methods perform well there is as yet no method that is generally applicable. In addition these techniques are usually complicated, difficult to implement and understand at large.

Degenerate elements based on Mindlin's theory, such as the eight node isoparametric plate element and the nine node isoparametric shell element, are frequently used for analyses of thick plates and shells. It is important to recognize that Mindlin's theory only approximately accounts for transverse shearing effects, i.e., the transverse shearing strain is assumed to be constant through the thickness and a shear correction factor κ is introduced to account for this approximation. A number of higher order plate theories exist such as those given by Lo et al. (1977), and Kant (1982). These theories eliminate the need for use of the shear correction factor κ by assuming a quadratic variation of the transverse shearing strain through the thickness. Furthermore, by allowing the out of plane normal strain to vary across the thickness its effects are included. In an effort to more accurately model thick plates Kant et al. (1982) used a higher order plate theory to formulate a new thick plate element. Although good results were reported they pointed out that further investigation was required to determine the behaviour of the element for those boundary conditions known to lead to the development of zero energy modes.

Based on all of the preceding considerations the main features of an 'ideal' shear deformable plate or shell element, according to Hinton and Owen (1984), would be as follows:

1. The element should not 'lock' in thin plate or thin shell structures.
2. The element should not contain any spurious zero energy modes.
3. The element should satisfy the usual isotropy and convergence requirements.
4. The formulation should not be based on numerically adjusted factors i.e. such as the shear correction factor κ.
5. The element should be capable of predicting accurately displacements and stresses.
6. The element should be easy to implement and use.

Much research activity in recent years has been directed towards the development of such an element. However, as of yet there appears to be no element available which satisfies all of the above criteria.

1.1.2 Finite Element Modelling of Reinforced Concrete Structures

One of the earliest applications of the finite element method to the analysis of reinforced concrete structures was by Ngo and Scordelis (1967). During recent years interest in the nonlinear analysis of concrete structures has increased steadily because of the wide use of reinforced and prestressed concrete as structural materials. Most of the past efforts have been directed toward improving the mathematical description of the concrete constitutive relations. To date a variety of constitutive models have been proposed. They include, but are not limited to elasticity Cedolin et al. (1977), elasto-plasticity Chen (1982)

and Pietruszczak et al. (1988) and endochronic theory by Bazant and Shieh (1978). However, at this time there is still no generally accepted material law available for modelling the complex behaviour of concrete.

While there have been developments in concrete constitutive relations there have also been developments in the finite element models of reinforced concrete structures. In an early attempt by Ngo and Scordelis (1967), simple beams were analysed in which the concrete and steel were represented by constant strain triangular elements. Concrete cracking was modelled using the discrete crack concept with predefined cracking patterns. This approach was later modified by Nilson (1968) who traced the progress of the discrete cracks by splitting the finite element nodes along the predetermined crack paths and then defining a new topology for subsequent analysis. At the same time another crack model was developed by Rashid (1968). In this model a discrete crack is numerically replaced by many finely spaced cracks perpendicular to the principle tensile stress direction. This model is referred to as the smeared crack model and has received extensive use since its introduction. Although attractive in its simplicity, questions have been raised regarding the smeared crack model. It was first pointed out by Bazant and Cedolin (1979) that when using the smeared crack model infinitesimally small element sizes may produce self-propagating cracks requiring negligible energy. This has raised concerns regarding the objectivity of the finite element solutions. This problem is currently being actively investigated; see for example Bazant and Oh (1983), Gajer and Dux (1989) and Choi and Kwak (1990). Developments have also taken place with regard to the modelling of the reinforcement. Most of the early reinforced concrete models employed the layer approach for modelling

reinforcement, see for example Hand et al. (1973) and Lin and Scordelis (1975). In this approach an element is divided into a number of layers through its thickness. Each layer is defined to be either concrete or steel depending upon the actual distribution of the reinforcement within the structure. The properties of the steel layers are determined by assuming that the reinforcement is smeared uniformly within the layer. This assumption can only be used when the steel bars are spaced at uniform distances and when all bars in a layer are oriented in the same direction. However, even in simple reinforced concrete slabs different regions have different spacings of the reinforcement. Even though the layered approach is still employed (for e.g. Harmon and Zhangyuan (1989), and Choi and Kwak (1990)) many researchers now employ discrete reinforcement elements within their models to enable them to more accurately model the response of the structure, see for example Marchertis et al. (1988), Bathe et al. (1989), Ranjbaran (1991) and Saturappan et al. (1992).

1.1.3 Finite Element Analysis of Laminated Fiber-Reinforced Composites

A composite is a mixture of two or more materials that are microscopically distinct but together form a single macroscopic entity. Although they have a long history, it has only been in the past two decades that they have found wide spread usage, specifically in the aerospace industry. The most commonly used composites are of the fiber-reinforced variety. They contain long continuous fibers imbedded in a matrix material. The fibers are either unidirectional or interwoven and are usually layered to form a laminate in which the fiber orientation varies from layer to layer. As a result, the strength and stiffness can be tailored to meet the specific design requirements of the

structural element being built by carefully choosing the fiber orientation in each layer of the laminate. For more information on laminated fiber-reinforced composites refer to Jones (1975) or Tsai and Hahn (1980).

In view of the increasing interest in composite materials the accurate analysis of laminated composite structures has become essential. A number of articles have appeared in the literature in this regard. In general they can be classified as being either global models or local models. Global models such as those given by Whiteney (1972), Panda and Natarajan (1979) and Phan and Reddy (1985) are displacement based formulations in which an effective laminate modulus is used. Although they adequately predict global responses such as displacements, natural frequencies and buckling loads they are not sufficiently accurate for stress prediction. On the other hand local models such as hybrid stress elements (Mau et al. 1972, Spilker 1982) or a highly refined three dimensional analysis (Barker et al. 1974) which represent each layer individually have yielded considerably better stress predictions. Although these models are superior to the global models with respect to the prediction of stresses they have certain disadvantages. The hybrid stress element formulation proposed by Mau et al. has been reported by Chaudhuri (1986) to give inaccurate predictions of the transverse shear stresses near an edge. Furthermore, the applicability of this method to asymmetrically laminated plates has not been demonstrated. Three dimensional finite element analyses become uneconomical even for a laminate with very few layers. A different approach first proposed by Pryor and Barker (1971) involves finding the inplane stresses first and then utilizing the equilibrium equations in terms of stresses to obtain the transverse shear stresses and out of plane normal stress. This method is

commonly referred to as the Equilibrium Method. Numerous researchers (Engblom and Ochoa 1985, Chaudhuri 1986, Pandya and Kant 1988, Kant and Manjunatha 1990) have adopted this approach. Although the results reported by the researchers show a definite improvement in the accuracy of the predicted laminate stresses as compared to the global methods there are still significant differences in many cases with the available elasticity solutions. Many researchers continue to work on the development of new finite element models which can predict all laminate stresses accurately. This has become increasingly important because of the role they play in the prediction of laminated composite failures.

1.2 Objectives and Scope

The objectives of the present study are as follows:

1. Development and testing of a new shell element which exhibits no 'locking' when applied to the analysis of thin plates or shells, is free of spurious zero-energy modes, does not use any numerical approximation factors, predicts accurately displacements and stresses and is easy to use and implement.
2. Development and testing of a beam element compatible with the new shell element.
3. Development and testing of a model for the analysis of composite structures of steel and concrete which includes a rational elasto-plastic model for concrete, discrete reinforcement elements, bond slip between concrete and reinforcement, supporting girders and shear connection between concrete and the supporting girders.

4. Development and testing of a new beam element and a new shell element for the analysis of laminated fiber-reinforced composites. They should provide accurate predictions of the stresses through the laminate thickness directly i.e. without requiring the use of any post analysis schemes such as the Equilibrium Method.

In Chapter Two the consistency of the formulation of the quadratic isoparametric beam element with respect to the polynomial approximations used is investigated. The existence of a spurious transverse shear strain mode is shown to be due to an inconsistency in its formulation. The formulation of a new beam element is discussed. The new element employs a consistent formulation and an improved representation of the transverse shear strain through its thickness. This eliminates the need for use of the shear correction factor κ. Material non-linearity is also included, and the nonlinear finite element analysis procedure is presented. Several examples are presented and comparisons are made for performance evaluation of the new element.

In Chapter Three a new shell element compatible with the beam element described in Chapter Two is formulated. Special attention has been given to the efficient implementation of the element by employing a stiffness sub-matrix formulation in conjunction with a modified frontal solution technique. Material non-linearity has also been included. Numerical results for a variety of problems are presented for performance evaluation of the new element.

In Chapter Four, a finite element model for reinforced concrete

structures is formulated. The new shell element described in Chapter Three is used to model reinforced and/or prestressed concrete plates or shells inconjunction with an elasto-plastic constitutive model for concrete. A one-dimensional curved bar element is formulated and used for modelling of the plane and prestressed reinforcing bars. The influence of the bond between the concrete and reinforcement is included through a joint element. Supporting girders are modelled using a modified form of the beam element described in Chapter Two. The connection of the supporting girders to the concrete shell is handled through a shear connector element. Predicted results are compared with the experimental data for verification and evaluation of the model.

In Chapter Five a new beam element and a new shell element are formulated for modelling of laminated composite beams and shells. The new elements are extensions of the beam element and the shell element described in Chapter Two and Chapter Three, respectively. In the formulation of the new elements special attention has been given to the accurate prediction of the stresses through the laminate thickness. For verification of the element formulations, and evaluation of their accuracy, several examples are presented and comparisons are made with the available elasticity solutions in the literature.

Conclusions drawn from this study, and recommendations for future research are presented in Chapter Six.

CHAPTER TWO

CONSISTENT BEAM ELEMENT FORMULATION AND APPLICATIONS

2.1 Introduction

Curved beam finite elements, which accommodate shear deformation by allowing independent displacement and rotational degrees of freedom, such as the quadratic isoparametric beam element (Hinton and Owen 1977), have been used extensively since their introduction. However, it is well known that these elements possess a spurious shear strain mode. This mode leads to overly stiff behaviour when the elements are applied to the analysis of thin beams and arches, and to unreliable predictions of the shear stress. The consistency of the formulation of these elements, with respect to the displacement fields used is examined in this chapter and the requirements for a consistent formulation which eliminates the spurious shear mode are determined.

A new curved beam element is formulated as an extension of the quadratic isoparametric beam element. This new element is referred to as the consistent beam element. The order of the polynomials used for approximation of displacements and rotations within the new element are chosen to ensure a consistent formulation. A new rotation, which varies quadratically through the thickness of the consistent beam element, is included. This new rotation allows for a parabolic representation of the shear stress and hence eliminates need for

use of the shear correction factor κ which is usually required to correct for the assumption of constant shear strain across the depth (Timoshenko 1955). In addition, the new rotation provides a cubic variation of the longitudinal displacement through the element depth. Thus warping of the section due to shearing is accounted for.

For material non-linearity an incremental elasto-plastic constitutive relation is used which employs the Huber von Mises yield criterion, an associated flow rule and isotropic hardening. The nonlinear finite element analysis is performed using a modified Newton Raphson method. Numerical results for a variety of problems are presented for performance evaluation of the consistent beam element. These include elastic, and elasto-plastic analysis of thin and thick beams and arches, and comparisons with results predicted by the quadratic isoparametric beam element.

2.2 Consistency of Formulation

The shear stress variation for beams and arches calculated using the quadratic isoparametric beam element reveals the existence of a spurious shear strain mode. A cantilever with a concentrated load applied at the free end as shown in Figure 2.1, was analysed using four quadratic isoparametric beam elements. The predicted variation of the average shear stress along the length of the cantilever is plotted in Figure 2.2 along with the variation given by Timoshenko beam theory. The existence of the spurious shear mode is apparent in the quadratic isoparametric beam element. This is explained next.

The potential energy Π for the beam is given by

$$\Pi = \frac{EI}{2}\int_0^L \left[\frac{d\theta}{dx}\right]^2 dx + \frac{GA_v}{2}\int_0^L \left[\frac{dw}{dx} - \theta\right]^2 dx - Pw(L). \qquad (2.1)$$

where

w = transverse displacement

θ = total rotation of the 'normal' to the centroidal axis

$\left[\frac{dw}{dx}\right]$ = flexural rotation of the 'normal' to the centroidal axis

$\left[\frac{d\theta}{dx}\right]$ = pseudo - curvature

EI = flexural rigidity

GA_v = shear rigidity

P = concentrated load

L = length of cantilever.

Taking the first variation of the potential energy Π yields the following Euler equations:

$$\delta\theta: \quad EI\left[\frac{d^2\theta}{dx^2}\right] + GA_v\left[\frac{dw}{dx} - \theta\right] = 0$$

$$\delta w: \quad -GA_v\left[\frac{d^2w}{dx^2} - \frac{d\theta}{dx}\right] = 0 \qquad (2.2,a\text{-}b)$$

and the following associated kinematic and natural boundary conditions:

$$\delta\theta: \quad \theta(x=0) = 0 \qquad EI\left[\frac{d\theta}{dx}\right]_{x=L} = 0$$

$$\delta w: \qquad w(x=0) = 0 \qquad GA_v \left[\frac{dw}{dx} - \theta \right]_{x=L} = P. \qquad (2.3,a\text{-}b)$$

The transverse displacement w, and the total rotation of the 'normal' to the beam axis θ can be approximated using quadratic polynomials as

$$\begin{aligned} w(x) &= a_1 + a_2 x + a_3 x^2 \\ \theta(x) &= b_1 + b_2 x + b_3 x^2. \end{aligned} \qquad (2.4,a\text{-}b)$$

These are also used in the quadratic isoparametric beam element. Substituting the polynomial approximations, equations 2.4, into the Euler equations, equations 2.2, and collecting the like terms gives

$$\begin{aligned} EI(2b_3) + GA_v(a_2 - b_1) &= 0 \\ GA_v(2a_3 - b_2) &= 0 \\ GA_v(-b_3) &= 0 \\ \\ -GA_v(2a_3 - b_2) &= 0 \\ -GA_v(-2b_3) &= 0. \end{aligned} \qquad (2.5,a\text{-}e)$$

Similarly, substituting the polynomial approximations, equations 2.4, into the boundary conditions, equations 2.3, and collecting the like terms gives

$$\begin{aligned} b_1 &= 0 \\ EI(b_2 + 2b_3 L) &= 0 \\ a_1 &= 0 \\ GA_v(a_2 + 2a_3 L - b_1 - b_2 L - b_3 L^2) &= P. \end{aligned} \qquad (2.6,a\text{-}d)$$

One possible solution of equations 2.5 and 2.6 is a trivial solution i.e. the applied load P and all coefficients of the polynomials in equations 2.4 are equal to zero. The only non-trivial solution possible is given by

$$a_1 = 0$$

$$b_1 = 0$$

$$a_2 = P\left[\frac{1}{GA_v} - \frac{L^2}{(2EI + GA_vL^2)}\right]$$

$$b_2 = \frac{2PL}{(2EI + GA_vL^2)} \qquad (2.7,a\text{-}f)$$

$$a_3 = \frac{PL}{(2EI + GA_vL^2)}$$

$$b_3 = \frac{-P}{(2EI + GA_vL^2)}$$

where coefficient b_3 is determined to be non-zero from flexural considerations according to

$$EI(2b_3) + GA_v(a_2 - b_1) = 0. \qquad (2.8)$$

As a result an inconsistency arises with equations 2.5, which require b_3 to be equal to zero. This leads to a loss of equilibrium since the Euler equations will not be satisfied. This conclusion is not restricted to the cantilever example presented. For a different configuration or loading condition only the boundary conditions change as the Euler equations remain valid in all situations for the

given formulation. It should be noted that only for the case of pure bending, is the coefficient b_3 calculated to be zero from Equation 2.8.

Following the Timoshenko beam theory, the shear strain is calculated as the difference between the flexural rotation $\left[\frac{dw}{dx}\right]$ and the total rotation θ as

$$\gamma = \left[\frac{dw}{dx} - \theta\right]. \tag{2.9}$$

Substituting the polynomial approximations for w and θ, equations 2.4, into the expression for the shear strain, Equation 2.9, gives

$$\gamma = \left[(a_2 + 2a_3x) - (b_1 + b_2x + b_3x^2)\right]. \tag{2.10}$$

Examination of Equation 2.10 reveals the absence of a quadratic term in the flexural rotation component to match that found in the total rotation. As coefficient b_3 is determined to be non-zero from flexural considerations the lack of the matching quadratic term in the flexural rotation allows a spurious quadratic mode to be superimposed over the legitimate constant and linear modes. This inconsistency in the displacement fields used in the formulation of the quadratic isoparametric beam element is responsible for the spurious shear stress variation shown in Figure 2.2. Only for the case of pure bending will no spurious shear stress variation appear.

A consistent formulation can be obtained if the transverse displacement w and the total rotation θ are approximated by cubic and quadratic polynomials, respectively, as

$$w(x) = a_1 + a_2x + a_3x^2 + a_4x^3$$
$$\theta(x) = b_1 + b_2x + b_3x^2. \qquad (2.11,a\text{-}b)$$

Substituting the polynomial approximations, equations 2.11, into the Euler equations, equations 2.2, and collecting the like terms yields

$$EI(2b_3) + GA_v(a_2) = 0$$
$$GA_v(2a_3 - b_2) = 0$$
$$GA_v(3a_4 - b_3) = 0 \qquad (2.12,a\text{-}e)$$
$$-GA_v(2a_3 - b_2) = 0$$
$$-GA_v(6a_4 - 2b_3) = 0.$$

Similarly, substituting the polynomial approximations, equations 2.11, into the boundary conditions, equations 2.3, and collecting the like terms gives

$$a_1 = 0$$
$$b_1 = 0$$
$$EI(b_2 + 2b_3 L) = 0 \qquad (2.13,a\text{-}d)$$
$$GA_v(a_2 + 2a_3L + 3a_4L^2 - b_1 - b_2L - b_3L^2) = P.$$

All coefficients of equations 2.12 and 2.13 can be uniquely determined as

$$a_2 = \frac{P}{GA}\ ;\ a_3 = \frac{PL}{2EI}\ ;\ a_4 = \frac{-P}{6EI}\ ;\ b_2 = \frac{PL}{EI}\ ;\ b_3 = \frac{-P}{2EI}. \qquad (2.14)$$

Hence the formulation is consistent and the equilibrium will always be satisfied.

The expression for the shear strain using the polynomial approximation for w and θ in equations 2.11 is given by

$$\gamma = \left[\frac{dw}{dx} - \theta \right] = \left[(a_2 + 2a_3x + 3a_4x^2) - (b_1 + b_2x + b_3x^2) \right]. \qquad (2.15)$$

Examination of Equation 2.15 reveals that the missing quadratic term in the flexural rotation component is now present. In the following sections it will be shown that the provision of a consistent formulation in this manner effectively eliminates the spurious shear strain mode.

In general, those beam elements in which the shear strain is determined as the difference between the total rotation and the flexural rotation contain an inconsistency in their formulations if the same degree polynomial is used for approximation of both displacements and rotations. A consistent formulation can be achieved for these elements by employing a polynomial for approximation of the displacements which is one degree higher than that used for approximation of the rotations.

2.3 Consistent Beam Element Formulation

2.3.1 Co-ordinate Systems and Geometry

Co-ordinate systems used in the formulation of the consistent beam element are shown in Figure 2.3, and defined as follows:

1. Global cartesian co-ordinate system x and z and the corresponding global displacements u and w.

2. Natural co-ordinates s and t where s is tangent to the curved line defined by t=constant, and t is normal to the s axis.
3. Local cartesian co-ordinate system x' and z' to define local strains and stresses; x' is tangent and z' is perpendicular to the curved centroidal axis in general.

For geometric distortion of the element a curvilinear transformation is used in terms of the s co-ordinate, and a linear transformation is used in terms of the t co-ordinate. The cross section of the beam can be arbitrary. The location of any point within the element in the global co-ordinate system (x,z) is determined by the co-ordinates of the nodal points (x_i,z_i) and vector $\mathbf{V}_i$ at each node as

$$\begin{Bmatrix} x \\ z \end{Bmatrix} = \Sigma N_i \begin{Bmatrix} x_i \\ z_i \end{Bmatrix} + \Sigma N_i \frac{t}{2} \mathbf{V}_i \tag{2.16}$$

where N_i are the quadratic interpolation functions and are given in Appendix A1 and vector $\mathbf{V}_i$ is defined as

$$\mathbf{V}_i = \begin{Bmatrix} x_i \\ z_i \end{Bmatrix}_{TOP} - \begin{Bmatrix} x_i \\ z_i \end{Bmatrix}_{BOTTOM}. \tag{2.17}$$

2.3.2 Displacement Field

To construct cubic approximations of displacements u and w, the displacement degrees of freedom at the end nodes and the one-third point nodes

are used. Quadratic approximation of rotations α and ϕ is achieved using the rotational degrees of freedom at the end nodes and the mid-side nodes. Thus, the number of degrees of freedom per node is different. Assuming that each node has four degrees of freedom (u_i, w_i, α_i, ϕ_i) then there are twenty degrees of freedom per element, however only fourteen of these are active. It should be noted that while rotation α is constant through the depth of the element, rotation ϕ varies quadratically. Hence, α produces a linear variation of displacements u and w through the depth, while ϕ gives a cubic variation as depicted in Figure 2.4.

The element displacement field is given as

$$\begin{Bmatrix} u \\ w \end{Bmatrix} = \Sigma \bar{N}_i \begin{Bmatrix} u_i \\ w_i \end{Bmatrix} - \Sigma N_i M_1 \begin{Bmatrix} \cos \gamma_i \\ \sin \gamma_i \end{Bmatrix} \alpha_i - \Sigma N_i M_2 \begin{Bmatrix} \cos \gamma_i \\ \sin \gamma_i \end{Bmatrix} \phi_i \quad (2.18)$$

where N_i and $\bar{N}_i$ are the quadratic and cubic shape functions, respectively, and γ_i is the angle between the local axes (x',z') and the global axes (x,z) at the i^{th} node. Shape functions M_1 and M_2 approximate the displacement field through the depth due to rotations α and ϕ, respectively, and are given by

$$M_1 = \frac{h_i t}{2} \qquad M_2 = \frac{h_i t}{2}(1 - t^2) \quad (2.19)$$

where h_i is the beam thickness at the i^{th} node. The derivation of the through thickness displacement field due to ϕ is given in Appendix B and shape functions N_i and $\bar{N}_i$ can be found in Appendix A1.

The cosine and sine of angle γ are given by

$$\cos\gamma = \frac{\partial x}{\partial s} \Bigg/ \sqrt{\left[\frac{\partial x}{\partial s}\right]^2 + \left[\frac{\partial z}{\partial s}\right]^2}$$

$$\sin\gamma = \frac{\partial z}{\partial s} \Bigg/ \sqrt{\left[\frac{\partial x}{\partial s}\right]^2 + \left[\frac{\partial z}{\partial s}\right]^2} \qquad (2.20)$$

where $\frac{\partial x}{\partial s}$ and $\frac{\partial z}{\partial s}$ are determined using Equation 2.16. It should be noted that the consistent beam element is subparametric because u and w are approximated cubically while the geometry is interpolated quadratically.

2.3.3 Strain-Displacement and Stress-Strain Relationships

The relationship between local strains $\{\epsilon'\}$ at any point within the element and the degrees of freedom is required. For small deflections, the strains in the local (x',z') co-ordinate system are given by

$$\{\epsilon'\} = \begin{Bmatrix} \epsilon_{x'x'} \\ \gamma_{x'z'} \end{Bmatrix} = \begin{bmatrix} \frac{\partial}{\partial x'} & 0 \\ \frac{\partial}{\partial z'} & \frac{\partial}{\partial x'} \end{bmatrix} \begin{Bmatrix} u' \\ w' \end{Bmatrix} \qquad (2.21)$$

where displacements u' and w' are along x' and z', respectively. The local displacements (u',w') are calculated from the global displacements (u, w) according to

$$\begin{Bmatrix} u' \\ w' \end{Bmatrix} = [\theta] \begin{Bmatrix} u \\ w \end{Bmatrix} = \begin{bmatrix} \cos\gamma & \sin\gamma \\ -\sin\gamma & \cos\gamma \end{bmatrix} \begin{Bmatrix} u \\ w \end{Bmatrix}. \qquad (2.22)$$

The transformation matrix $[\theta]$ is composed of the sine and cosine of the angle γ between the local axes (x',z') and the global axes (x,z) at the point in the element where the displacements are to be transformed.

Using Equation 2.18 the product in Equation 2.22 yields the local displacements in terms of the global degrees of freedom as

$$\begin{Bmatrix} u' \\ w' \end{Bmatrix} = \Sigma \bar{N}_i \begin{Bmatrix} \cos\gamma \\ -\sin\gamma \end{Bmatrix} u_i + \Sigma \bar{N}_i \begin{Bmatrix} \sin\gamma \\ \cos\gamma \end{Bmatrix} w_i - \Sigma N_i M_1 \begin{Bmatrix} \cos\gamma\cos\gamma_i \\ -\sin\gamma\cos\gamma_i \end{Bmatrix}$$

$$\begin{Bmatrix} +\sin\gamma\sin\gamma_i \\ +\cos\gamma\sin\gamma_i \end{Bmatrix} \alpha_i - \Sigma N_i M_2 \begin{Bmatrix} \cos\gamma\cos\gamma_i + \sin\gamma\sin\gamma_i \\ -\sin\gamma\cos\gamma_i + \cos\gamma\sin\gamma_i \end{Bmatrix} \phi_i. \qquad (2.23)$$

Substituting Equation 2.23 into Equation 2.21 and carrying out the required differentiation yields the desired relationship between the local strains and the global degrees of freedom as

$$\begin{Bmatrix} \epsilon_{x'x'} \\ \gamma_{x'z'} \end{Bmatrix} = \begin{bmatrix} \frac{\partial \bar{N}_i}{\partial x'} \cos\gamma & \frac{\partial \bar{N}_i}{\partial x'} \sin\gamma & -M_1 \, CU_i \frac{\partial N_i}{\partial x'} \\ -\frac{\partial \bar{N}_i}{\partial x'} \sin\gamma & \frac{\partial \bar{N}_i}{\partial x'} \cos\gamma & -N_i CU_i \frac{\partial M_1}{\partial z'} - M_1 \, CW_i \frac{\partial N_i}{\partial x'} \end{bmatrix}$$

$$\begin{bmatrix} & -M_2\ CU_i\ \dfrac{\partial N_i}{\partial x'} & \\ -N_i\ CU_i\ \dfrac{\partial M_2}{\partial z'} & -M_2\ CW_i\ \dfrac{\partial N_i}{\partial x'} & \end{bmatrix} \begin{Bmatrix} u_i \\ w_i \\ \alpha_i \\ \phi_i \end{Bmatrix} \tag{2.24}$$

where $CU_i = \cos\gamma \cos\gamma_i + \sin\gamma \sin\gamma_i$

$CW_i = -\sin\gamma \cos\gamma_i + \cos\gamma \sin\gamma_i$.

Equation 2.24 may also be written as

$$\{\epsilon'\} = [B']\{d\} \tag{2.25}$$

where $[B']$ = strain matrix relating degrees of freedom to local strains

$\{d\}$ = vector of global degrees of freedom.

The stress-strain relationship used is the generalized Hooke's Law given by

$$\{\sigma'\} = \begin{Bmatrix} \sigma_{x'x'} \\ \tau_{x'z'} \end{Bmatrix} = [D']\left[\{\epsilon'\} - \{\epsilon'_0\}\right] + \{\sigma'_0\} \tag{2.26}$$

where $[D']$ = elasticity matrix in the local co-ordinate system

$\{\epsilon'_0\} = \{\sigma'_0\}$ = vector of initial local strains and stresses, respectively.

The elasticity matrix $[D']$ for the beam problem is given by

$$[D'] = \begin{bmatrix} E & O \\ O & G \end{bmatrix} \tag{2.27}$$

where E and G are the modulus of elasticity and shear modulus, respectively. It should be noted that the shear correction factor κ is not required because of the parabolic approximation of the shear stress through the thickness.

2.3.4 Stiffness Matrix

Application of the principle of virtual work leads to the following expression for the discretized equations of equilibrium (Zienkiewicz 1977)

$$[k]\{d\} = \{f\}. \tag{2.28}$$

The element stiffness matrix [k] is given by

$$[k] = \int_V [B']^T [D'] [B'] \, dV \tag{2.29}$$

and the element load vector {f} is given by

$$\{f\} = \int_V [N]^T \{b\} \, dV + \int_S [N]^T \{T\} \, dS + [N]^T \{P\} \tag{2.30}$$

where

$[N]^T$ = matrix of shape functions relating the degrees of freedom to the global displacements u and w

$\{b\}$, $\{T\}$, $\{P\}$ = body force, surface traction and point load vectors, respectively.

Both the stiffness matrix and the load vector are obtained using numerical integration by employing the Gaussian-Quadrature scheme.

The partial derivatives with respect to the local (x',z') co-ordinate system found in the strain-displacement matrix [B'], Equation 2.24, can be written in terms of derivatives in the curvilinear co-ordinate system using the chain rule as

$$\frac{\partial}{\partial x'} = \frac{\partial s}{\partial x'}\frac{\partial}{\partial s} + \frac{\partial t}{\partial x'}\frac{\partial}{\partial t}$$
$$\frac{\partial}{\partial z'} = \frac{\partial s}{\partial z'}\frac{\partial}{\partial s} + \frac{\partial t}{\partial z'}\frac{\partial}{\partial t}. \qquad (2.31,a\text{-}b)$$

Since the local axes x' and z' are coincident with the curvilinear co-ordinates s and t, respectively, then

$$\frac{\partial t}{\partial x'} = \frac{\partial s}{\partial z'} = 0$$

$$\frac{\partial s}{\partial x'} = 1 \Big/ \sqrt{\left[\frac{\partial x}{\partial s}\right]^2 + \left[\frac{\partial z}{\partial s}\right]^2} \qquad (2.32,a\text{-}c)$$

$$\frac{\partial t}{\partial z'} = 1 \Big/ \sqrt{\left[\frac{\partial x}{\partial t}\right]^2 + \left[\frac{\partial z}{\partial t}\right]^2}$$

and $\frac{\partial x}{\partial s}$, $\frac{\partial z}{\partial s}$, $\frac{\partial x}{\partial t}$ and $\frac{\partial z}{\partial t}$ are determined using Equation 2.16.

Finally, the element stiffness matrix is calculated using the following

equation:

$$[k] = \int_{-1}^{+1} \int_{-1}^{+1} [B']^T [D'] [B'] \det|J| \; b \; dsdt \qquad (2.33)$$

where the determinant of the Jacobian matrix is given by

$$\det|J| = \left[\frac{\partial x}{\partial s} \cdot \frac{\partial z}{\partial t} \right] - \left[\frac{\partial z}{\partial s} \cdot \frac{\partial x}{\partial t} \right] \qquad (2.34)$$

and b is the width of the beam. Integration of Equation 2.33 is performed using three integration points along the s co-ordinate and three integration points through the thickness along t.

It should also be noted that an eigenvalue test of the element stiffness matrix [k] was performed. The results verified the existence of the required rigid body motions and the absence of any spurious zero-energy deformation modes.

2.4 Elasto-Plastic Formulation

For elasto-plastic analysis of beams and arches an incremental approach is adopted. This requires use of an instantaneous elasto-plastic constitutive relationship and formulation of an incremental load analysis procedure.

2.4.1 Elasto-Plastic Constitutive Relationship

The nonlinear material behaviour is described using plasticity theory. This requires the definition of three properties in addition to the elastic stress-strain relationship. These are a yield condition, a flow rule and a hardening rule. The construction of the elasto-plastic stress-strain matrix is performed in the usual manner. Only the information which is specific to the present formulation is presented. For more information on plasticity theory refer to Mendelson (1970) or Chen and Han (1988).

In this study the Huber von Mises yield criterion is adopted. The yield function F corresponding to the Huber von Mises yield criterion and a general state of stress is given by

$$F = \bar{\sigma} - \sigma_Y = [\frac{1}{2}(\sigma_{xx} - \sigma_{yy})^2 + \frac{1}{2}(\sigma_{yy} - \sigma_{zz})^2 + \frac{1}{2}(\sigma_{zz} - \sigma_{xx})^2 + 3\tau_{xy}^2 + 3\tau_{xz}^2 + 3\tau_{yz}^2]^{1/2} - \sigma_Y = 0. \tag{2.35}$$

Yielding occurs when the effective stress $\bar{\sigma}$ equals the uniaxial yield stress σ_Y, i.e. when the yield function F is equal to zero. For $\sigma_{yy} = \sigma_{zz} = \tau_{xy} = \tau_{yz} = 0$ the effective stress becomes

$$\bar{\sigma} = [\sigma_{xx}^2 + 3\tau_{xz}^2]^{1/2}. \tag{2.36}$$

Now re-writing the yield function F in terms of local stresses $\sigma_{x'x'}$ and $\tau_{x'z'}$ gives

$$F = \bar{\sigma} - \sigma_Y = [\, \sigma_{x'x'}^2 + 3\tau_{x'z'}^2 \,]^{1/2} - \sigma_Y = 0. \qquad (2.37)$$

Beyond the proportional limit an incremental stress-strain relationship is employed which is expressed as

$$\begin{Bmatrix} d\sigma_{x'x'} \\ d\tau_{x'z'} \end{Bmatrix} = [Dep'] \begin{Bmatrix} d\epsilon_{x'x'} \\ d\gamma_{x'z'} \end{Bmatrix} \qquad (2.38)$$

where [Dep′] is the instantaneous elasto-plastic constitutive matrix referred to the local co-ordinate system. For an associated flow rule and isotropic hardening it takes the following form (Zienkiewicz 1977)

$$[Dep'] = [D'] - [D'] \frac{1}{H' + \left\{ \frac{\partial F}{\partial \sigma} \right\}^T [D'] \left\{ \frac{\partial F}{\partial \sigma} \right\}} \left\{ \frac{\partial F}{\partial \sigma} \right\} \left\{ \frac{\partial F}{\partial \sigma} \right\}^T [D']. \qquad (2.39)$$

Parameter H′ is the plastic modulus and is the slope of the uniaxial stress-strain curve beyond the yield limit. Assuming a bilinear uniaxial stress-strain curve for elasto-plastic material behaviour the plastic modulus H′ is given as

$$H' = E_T / (1 - E_T / E) \qquad (2.40)$$

where E and E_T are the elastic and tangent moduli, respectively.

Using Equation 2.37 the vector $\left\{ \frac{\partial F}{\partial \sigma} \right\}$ can be obtained as

$$\left\{ \frac{\partial F}{\partial \sigma} \right\} = \begin{Bmatrix} \dfrac{\sigma_{x'x'}}{\bar{\sigma}} \\ \\ \dfrac{3\tau_{x'z'}}{\bar{\sigma}} \end{Bmatrix}. \tag{2.41}$$

Substituting $\left\{ \frac{\partial F}{\partial \sigma} \right\}$ and the elastic stress-strain matrix [D′], Equation 2.27, into Equation 2.39 and performing the required multiplications gives the elasto-plastic constitutive relation as

$$[Dep'] = \frac{1}{H' + \dfrac{[\sigma_{x'x'}^2 + 9G\tau_{x'z'}^2]}{\bar{\sigma}^2}} \begin{bmatrix} E\left\{ \dfrac{1 - E\sigma_{x'x'}^2}{\bar{\sigma}^2} \right\} & \left\{ \dfrac{3EG\sigma_{x'x'}\tau_{x'z'}}{\bar{\sigma}^2} \right\} \\ \left\{ \dfrac{3EG\sigma_{x'x'}\tau_{x'z'}}{\bar{\sigma}^2} \right\} & G\left\{ \dfrac{1 - 9G\tau_{x'z'}^2}{\bar{\sigma}^2} \right\} \end{bmatrix}. \tag{2.42}$$

2.4.2 Nonlinear Finite Element Analysis Procedure

Using the principle of virtual displacements the discretized equations of equilibrium can be written as

$$\int_V [B']^T \{\sigma'\}\, dV + \{R\} = 0 \tag{2.43}$$

where {R} is the applied load vector. In an incremental analysis the total load

{R} acting on the structure is applied in increments. Because of the impending nonlinearity a certain unbalance of forces will exist between the external and the internal forces. This unbalance is minimized to a tolerable magnitude by employing an iterative procedure.

For the m^{th} iteration during the n^{th} load increment Equation 2.43 can be re-written as

$$\{\phi\}_n^m = \int_V [B']^T \{\sigma'\}_n^m \, dV + \{R\}_n \tag{2.44}$$

where $\{\phi\}$ is the unbalanced force vector called the residual vector. In this study a modified Newton-Raphson iterative method is adopted. The displacement increment corresponding to the residual vector $\{\phi\}_n^m$ is calculated as

$$\{\Delta d\}_n^m = [K_T(\sigma')_n^m]^{-1} \{\phi\}_n^m \tag{2.45}$$

where $[K_T(\sigma')_n^m]$ is the tangential stiffness matrix evaluated at the beginning of each load increment. The updated displacements and stresses are then calculated and the residual vector for the next iteration $\{\phi\}_n^{m+1}$ is determined. This process continues until the magnitude of the residual load vector is suitably small. The combined incremental/iterative approach is shown schematically in Figure 2.5.

The frontal solution technique is used to solve the discretized equations of equilibrium. It has been designed to minimize the core storage

requirement and the number of arithmetic operations. For more information refer to Irons (1970) and Hinton and Owen (1977).

The steps used in the nonlinear analysis algorithm are summarized as follows:

1. After the iterative approach has converged for the $(n-1)^{th}$ load increment in m iterations, the residual load vector is $\{\phi\}^{m}_{n-1}$ which will be reasonably negligible. The tangential stiffness matrix $[K_T(\sigma')^0_n]$ for the next load increment (i.e. the n^{th} load increment) is evaluated using the elasto-plastic constitutive matrix, Equation 2.42, and the state of stress at the end of the previous load increment. For the first iteration of the n^{th} load increment, the displacement increment $\{\Delta d\}^1_n$ is given by

$$\{\Delta d\}^1_n = [K_T(\sigma')^0_n]^{-1} \left[\{\phi\}^0_n + \Delta\{R\}_n \right] \tag{2.46}$$

where $\{\phi\}^0_n = \{\phi\}^m_{n-1}$.

2. Update the displacements

$$\{d\}^m_n = \{d\}^0_n + \{\Delta d\}^m_n \tag{2.47}$$

where $\{d\}^0_n = \{d\}^m_{n-1}$ for the first iteration of the n^{th} load increment and $\{d\}^0_n = \{d\}^{m-1}_n$ for subsequent iterations.

3. For each element the elemental vector of displacement increments $\{\Delta d^e\}^m_n$ is extracted from $\{\Delta d\}^m_n$ and the following steps are

performed at each Gaussian integration point;

(a) Compute incremental strains and stresses

$$\{\Delta\epsilon'^{e}\}_n^m = [B'] \{\Delta d^e\}_n^m. \tag{2.48}$$

Determine the loading state (i.e. plastic loading, elastic loading, or unloading) corresponding to the strain increment. Using the appropriate constitutive matrix calculate the stress increment

$$\{\Delta\sigma'^{e}\}_n^m = [Dep'] \{\Delta\epsilon'^{e}\}_n^m. \tag{2.49}$$

The algorithm for stress calculation follows that given by Owen and Hinton (1980).

(b) Update stresses and strains

$$\begin{aligned} \{\epsilon'^{e}\}_n^m &= \{\epsilon'^{e}\}_n^0 + \{\Delta\epsilon'^{e}\}_n^m \\ \{\sigma'^{e}\}_n^m &= \{\sigma'^{e}\}_n^0 + \{\Delta\sigma'^{e}\}_n^m \end{aligned} \tag{2.50,a-b}$$

where $\{\epsilon'^{e}\}_n^0$ and $\{\sigma'^{e}\}_n^0$ are equal to $\{\epsilon'^{e}\}_{n-1}^m$ and $\{\sigma'^{e}\}_{n-1}^m$, respectively, for the first iteration of the n^{th} load increment and $\{\epsilon'^{e}\}_n^{m-1}$ and $\{\sigma'^{e}\}_n^{m-1}$, respectively, for subsequent iterations.

(c) Compute the elemental residual load vector

$$\{\phi^e\}_n^m = \int_V [B']^T \{\sigma'^{e}\}_n^m \, dV + \{R^e\}_n. \tag{2.51}$$

(d) Add the elemental residual load vectors $\{\phi^e\}_n^m$ to obtain the global residual vector $\{\phi\}_n^m$.

4. Compute the new displacement increment

$$\{\Delta d\}_n^{m+1} = [K_T(\sigma')_n^0]^{-1} \{\phi\}_n^m \tag{2.52}$$

using the new residual load vector.

5. Repeat steps 2 to 4 until the solution has converged to the desired tolerance which is achieved when

$$\frac{\{\Delta d\}^T{}_n^m \{\phi\}_n^m}{\{\Delta d\}^T{}_n^1 \{\phi\}_n^1} \leq TOL \tag{2.53}$$

i.e. m^{th} increment in the internal energy (i.e. the amount of work done by the out of balance loads on the displacement increments) is compared to the initial internal energy increment (Bathe 1982). Convergence is reached when the specified value of TOL is obtained. A typical value for TOL is between one and five percent.

6. Apply the next load increment.

2.5 Numerical Examples

In the following numerical examples the results have been obtained without employing the reduced integration technique for either the consistent beam element or the quadratic isoparametric beam element.

2.5.1 Elimination of Spurious Shear Stress Mode

To illustrate elimination of the spurious shear stress mode the cantilever shown in Figure 2.1 has been analysed using four consistent beam elements. The variation of the average shear stress along the length of the cantilever as calculated by the consistent beam element model is plotted in Figure 2.2 and compared with that given by the quadratic isoparametric beam element and Timoshenko beam theory. The figure clearly illustrates that the consistent beam element is free of spurious shear stress oscillations which plague the quadratic isoparametric beam element. Thus, the existence of the spurious shear stress oscillation in the quadratic isoparametric beam element is a direct result of the inconsistency in its formulation.

2.5.2 Degeneration to Slender Beam Solution

The behaviour of the consistent beam element, as the length to depth ratio increases, is now investigated. A prismatic beam fixed at both ends and subjected to a uniformly distributed load as shown in Figure 2.6 is used for this purpose.

The beam is modelled using four consistent beam elements and has been analysed for aspect ratios ranging from ten to two hundred. The normalized middle span deflection of the beam as predicted by the consistent beam element model versus the aspect ratio is plotted in Figure 2.7 and compared with the deflection from the beam theory. Also plotted in the figure is the normalized deflection predicted by the quadratic isoparametric beam

element. As the aspect ratio is increased the consistent beam element model exhibits convergence to the thin beam solution. However, the deflections predicted by the quadratic isoparametric beam element approach the thin beam solution and then diverge, yielding overly stiff results. This example clearly illustrates that the poor response exhibited by the quadratic isoparametric beam element for analysis of slender beams is a consequence of the inconsistency in its formulation.

2.5.3 Thick Beam Under Sinusoidal Transverse Loading

A simply supported thick beam has been analysed to illustrate the ability of the consistent beam element to predict the normal stress and shear stress distributions through the depth of the beam. The material properties, dimensions, and loading are as shown in Figure 2.8. Half of the beam has been modelled using four consistent beam elements by making use of symmetry. The beam has also been analysed using four quadratic isoparametric beam elements. The predicted mid-span deflection and stress distributions are compared with those determined using an elasticity solution given by Little (1973).

The predicted normal stress and shear stress distributions through the beam thickness are plotted in Figure 2.9 and Figure 2.10, respectively. Also plotted are the stress distributions given by the elasticity solution. As can be observed the normal stress and shear stress distributions predicted by the consistent beam model are in excellent agreement with the elasticity solution unlike the stress distributions predicted by the quadratic isoparametric beam model. In Table 2.1 the mid-span deflection predicted by the consistent beam

Table 2.1: Thick beam normalized mid-span deflections.	
Elasticity	1.00
Consistent beam model	1.09
Quadratic beam model	1.20

model and the quadratic isoparametric beam model are normalized with respect to the deflection given by the elasticity solution. The deflection predicted by the consistent beam model is seen to be in good agreement with that given by the elasticity solution and is considerably better than that predicted by the quadratic isoparametric beam model.

This example illustrates that by including the additional rotation ϕ excellent predictions of the normal stress and shear stress distributions through the thickness of the consistent beam element can be achieved.

2.5.4 Thin Pinched Ring

To illustrate the performance of the consistent beam element when distorted, the pinched ring shown in Figure 2.11 is analysed. The analysis has been performed using four consistent beam elements to model a quarter of the ring from point A to B. The quadrant AB has also been analysed using four quadratic isoparametric beam elements. An energy solution for the radial deflection at point A is given by Prathap and Babu (1986). In Table 2.2 the radial deflection at point A predicted by the consistent beam model and the quadratic isoparametric beam model are normalized with respect to the

Table 2.2: Pinched ring normalized radial deflections.	
Elasticity	1.00
Consistent beam model	0.913
Quadratic beam model	0.183

deflection given by the energy solution. The deflection predicted by the consistent beam model is in excellent agreement with that given by the energy solution, unlike that predicted by the quadratic isoparametric beam model. This example confirms that the consistent beam element performs very well when distorted. It also illustrates the severe effect the spurious shear mode has on the performance of the quadratic isoparametric beam element.

2.5.5 Elasto-Plastic Analysis of a Thick Beam

An elastic perfectly plastic analysis of a deep beam fixed at both ends with a concentrated load applied at mid-span is performed using ten consistent beam elements to model half of the beam. The predicted mid-span deflection, axial and shear stress distributions are compared with the results obtained using the ten node triangular planar elasto-plastic element. Six planar elasto-plastic elements through the depth and ten in the longitudinal direction have been employed for a total of one hundred and twenty elements. The geometry, material properties, and loading are as shown in Figure 2.12.

A plot of the applied load versus the mid-span deflection as predicted by the consistent beam element model and the planar elasto-plastic model is

shown in Figure 2.13. It is seen that the response predicted by the consistent beam elements is in very good agreement with that given by the planar elasto-plastic elements. The normal and shear stress distributions through the depth of the beam at the fixed end are plotted in Figure 2.14 and Figure 2.15 for load levels P = 3.0 MN (elastic) and P = 7.0 MN (ultimate), respectively. For P = 3.0 MN it is observed that the consistent beam element model predicts a normal stress distribution which is very close to that given by the planar elasticity elements. Also, the nonlinear distribution of the normal stress due to the restraint of warping is clearly visible. Even after yielding of the cross section (i.e. P = 7.0 MN) it is seen that the consistent beam element model predicts a normal stress distribution which is very close to that given by the planar elasto-plastic elements.

The shear stress distribution predicted by the consistent beam elements for P = 3.0 MN is seen to be in very good agreement with that given by the planar elasticity model. However, for P = 7.0 MN there is a significant difference in the two solutions. It is observed that the distribution predicted by the planar elasto-plastic model does not satisfy the stress free conditions on the top and bottom surfaces of the beam. It is believed that if the mesh used in the planar elasto-plastic model were refined through the depth of the beam the predicted distribution would more closely approximate the stress free conditions, and also the distribution of shear stress as given by the consistent beam elements. Needless to say that the stress distributions at the fixed section are generally very complex.

The normal stress and shear stress distributions through the depth of

the beam at 12 cm from the fixed end are plotted in Figure 2.16 and Figure 2.17 for load levels P = 3.0 MN and P = 7.0 MN, respectively. For both load levels the shear and normal stress distributions predicted by the consistent beam elements are observed to be in excellent agreement with the distributions given by the planar elasto-plastic elements. Also, the effect of the warping restraint at the fixed end on the normal stress distributions at one-fifth depth away is seen to be insignificant.

To illustrate the spread of plasticity effective stress contours predicted by the consistent beam elements and the planar elasto-plastic elements are plotted in Figure 2.18 and Figure 2.19 for load levels P = 3.0 MN and P = 7.0 MN, respectively. For P = 3.0 MN a very good agreement is observed. However, for P = 7.0 MN the consistent beam model predicts effective stresses near the fixed end at the centroidal axis which are higher than those predicted by the planar elasto-plastic elements. This discrepancy is due to the difference in the shear stress distributions predicted at the fixed end as discussed previously. Thus, the consistent beam element model presented is an accurate and computationally efficient model for the inelastic analysis of thin and thick beams.

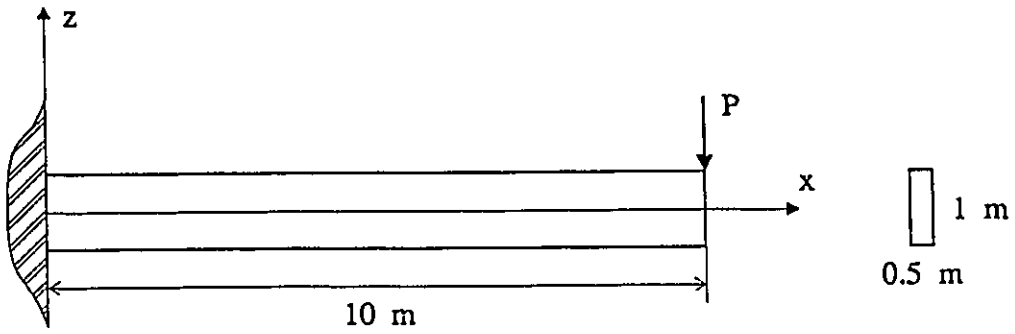

E = 200000 MPa $\quad \nu = 0.25$

P = 10 MN

Figure 2.1: Dimensions, loading and material properties of prismatic cantilever.

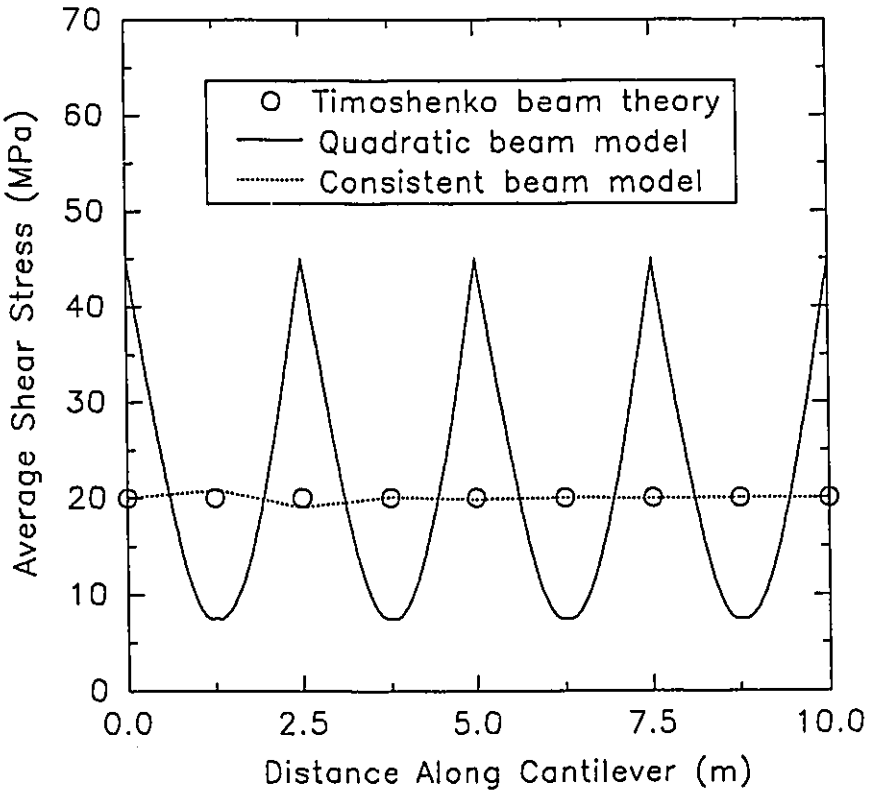

Figure 2.2: Average shear stress variation along the length of a prismatic cantilever subjected to a concentrated load at its free end.

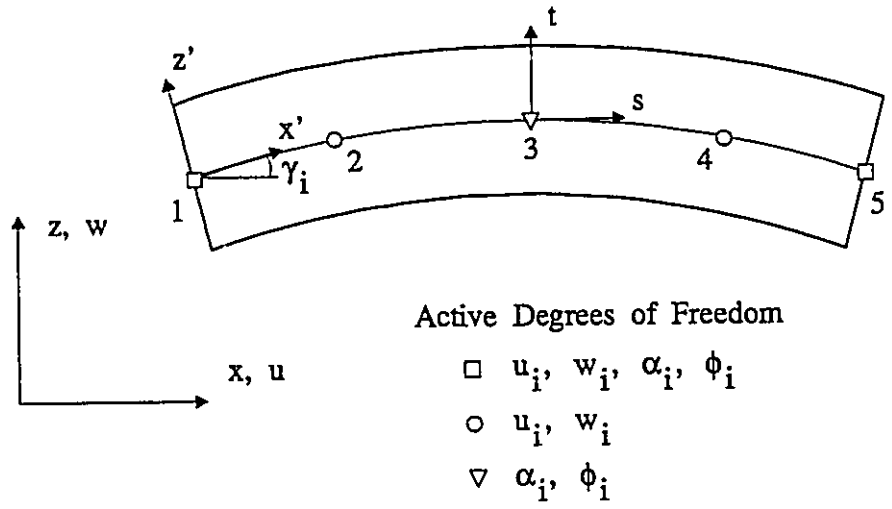

Figure 2.3: Consistent beam element co-ordinate systems and degrees of freedom.

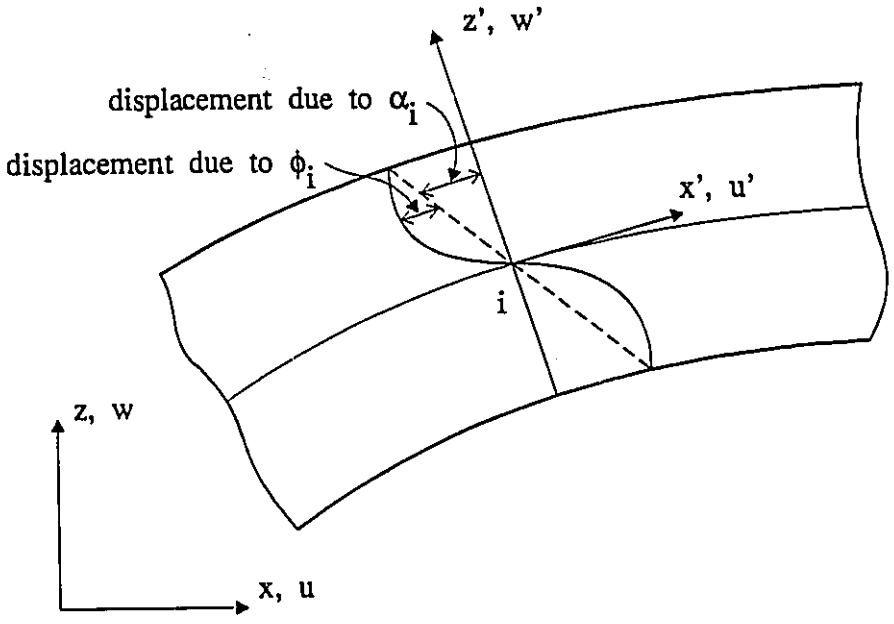

Figure 2.4: Cross sectional deformation due to rotations α_i and ϕ_i.

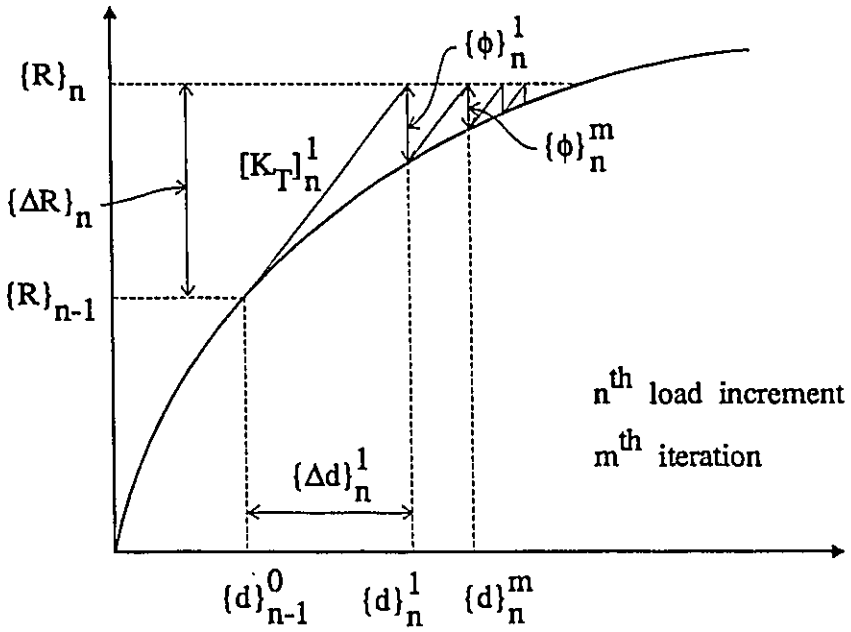

Figure 2.5: Incremental load analysis with modified Newton-Raphson iterative procedure.

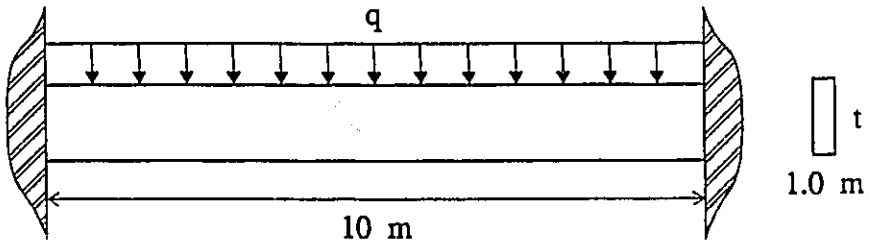

E = 200000 MPa $\quad$ ν = 0.25

t = 1 m, 0.4 m, 0.125 m, 0.08 m, 0.05m $\quad$ q = 1.0 MPa

Figure 2.6: Dimensions, loading and material properties of fix-fix beam subjected to a U.D.L.

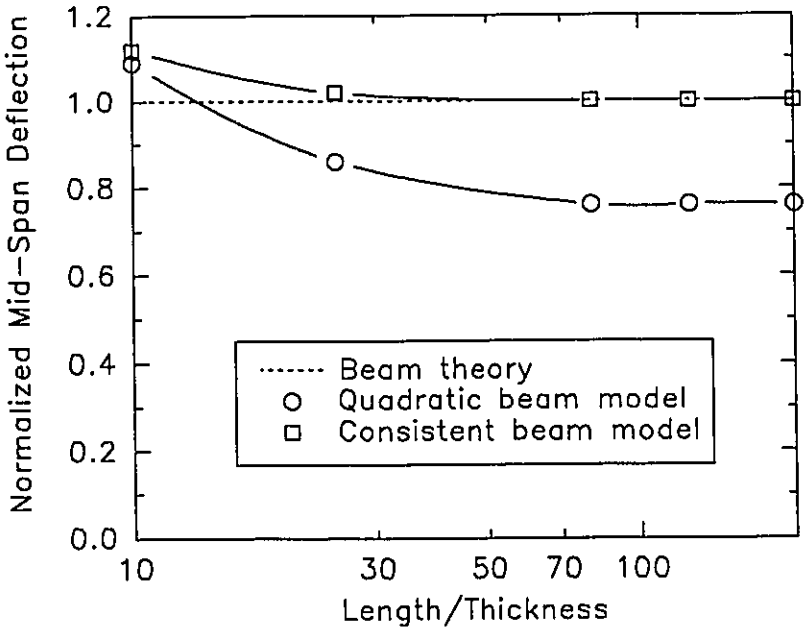

Figure 2.7: Normalized mid-span deflection versus length to thickness ratio for a fix-fix beam under a uniformly distributed load.

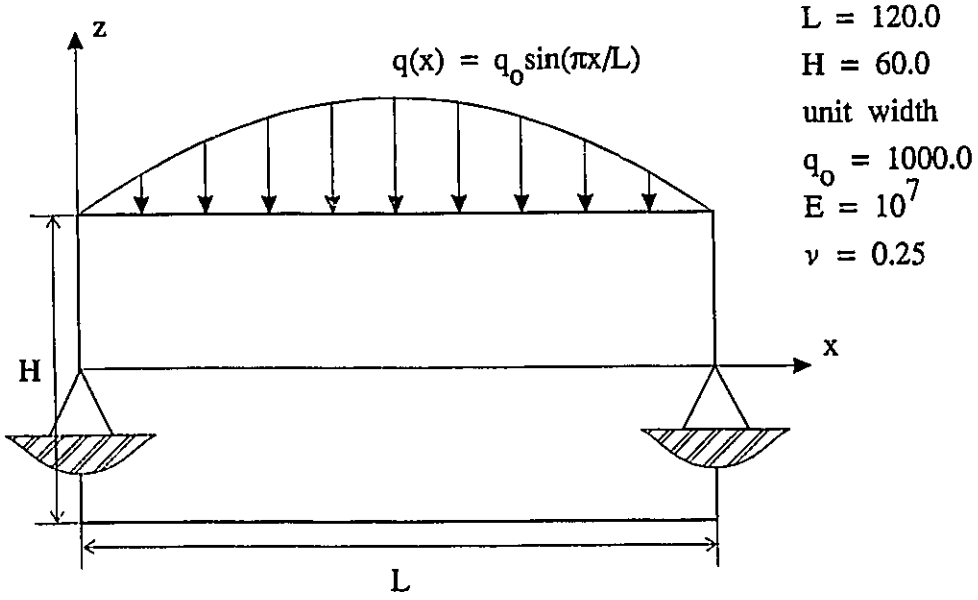

Figure 2.8: Dimensions, loading, and material properties of simply supported thick beam.

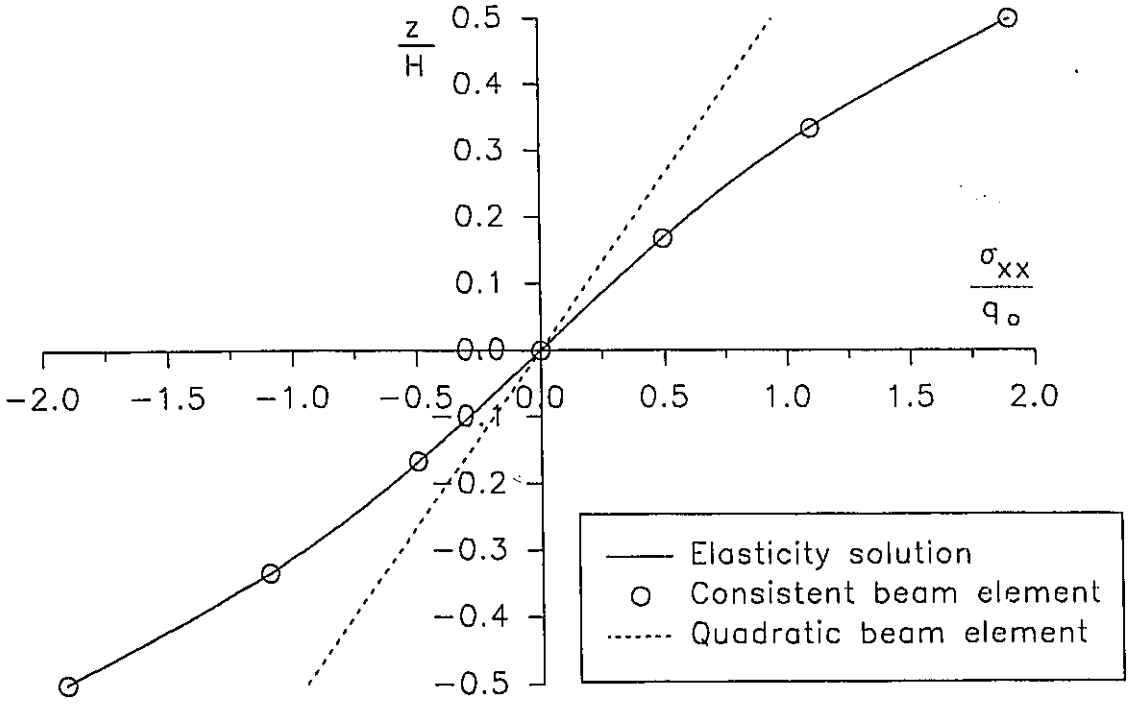

Figure 2.9: Thick beam normal stress distribution at x=L/4.

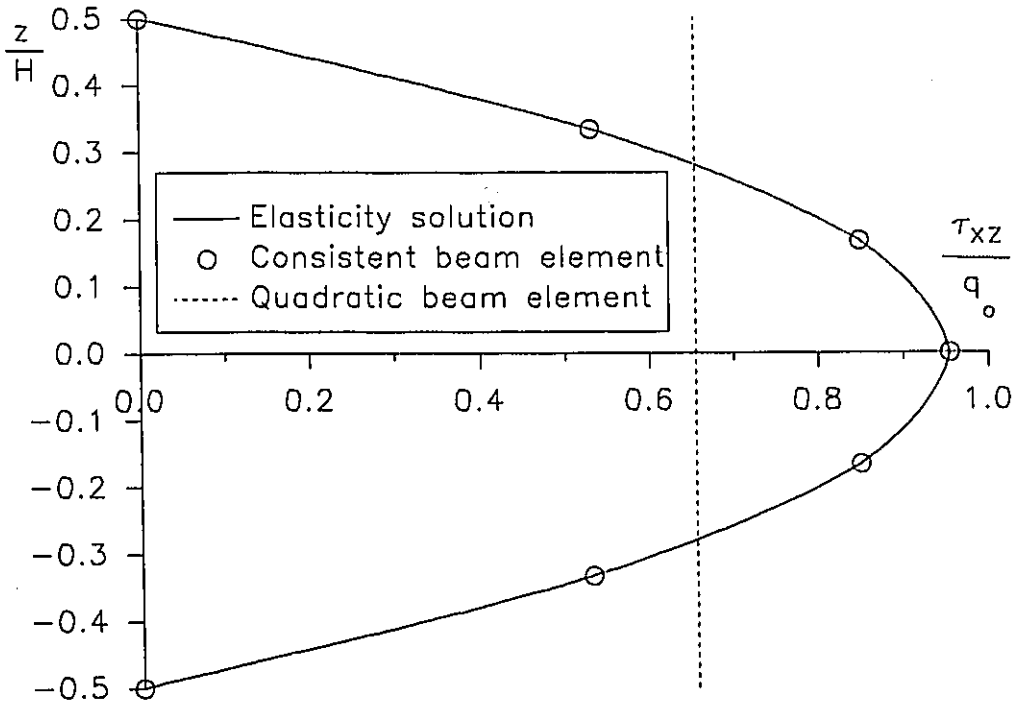

Figure 2.10: Thick beam shear stress distribution at x=0.

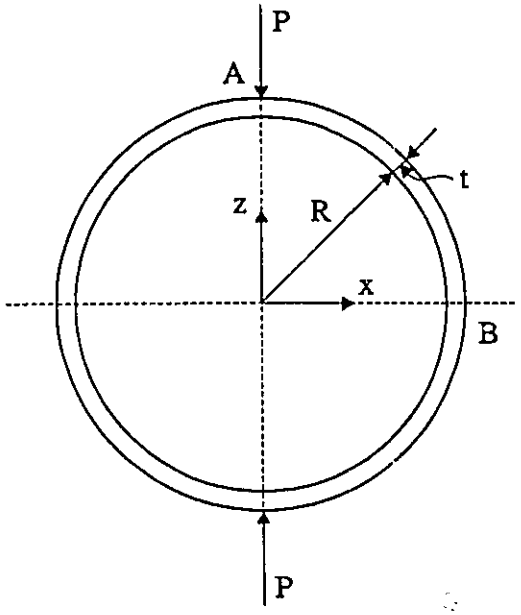

R = 4.953 in.
t = 0.094 in.
unit width
$E = 10.5 \times 10^6$ psi
$\nu = 0.3125$
P = 100 lbs

Figure 2.11: Geometry, loading and material properties of thin pinched ring.

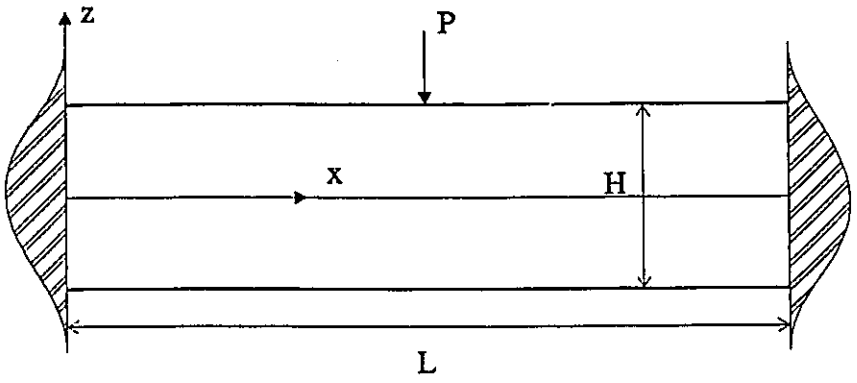

L = 2.4 m
H = 0.6 m
Width = 0.3 m

E = 200 GPa
$\nu = 0.25$
$\sigma_y = 250$ MPa
$E_T = 0.0$

Figure 2.12: Geometry, material properties and loading for fix-fix thick beam.

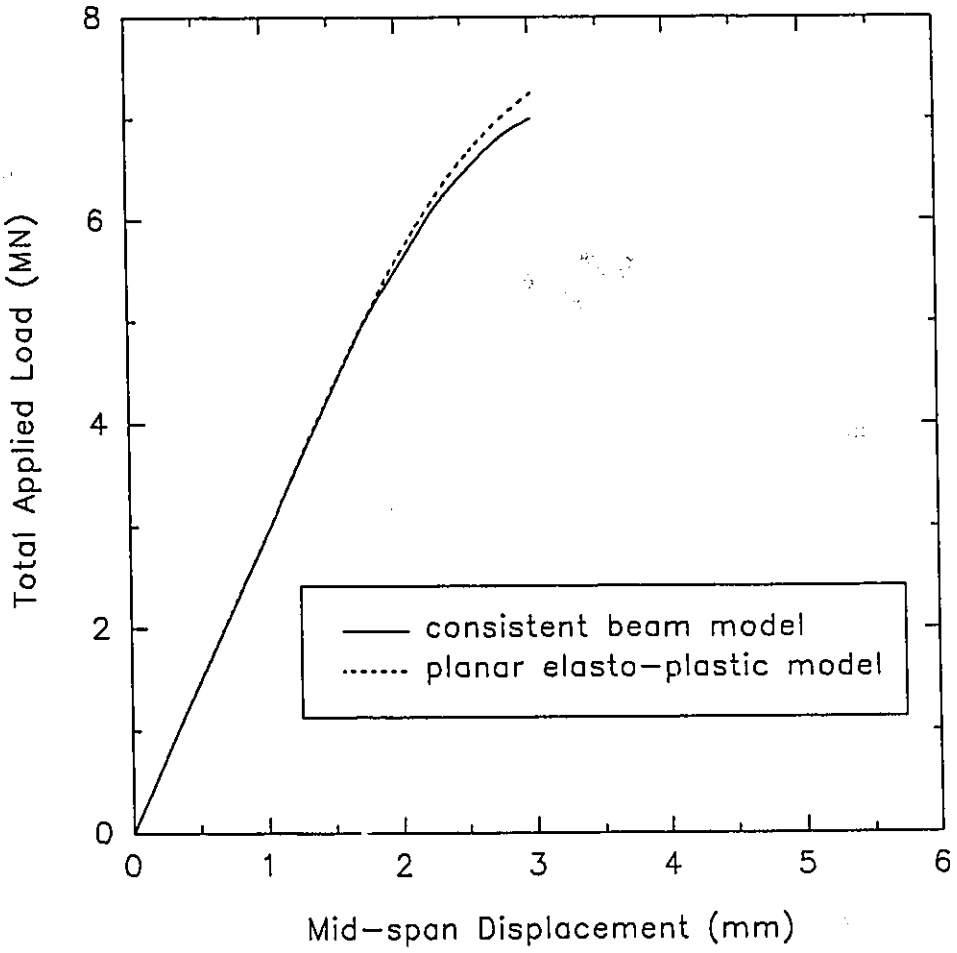

Figure 2.13: Applied load versus mid-span displacement for elasto-plastic analysis of thick fix-fix beam.

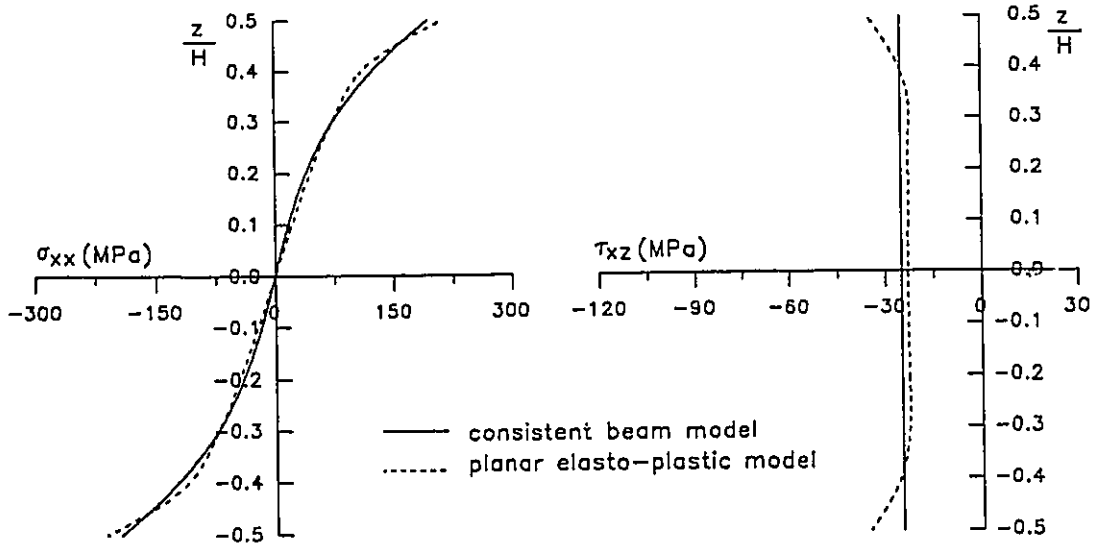

Figure 2.14: Normal stress and shear stress distributions at fixed end of beam for P = 3 MN.

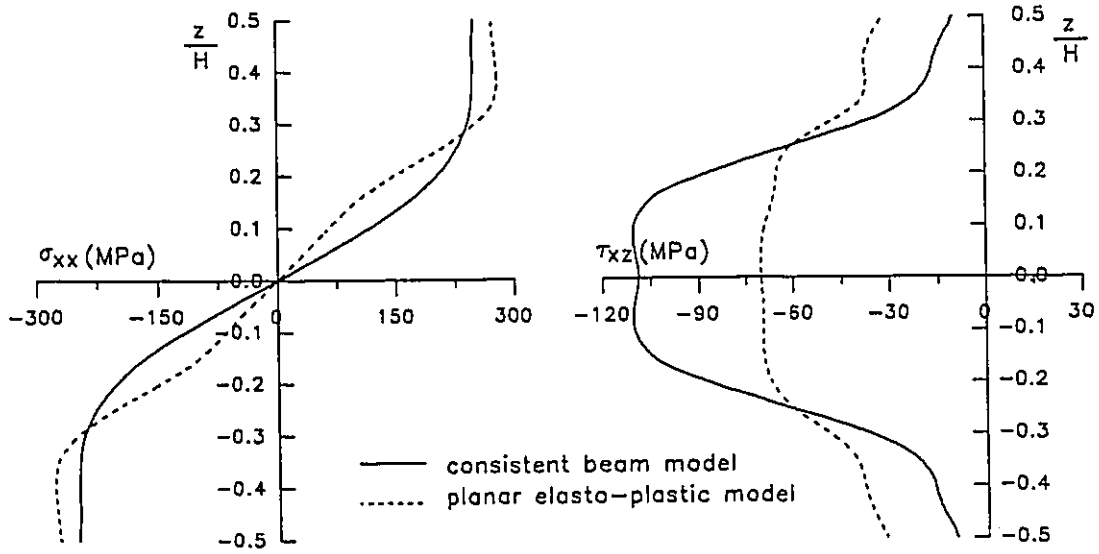

Figure 2.15: Normal stress and shear stress distributions at fixed end of beam for P = 7 MN.

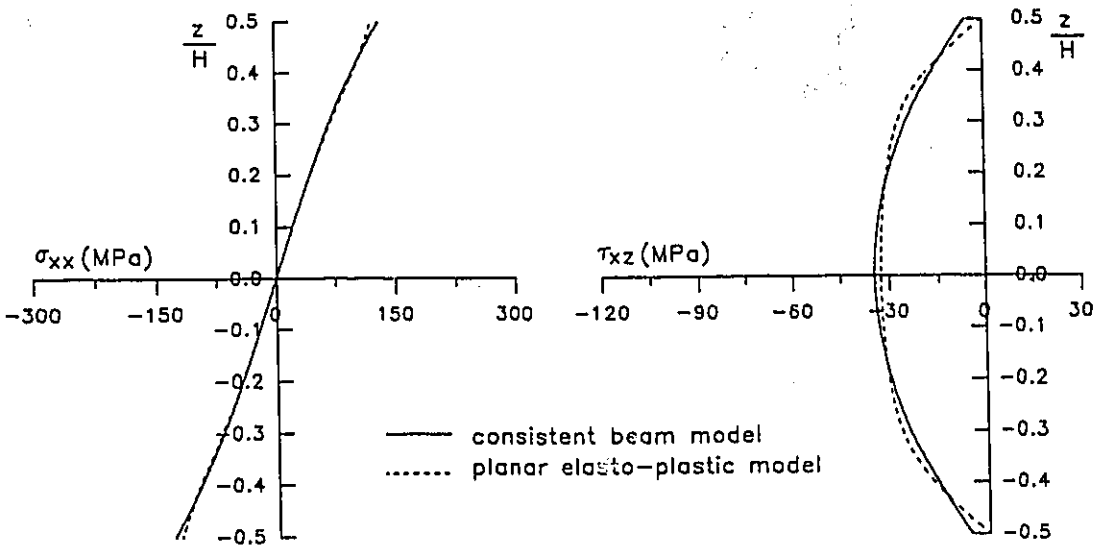

Figure 2.16: Normal stress and shear stress distributions 12 cm from fixed end of beam for P = 3 MN.

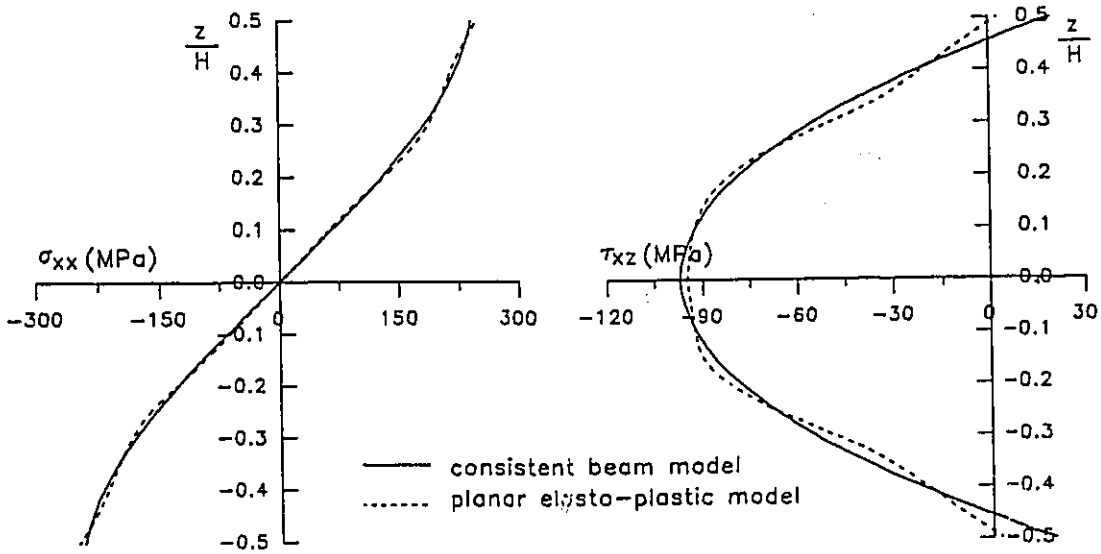

Figure 2.17: Normal stress and shear stress distributions 12 cm from fixed end of beam for P = 7 MN.

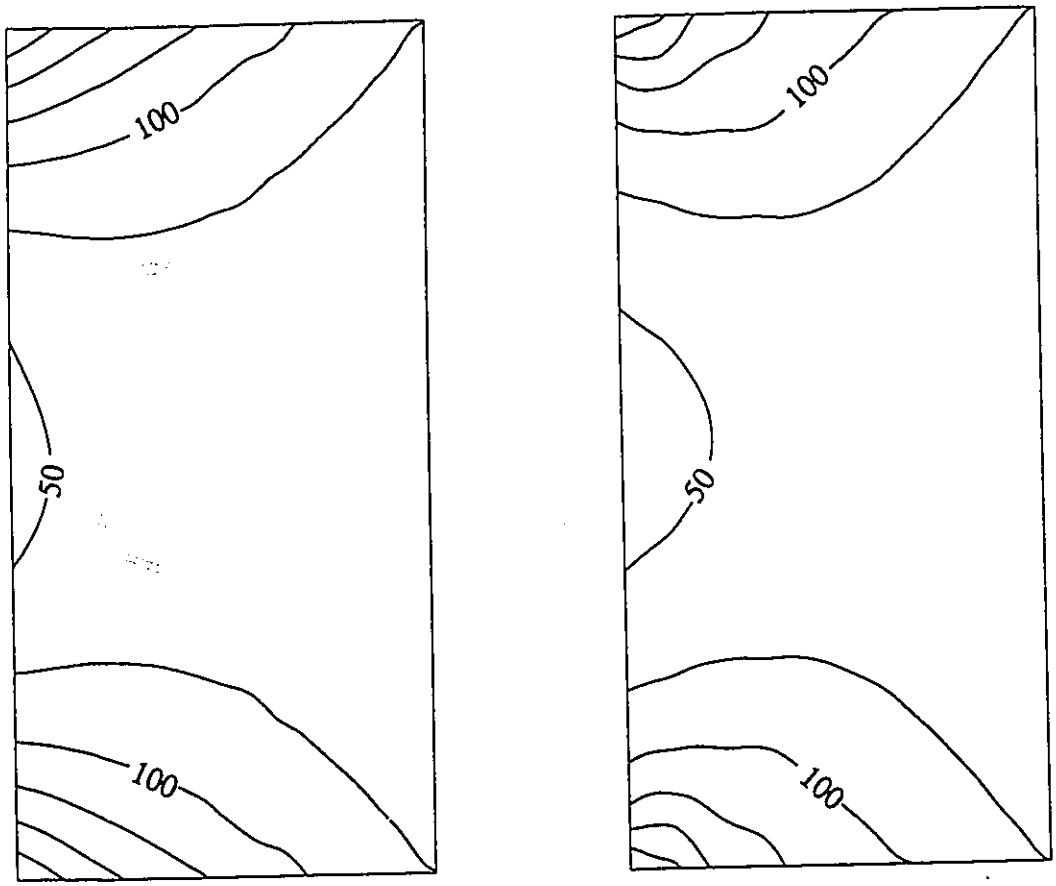

consistent beam model

planar elasto-plastic model

Contour Interval = 25 MPa

Figure 2.18: Effective stress contours for thick beam between fixed end and x = 30 cm for P = 3.0 MN.

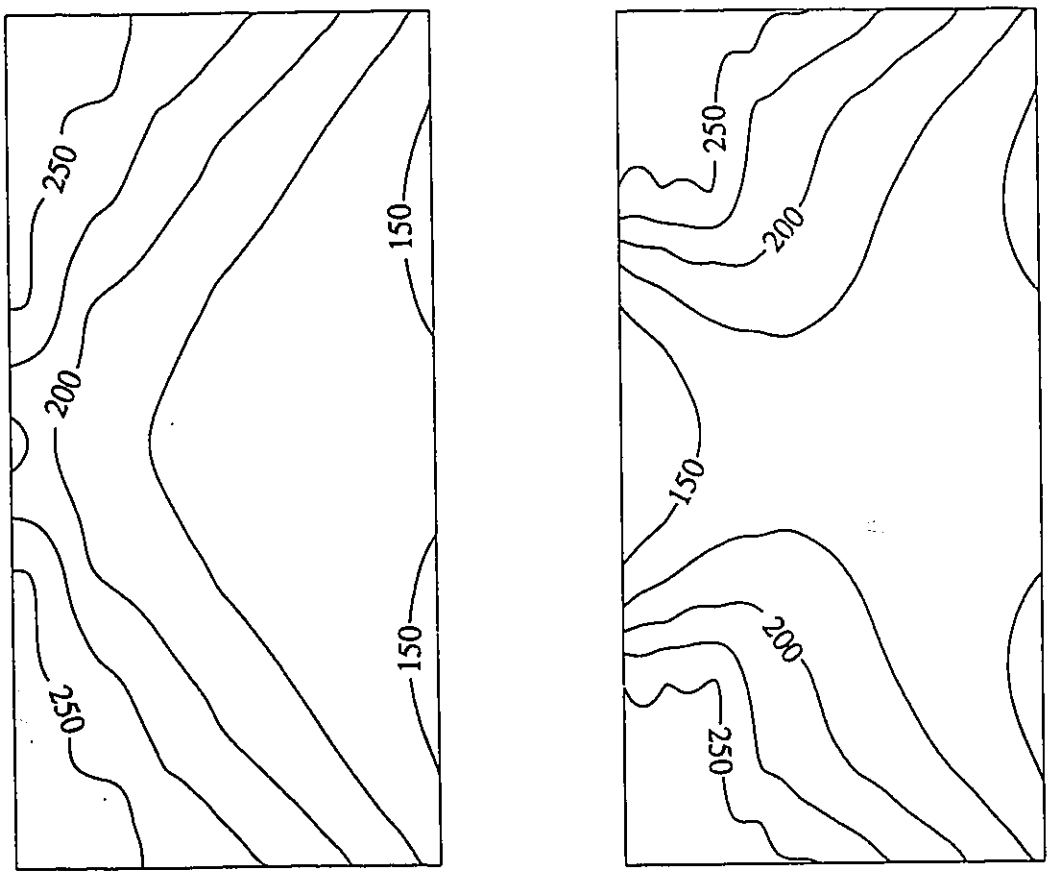

consistent beam model

planar elasto-plastic model

Contour Interval = 25 MPa

Figure 2.19: Effective stress contours for thick beam between fixed end and x = 30 cm for P = 7.0 MN.

CHAPTER THREE
CONSISTENT SHELL ELEMENT FORMULATION AND APPLICATIONS

3.1 Introduction

A new thick shell element compatible with the consistent beam element described in Chapter Two is formulated in this chapter. This new element is referred to as the consistent shell element.

By employing cubic polynomials for approximations of displacements and quadratic polynomials for approximations of rotations, a consistent formulation is ensured thereby eliminating the spurious transverse shear modes which plague other shear deformable shell elements, such as the eight and nine node isoparametric shell elements (Ergatoudis et al. 1968, Ahmed et al. 1970). A triangular parent element is adopted to provide complete polynomials for displacement and rotation approximations. Like the consistent beam element the new shell element employs two types of rotations. Those which are constant through the shell thickness and the others which vary quadratically. The quadratically varying rotations allow for a parabolic representation of the transverse shear strains through the depth of the element. This eliminates the need for use of the shear correction factor κ which is usually required to account for the assumption of constant shear strain across the depth (Mindlin 1951). In addition, the quadratically varying rotations produce a cubic variation of the

tangential displacements and hence the 'normal' to the middle surface does not remain straight or normal after bending and shearing. The stress normal to the middle surface is assumed to be negligible.

Special attention is given to the efficient implementation of the consistent shell element. For the same degrees of freedom per node the use of different order polynomials for approximation of displacements and rotations leads to the presence of many inactive degrees of freedom. These inactive degrees of freedom can result in increased computation time and the unnecessary use of memory. By employing a stiffness sub-matrix formulation in conjunction with a modified frontal solution technique these problems are avoided.

For material non-linearity an incremental elasto-plastic constitutive relation is used which employs the Huber von Mises yield criterion, an associated flow rule and isotropic hardening. The nonlinear finite element analysis is performed using a modified Newton Raphson method. Numerical results for a variety of problems are presented for performance evaluation of the consistent shell element. These include elastic, and elasto-plastic analysis of thin and thick plates and shells, and comparisons with results predicted by other shear deformable isoparametric shell elements, such as the eight and nine node isoparametric shell elements.

3.2 Consistent Shell Element Formulation

3.2.1 Co-ordinate Systems and Geometry

Co-ordinate systems used in the formulation of the consistent shell element are shown in Figure 3.1, and defined as follows:

1. Global cartesian co-ordinate system x, y, and z and the corresponding global displacements u, v, and w.
2. Curvilinear co-ordinate system (r,s,t), r and s are tangent to the surface defined by t=constant, and t is not necessarily normal to the r-s tangent plane.
3. Local cartesian co-ordinate system x', y', and z' to define local strains and stresses, z' is normal to the surface defined by t=constant and x' and y' are tangent to the surface.

For geometric distortion of the element a curvilinear transformation is used in terms of the parent r and s co-ordinates, and a linear transformation is used in terms of the t co-ordinate. The location of any point within the element in the global co-ordinate system is determined by the co-ordinates of the nodal points (x_i,y_i,z_i) and vector $\mathbf{V}_{3i}$ at each node as

$$\begin{Bmatrix} x \\ y \\ z \end{Bmatrix} = \Sigma N_i \begin{Bmatrix} x_i \\ y_i \\ z_i \end{Bmatrix} + \Sigma N_i \frac{t}{2} \mathbf{V}_{3i} \tag{3.1}$$

where quadratic interpolation functions N_i are given in Appendix A2 and the thickness vector $\mathbf{V}_{3i}$ is defined as

$$\mathbf{V}_{3i} = \begin{Bmatrix} x_i \\ y_i \\ z_i \end{Bmatrix}_{TOP} - \begin{Bmatrix} x_i \\ y_i \\ z_i \end{Bmatrix}_{BOTTOM}. \tag{3.2}$$

3.2.2 Displacement Field

To construct cubic approximations for displacements u, v and w, the displacement degrees of freedom at the corner nodes, one-third side nodes and center node are used. Quadratic approximations of rotations α, β, ϕ and ψ are achieved using the rotational degrees of freedom at the corner and mid-side nodes. Rotations α and ϕ are about the local y′ axis and rotations β and ψ are about the local x′ axis. Like the consistent beam element there are different number of degrees of freedom per node. Assuming that each node has seven degrees of freedom (u_i, v_i, w_i, α_i, β_i, ϕ_i, ψ_i) then there are ninety-one degrees of freedom per element. However, only fifty-four of these are active. It should be noted that rotations α and β are constant through the depth of the element while rotations ϕ and ψ vary quadratically. Thus, α and β provide a linear variation of displacements u, v and w along t while ϕ and ψ lead to a cubic variation of u, v and w.

The global displacements (u,v,w) can be written in terms of the nodal degrees of freedom as

$$\begin{Bmatrix} u \\ v \\ w \end{Bmatrix} = \Sigma \bar{N}_i \begin{Bmatrix} u_i \\ v_i \\ w_i \end{Bmatrix} + \Sigma N_i M_1 [\hat{V}_i] \begin{Bmatrix} \alpha_i \\ \beta_i \end{Bmatrix} + \Sigma N_i M_2 [\hat{V}_i] \begin{Bmatrix} \phi_i \\ \psi_i \end{Bmatrix} \qquad (3.3)$$

where N_i and $\bar{N}_i$ are the quadratic and cubic shape functions, respectively, and are given in Appendix A2. Matrix $[\hat{V}_i] = [\, \hat{V}_{1i} , - \hat{V}_{2i}]$ where unit vectors $\hat{V}_{1i}$ and $\hat{V}_{2i}$ are directed along the x′ and y′ axes, respectively, and form an orthogonal basis with unit vector $\hat{V}_{3i}$ at the i^{th} node as shown in Figure 3.2.

The procedure for construction of the orthogonal basis $(\hat{V}_{1i},\hat{V}_{2i},\hat{V}_{3i})$ is presented in Appendix C. The shape functions M_1 and M_2 approximate the displacement field through the depth due to the constant and quadratic rotations, respectively, and are given by

$$M_1 = \frac{h_i t}{2} \qquad M_2 = \frac{h_i t}{2}(1 - t^2) \tag{3.4}$$

where h_i is the shell thickness at the i^{th} node. The derivation of the through thickness displacement field due to quadratic rotations ϕ and ψ is given in Appendix B. Note that the consistent shell element is subparametric since u, v and w are approximated cubically while the geometric transformations are performed using quadratic expressions.

3.2.3 Strain-Displacement and Stress-Strain Relationships

For small deflections the local strains $\{\epsilon'\}$ are given by

$$\{\epsilon'\} = \begin{Bmatrix} \epsilon_{x'x'} \\ \epsilon_{y'y'} \\ \gamma_{x'y'} \\ \gamma_{x'z'} \\ \gamma_{y'z'} \end{Bmatrix} = [L] \begin{Bmatrix} u' \\ v' \\ w' \end{Bmatrix} = \begin{bmatrix} \frac{\partial}{\partial x'} & 0 & 0 \\ 0 & \frac{\partial}{\partial y'} & 0 \\ \frac{\partial}{\partial y'} & \frac{\partial}{\partial x'} & 0 \\ \frac{\partial}{\partial z'} & 0 & \frac{\partial}{\partial x'} \\ 0 & \frac{\partial}{\partial z'} & \frac{\partial}{\partial y'} \end{bmatrix} [\theta] \begin{Bmatrix} u \\ v \\ w \end{Bmatrix} \tag{3.5}$$

where u', v' and w' are displacements directed along the the local x', y' and

z′ axes, respectively, and [L] is the linear operator matrix. Transformation matrix [θ] is composed of the direction cosines between the local and global axes at the point where the displacements are to be transformed and is given as

$$[\theta] = \begin{array}{c} \\ x' \\ y' \\ z' \end{array} \begin{array}{c} \begin{array}{ccc} x & y & z \end{array} \\ \begin{bmatrix} l_1 & m_1 & n_1 \\ l_2 & m_2 & n_2 \\ l_3 & m_3 & n_3 \end{bmatrix} \end{array}. \tag{3.6}$$

Matrix [θ] is established using the Jacobian matrix as described in Appendix C. Using the transformation matrix [θ] and the expression for the global displacements, Equation 3.3, the local displacements can be written in terms of the nodal degrees of freedom as

$$\begin{Bmatrix} u' \\ v' \\ w' \end{Bmatrix} = \Sigma \tilde{N}_i[\theta] \begin{Bmatrix} u_i \\ v_i \\ w_i \end{Bmatrix} + \Sigma N_i M_1[C_i] \begin{Bmatrix} \alpha_i \\ \beta_i \end{Bmatrix} + \Sigma N_i M_2[C_i] \begin{Bmatrix} \phi_i \\ \psi_i \end{Bmatrix}. \tag{3.7}$$

where

$$[C_i] = [\theta]\,[\hat{V}_i] = \begin{bmatrix} C_i^{11} & C_i^{12} \\ C_i^{21} & C_i^{22} \\ C_i^{31} & C_i^{32} \end{bmatrix} = \begin{bmatrix} (l_1l_{1i}+m_1m_{1i}+n_1n_{1i}) & (-l_1l_{2i}-m_1m_{2i}-n_1n_{2i}) \\ (l_2l_{1i}+m_2m_{1i}+n_2n_{1i}) & (-l_2l_{2i}-m_2m_{2i}-n_2n_{2i}) \\ (l_3l_{1i}+m_3m_{1i}+n_3n_{1i}) & (-l_3l_{2i}-m_3m_{2i}-n_3n_{2i}) \end{bmatrix}.$$

The stress-strain relationship used is the generalized Hooke's Law given by

$$\{\sigma'\} = \begin{Bmatrix} \sigma_{x'x'} \\ \sigma_{y'y'} \\ \tau_{x'y'} \\ \tau_{x'z'} \\ \tau_{y'z'} \end{Bmatrix} = [D'] \left[\{ \epsilon' \} - \{ \epsilon'_0 \} \right] + \{ \sigma'_0 \} \qquad (3.8)$$

where $\{\epsilon'_0\}$ and $\{\sigma'_0\}$ are the initial local strain and stress vectors, respectively. The elasticity matrix [D′] is derived by substituting $\sigma_{z'z'} = 0$ into the general three dimensional constitutive relation and then eliminating $\epsilon_{z'z'}$. This yields

$$[D'] = \frac{E}{1-\nu^2} \begin{bmatrix} 1 & \nu & 0 & 0 & 0 \\ & 1 & 0 & 0 & 0 \\ & & \frac{1-\nu}{2} & 0 & 0 \\ & \text{symmetric} & & \frac{1-\nu}{2} & 0 \\ & & & & \frac{1-\nu}{2} \end{bmatrix} \qquad (3.9)$$

where E and ν are the elastic modulus and Poisson's ratio, respectively. It should be noted that the shear correction factor κ is not required in [D′] because of the parabolic approximation of the transverse shear strains through the thickness. Furthermore, at this stage we can incorporate any general constitutive equation, e.g. for orthotropic or anisotropic materials.

3.2.4 Sub-Matrix Formulation of Elastic Stiffness Matrix

For the same number of degrees of freedom per node there are ninety-one degrees of freedom per element. However, the number of active degrees of freedom per element is only fifty-four. When calculating the element

stiffness matrix in the usual manner through multiplication of $[B]^T[D][B]$ (Zienkiewicz 1977) the presence of the inactive degrees of freedom, and the banded nature of the elasticity matrix [D] result in many unnecessary multiplications with zero. This leads to a significant increase in the computer time required for problem solving, unnecessary use of large memory and potential loss of accuracy. These problems are avoided by employing a sub-matrix formulation which allows the stiffness matrix to be calculated at the sub-matrix level without performing any unnecessary multiplications.

The expression for the local displacements, Equation 3.7, can be re-written in terms of the degree of freedom sub-vectors and the shape function matrices as

$$\underset{3\times 1}{\begin{Bmatrix} u' \\ v' \\ w' \end{Bmatrix}} = \underset{3\times 30}{[\bar{N}^d]} \underset{30\times 1}{\begin{Bmatrix} \{u\} \\ \{v\} \\ \{w\} \end{Bmatrix}} + M_1 \underset{3\times 12}{[N^r]} \underset{12\times 1}{\begin{Bmatrix} \{\alpha\} \\ \{\beta\} \end{Bmatrix}} + M_2 \underset{3\times 12}{[N^r]} \underset{12\times 1}{\begin{Bmatrix} \{\phi\} \\ \{\psi\} \end{Bmatrix}} \qquad (3.10)$$

where $$\underset{3\times 30}{[\bar{N}^d]} = \underset{1\times 10}{\{\bar{N}\}^T} \begin{bmatrix} l_1 & m_1 & n_1 \\ l_2 & m_2 & n_2 \\ l_3 & m_3 & n_3 \end{bmatrix}$$

$$\{\bar{N}\}^T = < \bar{N}_1 \ \bar{N}_2 \ \bar{N}_3 \ \bar{N}_4 \ \bar{N}_6 \ \bar{N}_7 \ \bar{N}_9 \ \bar{N}_{10} \ \bar{N}_{12} \ \bar{N}_{13} >$$

$$\underset{3\times 12}{[N^r]} = \begin{bmatrix} \{N^{11}\}^T & \{N^{12}\}^T \\ \{N^{21}\}^T & \{N^{22}\}^T \\ \{N^{31}\}^T & \{N^{32}\}^T \end{bmatrix}$$

$$\{N^{ij}\}^T = < N_1C_1^{ij}\ N_2C_2^{ij}\ N_3C_3^{ij}\ N_5C_5^{ij}\ N_8C_8^{ij}\ N_{11}C_{11}^{ij} >.$$

The degree of freedom sub-vectors are given by

$$\begin{aligned}
\{u\}^T &= < u_1\ u_2\ u_3\ u_4\ u_6\ u_7\ u_9\ u_{10}\ u_{12}\ u_{13} > \\
\{v\}^T &= < v_1\ v_2\ v_3\ v_4\ v_6\ v_7\ v_9\ v_{10}\ v_{12}\ v_{13} > \\
\{w\}^T &= < w_1\ w_2\ w_3\ w_4\ w_6\ w_7\ w_9\ w_{10}\ w_{12}\ w_{13} > \\
\{\alpha\}^T &= < \alpha_1\ \alpha_2\ \alpha_3\ \alpha_5\ \alpha_8\ \alpha_{11} > \\
\{\beta\}^T &= < \beta_1\ \beta_2\ \beta_3\ \beta_5\ \beta_8\ \beta_{11} > \\
\{\phi\}^T &= < \phi_1\ \phi_2\ \phi_3\ \phi_5\ \phi_8\ \phi_{11} > \\
\{\psi\}^T &= < \psi_1\ \psi_2\ \psi_3\ \psi_5\ \psi_8\ \psi_{11} >
\end{aligned} \qquad (3.11,a\text{-}g)$$

where the subscripts denote the node number to which the degrees of freedom belong. Note that only those degrees of freedom which are active are included.

To establish the discretized equations of equilibrium the principle of minimum potential energy is used. The potential energy Π is given by

$$\Pi = U - W \qquad (3.12)$$

where U is the strain energy and W is the work done by the external forces. For more information refer to Zienkiewicz (1977). The minimization of the potential energy Π with respect to the degree of freedom sub-vectors yields the element stiffness coefficients in terms of the shape function matrices and the element load vector.

Using the expression for the local displacements, Equation 3.10, and the linear operator matrix [L] from Equation 3.5 the local strains can be written in terms of the displacement sub-vectors as

$$\epsilon_{x'x'} = l_1\frac{\partial\{\bar{N}\}^T}{\partial x'}\{u\} + m_1\frac{\partial\{\bar{N}\}^T}{\partial x'}\{v\} + n_1\frac{\partial\{\bar{N}\}^T}{\partial x'}\{w\} + \left[M_1\frac{\partial\{N^{11}\}^T}{\partial x'} + \frac{\partial M_1}{\partial x'}\{N^{11}\}^T\right]\{\alpha\} + \left[M_1\frac{\partial\{N^{12}\}^T}{\partial x'} + \frac{\partial M_1}{\partial x'}\{N^{12}\}^T\right]\{\beta\} + \left[M_2\frac{\partial\{N^{11}\}^T}{\partial x'} + \frac{\partial M_2}{\partial x'}\{N^{11}\}^T\right]\{\phi\} + \left[M_2\frac{\partial\{N^{12}\}^T}{\partial x'} + \frac{\partial M_2}{\partial x'}\{N^{12}\}^T\right]\{\psi\} \quad (3.13,a)$$

$$\epsilon_{y'y'} = l_2\frac{\partial\{\bar{N}\}^T}{\partial y'}\{u\} + m_2\frac{\partial\{\bar{N}\}^T}{\partial y'}\{v\} + n_2\frac{\partial\{\bar{N}\}^T}{\partial y'}\{w\} + \left[M_1\frac{\partial\{N^{21}\}^T}{\partial y'} + \frac{\partial M_1}{\partial y'}\{N^{21}\}^T\right]\{\alpha\} + \left[M_1\frac{\partial\{N^{22}\}^T}{\partial y'} + \frac{\partial M_1}{\partial y'}\{N^{22}\}^T\right]\{\beta\} + \left[M_2\frac{\partial\{N^{21}\}^T}{\partial y'} + \frac{\partial M_2}{\partial y'}\{N^{21}\}^T\right]\{\phi\} + \left[M_2\frac{\partial\{N^{22}\}^T}{\partial y'} + \frac{\partial M_2}{\partial y'}\{N^{22}\}^T\right]\{\psi\} \quad (3.13,b)$$

$$\gamma_{x'y'} = \left[l_1\frac{\partial\{\bar{N}\}^T}{\partial y'} + l_2\frac{\partial\{\bar{N}\}^T}{\partial x'}\right]\{u\} + \left[m_1\frac{\partial\{\bar{N}\}^T}{\partial y'} + m_2\frac{\partial\{\bar{N}\}^T}{\partial x'}\right]\{v\} + \left[n_1\frac{\partial\{\bar{N}\}^T}{\partial y'} + n_2\frac{\partial\{\bar{N}\}^T}{\partial x'}\right]\{w\} + \left[M_1\frac{\partial\{N^{11}\}^T}{\partial y'} + \frac{\partial M_1}{\partial y'}\{N^{11}\}^T + M_1\frac{\partial\{N^{21}\}^T}{\partial x'} + \frac{\partial M_1}{\partial x'}\{N^{21}\}^T\right]\{\alpha\} + \left[M_1\frac{\partial\{N^{12}\}^T}{\partial y'} + \frac{\partial M_1}{\partial y'}\{N^{12}\}^T + M_1\frac{\partial\{N^{22}\}^T}{\partial x'} + \frac{\partial M_1}{\partial x'}\{N^{22}\}^T\right]\{\beta\} + \left[M_2\frac{\partial\{N^{11}\}^T}{\partial y'} + \frac{\partial M_2}{\partial y'}\{N^{11}\}^T + M_2\frac{\partial\{N^{21}\}^T}{\partial x'} + \frac{\partial M_2}{\partial x'}\{N^{21}\}^T\right]\{\phi\} +$$

$$\left[M_2\frac{\partial\{N^{12}\}^T}{\partial y'} + \frac{\partial M_2}{\partial y'}\{N^{12}\}^T + M_2\frac{\partial\{N^{22}\}^T}{\partial x'} + \frac{\partial M_2}{\partial x'}\{N^{22}\}^T\right]\{\psi\} \quad (3.13,c)$$

$$\begin{aligned}\gamma_{x'z'} = {} & \left[l_1\frac{\partial\{\bar{N}\}^T}{\partial z'} + l_3\frac{\partial\{\bar{N}\}^T}{\partial x'}\right]\{u\} + \left[m_1\frac{\partial\{\bar{N}\}^T}{\partial z'} + m_3\frac{\partial\{\bar{N}\}^T}{\partial x'}\right]\{v\} + \\ & \left[n_1\frac{\partial\{\bar{N}\}^T}{\partial z'} + n_3\frac{\partial\{\bar{N}\}^T}{\partial x'}\right]\{w\} + \\ & \left[M_1\frac{\partial\{N^{11}\}^T}{\partial z'} + \frac{\partial M_1}{\partial z'}\{N^{11}\}^T + M_1\frac{\partial\{N^{31}\}^T}{\partial x'} + \frac{\partial M_1}{\partial x'}\{N^{31}\}^T\right]\{\alpha\} + \\ & \left[M_1\frac{\partial\{N^{12}\}^T}{\partial z'} + \frac{\partial M_1}{\partial z'}\{N^{12}\}^T + M_1\frac{\partial\{N^{32}\}^T}{\partial x'} + \frac{\partial M_1}{\partial x'}\{N^{32}\}^T\right]\{\beta\} + \\ & \left[M_2\frac{\partial\{N^{11}\}^T}{\partial z'} + \frac{\partial M_2}{\partial z'}\{N^{11}\}^T + M_2\frac{\partial\{N^{31}\}^T}{\partial x'} + \frac{\partial M_2}{\partial x'}\{N^{31}\}^T\right]\{\phi\} + \\ & \left[M_2\frac{\partial\{N^{12}\}^T}{\partial z'} + \frac{\partial M_2}{\partial z'}\{N^{12}\}^T + M_2\frac{\partial\{N^{32}\}^T}{\partial x'} + \frac{\partial M_2}{\partial x'}\{N^{32}\}^T\right]\{\psi\} \quad (3.13,d)\end{aligned}$$

$$\begin{aligned}\gamma_{y'z'} = {} & \left[l_1\frac{\partial\{\bar{N}\}^T}{\partial z'} + l_3\frac{\partial\{\bar{N}\}^T}{\partial y'}\right]\{u\} + \left[m_1\frac{\partial\{\bar{N}\}^T}{\partial z'} + m_3\frac{\partial\{\bar{N}\}^T}{\partial y'}\right]\{v\} + \\ & \left[n_1\frac{\partial\{\bar{N}\}^T}{\partial z'} + n_3\frac{\partial\{\bar{N}\}^T}{\partial y'}\right]\{w\} + \\ & \left[M_1\frac{\partial\{N^{11}\}^T}{\partial z'} + \frac{\partial M_1}{\partial z'}\{N^{11}\}^T + M_1\frac{\partial\{N^{31}\}^T}{\partial y'} + \frac{\partial M_1}{\partial y'}\{N^{31}\}^T\right]\{\alpha\} + \\ & \left[M_1\frac{\partial\{N^{12}\}^T}{\partial z'} + \frac{\partial M_1}{\partial z'}\{N^{12}\}^T + M_1\frac{\partial\{N^{32}\}^T}{\partial y'} + \frac{\partial M_1}{\partial y'}\{N^{32}\}^T\right]\{\beta\} + \\ & \left[M_2\frac{\partial\{N^{11}\}^T}{\partial z'} + \frac{\partial M_2}{\partial z'}\{N^{11}\}^T + M_2\frac{\partial\{N^{31}\}^T}{\partial y'} + \frac{\partial M_2}{\partial y'}\{N^{31}\}^T\right]\{\phi\} + \\ & \left[M_2\frac{\partial\{N^{12}\}^T}{\partial z'} + \frac{\partial M_2}{\partial z'}\{N^{12}\}^T + M_2\frac{\partial\{N^{32}\}^T}{\partial y'} + \frac{\partial M_2}{\partial y'}\{N^{32}\}^T\right]\{\psi\} \quad (3.13,e)\end{aligned}$$

For the components of strain given in equations 3.13 the strain energy U is given by

$$U = \frac{E}{2(1-\nu^2)}\int_V \Big[\epsilon_{x'x'}^2 + \epsilon_{y'y'}^2 + 2\nu\epsilon_{x'x'}\epsilon_{y'y'} + \frac{1-\nu}{2}(\gamma_{x'y'}^2 + \gamma_{x'z'}^2 + \gamma_{y'z'}^2)\Big]dV. \tag{3.14}$$

The minimization process described above gives the stiffness contributions to each sub-matrix of the element stiffness matrix in terms of the shape function matrices prior to integration over the element volume. The element stiffness matrix [k] is divided into stiffness sub-matrices $[k^S]_{ij}$ as follows

$$[k] = \begin{array}{c} \begin{matrix} \{u\} & \{v\} & \{w\} & \{\alpha\} & \{\beta\} & \{\phi\} & \{\psi\} \end{matrix} \\ \left[\begin{array}{ccccccc} [k^S]_{11} & [k^S]_{12} & [k^S]_{13} & [k^S]_{14} & [k^S]_{15} & [k^S]_{16} & [k^S]_{17} \\ [k^S]_{21} & [k^S]_{22} & [k^S]_{23} & [k^S]_{24} & [k^S]_{25} & [k^S]_{26} & [k^S]_{27} \\ [k^S]_{31} & [k^S]_{32} & [k^S]_{33} & [k^S]_{34} & [k^S]_{35} & [k^S]_{36} & [k^S]_{37} \\ [k^S]_{41} & [k^S]_{42} & [k^S]_{43} & [k^S]_{44} & [k^S]_{45} & [k^S]_{46} & [k^S]_{47} \\ [k^S]_{51} & [k^S]_{52} & [k^S]_{53} & [k^S]_{54} & [k^S]_{55} & [k^S]_{56} & [k^S]_{57} \\ [k^S]_{61} & [k^S]_{62} & [k^S]_{63} & [k^S]_{64} & [k^S]_{65} & [k^S]_{66} & [k^S]_{67} \\ [k^S]_{71} & [k^S]_{72} & [k^S]_{73} & [k^S]_{74} & [k^S]_{75} & [k^S]_{76} & [k^S]_{77} \end{array}\right] \begin{matrix} \{u\} \\ \{v\} \\ \{w\} \\ \{\alpha\} \\ \{\beta\} \\ \{\phi\} \\ \{\psi\} \end{matrix} \\ (54x54) \end{array} \tag{3.15}$$

The stiffness sub-matrices $[k^S]_{ij}$ are defined in terms of the shape function matrices in Appendix D. The integration of these sub-matrices is performed numerically using the Gaussian-Quadrature scheme.

Derivatives in the curvilinear (r,s,t) co-ordinate system are related to the derivatives in the global (x,y,z) co-ordinate system through the Jacobian matrix as

$$\begin{Bmatrix} \frac{\partial}{\partial r} \\ \frac{\partial}{\partial s} \\ \frac{\partial}{\partial t} \end{Bmatrix} = \begin{bmatrix} \frac{\partial x}{\partial r} & \frac{\partial y}{\partial r} & \frac{\partial z}{\partial r} \\ \frac{\partial x}{\partial s} & \frac{\partial y}{\partial s} & \frac{\partial z}{\partial s} \\ \frac{\partial x}{\partial t} & \frac{\partial y}{\partial t} & \frac{\partial z}{\partial t} \end{bmatrix} \begin{Bmatrix} \frac{\partial}{\partial x} \\ \frac{\partial}{\partial y} \\ \frac{\partial}{\partial z} \end{Bmatrix} \tag{3.16}$$

where the components of the Jacobian matrix i.e. $\frac{\partial x}{\partial r}$, $\frac{\partial y}{\partial r}$, etc. are determined using Equation 3.1. The differential volume dV is transformed as

$$dV = \det|J| \, drdsdt \tag{3.17}$$

where $\det|J|$ is the determinant of the Jacobian matrix. The Jacobian matrix is also used to compute the direction cosine matrix $[\theta]$, Equation 3.6, as described in Appendix C. The partial derivatives with respect to the local (x',y',z') co-ordinates appearing in the sub-matrices in Appendix D can be written in terms of derivatives in the curvilinear co-ordinate system using

$$\begin{Bmatrix} \frac{\partial}{\partial x'} \\ \frac{\partial}{\partial y'} \\ \frac{\partial}{\partial z'} \end{Bmatrix} = \begin{bmatrix} \frac{\partial r}{\partial x'} & \frac{\partial s}{\partial x'} & \frac{\partial t}{\partial x'} \\ \frac{\partial r}{\partial y'} & \frac{\partial s}{\partial y'} & \frac{\partial t}{\partial y'} \\ \frac{\partial r}{\partial z'} & \frac{\partial s}{\partial z'} & \frac{\partial t}{\partial z'} \end{bmatrix} \begin{Bmatrix} \frac{\partial}{\partial r} \\ \frac{\partial}{\partial s} \\ \frac{\partial}{\partial t} \end{Bmatrix} = [J']^{-1} \begin{Bmatrix} \frac{\partial}{\partial r} \\ \frac{\partial}{\partial s} \\ \frac{\partial}{\partial t} \end{Bmatrix} \tag{3.18}$$

where matrix $[J']$ relates derivatives in the local co-ordinate system to the derivatives in the curvilinear system and is given by

$$[J'] = \begin{bmatrix} \frac{\partial x'}{\partial r} & \frac{\partial y'}{\partial r} & \frac{\partial z'}{\partial r} \\ \frac{\partial x'}{\partial s} & \frac{\partial y'}{\partial s} & \frac{\partial z'}{\partial s} \\ \frac{\partial x'}{\partial t} & \frac{\partial y'}{\partial t} & \frac{\partial z'}{\partial t} \end{bmatrix}. \tag{3.19}$$

The components of [J'] are determined using Equation 3.1, the matrix of direction cosines [θ] and the chain rule as

$$\frac{\partial a'_i}{\partial r} = \frac{\partial x}{\partial r}\frac{\partial a'_i}{\partial x} + \frac{\partial y}{\partial r}\frac{\partial a'_i}{\partial y} + \frac{\partial z}{\partial r}\frac{\partial a'_i}{\partial z} = l_i\frac{\partial x}{\partial r} + m_i\frac{\partial y}{\partial r} + n_i\frac{\partial z}{\partial r}$$

$$\frac{\partial a'_i}{\partial s} = \frac{\partial x}{\partial s}\frac{\partial a'_i}{\partial x} + \frac{\partial y}{\partial s}\frac{\partial a'_i}{\partial y} + \frac{\partial z}{\partial s}\frac{\partial a'_i}{\partial z} = l_i\frac{\partial x}{\partial s} + m_i\frac{\partial y}{\partial s} + n_i\frac{\partial z}{\partial s} \tag{3.20,a-c}$$

$$\frac{\partial a'_i}{\partial t} = \frac{\partial x}{\partial t}\frac{\partial a'_i}{\partial x} + \frac{\partial y}{\partial t}\frac{\partial a'_i}{\partial y} + \frac{\partial z}{\partial t}\frac{\partial a'_i}{\partial z} = l_i\frac{\partial x}{\partial t} + m_i\frac{\partial y}{\partial t} + n_i\frac{\partial z}{\partial t}$$

where $a'_{i=1,2,3} = x', y', z'$. Using the above transformations the sub-matrices are integrated numerically using seven integration points in the r-s plane and five integration points along t.

It should also be noted that an eigenvalue test of the element stiffness matrix [k] was performed. The results verified the existence of the required rigid body modes and the absence of any spurious zero-energy deformation modes. In addition, the validity of the formulation was further verified through constant stress and constant curvature patch tests.

Following the minimization of the potential energy the element load vector {r} is obtained as

$$\{r\} = \int_V [N]^T \{b\}\, dV + \int_S [N]^T \{T\}\, dS + [N]^T \{p\} \qquad (3.21)$$

where {b}, {T} and {p} are the body force, surface traction and point load vectors, respectively. Matrix [N] relates the nodal degrees of freedom to the global displacements and is given by

$$[N] = \begin{bmatrix} \{\bar{N}\}^T & 0 & 0 \\ 0 & \{\bar{N}\}^T & 0 \\ 0 & 0 & \{\bar{N}\}^T \\ l_1 M_1 \{N\}^T & m_1 M_1 \{N\}^T & n_1 M_1 \{N\}^T \\ -l_2 M_1 \{N\}^T & -m_2 M_1 \{N\}^T & -n_2 M_1 \{N\}^T \\ l_1 M_2 \{N\}^T & m_1 M_2 \{N\}^T & n_1 M_2 \{N\}^T \\ -l_2 M_2 \{N\}^T & -m_2 M_2 \{N\}^T & -n_2 M_2 \{N\}^T \end{bmatrix}. \qquad (3.22)$$

The element load vector {r} is integrated numerically through use of the Jacobian matrix, Equation 3.16, to accommodate the required transformations.

3.2.5 Assembly and Solution of Global Equilibrium Equations

Having established the stiffness sub-matrices, the global equations of equilibrium can now be assembled. For this purpose the frontal solution scheme (Irons 1970, Hinton and Owen 1977) is used. Incorporation of the degree of freedom sub-vectors and the stiffness sub-matrices into the frontal solution scheme requires modification of the present algorithm.

The modified frontal solution algorithm allows the global equations of equilibrium to be assembled directly without the use of the full element stiffness matrix. This is accomplished with the use of seven new vectors which are referred to as sub-variable location vectors. They locate each term of the degree of freedom sub-vectors in the vector containing all ninety-one degrees of freedom (active and inactive) and are given by

$$\begin{aligned}
\{LSu\}^T &= < 1\ \ 8\ \ 15\ \ 22\ \ 36\ \ 43\ \ 57\ \ 64\ \ 78\ \ 85 > \\
\{LSv\}^T &= < 2\ \ 9\ \ 16\ \ 23\ \ 37\ \ 44\ \ 58\ \ 65\ \ 79\ \ 86 > \\
\{LSw\}^T &= < 3\ \ 10\ \ 17\ \ 24\ \ 38\ \ 45\ \ 59\ \ 66\ \ 80\ \ 87 > \\
\{LS\alpha\}^T &= < 4\ \ 11\ \ 18\ \ 32\ \ 53\ \ 74 > \\
\{LS\beta\}^T &= < 5\ \ 12\ \ 19\ \ 33\ \ 54\ \ 75 > \\
\{LS\phi\}^T &= < 6\ \ 13\ \ 20\ \ 34\ \ 55\ \ 76 > \\
\{LS\psi\}^T &= < 7\ \ 14\ \ 21\ \ 35\ \ 56\ \ 77 >
\end{aligned} \qquad (3.23,a\text{-}g)$$

For example the sub-variable location vector {LSu} contains addresses of the degrees of freedom in the displacement sub-vector {u}. The sub-variable location vectors allow each term of a specific stiffness sub-matrix to be added directly into the appropriate positions in the global stiffness matrix. Solution of the equations then proceeds in the usual manner. If an alternate solution scheme, such as a banded solver, is employed the global stiffness matrix can be assembled in a manner similar to that described above using the sub-variable location vectors at the sub-level. The ordinary referencing for the sub-level formulation, in terms of the sub-level vectors is shown in Figure 3.3.

3.3 Elasto-Plastic Formulation

For elasto-plastic analysis of plates and shells an incremental approach is adopted. The instantaneous constitutive relation is formulated using the Huber von Mises yield criterion, an associated flow rule and isotropic hardening. Special attention is given to the formulation of the elasto-plastic element stiffness matrix to ensure computational efficiency. The nonlinear finite element analysis procedure is the same as that described in Chapter 2 section 2.4.2.

3.3.1 Elasto-Plastic Constitutive Relationship

The nonlinear material behaviour is described using plasticity theory. Only the details which are specific to the present formulation are presented. For more information on plasticity theory refer to Mendelson (1970) or Han and Chen (1988).

The onset of plastic deformation is determined by the yield criterion. The yield function F corresponding to the Huber von Mises yield criterion and a general state of stress is given by

$$F = \sqrt{3J_2} - \sigma_Y = \bar{\sigma} - \sigma_Y = 0 \tag{3.24}$$

where σ_Y and $\bar{\sigma}$ are the uniaxial yield stress and the effective stress, respectively. The second stress invariant of the stress deviator tensor J_2 can be written as

$$J_2 = \frac{1}{2} s_{ij}\, s_{ij} \tag{3.25}$$

where s_{ij} is the stress deviator tensor which is given by

$$s_{ij} = \sigma_{ij} - \delta_{ij}\, \sigma_m \tag{3.26}$$

and $\sigma_m = \sigma_{ii}/3$ is the first invariant of the stress tensor. Yielding occurs when the yield function F, Equation 3.24, is equal to zero i.e. when the effective stress $\bar{\sigma}$ equals the uniaxial yield stress σ_Y.

Beyond the proportional limit an incremental stress-strain relationship is employed which can be written as

$$d\{\sigma'\} = [Dep']\, d\{\epsilon'\} \tag{3.27}$$

where [Dep′] is the instantaneous elasto-plastic constitutive matrix in the local co-ordinate system. For an associated flow rule and isotropic hardening it takes the following form (Zienkiewicz 1977)

$$[Dep'] = [D'] - [D'] \frac{1}{H' + \left\{ \frac{\partial F}{\partial \sigma} \right\}^T [D'] \left\{ \frac{\partial F}{\partial \sigma} \right\}} \left\{ \frac{\partial F}{\partial \sigma} \right\} \left\{ \frac{\partial F}{\partial \sigma} \right\}^T [D'] \tag{3.28}$$

where [D′] is the elastic constitutive matrix, Equation 3.9, and H′ is the plastic modulus which is the slope of the uniaxial stress-strain curve beyond the yield limit. Assuming a bilinear stress-strain curve for elasto-plastic material behaviour the plastic modulus is given by

$$H' = E_T / (1 - E_T / E) \tag{3.29}$$

where E and E_T are the elastic and tangent moduli, respectively.

After substituting J_2, Equation 3.25, into the yield function F, Equation 3.24, the vector $\left\{ \frac{\partial F}{\partial \sigma} \right\}$ can be obtained as

$$\left\{ \frac{\partial F}{\partial \sigma} \right\}^T = \frac{3}{2\bar{\sigma}} s_{ij} \tag{3.30}$$

which for $\sigma_z'_{z'} = 0$ gives

$$\left\{ \frac{\partial F}{\partial \sigma} \right\} = \frac{1}{\bar{\sigma}} \begin{Bmatrix} \sigma_x'_{x'} - \sigma_y'_{y'}/2 \\ \sigma_y'_{y'} - \sigma_x'_{x'}/2 \\ 3\tau_x'_{y'} \\ 3\tau_x'_{z'} \\ 3\tau_y'_{z'} \end{Bmatrix}. \tag{3.31}$$

Having defined all of the terms, one can now compute the elastic-plastic constitutive matrix [Dep'] as given in Equation 3.28.

3.3.2 Elasto-Plastic Stiffness Matrix

As described previously in section 3.2.4 many unnecessary multiplications with zero occur when the stiffness matrix is calculated in the usual manner using $[B]^T[D][B]$ due to the presence of inactive degrees of freedom and the banded nature of [D]. However, once yielding has occurred

the elasto-plastic constitutive matrix [Dep] is used in place of the elastic constitutive matrix [D]. Since [Dep] is a fully populated matrix the only unnecessary multiplications which occur when $[B]^T[Dep][B]$ is carried out are those with columns of [B] which correspond to inactive degrees of freedom. Elimination of these columns from [B] prior to calculation of $[B]^T[Dep][B]$ allows for more efficient and accurate computation of the elasto-plastic element stiffness matrix.

Substituting the expression for the local displacements, Equation 3.7, into the strain-displacement relation, Equation 3.5, and multiplying yields

$$\{\epsilon'\} = [B'] \{d\} \tag{3.32}$$

where matrix [B'] relates the nodal degree of freedom vector to the local strains and is presented in Appendix E.

After applying the principle of virtual work (Zienkiewicz 1977) the elasto-plastic element stiffness matrix is calculated as

$$[k_r] = \int_V [B'_r]^T [Dep'] [B'_r] \, dV \tag{3.33}$$

where $[B'_r]$ and $[k_r]$ are the reduced dimension strain displacement and element stiffness matrices, respectively. Matrix $[B'_r]$ is obtained from [B'] by eliminating those columns which correspond to the inactive degrees of freedom. Obviously, the resulting reduced matrix has fifty-four columns instead of ninety-one.

Integration of Equation 3.33 is performed numerically by employing the Gaussian Quadrature scheme. The partial derivatives with respect to the local co-ordinates in matrix $[B'_r]$ are transformed to derivatives with respect to the curvilinear co-ordinates as described previously in section 3.2.4. After which the stiffness matrix is calculated as follows

$$[k^e_r] = \int_{+1}^{+1}\int_{0}^{+1}\int_{0}^{+1} [B'_r]^T\,[Dep']\,[B'_r]\,\det|J|\,drdsdt. \qquad (3.34)$$

The integration is performed using seven integration points in the r-s plane and three integration points along t.

3.4 Numerical Examples

3.4.1 Convergence to Thin Plate Solution

A simply supported thin square plate subjected to a uniformly distributed load has been analysed. Due to double symmetry only one quarter of the plate has been modelled using 8 (2x2) consistent shell elements. Analyses have been made using the full matrix formulation and the sub-matrix formulation. For the full matrix formulation the computer time required for analysis was 114 seconds and for the sub-matrix formulation the computer time required was 58 seconds. Thus, by employing the sub-matrix formulation a 50% reduction in the computer time required for problem solution is achieved.

This problem is typically used in the literature as a test for shear

locking. For this purpose the ratio of the plate width to thickness is increased and the predicted solutions are checked for convergence to the theoretical solution. In the present case plates having width to thickness ratios ranging from 10 to 200 have been analysed. The predicted deflections of the center of the plate have been normalized and plotted in Figure 3.4 along with the theoretical solution given by Timoshenko (1959). Also plotted are results obtained by Zienkiewicz et al. (1971) using four eight node isoparametric shell elements with full 3x3 quadrature in the r-s plane. It can be seen that the transverse displacements predicted by the consistent shell element becomes asymptotic to the theoretical solution while those predicted by the eight node isoparametric shell element are divergent. By ensuring a consistent formulation the consistent shell element is free of the spurious transverse shear strain modes which plague the eight node isoparametric shell element.

3.4.2 Cylindrical Panel

A cylindrical shell roof with two edges simply supported and the remaining two edges free as shown in Figure 3.5 is now considered. The panel is loaded vertically by its uniform dead weight. The analyses using the consistent shell element have been carried out using three different meshes. The first uses 2 elements (1x1), the second 8 (2x2) and the third 32 (4x4). Only one quarter of the panel has been modelled because of double symmetry. In each case two solutions have been obtained. The first using the full matrix formulation and the second using the sub-matrix formulation. The results of these analyses are shown in Table 3.1 which gives the normalized vertical deflection at point A, and the computer run times. The exact deflection at point

Table 3.1: Results of cylindrical panel analysis using the consistent thick shell element.

Elements	Degrees of Freedom	Normalized Deflection	Time (sec.) Sub	Full
2	57	0.630	15	26
8	188	0.930	55	95
32	576	0.968	281	448

A has been taken as 0.3024 (MacNeal and Harder 1985). The efficiency of the sub-matrix formulation over the full matrix formulation is again quite obvious. The computing time required is approximately 40% less than that required by the full matrix formulation.

As this problem is dominated by its membrane response it has been used by numerous investigators as a membrane locking test. For the purpose of comparison, the results from an analysis of the shell using the nine node isoparametric shell element with full 3x3 quadrature in the r-s plane, as given by Belytschko et al. (1989), are shown in Table 3.2. The slow convergence exhibited by the nine node isoparametric shell element is a result of the

Table 3.2: Results of cylindrical panel analysis using the nine node isoparametric shell element without reduced integration.

Elements	Degrees of Freedom	Normalized Deflection
4	96	0.265
16	352	0.818
64	1344	0.987

inconsistency in the displacement fields used in its formulation. This is because the spurious shear modes are not suppressed even though the transverse shear stresses are negligible. The consistent shell element on the other hand demonstrates very good accuracy even for coarse meshes since the locking problem has been eliminated through the provision of a consistent formulation and use of complete polynomials.

3.4.3 Hemispherical Shell Under Point Loads

A quadrant of a hemispherical shell (because of double symmetry) subjected to two concentrated loads at the equator is shown in Figure 3.6. All degrees of freedom at the pole at point A are constrained, while those along the equator are free. Analysis of the shell quadrant has been performed using from 9 to 121 consistent shell elements as indicated in Table 3.3. The radial deflections predicted at node B by the consistent shell element models are normalized with respect to 0.0924, which is the deflection obtained by Morley and Morris (1978). The normalized deflections are listed in Table 3.3.

The shell has also been analysed by Belytschko et al. (1989) using two different versions of the nine node isoparametric shell element. The first employs full 3x3 quadrature in the r-s plane and the second employs selective reduced integration (i.e. 2x2 quadrature for transverse shear stiffness and 3x3 quadrature for flexural stiffness). The results of the analysis are given in Table 3.4. The results obtained using the consistent shell element indicate convergence to a displacement which is approximately 10% less than that obtained by Morley and Morris. However, Vu-Quoc and Mora (1989) question

Table 3.3: Results of hemispherical shell analysis using the consistent shell element.

Elements	Normalized Deflection	Elements	Normalized Deflection
9	0.116	64	0.819
25	0.538	81	0.849
36	0.684	100	0.868
49	0.770	121	0.880

the correctness of the analytical solution given by Morley and Morris. Specifically, they point out that the solution obtained by Morley and Morris has been obtained without considering the local effects due to the concentrated forces. In this light the deflections predicted by the consistent shell element can be considered good. However, the deflections predicted by both of the nine node isoparametric shell element models appear to be in very poor agreement with the reference solution. This again illustrates that the provision of a consistent formulation eliminates the locking behaviour associated with the presence of the spurious transverse shear strain modes.

Table 3.4: Results of hemispherical shell analysis using the nine node isoparametric shell element.

Elements	Normalized Deflection	
	Full Int.	Reduced Int.
3	0.001	0.004
15	0.014	0.032
63	0.173	0.196

3.4.4 Elasto-Plastic Thin Plate

An elastic perfectly plastic analysis of a simply supported thin square plate subjected to a uniformly distributed load as shown in Figure 3.7 has been performed. A quarter of the plate (due to double symmetry) has been analysed using eight consistent shell elements. The predicted load deflection curve at the center of the plate is shown in Figure 3.8. Also plotted in the figure are the results obtained by Owen and Hinton (1980) using four selectively integrated (i.e. 2x2 quadrature for transverse shear stiffness and 3x3 quadrature for flexural stiffness) Heterosis plate elements (Hughes and Cohen 1978). The Heterosis element employs the nine node Lagrangian shape functions for approximation of rotations and the eight node Serendipity shape functions for approximation of the transverse displacement w.

The load deflection curve predicted by the consistent shell element model is in very good agreement with that given by Heterosis model in both the elastic and elasto-plastic ranges. The plate was analysed using the full matrix formulation and the reduced strain-displacement matrix formulation of the consistent shell element. The computer time required for solution of the problem using the reduced strain-displacement matrix formulation was 46% less than that required by the full matrix formulation. This example illustrates the accuracy of the elasto-plastic formulation of the consistent shell element and the computational efficiency of the reduced strain-displacement matrix formulation.

3.4.5 Consistent Shell Element Convergence

Consider an element similar to the consistent shell element but which employs a quadratic and linear approximation of the displacements and rotations, respectively, instead of cubic and quadratic approximations. In this example the consistent shell element is referred to as the cubic-quadratic shell element and its lower order counterpart will be referred to as the quadratic linear shell element. The purpose of this example is to compare the convergence and accuracy of the consistent shell elements to each other and to solutions obtained using the nine node isoparametric shell element.

A thin clamped square plate subjected to a uniformly distributed load is analysed using the cubic-quadratic and quadratic-linear consistent shell elements. The elastic modulus, Poisson's ratio and length to thickness ratio of the plate are 30000, 0.3 and 200, respectively. Any units can be assumed. Due to symmetry only one quarter of the plate has been analysed. The central plate deflection predicted by the finite element models is normalized with respect to the solution given by Timoshenko (1959) and plotted against the number of degrees of freedom in Figure 3.9. Also plotted are the results predicted by the nine-node isoparametric shell element. For each finite element model, subsequent analyses have been carried out after uniform refinement of the previous mesh. The cubic-quadratic model converges rapidly to the reference solution, followed by the nine-node shell element model and then the quadratic-linear model. This is because in both the cubic-quadratic element and the nine-node isoparametric shell element the bending moments vary linearly, while in the quadratic-linear element they are constant. In addition, the

transverse displacement is approximated by a cubic polynomial in the cubic-quadratic element, and by a quadratic polynomial in both the nine-node isoparametric shell element and the quadratic-linear element. The results show that the cubic-quadratic shell element converges more rapidly and provides a more accurate solution than either of the other elements. Of course, the cubic-quadratic shell element will always yield better results than its quadratic-linear counterpart.

A clamped thick circular plate subjected to a uniformly distributed load has also been analysed using the cubic-quadratic and quadratic-linear shell elements. The radius, thickness, elastic modulus and Poisson's ratio for the plate are 5, 2, 30000 and 0.3, respectively. Again, any units can be used. The central plate deflection predicted by the finite element models is normalized with respect to the solution given by Young (1989) and plotted against the number of degrees of freedom in Figure 3.10. Also plotted are the results predicted by the nine-node isoparametric shell element. Again the accuracy and rate of convergence of the cubic-quadratic shell element are excellent.

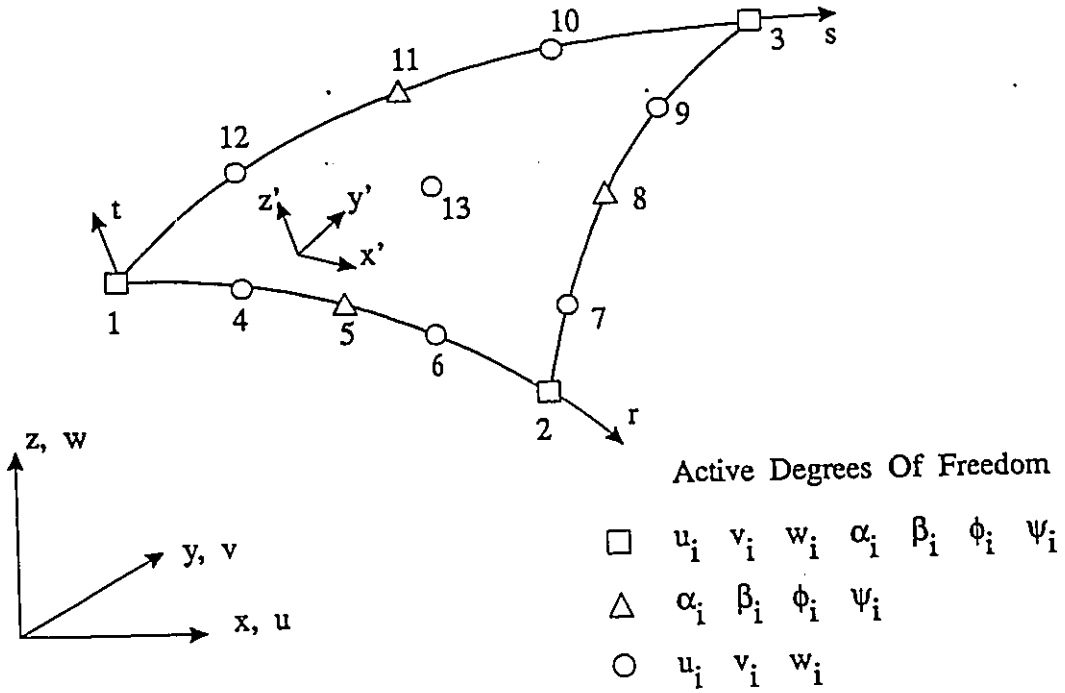

Figure 3.1: Consistent shell element co-ordinate systems and nodal degrees of freedom.

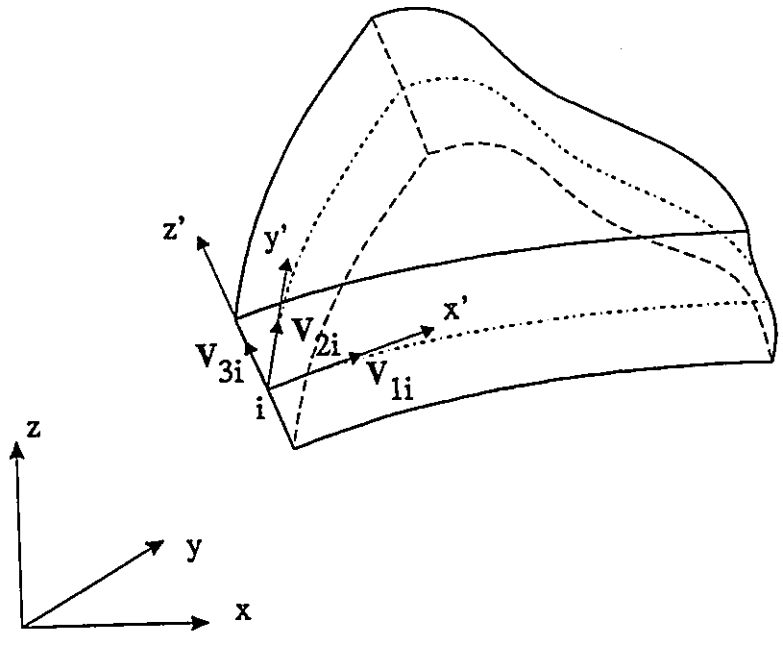

Figure 3.2: Consistent shell element nodal unit vectors.

$$< u_1\ v_1\ w_1\ \ldots\ u_{13}\ v_{13}\ w_{13}\ 0\ 0\ 0\ 0 >$$

$$\overbrace{\underbrace{\{LSu\}}_{\{u\}}\ \underbrace{\{LSv\}}_{\{v\}}\ \underbrace{\{LSw\}}_{\{w\}}\ \underbrace{\{LS\alpha\}}_{\{\alpha\}}\ \underbrace{\{LS\beta\}}_{\{\beta\}}\ \underbrace{\{LS\phi\}}_{\{\phi\}}\ \underbrace{\{LS\psi\}}_{\{\psi\}}}$$

$$\left[\begin{array}{ccccccc|c|c}
[k^S]_{11} & [k^S]_{12} & [k^S]_{13} & [k^S]_{14} & [k^S]_{15} & [k^S]_{16} & [k^S]_{17} & \{u\} \mid \{LSu\} & \\
[k^S]_{21} & [k^S]_{22} & [k^S]_{23} & [k^S]_{24} & [k^S]_{25} & [k^S]_{26} & [k^S]_{27} & \{v\} \mid \{LSv\} & \\
[k^S]_{31} & [k^S]_{32} & [k^S]_{33} & [k^S]_{34} & [k^S]_{35} & [k^S]_{36} & [k^S]_{37} & \{w\} \mid \{LSw\} & \\
[k^S]_{41} & [k^S]_{42} & [k^S]_{43} & [k^S]_{44} & [k^S]_{45} & [k^S]_{46} & [k^S]_{47} & \{\alpha\} \mid \{LS\alpha\} & \Rightarrow \\
[k^S]_{51} & [k^S]_{52} & [k^S]_{53} & [k^S]_{54} & [k^S]_{55} & [k^S]_{56} & [k^S]_{57} & \{\beta\} \mid \{LS\beta\} & \\
[k^S]_{61} & [k^S]_{62} & [k^S]_{63} & [k^S]_{64} & [k^S]_{65} & [k^S]_{66} & [k^S]_{67} & \{\phi\} \mid \{LS\phi\} & \\
[k^S]_{71} & [k^S]_{72} & [k^S]_{73} & [k^S]_{74} & [k^S]_{75} & [k^S]_{76} & [k^S]_{77} & \{\psi\} \mid \{LS\psi\} &
\end{array}\right]
\left\{\begin{array}{c} u_1 \\ v_1 \\ w_1 \\ \vdots \\ u_{13} \\ v_{13} \\ w_{13} \\ 0 \\ 0 \\ 0 \\ 0 \end{array}\right\}$$

Figure 3.3: Stiffness sub-matrix referencing using sub-variable location vectors.

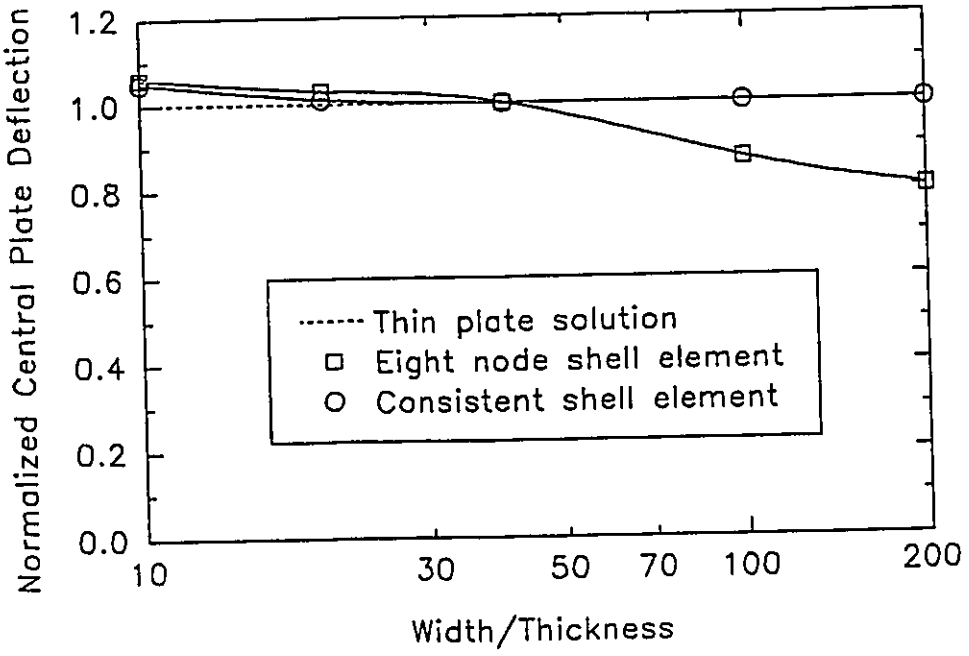

Figure 3.4: Normalized center plate deflection versus width to thickness ratio for a simply supported square plate under uniform load q.

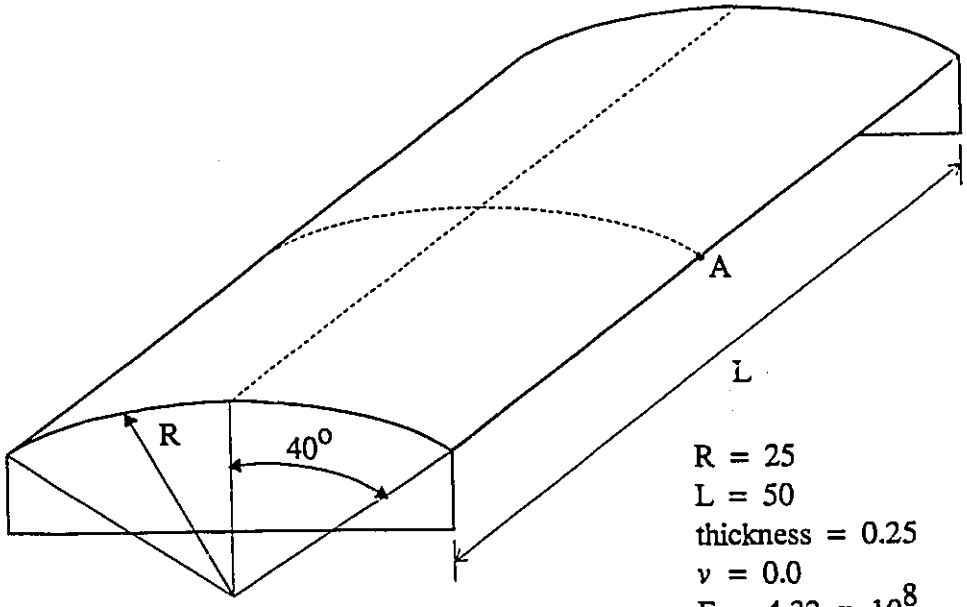

Figure 3.5: Cylindrical shell roof dimensions, loading and material properties.

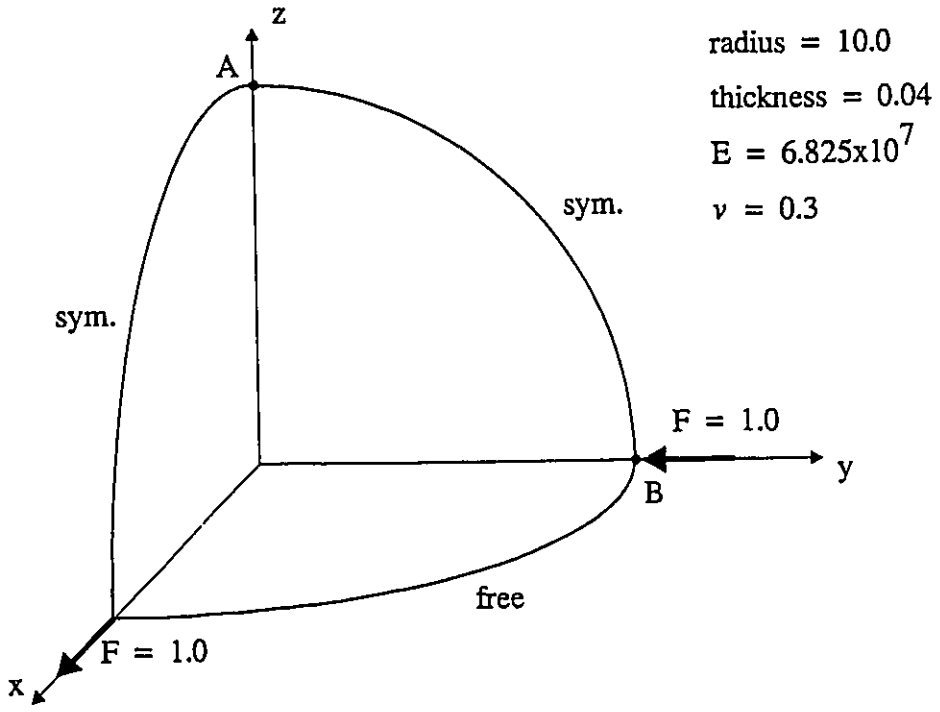

Figure 3.6: Hemispherical shell geometry, loading and material properties.

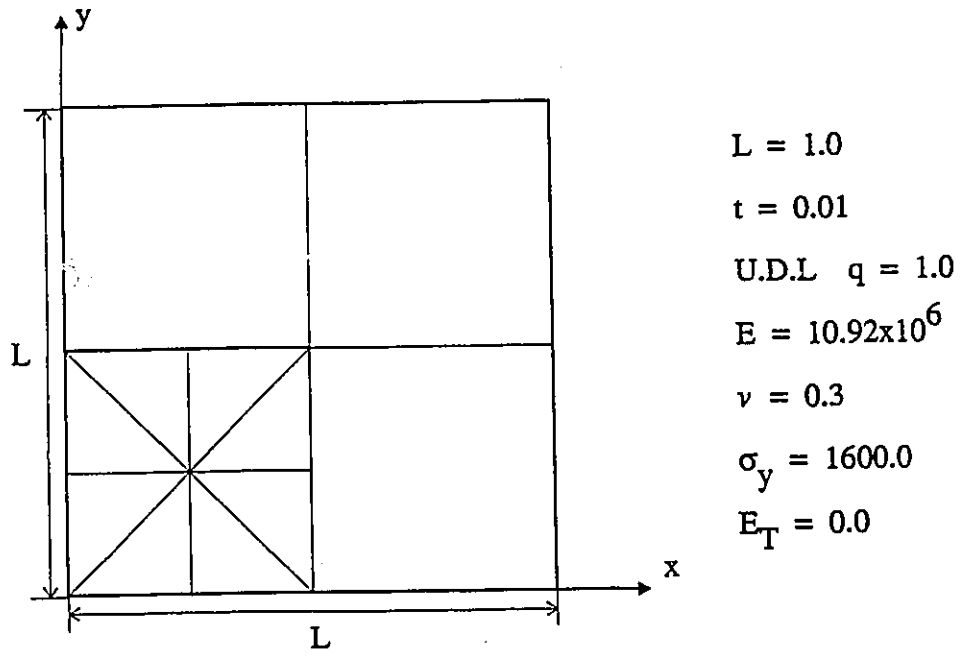

Figure 3.7: Geometry, material properties and loading for simply supported thin square plate.

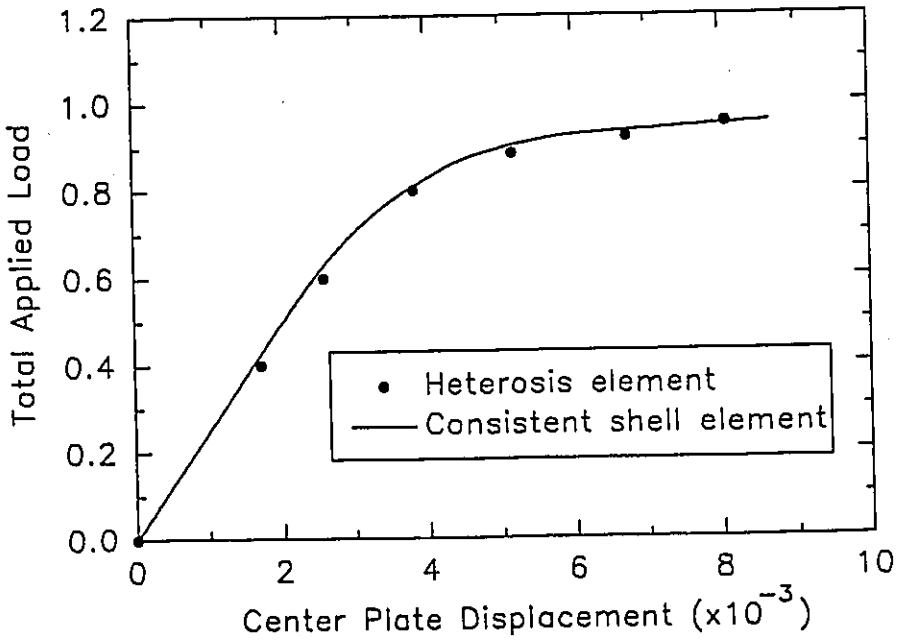

Figure 3.8: Total applied load versus center plate displacement for a simply supported square plate loaded by uniform load q.

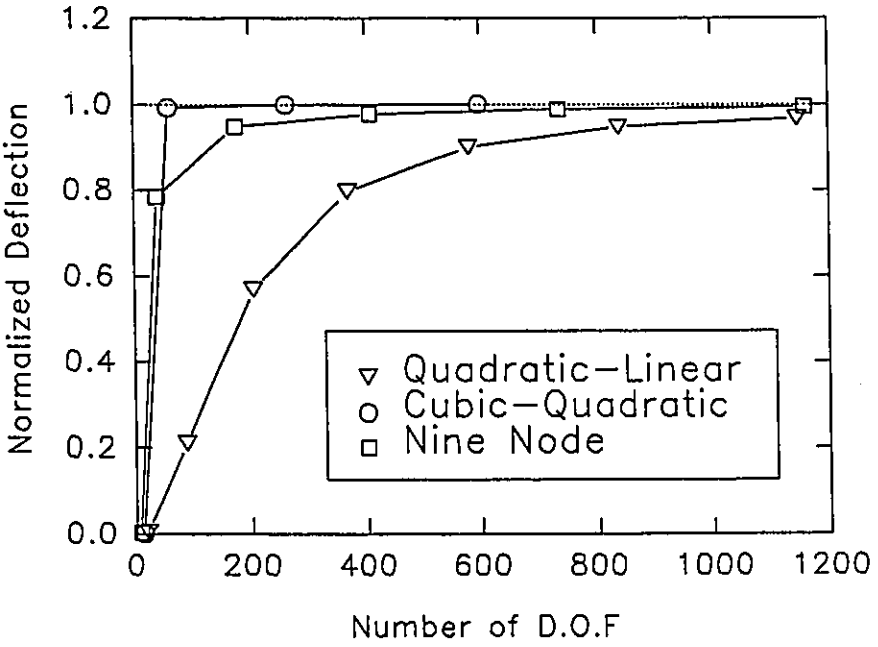

Figure 3.9: Convergence of center plate deflection for a clamped thin square plate subjected to a u.d.l.

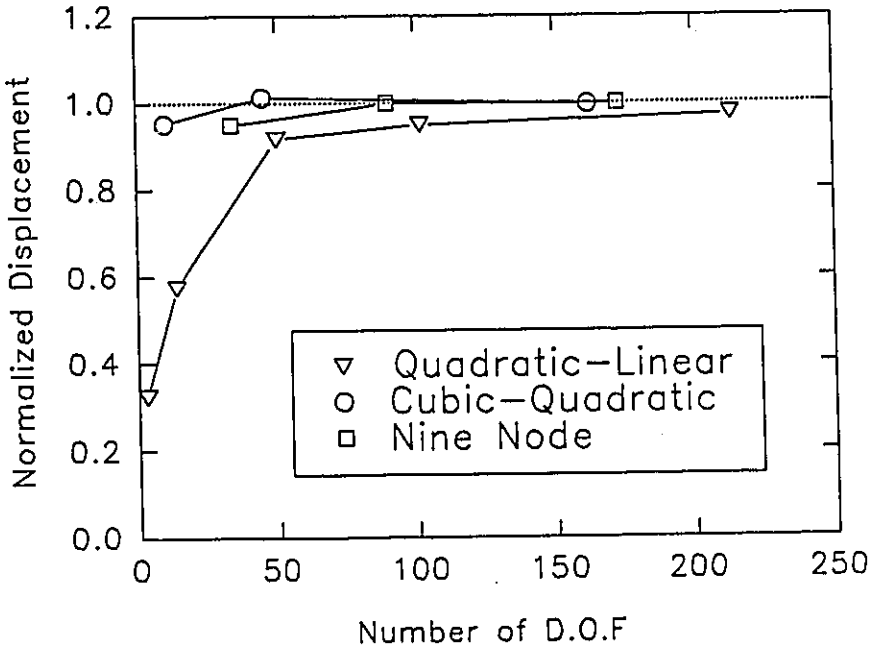

Figure 3.10: Convergence of center plate deflection for a clapmed thick circular plate subjected to a u.d.l.

CHAPTER FOUR

FINITE ELEMENT MODEL FOR COMPOSITE STRUCTURES OF STEEL AND CONCRETE

4.1 Introduction

Composite steel and concrete construction has been applied in many important areas such as buildings, bridges, off shore oil platforms, nuclear containment structures, dams and pressure vessels. In this chapter a finite element model for the analysis of composite structures of steel and concrete is developed as an extension of work done by Chow (1984), Jiang (1985), Jiang (1988) and Zhou (1991).

The behaviour of a composite structure of steel and concrete involves a complex interaction between its constituents. These constituents commonly include concrete, embedded reinforcement either plain or prestressed, shear connectors and supporting girders as shown in Figure 4.1. The concrete constitutive model developed by Pietruszczak et al. (1988) and Jiang (1989) has been shown to adequately reflect certain typical trends in concrete behaviour. This constitutive model in combination with the consistent shell element formulated in Chapter Three is used to model concrete plates and shells. A required one dimensional curved bar element is formulated and used for modelling of the plain and prestressed reinforcing bars. The influence of bond between the reinforcement and the surrounding concrete on the response of the

structure is simulated through a joint element which can allow slippage to occur along the interface. Supporting girders are modelled using a modified form of the consistent beam element formulated in Chapter Two. These supporting members are typically connected to the concrete plate or shell by means of mechanical connectors. Due to the deformable nature of these connectors slippage can occur at the interface of the supporting member and the concrete. This behaviour is modelled through a shear connector element which allows for slippage along the interface depending upon the load deformation characteristics of the connectors. For verification of the model a reinforced concrete plate and a multi-girder prestressed concrete deck have been analysed and the predicted results have compared with the available experimental data.

4.2 Finite Element Models

4.2.1 Reinforcement Element

A one dimensional cubic isoparametric bar element is used to model both the plain and prestressed reinforcement. Co-ordinate systems used in the element formulation are shown in Figure 4.2, and defined as follows:

1. Global cartesian co-ordinate system x^r, y^r and z^r and corresponding global displacements u^r, v^r and w^r.
2. Curvilinear co-ordinate ζ tangent to the element.
3. Local dimensional co-ordinate $\bar{\zeta}$ tangent to the element to define the local axial displacement $d^r_{\bar{\zeta}}$, local strain $\epsilon^r_{\bar{\zeta}}$ and local stress $\sigma^r_{\bar{\zeta}}$.

For geometric distortion of the element a curvilinear transformation is

used in terms of ζ. Thus, the location of any point along the element in the global co-ordinate system is given as

$$\begin{Bmatrix} x^r \\ y^r \\ z^r \end{Bmatrix} = \Sigma N_i^r \begin{Bmatrix} x_i^r \\ y_i^r \\ z_i^r \end{Bmatrix} \tag{4.1}$$

where cubic interpolation functions N_i^r are given in Appendix A3 and x_i^r, y_i^r and z_i^r are the global co-ordinates of the i^{th} node.

Cubic approximations of displacements u^r, v^r and w^r are constructed using the global displacement degrees of freedom (u_i^r, v_i^r, w_i^r) at each of the four nodes. This gives a total of twelve degrees of freedom per element. The axial displacement $d_{\bar{\zeta}}^r$ at any point along the element can be written in terms of the nodal degrees of freedom as

$$d_{\bar{\zeta}}^r = \Sigma N_i^r \begin{bmatrix} \lambda_1^r & \lambda_2^r & \lambda_3^r \end{bmatrix} \begin{Bmatrix} u_i^r \\ v_i^r \\ w_i^r \end{Bmatrix} \tag{4.2}$$

where direction cosines $(\lambda_1^r, \lambda_2^r, \lambda_3^r)$ relate the local co-ordinate axis $\bar{\zeta}$ to the global axes (x^r, y^r, z^r) at the point along the element where displacement $d_{\bar{\zeta}}^r$ is to be calculated. Using Equation 4.1 the direction cosines are computed as follows

$$\lambda_1^r = \frac{dx^r}{d\zeta} \Big/ \sqrt{\left[\frac{dx^r}{d\zeta}\right]^2 + \left[\frac{dy^r}{d\zeta}\right]^2 + \left[\frac{dz^r}{d\zeta}\right]^2}$$

$$\lambda_2^r = \frac{dy^r}{d\zeta} \Big/ \sqrt{\left[\frac{dx^r}{d\zeta}\right]^2 + \left[\frac{dy^r}{d\zeta}\right]^2 + \left[\frac{dz^r}{d\zeta}\right]^2} \qquad (4.3,a\text{-}c)$$

$$\lambda_3^r = \frac{dz^r}{d\zeta} \Big/ \sqrt{\left[\frac{dx^r}{d\zeta}\right]^2 + \left[\frac{dy^r}{d\zeta}\right]^2 + \left[\frac{dz^r}{d\zeta}\right]^2}.$$

The local axial strain $\epsilon^r_{\bar{\zeta}}$ is given by

$$\epsilon^r_{\bar{\zeta}} = \frac{d\ d^r}{d\bar{\zeta}}\bar{\zeta} = \sum_i^4 \frac{dN^r_i}{d\bar{\zeta}} \left[\lambda^r_1\ \lambda^r_2\ \lambda^r_3\right] \begin{Bmatrix} u^r_i \\ v^r_i \\ w^r_i \end{Bmatrix} \qquad (4.4)$$

which can also be written as $\epsilon^r_{\bar{\zeta}} = [B^r]\ \{d^r\}$. Here vector $\{d^r\}$ is the vector of nodal degrees of freedom and matrix $[B^r]$ is the strain-displacement matrix. Matrix $[B^r]$ contains the derivatives of the shape functions N^r with respect to the local dimensional co-ordinate $\bar{\zeta}$. The relationship between the axial stress $\sigma^r_{\bar{\zeta}}$ and the axial strain $\epsilon^r_{\bar{\zeta}}$ is defined as

$$\sigma^r_{\bar{\zeta}} = \begin{cases} E^r\ \epsilon^r_{\bar{\zeta}} & \text{when } \sigma^r_{\bar{\zeta}} \le \sigma^r_Y \\ E^r_T\ \epsilon^r_{\bar{\zeta}} & \text{when } \sigma^r_{\bar{\zeta}} > \sigma^r_Y \end{cases} \qquad (4.5)$$

where σ^r_Y is the uniaxial yield stress and E^r and E^r_T are the elastic and tangent moduli, respectively. It should be noted that all strains other than the axial strain are assumed to be zero.

The element stiffness matrix $[k^r]$ is computed according to

$$[k^r] = \int_V [B^r]^T E^r [B^r] \, dV. \tag{4.6}$$

and the load vector $\{p^r\}$ due to the internal prestress $\sigma^r_{\bar{\zeta}}$ is calculated as

$$\{p^r\} = \int_V [B^r]^T \sigma^r_{\bar{\zeta}} \, dV. \tag{4.7}$$

Both $[k^r]$ and $\{p^r\}$ are integrated numerically using the Gaussian Quadrature scheme. Differential $d\zeta$ in the non-dimensional co-ordinate system is related to differential $d\bar{\zeta}$ in the dimensional co-ordinate system through

$$d\bar{\zeta} = \sqrt{\left[\frac{dx^r}{d\zeta}\right]^2 + \left[\frac{dy^r}{d\zeta}\right]^2 + \left[\frac{dz^r}{d\zeta}\right]^2}\, d\zeta. \tag{4.8}$$

Using Equation 4.8 and the chain rule the shape function derivatives in Equation 4.4 are transformed as follows

$$\frac{dN_i}{d\bar{\zeta}} = \frac{dN_i}{d\zeta}\frac{d\zeta}{d\bar{\zeta}} = \frac{dN_i}{d\zeta} \Big/ \sqrt{\left[\frac{dx^r}{d\zeta}\right]^2 + \left[\frac{dy^r}{d\zeta}\right]^2 + \left[\frac{dz^r}{d\zeta}\right]^2}. \tag{4.9}$$

Finally, the element stiffness matrix $[k^r]$ and load vector $\{p^r\}$ are calculated using the following equations

$$[k^r] = \int_{-1}^{+1} [B^r]^T E^r [B^r] A^r \sqrt{\left[\frac{dx^r}{d\zeta}\right]^2 + \left[\frac{dy^r}{d\zeta}\right]^2 + \left[\frac{dz^r}{d\zeta}\right]^2}\, d\zeta$$

$$\{p^r\} = \int_{-1}^{+1} [B^r]^T \sigma_{\zeta}^r A^r \sqrt{\left[\frac{dx^r}{d\zeta}\right]^2 + \left[\frac{dy^r}{d\zeta}\right]^2 + \left[\frac{dz^r}{d\zeta}\right]^2}\, d\zeta \quad (4.10,a\text{-}b)$$

where A^r is the cross-sectional area of the element. Integration of equations 4.10 is performed using three integration points along the ζ co-ordinate.

4.2.2 Joint Element

A joint element is used to simulate bond slip along the concrete/reinforcement interface. The element is composed of springs which are tangent and uniformly distributed along the concrete and reinforcement interface. The joint element stiffness matrix is formulated in terms of the relative tangential displacement d_{rel}^{joint} along the concrete/reinforcement interface which is given by

$$d_{rel}^{joint} = d_{\zeta}^{c} - d_{\zeta}^{r} \quad (4.11)$$

where d_{ζ}^{c} is the displacement of the concrete at the interface in the direction tangent to the reinforcement element, and d_{ζ}^{r} is the axial displacement of the reinforcement element. Displacement d_{ζ}^{r} is given in Equation 4.2 in the previous section. It should be noted that the concrete and reinforcing bar are assumed to have the same displacement normal to the interface. However, the transverse stiffness of the reinforcement has been ignored.

The concrete displacement at the interface in the direction tangent to

the reinforcement element is given by

$$d^c_{\zeta} = [\ \lambda^r_1\ \lambda^r_2\ \lambda^r_3\ ] \begin{Bmatrix} u^c \\ v^c \\ w^c \end{Bmatrix} = \{\lambda^r\}^T \begin{Bmatrix} u^c \\ v^c \\ w^c \end{Bmatrix} \tag{4.12}$$

where displacements u^c, v^c and w^c are the global displacements of the concrete (i.e. the consistent shell element) at the interface. The global displacements (u,v,w) of the consistent shell element have been given in terms of the shell element nodal degrees of freedom in Equation 3.3 of Chapter Three. Substituting Equation 3.3 into Equation 4.12 and multiplying gives displacement d^c_{ζ} in terms of the consistent shell element nodal degrees of freedom and the direction cosines $\{\lambda^r\}$ as

$$d^c_{\zeta} = \Sigma\, \tilde{N}_i\, \{\lambda^r\}^T \begin{Bmatrix} u_i \\ v_i \\ w_i \end{Bmatrix} + \Sigma\, N_i\, M_1\, \{\lambda^r\}^T\, [\hat{V}_i] \begin{Bmatrix} \alpha_i \\ \beta_i \end{Bmatrix}$$

$$+ \Sigma\, N_i\, M_2\, \{\lambda^r\}^T\, [\hat{V}_i] \begin{Bmatrix} \phi_i \\ \psi_i \end{Bmatrix}. \tag{4.13}$$

The nodal degrees of freedom of the consistent shell element $\{d\}$ and the reinforcement element degrees of freedom $\{d^r\}$ are combined to give

$$\underset{103x1}{\{d^{joint}\}} = \begin{Bmatrix} \{d\}_{91x1} \\ \{d^r\}_{12x1} \end{Bmatrix} \tag{4.14}$$

which is the joint element degree of freedom vector. Substituting the expressions for d^c_{ζ}, Equation 4.13, and d^r_{ζ}, Equation 4.2, into Equation 4.11

gives the relative displacement in terms of $\{d^{joint}\}$ as

$$d^{joint}_{rel} = \underset{1\times 91}{\left[[N^c] \right.} \quad \underset{1\times 12}{\left. - [N^r] \right]} \begin{Bmatrix} \{d\} \\ \{d^r\} \end{Bmatrix} = \underset{1\times 103}{[N^{joint}]} \; \underset{103\times 1}{\{d^{joint}\}} \tag{4.15}$$

where

$$[N^r] = \sum_i^4 [\, \lambda^r_1 N^r_i \quad \lambda^r_2 N^r_i \quad \lambda^r_3 N^r_i \,]$$

$$\begin{aligned} [N^c] = \sum_i^{13} [\; & \lambda^r_1 \bar{N}_i \quad \lambda^r_2 \bar{N}_i \quad \lambda^r_3 \bar{N}_i \quad M_1 N_i(\lambda^r_1 l_{1i} + \lambda^r_2 m_{1i} + \lambda^r_3 n_{1i}) \\ & -M_1 N_i(\lambda^r_1 l_{2i} + \lambda^r_2 m_{2i} + \lambda^r_3 n_{2i}) \quad M_2 N_i(\lambda^r_1 l_{1i} + \lambda^r_2 m_{1i} + \lambda^r_3 n_{1i}) \\ & -M_2 N_i(\lambda^r_1 l_{2i} + \lambda^r_2 m_{2i} + \lambda^r_3 n_{2i}) \;]. \end{aligned}$$

Interpolation functions N^r_i of matrix $[N^r]$ are evaluated at ζ corresponding to the point along the interface where the relative displacement is to be calculated. Similarly, functions $\bar{N}_i$, N_i, M_1 and M_2 of matrix $[N^c]$ are evaluated at curvilinear co-ordinates r, s and t which correspond to the point of interest on the concrete/reinforcement interface.

The strain energy due to the relative displacement d^{joint}_{rel} is given by

$$U = \frac{1}{2} \int_0^L k_{joint} \, (d^{joint}_{rel})^2 \, d\bar{\zeta} \tag{4.16}$$

which then leads to the stiffness matrix $[k^{joint}]$ of the joint element as

$$[k^{joint}]_{103x103} = \int_0^L [N^{joint}]^T_{103x1}\, k_{joint}\, [N^{joint}]_{1x103}\, d\bar{\zeta} \qquad (4.17)$$

and k_{joint} represents the distributed stiffness along the interface due to bonding. Since a simple general expression for k_{joint} is not yet available, various values of k_{joint} are assumed and the effect on the predicted response of the structure can be investigated. It should be noted that the influence of k_{joint} in slabs is usually negligible. Integration of Equation 4.17 is performed numerically using the Gaussian Quadrature scheme. Changing the limits of integration in Equation 4.17 and transforming $d\bar{\zeta}$ using Equation 4.8 gives

$$[k^{joint}] = \int_{-1}^{+1} [N^{joint}]^T\, k_{joint}\, [N^{joint}] \sqrt{\left[\frac{dx^r}{d\zeta}\right]^2 + \left[\frac{dy^r}{d\zeta}\right]^2 + \left[\frac{dz^r}{d\zeta}\right]^2}\, d\zeta \qquad (4.18)$$

which is integrated using three integration points along the ζ co-ordinate direction. The element load vector $\{p^{joint}\}$ due to bond stresses along the interface is calculated from

$$\{p^{joint}\}_{103x1} = [k^{joint}]_{103x103}\, \{d^{joint}\}_{103x1} \qquad (4.19)$$

according to linear elastic theory. An incremental approach must be adopted for the case of deteriorating k_{joint}.

4.2.3 Transformation of Boundary Degrees of Freedom

Nodal degrees of freedom at a joint element or a reinforcement

element boundary node must be transformed in order to satisfy deformation compatibility on the boundary. This is accomplished by expressing the degrees of freedom at the boundary node in terms of the consistent shell element nodal degrees of freedom.

For example, when node one of a reinforcement element is on the boundary the vector of reinforcement element degrees of freedom $\{d^r\}$ is equal to

$$\underset{12x1}{\{d^r\}} = \underset{12x100}{[T_1]} \; \underset{100x1}{\{d^{r\prime}\}} \tag{4.20}$$

where $\{d^{r\prime}\}$ is obtained by combining the shell element nodal degrees of freedom and the remaining independent reinforcement element degrees of freedom at nodes 2 through 4 to give

$$\underset{1x100}{\{d^{r\prime}\}^T} = < \underset{1x91}{\{d\}^T} \; u_2 \; v_2 \; w_2 \; u_3 \; v_3 \; w_3 \; u_4 \; v_4 \; w_4 > . \tag{4.21}$$

Transformation matrix $[T_1]$ is given by

$$\underset{12x100}{[T_1]} = \begin{bmatrix} \sum_i^{13} \begin{bmatrix} \bar{N}_i & 0 & 0 & N_iM_1l_{1i} & -N_iM_1l_{2i} & N_iM_2l_{1i} & -N_iM_2l_{2i} \\ 0 & \bar{N}_i & 0 & N_iM_1m_{1i} & -N_iM_1m_{2i} & N_iM_2m_{1i} & -N_iM_2m_{2i} \\ 0 & 0 & \bar{N}_i & N_iM_1n_{1i} & -N_iM_1n_{2i} & N_iM_2n_{1i} & -N_iM_2n_{2i} \end{bmatrix} & \underset{3x9}{[0]} \\ \underset{9x91}{[0]} & \underset{9x9}{[I]} \end{bmatrix} \tag{4.22}$$

where $\bar{N}_i$ and N_i are evaluated at curvilinear co-ordinates r, s and t

corresponding to the location of node one of the reinforcement element. Using transformation matrix $[T_1]$ the transformed reinforcement element stiffness matrix $[k^{r\prime}]$ and transformed load vector $\{p^{r\prime}\}$ are given by

$$\underset{100x100}{[k^{r\prime}]} = \underset{100x12}{[T_1]^T} \; \underset{12x12}{[k^r]} \; \underset{12x100}{[T_1]} \tag{4.23,a-b}$$

$$\underset{100x1}{\{p^{r\prime}\}} = \underset{100x12}{[T_1]^T} \; \underset{12x1}{\{d^r\}}.$$

When node four of a reinforcement element is on the boundary the degrees of freedom, the stiffness matrix and load vector are transformed in a similar manner. However, transformation matrix $[T_4]$ is used instead of transformation matrix $[T_1]$. Transformation matrix $[T_4]$ is given in Appendix F. For joint elements having nodes on the boundary the same procedure is employed. However, instead of using transformation matrices $[T_1]$ and $[T_4]$ matrices $[T_1^{joint}]$ and $[T_4^{joint}]$ are employed in their place. Matrices $[T_1^{joint}]$ and $[T_4^{joint}]$ are also defined in Appendix F.

4.2.4 Girder Element

A beam element similar to the consistent beam element formulated in Chapter Two is used to model the supporting members such as girders. The co-ordinate systems used in the formulation are shown in Figure 4.3, and defined as follows:

1. Global cartesian co-ordinate system x^g,y^g and z^g, and corresponding displacements u^g, v^g and w^g.

2. Natural co-ordinates ζ and ξ where ζ is tangent to the curved line defined by ξ=constant, and ξ is normal to the ζ axis.
3. Local dimensional co-ordinates $\bar{\zeta}$ and $\bar{\xi}$ to define local displacements, strains and stresses; $\bar{\zeta}$ is tangent and $\bar{\xi}$ is perpendicular to the curved centroidal axis in general.

The element is distorted geometrically using a curvilinear transformation along the ζ co-ordinate direction and a linear transformation in the ξ co-ordinate direction. The location of any point within the element in the global co-ordinate system is given by

$$\begin{Bmatrix} x^g \\ y^g \\ z^g \end{Bmatrix} = \Sigma N_i^g \begin{Bmatrix} x_i^g \\ y_i^g \\ z_i^g \end{Bmatrix} + \Sigma N_i^g \frac{\xi}{2} V_i^g \qquad (4.24)$$

where x_i^g, y_i^g and z_i^g are the global co-ordinates of the i^{th} node and N_i^g are quadratic shape functions which are given in Appendix A4 and vector V_i^g is defined as

$$V_i^g = \begin{Bmatrix} x_i^g \\ y_i^g \\ z_i^g \end{Bmatrix}_{TOP} - \begin{Bmatrix} x_i^g \\ y_i^g \\ z_i^g \end{Bmatrix}_{BOTTOM}. \qquad (4.25)$$

The girder element, like the consistent beam element employs cubic polynomials for approximation of the displacements and quadratic polynomials for approximation of the rotations. For displacement interpolation the

displacement degrees of freedom (u_i^g, v_i^g, w_i^g) at the end nodes and one-third point nodes are used. The rotations are interpolated using the rotational degrees of freedom (α_i^g, ϕ_i^g) at the end nodes and mid-side node. For the same number of degrees of freedom per node there will be twenty-five degrees of freedom per element. However only seventeen of these are active. Rotation α^g produces a linear variation of the displacements through the thickness while ϕ^g gives a cubic variation. The element displacement field is given as

$$\begin{Bmatrix} u^g \\ v^g \\ w^g \end{Bmatrix} = \sum \bar{N}_i^g \begin{Bmatrix} u_i^g \\ v_i^g \\ w_i^g \end{Bmatrix} - \sum N_i^g M_1^g \begin{Bmatrix} \lambda_{1i}^g \\ \lambda_{2i}^g \\ \lambda_{3i}^g \end{Bmatrix} \alpha_i^g - \sum N_j^g M_2^g \begin{Bmatrix} \lambda_{1i}^g \\ \lambda_{2i}^g \\ \lambda_{3i}^g \end{Bmatrix} \phi_i^g \qquad (4.26)$$

where $\bar{N}_i^g$ are the cubic interpolation functions which are defined in Appendix A4. Direction cosines λ_{1i}^g, λ_{2i}^g and λ_{3i}^g relate the global axes (x^g, y^g, z^g) to the local $\bar{\zeta}$ axis at the i^{th} node and are determined using Equation 4.24 as follows

$$\lambda_1^g = \frac{\partial x^g}{\partial \zeta} \Big/ \sqrt{\left[\frac{\partial x^g}{\partial \zeta}\right]^2 + \left[\frac{\partial y^g}{\partial \zeta}\right]^2 + \left[\frac{\partial z^g}{\partial \zeta}\right]^2}$$

$$\lambda_2^g = \frac{\partial y^g}{\partial \zeta} \Big/ \sqrt{\left[\frac{\partial x^g}{\partial \zeta}\right]^2 + \left[\frac{\partial y^g}{\partial \zeta}\right]^2 + \left[\frac{\partial z^g}{\partial \zeta}\right]^2} \qquad (4.27,a\text{-}c)$$

$$\lambda_3^g = \frac{\partial z^g}{\partial \zeta} \Big/ \sqrt{\left[\frac{\partial x^g}{\partial \zeta}\right]^2 + \left[\frac{\partial y^g}{\partial \zeta}\right]^2 + \left[\frac{\partial z^g}{\partial \zeta}\right]^2}.$$

Shape functions M_1^g and M_2^g approximate the displacement field through the depth due to rotations α^g and ϕ^g, respectively, and are given by

$$M_1^g = \frac{h_i \xi}{2} \qquad M_2^g = \frac{h_i \xi}{2}(1 - \xi^2) \tag{4.28}$$

where h_i is the girder thickness at the i^{th} node.

For small deflections the local strains $\{\epsilon^g\}$ are written as

$$\begin{Bmatrix} \epsilon^g_{\bar{\zeta}\bar{\zeta}} \\ \epsilon^g_{\bar{\zeta}\bar{\xi}} \end{Bmatrix} = \begin{bmatrix} \frac{\partial}{\partial \bar{\zeta}} & 0 \\ \frac{\partial}{\partial \bar{\zeta}} & \frac{\partial}{\partial \bar{\xi}} \end{bmatrix} \begin{Bmatrix} d^g_{\bar{\zeta}} \\ d^g_{\bar{\xi}} \end{Bmatrix} \tag{4.29}$$

where the local displacements $d^g_{\bar{\zeta}}$ and $d^g_{\bar{\xi}}$ are directed along the $\bar{\zeta}$ and $\bar{\xi}$ axes, respectively, and can be expressed in terms of the global displacements using the direction cosines as follows

$$\begin{Bmatrix} d^g_{\bar{\zeta}} \\ d^g_{\bar{\xi}} \end{Bmatrix} = \begin{bmatrix} \lambda^g_1 & \lambda^g_2 & \lambda^g_3 \\ \Lambda^g_1 & \Lambda^g_2 & \Lambda^g_3 \end{bmatrix} \begin{Bmatrix} u^g \\ v^g \\ w^g \end{Bmatrix} = [\theta^g] \begin{Bmatrix} u^g \\ v^g \\ w^g \end{Bmatrix}. \tag{4.30}$$

Direction cosines Λ^g_1, Λ^g_2 and Λ^g_3 are directed along the local $\bar{\xi}$ axis and are determined using Equation 4.24 as follows

$$\Lambda^g_1 = \frac{\partial x^g}{\partial \xi} \Big/ \sqrt{\left[\frac{\partial x^g}{\partial \xi}\right]^2 + \left[\frac{\partial y^g}{\partial \xi}\right]^2 + \left[\frac{\partial z^g}{\partial \xi}\right]^2}$$

$$\Lambda^g_2 = \frac{\partial y^g}{\partial \xi} \Big/ \sqrt{\left[\frac{\partial x^g}{\partial \xi}\right]^2 + \left[\frac{\partial y^g}{\partial \xi}\right]^2 + \left[\frac{\partial z^g}{\partial \xi}\right]^2} \tag{4.31,a-c}$$

$$\Lambda_3^g = \frac{\partial z^g}{\partial \xi} \Big/ \sqrt{\left[\frac{\partial x^g}{\partial \xi}\right]^2 + \left[\frac{\partial y^g}{\partial \xi}\right]^2 + \left[\frac{\partial z^g}{\partial \xi}\right]^2}.$$

It should be noted that the direction cosines in transformation matrix $[\theta^g]$ are determined at the point within the girder element where the local displacements $d^g_{\bar{\zeta}}$ and $d^g_{\bar{\xi}}$ are to be calculated. Substituting the expression for the global displacements, Equation 4.26, into Equation 4.30 and multiplying gives the local displacements in terms of the nodal degrees of freedom. This expression is then substituted into Equation 4.29 to yield the local strains in terms of the nodal degrees of freedom as

$$\begin{Bmatrix} \epsilon^g_{\bar{\zeta}\bar{\zeta}} \\ \epsilon^g_{\bar{\zeta}\bar{\xi}} \end{Bmatrix} = \sum_i^5 \begin{bmatrix} \lambda^g_1 \frac{\partial \bar{N}^g_i}{\partial \bar{\zeta}} & \lambda^g_2 \frac{\partial \bar{N}^g_i}{\partial \bar{\zeta}} & \lambda^g_3 \frac{\partial \bar{N}^g_i}{\partial \bar{\zeta}} & -M^g_1 \, CP1_i \frac{\partial N^g_i}{\partial \bar{\zeta}} & \\ \Lambda^g_1 \frac{\partial \bar{N}^g_i}{\partial \bar{\zeta}} & \Lambda^g_2 \frac{\partial \bar{N}^g_i}{\partial \bar{\zeta}} & \Lambda^g_3 \frac{\partial \bar{N}^g_i}{\partial \bar{\zeta}} & -N^g_i \, CP1_i \frac{\partial M^g_1}{\partial \bar{\xi}} & -M^g_1 \, CP2_i \frac{\partial N^g_i}{\partial \bar{\zeta}} \end{bmatrix}$$

$$\begin{bmatrix} & -M^g_2 \, CP1_i \frac{\partial N^g_i}{\partial \bar{\zeta}} \\ -N^g_i \, CP1_i \frac{\partial M^g_2}{\partial \bar{\xi}} & -M^g_2 \, CP2_i \frac{\partial N^g_i}{\partial \bar{\zeta}} \end{bmatrix} \begin{Bmatrix} u^g_i \\ v^g_i \\ w^g_i \\ \alpha^g_i \\ \phi^g_i \end{Bmatrix} \qquad (4.32)$$

where

$$CP1_i = \lambda^g_1 \lambda^g_{1i} + \lambda^g_2 \lambda^g_{2i} + \lambda^g_3 \lambda^g_{3i}$$
$$CP2_i = \Lambda^g_1 \lambda^g_{1i} + \Lambda^g_2 \lambda^g_{2i} + \Lambda^g_3 \lambda^g_{3i}.$$

Equation 4.32 may also be written as

$$\{\epsilon^g\} = [B^g]\,\{d^g\} \tag{4.33}$$

where $[B^g]$ = strain matrix relating degrees of freedom to local strains

$\{d^g\}$ = vector of nodal degrees of freedom

The stress-strain relationship used is the generalized Hooke's Law given by

$$\{\sigma^g\} = \begin{Bmatrix} \sigma^g_{\bar{\zeta}\bar{\zeta}} \\ \sigma^g_{\bar{\zeta}\bar{\xi}} \end{Bmatrix} = [D^g]\left[\{\epsilon^g\} - \{\epsilon^g_o\}\right] + \{\sigma^g_o\} \tag{4.34}$$

where $\{\epsilon^g_o\}$ and $\{\sigma^g_o\}$ are initial local strains and stresses, respectively. The matrix $[D^g]$ is identical to matrix $[D']$, Equation 2.27, given for the consistent beam element. Beyond the proportional limit the elasto-plastic constitutive matrix $[Dep']$, Equation 2.42, is used in place of $[D^g]$.

The element stiffness matrix $[k^g]$ is given by

$$\underset{25x25}{[k^g]} = \int_V \underset{25x2}{[B^g]^T}\ \underset{2x2}{[D^g]}\ \underset{2x25}{[B^g]}\,dV \tag{4.35}$$

which is integrated numerically using the Gaussian Quadrature scheme. The partial derivatives with respect to the local co-ordinates $(\bar{\zeta},\bar{\xi})$ found in matrix $[B^g]$ can be expressed in terms of the derivatives in the curvilinear co-ordinate system as follows

$$\frac{\partial}{\partial \bar{\zeta}} = \frac{\partial}{\partial \zeta}\frac{\partial \zeta}{\partial \bar{\zeta}} = \frac{\partial}{\partial \zeta} \Big/ \sqrt{\left[\frac{\partial x^g}{\partial \zeta}\right]^2 + \left[\frac{\partial y^g}{\partial \zeta}\right]^2 + \left[\frac{\partial z^g}{\partial \zeta}\right]^2}$$

$$\frac{\partial}{\partial \bar{\xi}} = \frac{\partial}{\partial \xi}\frac{\partial \xi}{\partial \bar{\xi}} = \frac{\partial}{\partial \xi} \Big/ \sqrt{\left[\frac{\partial x^g}{\partial \xi}\right]^2 + \left[\frac{\partial y^g}{\partial \xi}\right]^2 + \left[\frac{\partial z^g}{\partial \xi}\right]^2}. \qquad (4.36,a\text{-}b)$$

It should be noted that local axes $\bar{\zeta}$ and $\bar{\xi}$ are parallel to the curvilinear co-ordinates ζ and ξ, respectively. After transforming and changing the limits of integration the element stiffness matrix is calculated using the following equation:

$$[k^g] = \int_{-1}^{+1}\int_{-1}^{+1} [B^g]^T [D^g] [B^g] \, b \, DA \, d\zeta d\xi \qquad (4.37)$$

where b is the width of the girder and DA is the area of the parallelogram formed by differentials $d\bar{\zeta}$ and $d\bar{\xi}$ and is given by

$$DA = \sqrt{\left[\frac{\partial y}{\partial \zeta}\frac{\partial z}{\partial \xi} - \frac{\partial z}{\partial \zeta}\frac{\partial y}{\partial \xi}\right]^2 + \left[\frac{\partial x}{\partial \zeta}\frac{\partial z}{\partial \xi} - \frac{\partial z}{\partial \zeta}\frac{\partial x}{\partial \xi}\right]^2}$$

$$\overline{+ \left[\frac{\partial x}{\partial \zeta}\frac{\partial y}{\partial \xi} - \frac{\partial y}{\partial \zeta}\frac{\partial x}{\partial \xi}\right]^2}. \qquad (4.38)$$

Integration of Equation 4.37 is performed using three integration points along both the ζ and ξ co-ordinates.

4.2.5 Shear Connector Element

Shear connectors between the concrete shell and the supporting girders are assumed to act as a continuous spring between the concrete/girder interface. To model the shear connectors an interface element similar to the joint element defined in section 4.2.2 is used. The relative displacement d_{rel}^{shear} between the concrete and the girder at their interface is written as

$$d_{rel}^{shear} = d_{\bar{\zeta}}^{c} - d_{\bar{\zeta}}^{g} \tag{4.39}$$

where $d_{\bar{\zeta}}^{c}$ and $d_{\bar{\zeta}}^{g}$ are the displacements of the concrete and the girder, respectively, in a direction tangent to the concrete/girder interface i.e. along the local $\bar{\zeta}$ axis of the girder element. It is assumed that the concrete and the girder have the same displacement normal to their interface.

The concrete displacement at the interface $d_{\bar{\zeta}}^{c}$ is given by

$$d_{\bar{\zeta}}^{c} = [\lambda_1^g \ \lambda_2^g \ \lambda_3^g] \begin{Bmatrix} u^c \\ v^c \\ w^c \end{Bmatrix} \tag{4.40}$$

where u^c, v^c and w^c are the global displacements of the concrete (i.e. the consistent shell element) at the interface. The consistent shell element global displacements are given in terms of the shell element nodal degrees of freedom in Equation 3.3 of Chapter Three. The girder displacement $d_{\bar{\zeta}}^{g}$ at the concrete/girder interface is given in terms of the girder nodal degrees of

freedom in Equation 4.30 of the previous section.

The nodal degrees of freedom of the consistent shell element {d}, and the degrees of freedom of the girder element $\{d^g\}$ are combined to yield

$$\underset{116x1}{\{d^{shear}\}} = \begin{Bmatrix} \underset{91x1}{\{d\}} \\ \underset{25x1}{\{d^g\}} \end{Bmatrix} \tag{4.41}$$

which is the shear connector element degree of freedom vector. Substituting the expressions for $\underset{\zeta}{d^c}$, Equation 4.40, and $\underset{\zeta}{d^g}$, Equation 4.30, into Equation 4.39 gives the relative displacement in terms of $\{d^{shear}\}$ as

$$\underset{rel}{d^{shear}} = \underset{91x1}{\left[[N^c] \right.} \quad \underset{25x1}{\left. - [N^g] \right]} \underset{116x1}{\begin{Bmatrix} \{d\} \\ \{d^g\} \end{Bmatrix}} = \underset{1x116}{[N^{shear}]} \underset{116x1}{\{d^{shear}\}} \tag{4.42}$$

where

$$[N^g] = \sum_i^5 [\ \lambda^g_1 \bar{N}^g_i \quad \lambda^g_2 \bar{N}^g_i \quad \lambda^g_3 \bar{N}^g_i \quad -M^g_1 CP1_i N^g_i \quad -M^g_2 CP1_i N^g_i\ ]$$

$$[N^c] = \sum_i^{13} [\ \lambda^g_1 \bar{N}_i \quad \lambda^g_2 \bar{N}_i \quad \lambda^g_3 \bar{N}_i \quad M_1 N_i(\lambda^g_1 l_{1i} + \lambda^g_2 m_{1i} + \lambda^g_3 n_{1i})$$
$$-M_1 N_i(\lambda^g_1 l_{2i} + \lambda^g_2 m_{2i} + \lambda^g_3 n_{2i}) \quad M_2 N_i(\lambda^g_1 l_{1i} + \lambda^g_2 m_{1i} + \lambda^g_3 n_{1i})$$
$$-M_2 N_i(\lambda^g_1 l_{2i} + \lambda^g_2 m_{2i} + \lambda^g_3 n_{2i})\ ].$$

Interpolation functions $\bar{N}^g_i$, N^g_i, M^g_1 and M^g_2 of matrix $[N^g]$ are evaluated at ζ and ξ corresponding to the point on the concrete/girder interface where the relative displacement is to be calculated. Similarly, functions $\bar{N}_i$, N_i, M_1 and

M_2 of matrix $[N^c]$ are evaluated at r, s and t corresponding to the point of interest on the concrete/girder interface. Note that direction cosines λ^g_1, λ^g_2 and λ^g_3, Equation 4.27, define the unit vector tangent to the interface at the point where the relative displacement is to be calculated.

The strain energy due to the relative displacement d^{shear}_{rel} is given by

$$U = \frac{1}{2}\int_0^L k_{shear}\,(d^{shear}_{rel})^2\,d\bar{\zeta} \tag{4.43}$$

and the ensuing shear connector stiffness matrix $[k^{shear}]$ is as follows

$$[k^{shear}]_{116x116} = \int_0^L [N^{shear}]^T_{116x1}\, k_{shear}\, [N^{shear}]_{1x116}\, d\bar{\zeta} \tag{4.44}$$

and k_{shear} is the distributed connector stiffness. An elastic-perfectly plastic shear spring model proposed by Mirza and Koral (1983) is used to estimate k_{shear} as

$$k_{shear} = \frac{GA_{shear}}{dhD} \tag{4.45}$$

where G is the shear modulus, dh is the effective thickness of the shear layer, A_{shear} is the cross-sectional area of the connector and D is the spacing of the connectors.

Integration of Equation 4.44 is performed numerically using the Gaussian Quadrature scheme with three integration points along ζ.

Transforming $d\bar{\zeta}$ using Equation 4.36 and changing the limits of integration gives

$$[k^{shear}] = \int_{-1}^{+1} [N^{shear}]^T \, k_{shear} \, [N^{shear}] \sqrt{\left[\frac{\partial x^g}{\partial \zeta}\right]^2 + \left[\frac{\partial y^g}{\partial \zeta}\right]^2 + \left[\frac{\partial z^g}{\partial \zeta}\right]^2} \, d\zeta. \quad (4.46)$$

The shear force $\{p^{shear}\}$ acting along the interface is calculated as

$$\underset{116x1}{\{p^{shear}\}} = \underset{116x116}{[k^{shear}]} \; \underset{116x1}{\{d^{shear}\}} \quad (4.47)$$

in the linear elastic range. Again, an incremental approach must be adopted for the case of nonlinear behaviour, i.e. due to deterioration.

4.2.6 Elasto-Plastic Constitutive Model For Concrete

The constitutive model developed by Pietruszczak et al. (1988) is adopted in this study for modelling concrete behaviour. This model fairly adequately reflects certain typical trends in concrete behaviour. These being: a progressive transition from compaction to dilatancy; sensitivity of material characteristics to confining pressure and a continuous transition in failure mechanism from a ductile mode to a brittle mode. The theory is given within the framework of rate independent plasticity theory. Deformation is governed by a non-associated flow rule and involves a progressive evolution of the yield surface which is described in terms of a hardening/softening parameter. The theory is applicable to the modelling of concrete response under monotonic loading conditions. Only the key components of the constitutive model will be

described. For more detailed information refer to Pietruszczak et al. (1988) and Jiang (1988).

In the adopted concrete constitutive relationship the following stress invariants are used

$$I = \sigma_{ii}$$

$$\bar{\sigma} = \sqrt{\frac{1}{2} s_{ij} s_{ij}} \qquad (4.48,a\text{-}c)$$

$$\theta = \frac{1}{3} \sin^{-1}\left[\frac{-3\sqrt{3}}{2} \frac{J_3}{\bar{\sigma}^3} \right] \qquad \frac{-\pi}{6} \leq \theta \leq \frac{\pi}{6}$$

where $\bar{\sigma}$ is the effective stress and $s_{ij} = \sigma_{ij} - \delta_{ij}\, \sigma_{kk} / 3$ is the stress deviator tensor. The angle θ is a measure of the third invariant of the stress deviator tensor $J_3 = s_{ij}\, s_{jk}\, s_{ki} / 3$.

For any combination of stresses the concrete strength is defined by the failure criterion which is given as

$$F = \bar{\sigma} - g(\theta)\, \bar{\sigma}_c = 0 \qquad (4.49)$$

and which describes the failure surface shown in Figure 4.4. Constant $\bar{\sigma}_c$ is given by

$$\bar{\sigma}_c = \frac{-a_1 + \sqrt{(a_1^2 + 4a_2(a_3 + I/f'_c))}}{2a_2} f'_c \qquad (4.50)$$

where the concrete uniaxial compressive strength is denoted by f'_c and a_1, a_2 and a_3 are dimensionless material constants. Function $g(\theta)$ defines the shape of the π-plane sections and is influenced by the magnitude of the confining pressure. It can be written as

$$g(\theta) = \frac{(\sqrt{(1+a)} - \sqrt{(1-a)})K}{K\sqrt{(1+a)} - \sqrt{(1-a)} + (1-K)\sqrt{(1-a\sin 3\theta)}} \tag{4.51}$$

where $a = 0.999$ and K is given by

$$K = 1 - K_0 e^{-K_1(a_3 + I/f'_c)}. \tag{4.52}$$

The yield function f is described by a function similar to that used to define the failure criterion, namely

$$f = \bar{\sigma} - \beta(\xi)\, g(\theta)\, \bar{\sigma}_c = 0 \tag{4.53}$$

where $\beta(\xi)$ represents a hardening/softening function. Parameter ξ is defined by

$$\xi = \int d\xi \quad \text{where} \quad d\xi = \frac{d\bar{\epsilon}^p}{\bar{\phi}} \tag{4.54}$$

and $d\bar{\epsilon}^p$ is a measure of the plastic deformation given by

$$d\bar{\epsilon}^p = \sqrt{(de^p_{ij}\, de^p_{ij})} \tag{4.55}$$

where de^p_{ij} is expressed as

$$de^{P}_{ij} = d\epsilon^{P}_{ij} - \delta_{ij}\, d\epsilon^{P}_{kk} / 3. \tag{4.56}$$

Parameter $\bar{\phi}$ in Equation 4.54 allows for simulation of a variation in material characteristics with respect to I and θ and is given by

$$\phi(I,\theta) = \left[g(\theta)\left[a_3 + \frac{I}{f'_c} \right] \right]^2 = \bar{\phi}. \tag{4.57}$$

The available experimental results show that as the confining pressure decreases a gradual transition from ductile to brittle behaviour takes place. The transition from a stable (ductile) to unstable (brittle) response is modelled by the hardening/softening function $\beta(\xi)$ which is given by

$$\beta(\xi) = \frac{\xi}{A + B\xi}\left[1 - \bar{\phi}_r\left(1 - e^{-C< \xi - \xi_f >^{\gamma}} \right) \right] \tag{4.58}$$

where A, B and γ are material constants, $\bar{\phi}_r$ defines the residual strength of the concrete and ξ_f represents the value of ξ corresponding to the maximum value of β i.e. β_f. Constant C is written as

$$C = H\left[\left\langle \frac{(I/f'_c)^T - (I/f'_c)_f}{a_3 + (I/f'_c)_f} \right\rangle \right]^{\mu} \tag{4.59}$$

where μ and H are material constants, $(I/f'_c)_f$ is evaluated at $\beta = \beta_f$ and $(I/f_c)^T$ denotes the normalized confining pressure at which the transition from ductile to brittle behaviour takes place. Angular brackets $< >$ represent the singularity function defined as

$$< x > = \begin{cases} 0 & \text{if } x \leq 0 \\ x & \text{if } x > 0. \end{cases} \tag{4.60}$$

Function $\beta(\xi)$, Equation 4.58, reflects a gradual change in material characteristics from strain hardening (high confining pressure) to strain softening, with a progressively increasing rate.

Experimental evidence indicates that in the ductile regime concrete undergoes a smooth transition from compaction to dilatancy prior to failure. This behaviour is accounted for through the plastic potential function Ψ which is given by

$$\Psi = \bar{\sigma} + \eta_c g(\theta)\bar{I} \ln\left[\frac{\bar{I}}{\bar{I}_0}\right] = 0 \tag{4.61}$$

where $\bar{I} = a_0 f'_c + I$ and a_0 is a constant which defines the location of the apex of the plastic potential surface in the tensile domain. Parameter η_c represents the value of $\eta = \bar{\sigma}/(g(\theta)\bar{I})$ at which the transition from compaction to dilatancy occurs i.e. at $\eta = \eta_c$ $d\epsilon^p_{ii} = 0$. It is assumed that this transition takes place along the locus defined by

$$\bar{f} = \bar{\sigma} - \alpha g(\theta)\bar{\sigma}_c = 0 \tag{4.62}$$

where α is a material constant. The meridional section of the family of plastic potential surfaces is shown in Figure 4.5. In order to satisfy the condition of irreversibility all plastic potential surfaces are assumed to be convex with respect to the origin of the stress space. To comply with the convexity

requirement, an appropriate evolution law for the plastic potential surfaces, Equation 4.61, is provided. Denote by η_0 the value of η_c at $I = 0$ and $a_0 = a_3$ as

$$\eta_0 = \frac{\alpha(-a_1+\sqrt{(a_1^2+4a_2a_3)})}{2a_2a_3} \tag{4.63}$$

and let the corresponding plastic potential surface be Ψ_0 as shown in Figure 4.5. It is assumed that for $\eta_c < \eta_0$ all subsequent plastic potential surfaces are obtained by an isotropic expansion of $\Psi_0 = 0$ under $a_0 = a_3 =$ constant. If the stress point falls inside the domain enclosed by $\Psi_0 = 0$ all subsequent loci are reduced in size and the apex gradually migrates towards the origin i.e. $0 \leq a_0 \leq a_3$.

Having defined the failure criterion, yield surface and plastic potential surface it can be shown (Pietruszczak et al. 1988, Jiang 1988) that the incremental stress-strain relationship takes the following form

$$d\sigma' = \left[[D'] - \frac{[D'] \left\{\frac{\partial \Psi}{\partial \sigma'}\right\} \left\{\frac{\partial f}{\partial \sigma'}\right\} [D']}{H_e + H_p} \right] d\epsilon' \tag{4.64}$$

where the hardening moduli H_p and H_e are given by

$$H_e = \left\{\frac{\partial f}{\partial \sigma'}\right\} [D'] \left\{\frac{\partial \Psi}{\partial \sigma'}\right\} \tag{4.65,a-b}$$

$$H_p = -\frac{\partial f}{\partial \beta}\frac{d\beta}{d\xi}\frac{\left[\ \mathrm{dev}\left\{\frac{\partial \Psi}{\partial \sigma'}\right\}\ \mathrm{dev}\left\{\frac{\partial \Psi}{\partial \sigma'}\right\}\ \right]^{1/2}}{\bar{\phi}} \ .$$

In the hardening regime where $H_p > 0$ the following conditions

$$f = 0 \quad \text{and} \quad \frac{\partial f}{\partial \sigma'} d\sigma' > 0 \tag{4.66}$$

define an active loading process during which irreversible deformations are generated. In the softening regime where $H_p < 0$ the criteria for an active loading process are

$$f = 0 \quad \text{and} \quad \frac{\partial f}{\partial \sigma'} [D'] d\epsilon' > 0 \tag{4.67}$$

which state that plastic deformation occurs whenever the stress increment obtained from the elastic solution is directed outside the yield surface. It should be noted that Equation 4.67 is only valid for cases where $H_e + H_p > 0$.

The material parameters involved in the constitutive model have been determined through calibration with experimental data available in the literature. For more information on the calibration procedure refer to Pietruszczak et al. (1988) and Jiang (1988). The results of their calibration are as follows:

1. Hardening function parameters

$$A = 0.000085 \qquad B = 0.95 \tag{4.68,a-b}$$

2. Dilatancy parameter

$$\alpha = 0.95 \tag{4.69}$$

3. Failure envelope parameters

$$a_1 = 1.9253 \qquad a_2 = 0.5635 \qquad a_3 = 3f'_t/f'_c$$

$$K_1 = \frac{1}{(f'_t/f'_c)-2(f_{bc}/f'_c)} \ln\left[\frac{1-K_t}{1-K_{bc}}\right] \qquad (4.70,a\text{-}e)$$

$$K_0 = (1-K_t)e^{2K_1(f'_t/f'_c)}$$

where K_t and K_{bc} represent values of K corresponding to uniaxial tension and biaxial compression, respectively

$$K_t = \frac{2\sqrt{3}}{3} \frac{a_2 f'_t/f'_c}{-a_1+\sqrt{(a_1^2+8a_2 f'_t/f'_c)}}$$

$$K_{bc} = -\frac{2\sqrt{3}}{3} \frac{a_2 f_{bc}/f'_c}{-a_1+\sqrt{(a_1^2+4a_2(3f'_t/f'_c-2f_{bc}/f'_c)}} \qquad (4.71,a\text{-}b)$$

and $f_{bc} = 1.16f'_c$. If the uniaxial tensile strength f'_t is unavailable then the usual approximation $f'_t = 0.1f'_c$ is used.

4. Strain softening parameters H, μ, γ, $(I/f'_c)_T$ and $\bar{\phi}_r$ cannot be determined precisely due to lack of experimental data (Pietruszczak et al. 1988, Jiang 1988). However, based on the results obtained by Jiang (1989) the following values are assumed

$$\gamma = 2 \qquad (I/f'_c)_T = 2 \qquad \bar{\phi}_r = 0.7 \text{ to } 0.8 \qquad (4.72,a\text{-}c)$$

This leaves H and μ which control the rate of strain softening. Both of these constants can be determined from a uniaxial compression test by matching the predicted and actual strain softening characteristics. However since the actual strain softening behaviour from such a test is dependent on the size of the specimen it is reasonable to assume that H and μ will also be a function of size i.e. show a dependency on the size of the finite elements. This will be investigated in a following numerical example.

In addition to the parameters specified above, the elastic properties i.e. elastic modulus E and Poisson's ratio ν are required.

4.3 Numerical Examples

The finite element model described in the previous sections has been implemented in the program called RCSHL (Reinforced Concrete Shell Element). The non-linear finite element analysis procedure follows that described in section 2.4.2 of Chapter Two with one exception. The initial stiffness method is employed instead of the modified Newton-Raphson procedure. Thus, the tangential stiffness matrix is evaluated only at the beginning of the first load increment, instead of at the beginning of each load increment.

4.3.1 Simply Supported Reinforced Concrete Slab

A simply supported square reinforced concrete slab subjected to a uniformly distributed load has been analysed in order to verify the finite element model. The geometry of the slab and reinforcement details are shown in Figure 4.6. The material properties of the concrete and steel are given in Table 4.1. An experimental investigation of this slab has been conducted by Taylor et al. (1966).

Table 4.1: Reinforced concrete slab material properties.

Concrete	Reinforcing Steel
$E = 32420$ MPa	$E^r = 206910$ MPa
$f'_c = 35.04$ MPa	$E^r_T = 13790$ MPa
$f'_t = 3.60$ MPa	$\sigma^r_y = 375.9$ MPa
$\nu = 0.18$	

Due to the double symmetry of the structure only one quarter of the slab has been analysed. This has been done for three different meshes which consist of 2, 8 and 32 consistent shell elements, respectively. The material parameters used in the concrete constitutive model are the same as those given in section 4.2.6 with the exception of the values for the residual strength parameter $\bar{\phi}_r$ and the strain softening parameters H and μ. The residual strength parameter $\bar{\phi}_r$ has been set equal to 0.8 which is consistent with the values recommended by Jiang (1989). The strain softening parameters H and μ used in the analyses are 50 and 3, respectively. These values were found to be the optimum values through a trial and error process. The distributed stiffness

k^{joint} along the concrete/reinforcement interface due to bonding has been assumed to be $100x10^3$ MN/m. The load deflection responses of the slab (at the center) predicted by the three finite element meshes are plotted in Figure 4.7 along with the experimental curve obtained by Taylor. It can be seen from Figure 4.7 that overall the predicted responses are in very good agreement with the experimental data. However, the results indicate that the predicted response improves in the cracking range with improvement of the finite element mesh. The discrepancies could be due to a dependence of the strain softening parameters on the finite element size as alluded to earlier. It must also be recognized that the actual test has been carried out using displacement control whereas in the present analysis it is the load that is controlled. This example demonstrates the ability of the present finite element model to accurately predict the behaviour of reinforced concrete plates.

4.3.2 Multi-girder Prestressed Concrete Slab

A multi-girder prestressed concrete slab subjected to a concentrated load has been analysed. The geometric details of the composite structure are shown in Figure 4.8. The dimensions of the prestressed and non-prestressed reinforcement as well as its arrangement is shown in Figure 4.9. The supporting girders are connected to the concrete slab using the shear connectors depicted in Figure 4.10. There are a total of 128 shear connectors per girder. They have been assumed to be uniformly distributed in the present analysis with k^{shear} equal to $200x10^3$ kN/cm. The material properties of the concrete, reinforcement, girders and shear connectors are given in Table 4.2. An experimental investigation of this structure has been conducted by Batchelor

(1990).

As a result of the symmetry only half of the structure has been analysed. The consistent shell element grid used is shown in Figure 4.11. The residual strength parameter $\bar{\phi}_r$ has been set equal to 0.8 and the strain softening

Table 4.2: Multi-girder concrete slab material properties.

Concrete:	Reinforcing Steel:
$E = 33910$ MPa	$E^r = 166850$ MPa
$f'_c = 46$ MPa	$E^r_T = 11120$ MPa
$f'_t = 3.168$ MPa	$\sigma^r_y = 427$ MPa
$\nu = 0.18$	Prestressing Steel:
Girder and Shear Connectors:	$E^r = 205460$ MPa
$E = 200000$ MPa	$E^r_T = 68410$ MPa
$\nu = 0.25$	$\sigma^r_y = 1450$ MPa

parameters H and μ have been chosen to be 100 and 2, respectively. These values are different then the values (H = 50, μ = 3) used in the previous example. This is to be expected since the concrete material parameters are different and also the concrete in the present example is subjected to an initial prestress. The distributed stiffness k^{joint} along the concrete/reinforcement interface has been assumed to be 100×10^3 MN/m. The load is incremented until the damage functions at the integration points in the vicinity of the loading point all approach unity i.e. $\beta(\xi) \rightarrow 1$. When this state is reached local failure has been predicted and the analysis is terminated. The load deflection response of the structure at the loading point predicted by the finite element model is plotted

in Figure 4.12 along with the response determined experimentally by Batchelor (1990). The predicted load deflection response is in very good agreement with the experimental response and also predicts a failure load which is very close to the experimental value. The finite element predictions for this application are much better than the previous application. This fact can be attributed to the delayed cracking in the slab due to the transverse prestressing. A remarkable fact is that the finite element model is capable of predicting the punching shear failure mode in the vicinity of the point load as shown in Figure 4.13. This example demonstrates further the applicability of the finite element model by accurately predicting the punching shear failure of the structure.

4.3.3 Plain Concrete Tension Test

In this example the objectivity of the adopted concrete material model with respect to refinement of the finite element mesh is investigated. For this purpose the notched plain concrete specimen shown in Figure 4.14 has been analysed. Due to the double symmetry only one-quarter of the tension specimen has been modelled using three different finite element meshes. The first employs 6, the second 16 and the third 36 consistent shell elements. The finite element solutions have been obtained using a displacement control scheme which involves the prescription of equal displacement increments along the upper surface of the specimen.

The force versus displacement along the upper surface of the specimen is plotted in Figure 4.15 for analyses using all three meshes with H and μ equal to 10 and 1, respectively. The finite element predictions for all three meshes

are the same up to the peak load after which some variations occur. The softening behaviour predicted by the 6 element model and the 16 element model is very nearly the same. However, the softening behaviour predicted by the 36 element model is somewhat different. These discrepancies tend to indicate that there is a dependency of the predicted behaviour on the finite element size employed. However, the difference is not more than the improvements in stresses expected with the improvement in the finite element mesh. To further study this issue the specimen was analysed again using all three finite element models. However, this time μ was increased from 1 to 3. The predicted force versus displacement curves are plotted in Figure 4.16. It can be seen from the figure that the predicted load displacement curves for all three meshes are almost identical even in the post peak load region. This is due to the fact that very little softening occurs in this case. Instead a brittle response has been simulated. Considering these results together with those of the previous test it can be concluded that in general the strain softening behaviour predicted by the constitutive model is fairly objective with respect to refinement of the finite element mesh. The specimen has also been analysed using the 6 element mesh with H equal to 10 and μ varied from 0.5 to 3. The predicted load displacement curves are plotted in Figure 4.17 and indicate the expected post peak load behaviour. To further investigate the sensitivity of the softening behaviour to variation of the parameters H and μ the specimen was again analysed using the 6 element mesh. However, this time μ was set equal to 1 and H was varied between 10 and 110. The predicted load displacement curves are plotted in Figure 4.18. When compared with the curves plotted in Figure 4.17 it can be seen that the predicted softening behaviour is more sensitive to variations in μ than to variations in H. Finally, the specimen was analysed using the 6 element

mesh for values of the residual strength parameter $\bar{\phi}_r$ equal to 0.8 and 0.975. The constants H and μ were held constant at 10 and 1, respectively. The predicted load versus displacement curves are shown in Figure 4.19 and indicate the post peak load behaviour anticipated.

The simply supported reinforced concrete slab, example 4.3.1, and the multi-girder prestressed concrete slab, example 4.3.2, have been tested using displacement control and analysed using load control. Considering the above results it is likely that a large portion of the discrepancy between the predicted and experimental results for the simply supported reinforced concrete slab is due to the different method of analysis i.e. load control versus displacement control. However, for the multi-girder prestressed concrete slab the influence of the load control analysis is much less significant due to delayed cracking of the slab caused by the initial prestress.

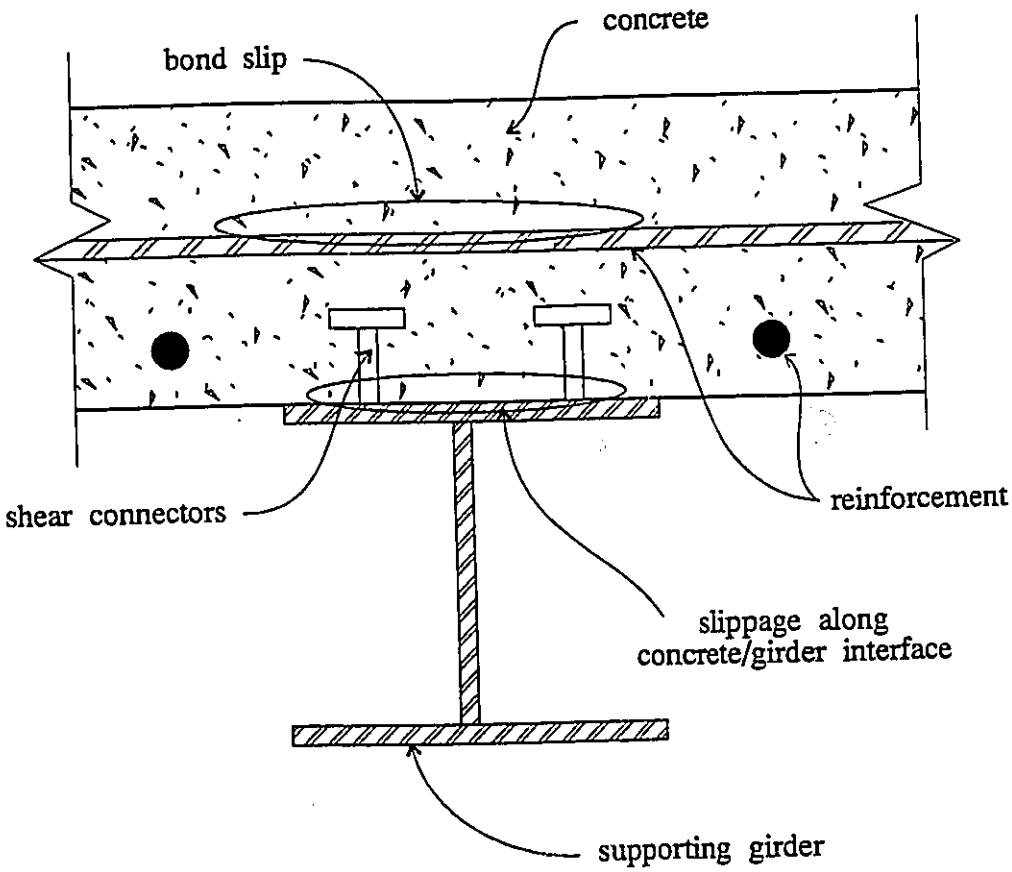

Figure 4.1: Components of reinforced concrete finite element model.

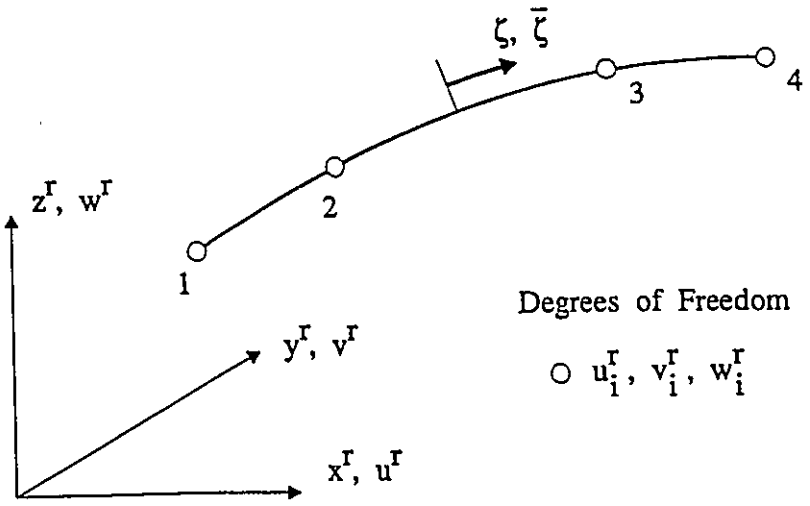

Figure 4.2: Reinforcement element co-ordinate systems and nodal degrees of freedom.

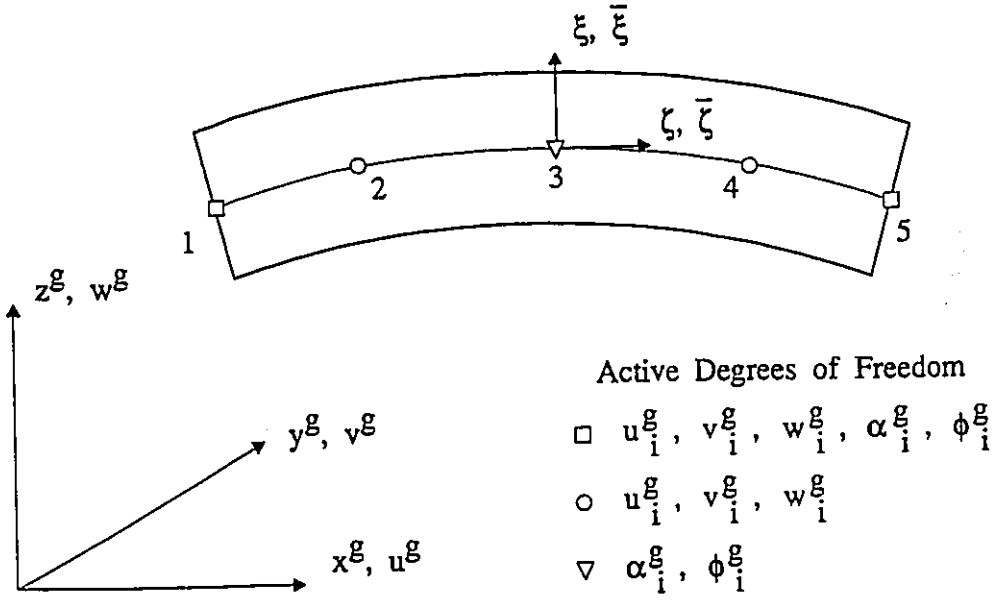

Figure 4.3: Girder element co-ordinate systems and nodal degrees of freedom.

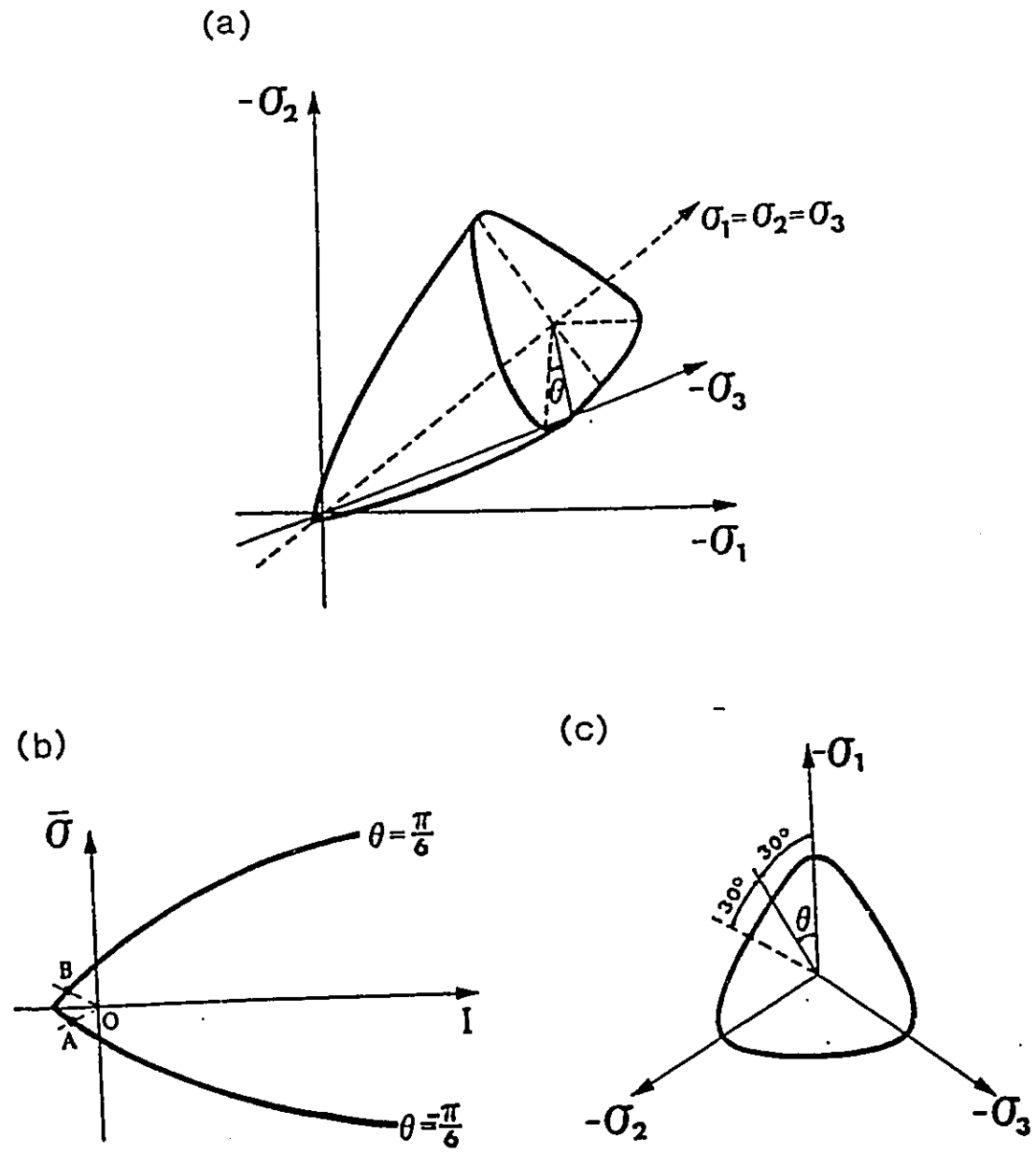

Figure 4.4: Failure surface in (a) principal stress space; (b) meridional plane; (c) deviatoric plane (Jiang 1988).

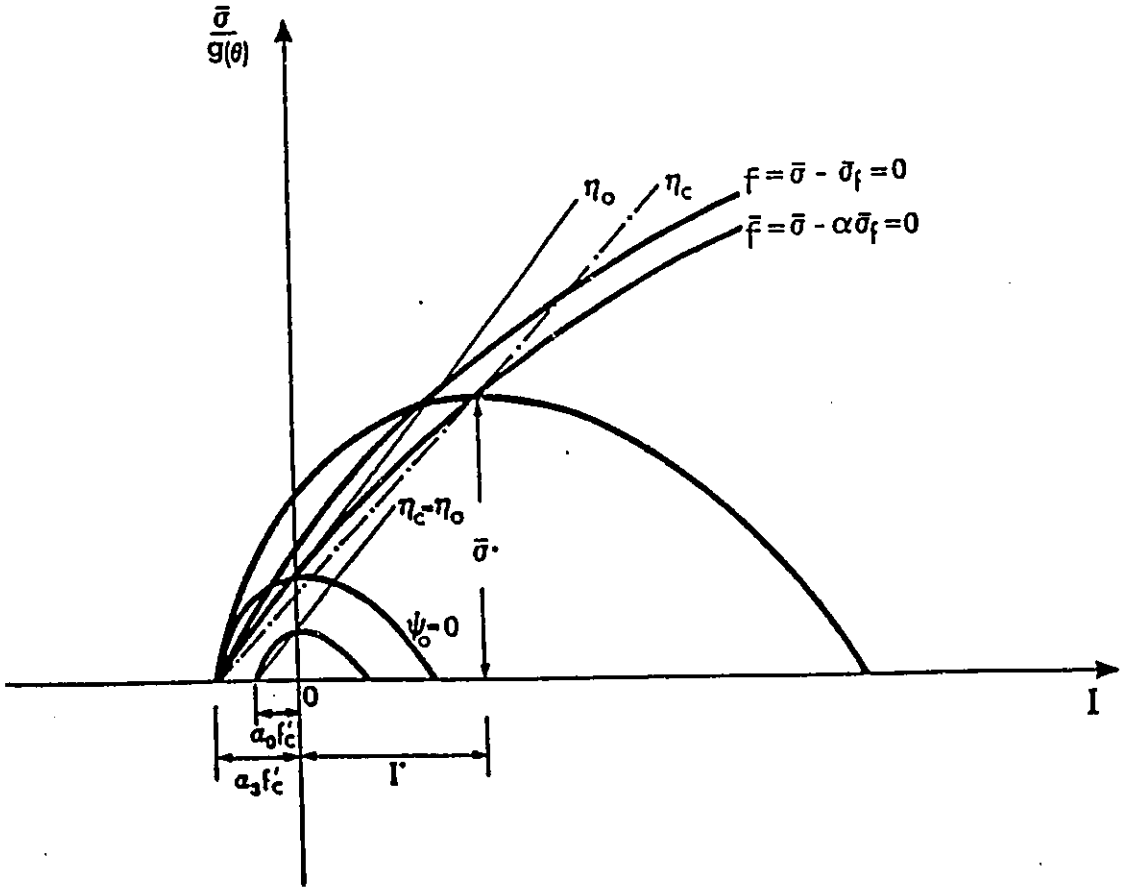

Figure 4.5: Plastic potential surfaces in meridional plane (Jiang 1988).

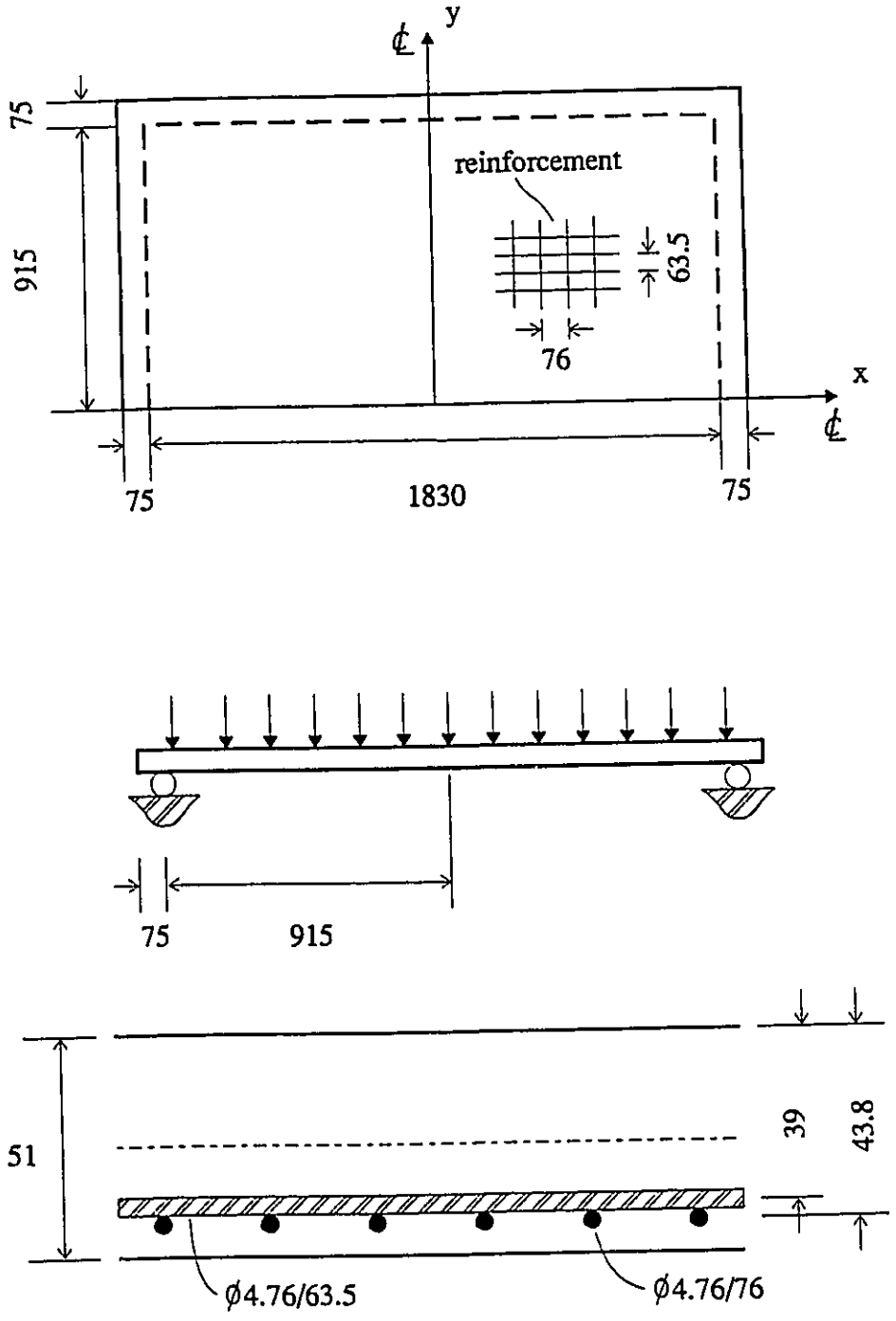

Figure 4.6: Geometry and reinforcement details for simply supported reinforced concrete slab (dimensions in mm).

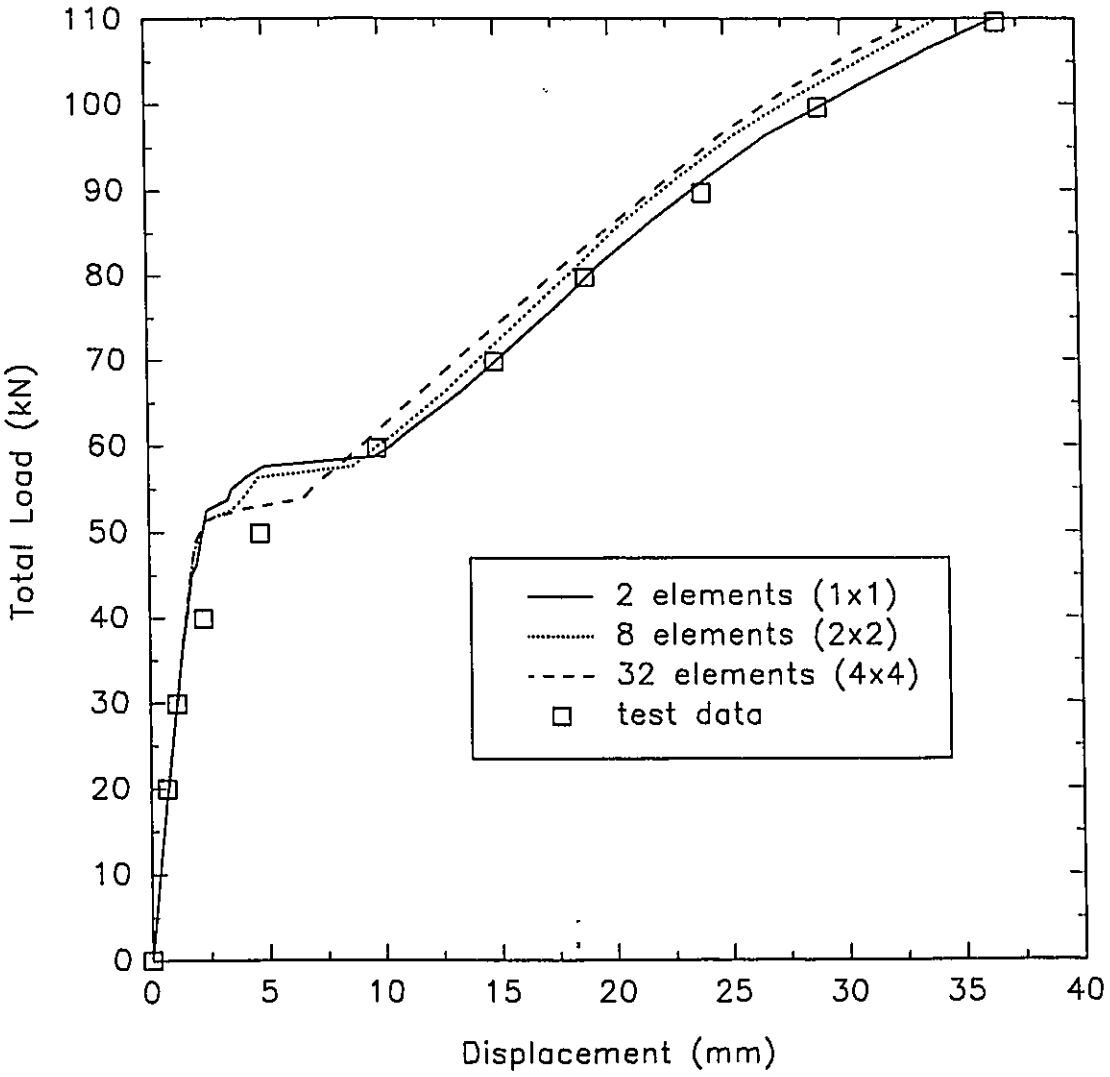

Figure 4.7: Central deflection of simply supported reinforced concrete slab under a uniformly distributed load.

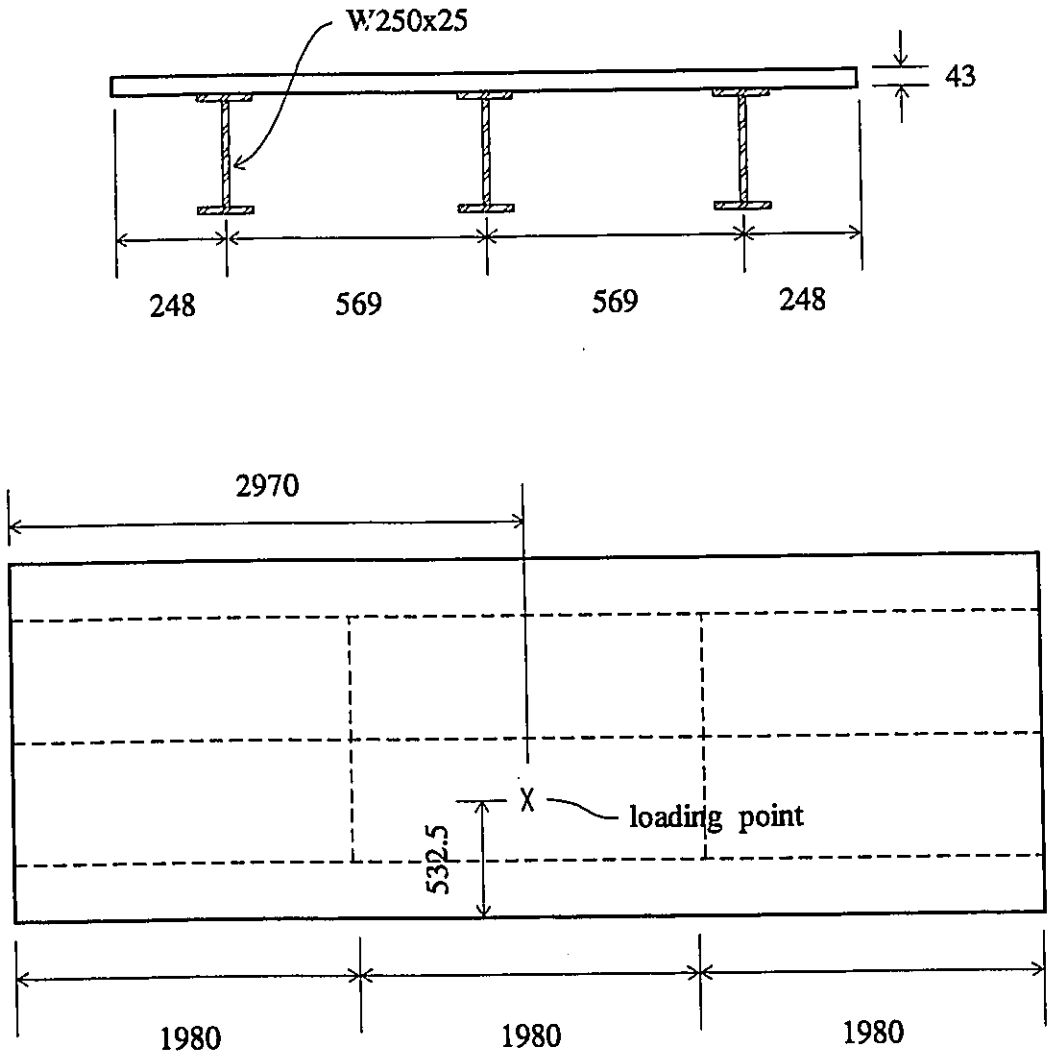

Figure 4.8: Geometry and cross-section of multigirder prestressed concrete slab (dimensions in mm).

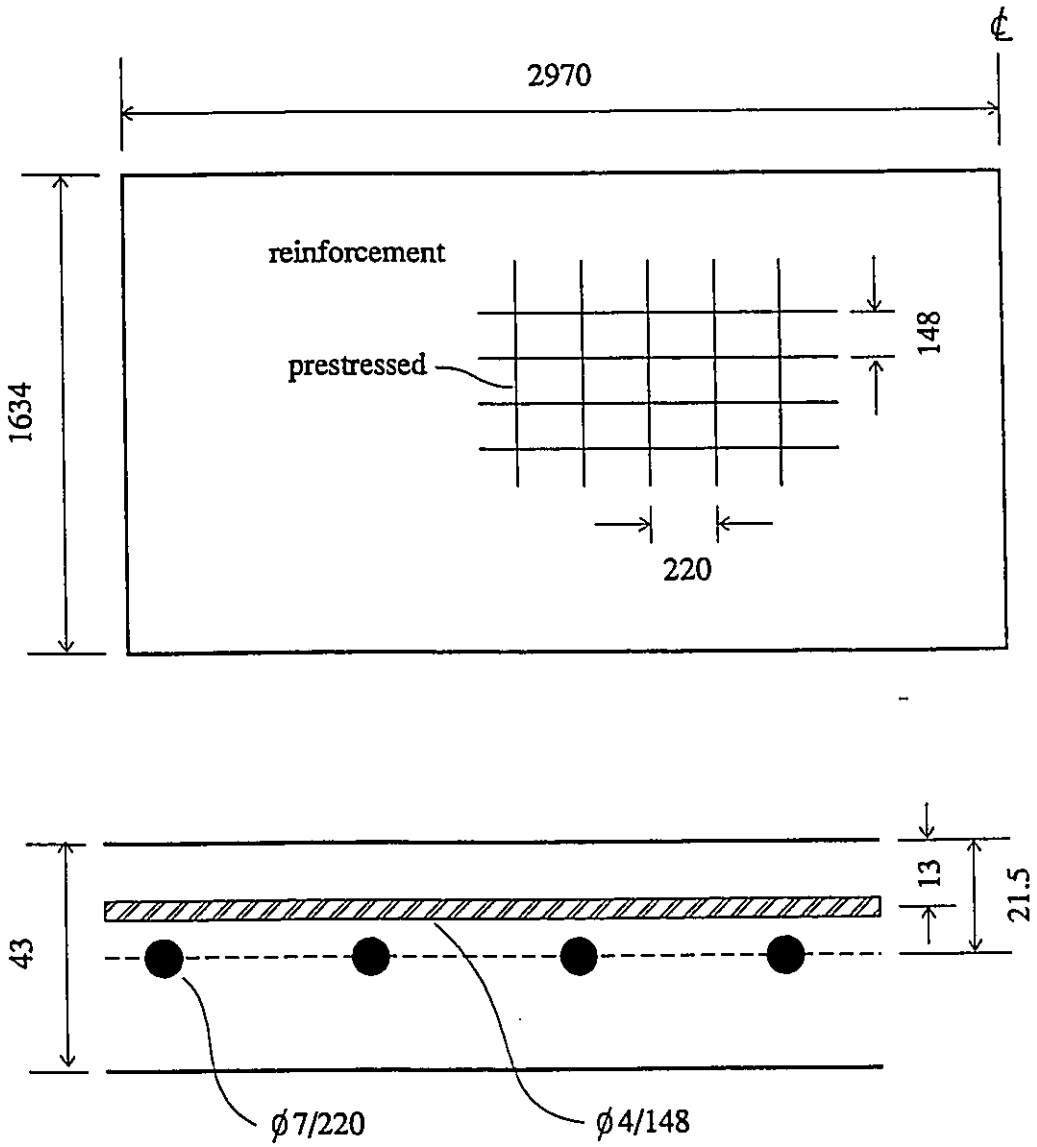

Figure 4.9: Placement of reinforcement for multigirder prestressed concrete slab (dimensions in mm).

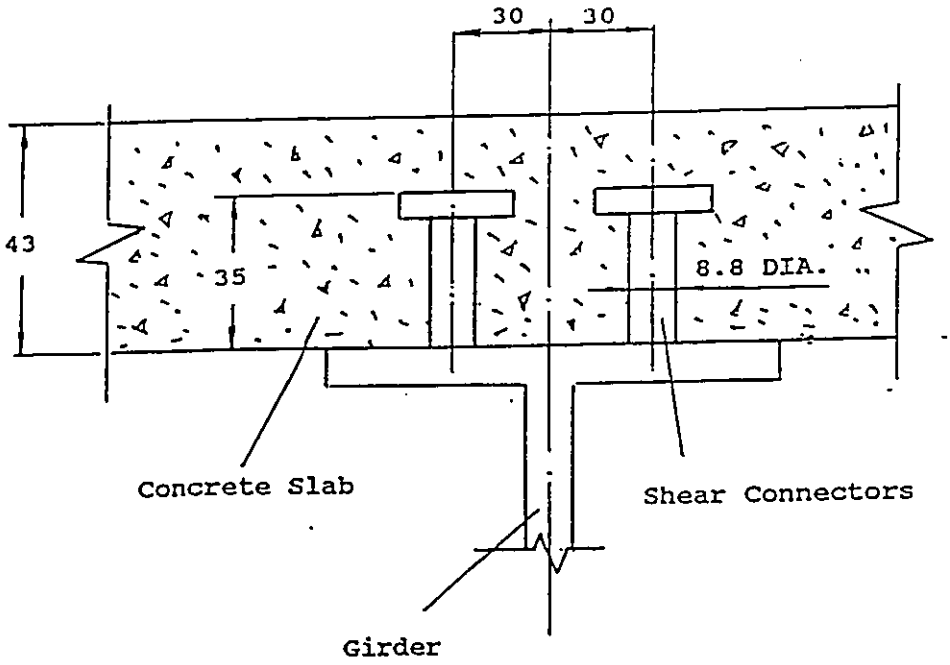

Figure 4.10: Detail of a typical shear connector (Batchelor 1990).

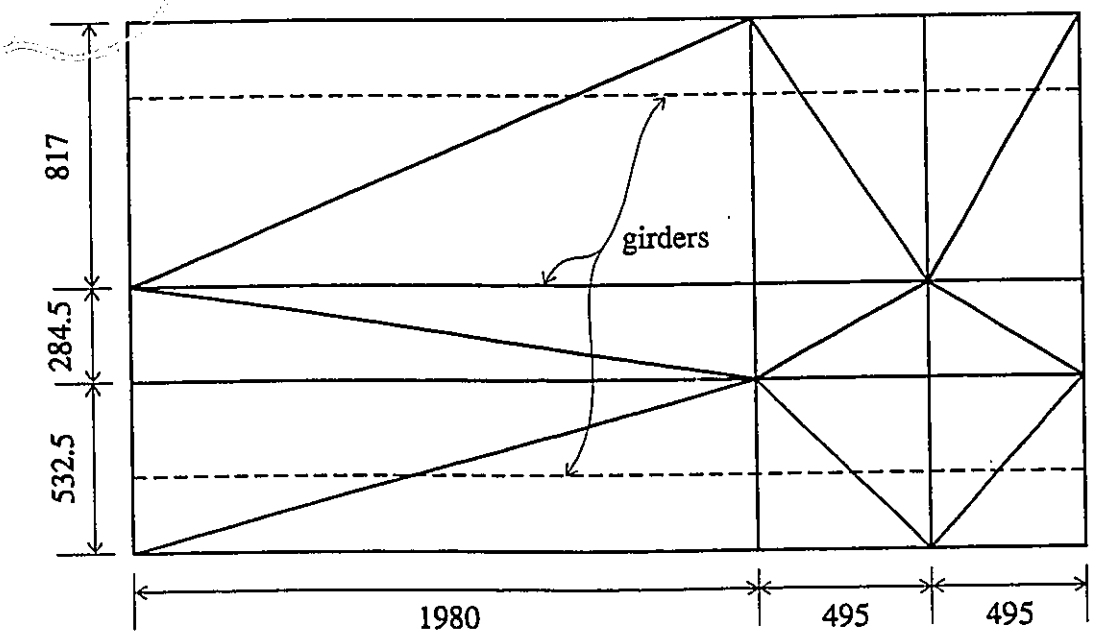

Figure 4.11: Finite element mesh for multigirder prestressed concrete slab (dimensions in mm).

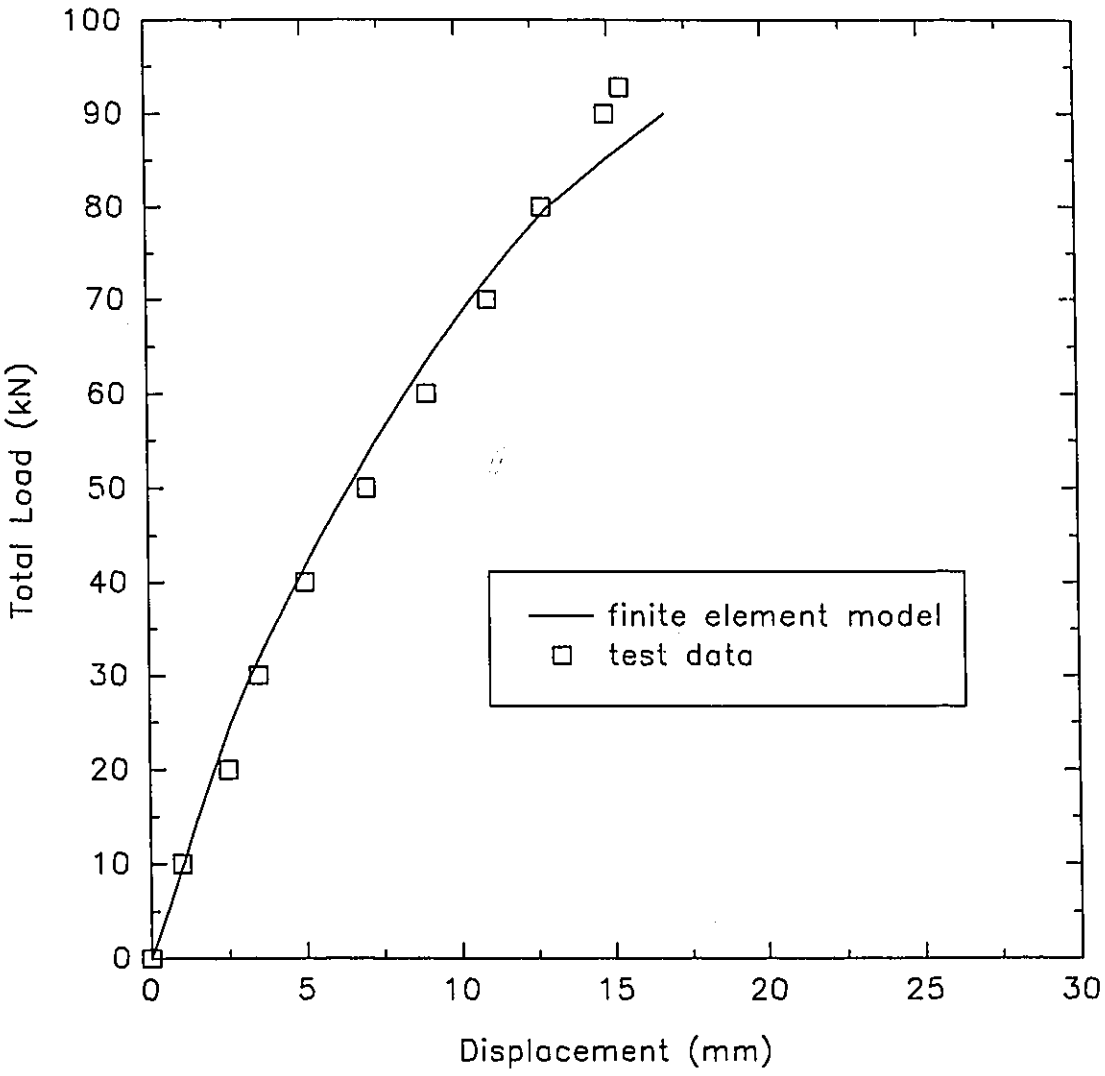

Figure 4.12: Load deflection curve for multigirder prestressed concrete slab at the loading point.

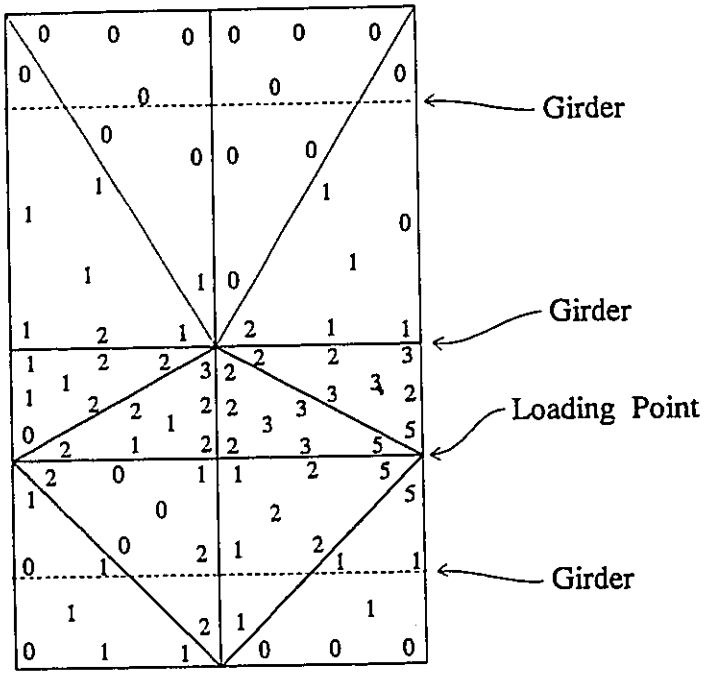

Figure 4.13: Cracking pattern around loading point at failure; P = 90 kN (0,1,2,3,4,5 denote the number of cracked integration points).

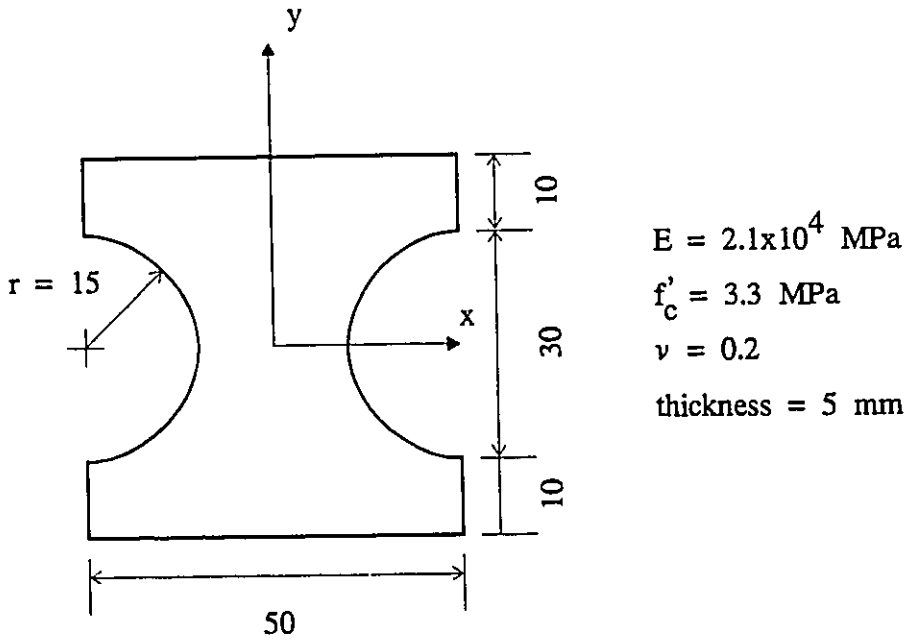

Figure 4.14: Geometry and material properties of notched plain concrete specimen (dimensions in mm).

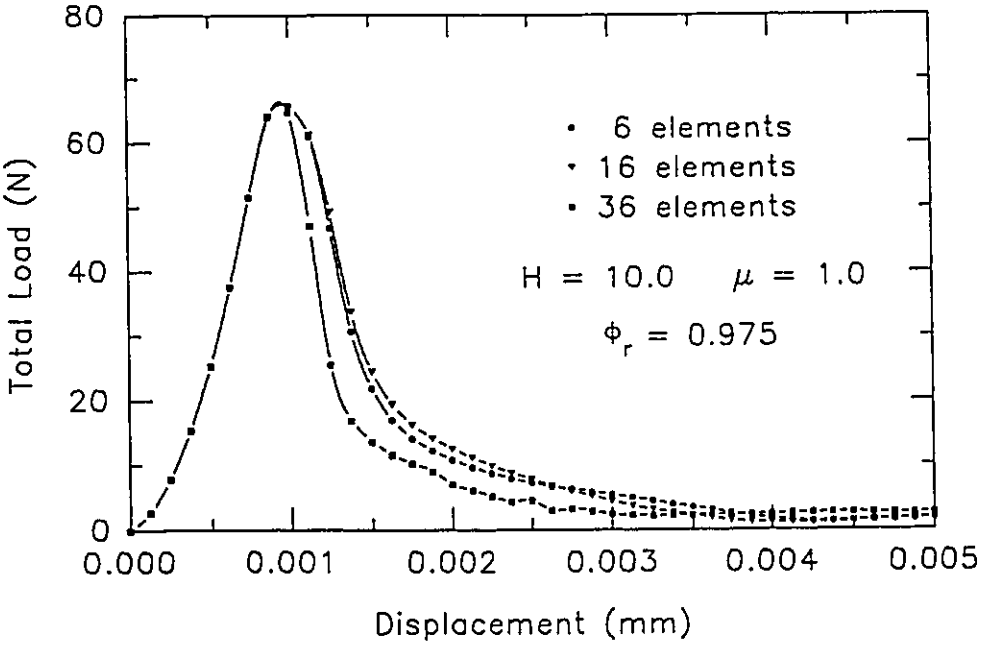

Figure 4.15: Force versus displacement curves for variation of finite element mesh with μ = 1.0.

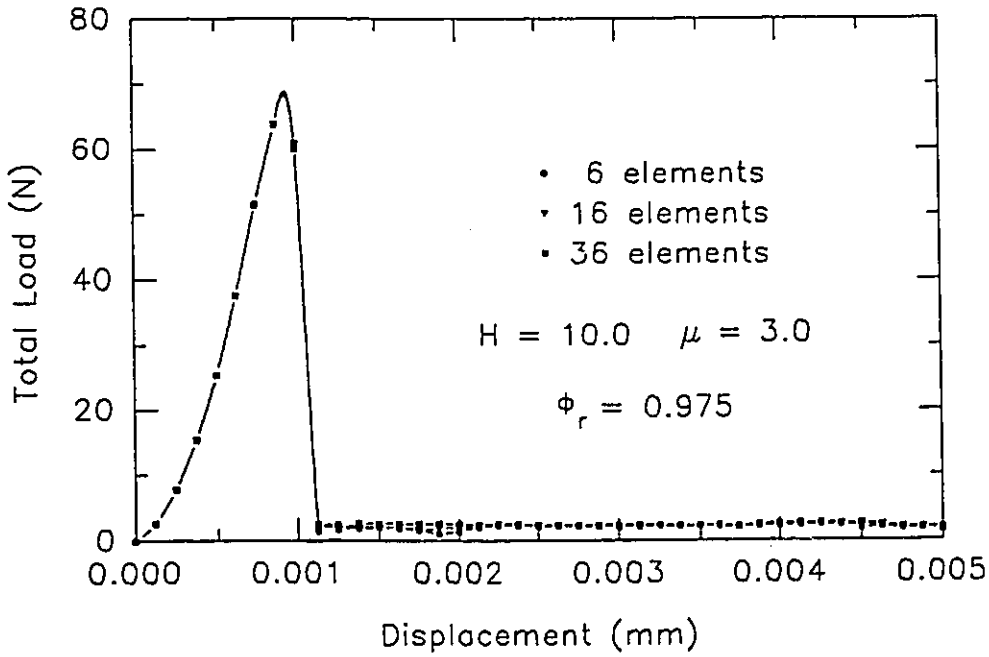

Figure 4.16: Force versus displacement curves for variation of finite element mesh with μ = 3.0.

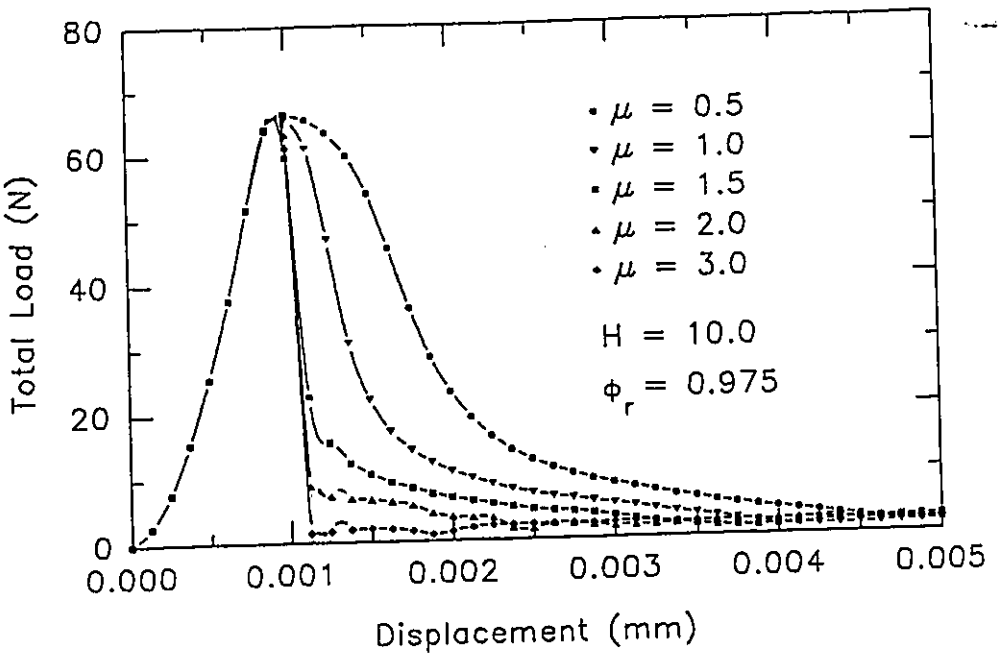

Figure 4.17: Load versus displacement curves for variation of μ using a six element mesh.

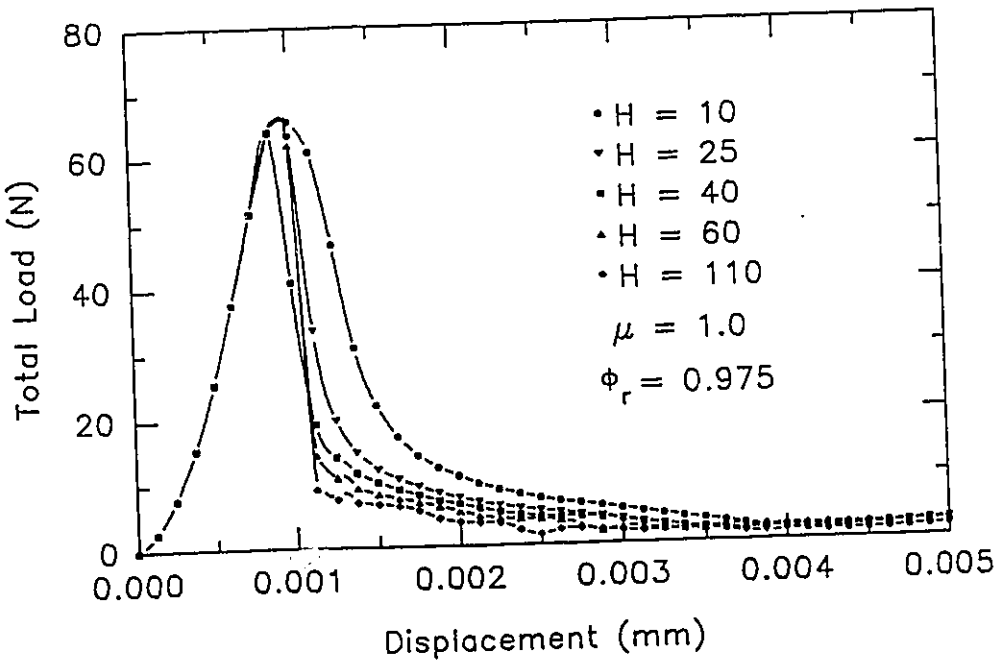

Figure 4.18: Load versus displacement curves for variation of H using a six element mesh.

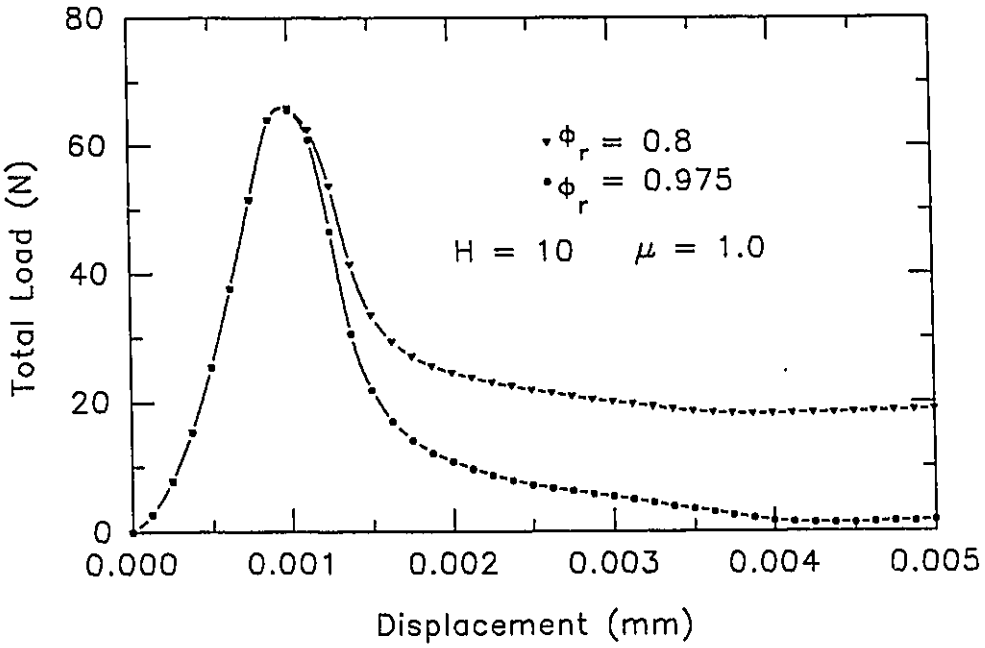

Figure 4.19: Load versus displacement curves for variation of residual strength using a six element mesh.

CHAPTER FIVE

FORMULATIONS AND APPLICATIONS OF CONSISTENT LAMINATED BEAM AND CONSISTENT LAMINATED SHELL ELEMENTS

5.1 Introduction

Laminated composites are receiving increasing use as structural elements in applications where high strength to weight and stiffness to weight ratios are desired, such as in aerospace applications. In this chapter two new elements are formulated. These are the consistent laminated beam element and the consistent laminated shell element which are extensions of the consistent beam element and the consistent shell element, respectively.

Laminated fiber reinforced composites are constructed by stacking several layers of fiber reinforced material. The fibers within each layer are unidirectional. However, when built up to form a laminate the layers are typically arranged so that the orientation of the fiber varies from layer to layer. This allows laminates to be constructed which have strengths and stiffnesses which change with direction. Thus, the strengths and stiffnesses of the laminate can be carefully chosen to satisfy the specific design requirements of the structural element being built. Fiber reinforced composite materials are primarily orthotropic since they usually possess three orthogonal planes of material symmetry. These orthogonal planes define the principal material directions denoted by 1, 2, and 3 as shown in Figure 5.1. Material axis 3 is

normal to the material layer which is defined by axes 1 and 2. Material axis 1 runs parallel to the fibers while axis 2 is transverse to the fibers. Special attention is given to the prediction of the variation of the transverse shear stress(es) through the thickness of the laminate because of their importance in causing delamination failures in composites. In this regard the displacement fields of the consistent beam element and the consistent shell element are modified in order to allow the transverse shear strain(s) at the interface of two plys to be discontinuous. However, continuity of the global displacements is maintained across the interface. Numerical results for a variety of problems are presented for performance evaluation of the consistent laminated beam element and the consistent laminated shell element. These include analyses of laminated beams, laminated plates and a laminated cylindrical shell. Comparisons are made with the elasticity solutions available in the literature.

5.2 Consistent Laminated Beam Element

5.2.1 Co-ordinate Systems and Geometry

The co-ordinate systems used in the formulation of the consistent laminated beam element are shown in Figure 5.2 and are the same as those defined for the consistent beam element with one exception. A new natural co-ordinate t_L is defined in addition to the existing natural co-ordinates s and t defined in section 2.3.1 of Chapter Two. Co-ordinate t_L is parallel to the t co-ordinate and varies from -1 to +1 in the L^{th} layer instead of through the thickness of the beam like t.

The consistent laminated beam element is distorted using the same transformations that were used for the consistent beam element. Therefore, the location of any point within the element in the global co-ordinate system (x,z) is also given by Equation 2.16 of Chapter Two.

5.2.2 Displacement Field

Global displacements u and w are approximated by cubic polynomials within the element by employing the displacement degrees of freedom (u_i,w_i) at the end nodes and one-third point nodes. Rotation α, which produces a linear variation of the displacements u and w through the element depth, is approximated by a quadratic polynomial within the element. This is achieved using the rotational degree of freedom α_i at the end nodes and mid-side node. Thus far the displacement field is identical to that given for the consistent beam element in Chapter Two. However, the approximation of the nonlinear variation of the displacements u and w through the element depth is achieved in a different manner. For each layer of the laminate two rotational degrees of freedom ($\phi^T_{i,L}$, $\phi^B_{i,L}$) and two displacement degrees of freedom ($d\phi^T_{i,L}$, $d\phi^B_{i,L}$) are employed. Superscripts T and B designate the top and bottom, respectively, of the lamina as shown in Figure 5.3. Taken together these degrees of freedom provide a cubic variation of displacements u and w through the thickness of each lamina. Displacement degrees of freedom $d\phi^T_{i,L}$ and $d\phi^B_{i,L}$ are directed along the local x′ axis. Rotational degrees of freedom $\phi^T_{i,L}$ and $\phi^B_{i,L}$ at the end nodes and mid-side node are used to construct quadratic approximations of rotations ϕ^T_L and ϕ^B_L along the beam axis. Quadratic approximations of displacements $d\phi^T_L$ and $d\phi^B_L$ are achieved in a similar manner. Like the consistent beam element

there are a different number of degrees of freedom per node. For the same degrees of freedom ($u_i, w_i, \alpha_i, \phi^T_{i,L}, d\phi^T_{i,L}, \phi^B_{i,L}, d\phi^B_{i,L}, \ldots, d\phi^B_{i,NL}$) at each node there are 15+20*NL degrees of freedom per element, where NL equals the total number of layers. However, only 11+12*NL of these are active.

The global displacements (u,w) are written in terms of the nodal degrees of freedom as follows

$$\begin{Bmatrix} u \\ w \end{Bmatrix} = \Sigma \bar{N}_i \begin{Bmatrix} u_i \\ w_i \end{Bmatrix} - \Sigma N_i M_1 \begin{Bmatrix} \cos\gamma_i \\ \sin\gamma_i \end{Bmatrix} \alpha_i - \Sigma N_i \begin{Bmatrix} \cos\gamma_i \\ \sin\gamma_i \end{Bmatrix} \sum_{L}^{NL} \left[M_3 \phi^T_{i,L} + M_4 d\phi^T_{i,L} + M_5 \phi^B_{i,L} + M_6 d\phi^B_{i,L} \right] \tag{5.1}$$

where $\bar{N}_i$ and N_i are the cubic and quadratic interpolation functions, respectively, and γ_i is the angle between the local axes (x',z') and the global axes (x,z) at the i^{th} node. Shape functions $\bar{N}_i$ and N_i are given in Appendix A1. Angle γ_i is computed according to Equation 2.2 of Chapter Two. Shape function M_1 approximates the displacement field through the depth of the element due to rotation α and is given by

$$M_1 = \frac{H_i t}{2} \tag{5.2}$$

where H_i is the beam thickness at the i^{th} node. Functions M_3, M_4, M_5 and M_6 approximate the nonlinear displacement field through the thickness of each layer and are given by

$$M_3 = h_L(-t_L + t_L^2 + t_L^3 - 1)/8$$

$$M_4 = (2 + 3t_L - t_L^3)/4$$

$$M_5 = h_L(-t_L - t_L^2 + t_L^3 + 1)/8 \qquad (5.3,a\text{-}d)$$

$$M_6 = (2 - 3t_L + t_L^3)/4$$

where $h_{L,i}$ is the thickness of the L^{th} lamina at the i^{th} node. The derivation of the lamina through thickness displacement field due to degrees of freedom ϕ_L^T, ϕ_L^B, $d\phi_L^T$ and $d\phi_L^B$ is given in Appendix G. Non-dimensional co-ordinate t_L varies from -1 at the bottom to +1 at the top of the L^{th} layer and is related to curvilinear co-ordinate t according to

$$t_L = \frac{(t + 1)\, H - 2 \sum_{k}^{L-1} h_k}{h_L} - 1. \qquad (5.4)$$

where H is the thickness of the beam. It should be emphasized that displacements $d\phi_L^T$ and $d\phi_L^B$, and rotations ϕ_L^T and ϕ_L^B are used to approximate the through thickness variation of displacements u and w only within the L^{th} layer of the laminate. Also, the thickness of each lamina need not be the same nor are the laminae required to be symmetric about the centroidal axis.

To transform the global displacements (u,w) to displacements u′ and w′ directed along the local axes (x′,z′) Equation 5.1 is substituted into

Equation 2.2 of Chapter Two to give the local displacements in terms of the nodal degrees of freedom as

$$\begin{Bmatrix} u' \\ w' \end{Bmatrix} = \Sigma \bar{N}_i \begin{Bmatrix} \cos\gamma \\ -\sin\gamma \end{Bmatrix} u_i + \Sigma \bar{N}_i \begin{Bmatrix} \sin\gamma \\ \cos\gamma \end{Bmatrix} v_i - \Sigma N_i M_1 \begin{Bmatrix} CU_i \\ CW_i \end{Bmatrix} \alpha_i$$

$$- \Sigma N_i \begin{Bmatrix} CU_i \\ CW_i \end{Bmatrix} \sum_{L}^{NL} \left[M_3 \phi^{T}_{i,L} + M_4 d\phi^{T}_{i,L} + M_5 \phi^{B}_{i,L} + M_6 d\phi^{B}_{i,L} \right] \quad (5.5)$$

where $CU_i = \cos\bar{\gamma}\cos\gamma_i + \sin\gamma\sin\gamma_i$

$CW_i = -\sin\gamma\cos\gamma_i + \cos\gamma\sin\gamma_i.$

5.2.3 Strain-Displacement and Stress-Strain Relationships

The local strains $\epsilon_{x'x'}$ and $\gamma_{x'z'}$ are defined in terms of the local displacements u′ and w′ by Equation 2.21 of Chapter Two. Substituting the expression for the local displacements, Equation 5.5, into Equation 2.21 gives the local strains in terms of the nodal degrees of freedom as

$$\{\epsilon'\} = [B'] \{d\} \quad (5.6)$$

where matrix [B′] relates the nodal degrees of freedom to the local strains and is given in Appendix H. Vector {d} is the vector of nodal degrees of freedom.

The stress-strain relationship employs the typical orthotropic elasticity matrix. The fibers within a lamina can be either parallel to the centroidal axis

of the beam (i.e. along the local x′ axis) or directed normal to the plane of the beam (i.e. normal to the plane defined by the local axes x′ and z′). In the first case the material matrix [D′] can be written as

$$[D'] = \begin{bmatrix} E_1 & O \\ O & G_{13} \end{bmatrix} \tag{5.7}$$

while in the second case it is given by

$$[D'] = \begin{bmatrix} E_2 & O \\ O & G_{23} \end{bmatrix} \tag{5.8}$$

where E_i is the elastic modulus in the i^{th} material direction and G_{ij} is the shear modulus in the i-j plane.

5.2.4 Element Stiffness Matrix

The element stiffness matrix [k] is given by

$$[k] = \int_V [B']^T [D'] [B'] \, dV \tag{5.9}$$

which is integrated numerically using the Gaussian-Quadrature scheme. The integration is performed along co-ordinates s and t_L instead of along co-ordinates s and t. This gives

$$[k] = \int_{-1}^{+1} \sum_{L}^{NL} \left[\int_{-1}^{+1} [B'_L]^T [D'_L] [B'_L] \frac{h_L}{H} \, dt_L \right] \det|J| \, bds \tag{5.10}$$

where $\det|J|$ is the determinant of the Jacobian matrix which has been given previously in Equation 2.34 of Chapter Two. The width of the beam is denoted by b. The constant h_L/H relates differential dt_L to differential dt and is computed using Equation 5.4 which expresses t_L in terms of t. Matrix $[D'_L]$ is the material property matrix for the L^{th} layer (i.e. Equation 5.7 or Equation 5.8) and the strain-displacement matrix $[B'_L]$ is given in Appendix H. The partial derivatives of the interpolation functions $\bar{N}_i$, N_i and M_i with respect to the local (x',z') co-ordinate system found in $[B'_L]$ must be transformed to derivatives in the curvilinear co-ordinate system. These transformations are performed in a manner similar to that used for the consistent beam element which has been described in section 2.3.4 of Chapter Two. Interpolation functions M_3, M_4, M_5 and M_6 however are functions of t_L. Derivatives of these functions with respect to the local z' axis can be written in terms of derivatives with respect to t_L using the chain rule as

$$\frac{d}{dz'} = \frac{dt}{dz'}\frac{d}{dt} = \frac{dt}{dz'}\frac{dt_L}{dt}\frac{d}{dt_L} = \frac{dt}{dz'}\frac{H}{h_L}\frac{d}{dt_L} \qquad (5.11)$$

where factor dt_L/dt is computed using Equation 5.4. The integration of Equation 5.10 is performed using three integration points along the s co-ordinate and three integration points through each of the layers along t_L. The computation of the stiffness matrix in this manner requires that columns of $[B'_L]$ associated with degrees of freedom other than those associated with the current layer should be zeroed.

5.3 Consistent Laminated Shell Element

5.3.1 Co-ordinate Systems and Geometry

The co-ordinate systems used in the formulation of the consistent laminated shell element are shown in Figure 5.4. They are identical to those defined for the consistent shell element in section 3.2.1 of Chapter Three with one exception. In addition to curvilinear co-ordinates r,s and t a new curvilinear co-ordinate t_L has been included. Co-ordinate t_L is in the t direction but varies from -1 to +1 within the L^{th} layer. The same transformations used for distortion of the consistent shell element are used for the consistent laminated shell element. Thus, the location of any point within the consistent laminated shell element in the global co-ordinate system (x,y,z) is also given by Equation 3.1 of Chapter Three.

5.3.2 Displacement Field

Approximation of global displacements u, v and w and rotations α and β within the consistent laminated shell element is achieved in a manner identical to that employed in the consistent shell element. Refer to section 3.2.2 of Chapter Three. However, instead of using rotations ϕ and ψ to provide a cubic variation of the global displacements through the full shell thickness, as in the consistent shell element, the approach employed in the consistent laminated beam element is adopted. This is described next.

For each lamina, rotations ϕ_L^T, ψ_L^T, ϕ_L^B and ψ_L^B, and displacements $d\phi_L^T$,

$d\psi_L^T$, $d\phi_L^B$ and $d\psi_L^B$ are used to provide a cubic variation of the global displacements through the thickness of the L^{th} lamina. Superscripts T and B designate the displacements and rotations at the top and bottom of the layer, respectively. Rotations ϕ_L^T and ϕ_L^B are about the local y′ axis and rotations ψ_L^T and ψ_L^B are about the x′ axis. Displacements $d\phi_L^T$ and $d\phi_L^B$ are directed along the local x′ axis and displacements $d\psi_L^T$ and $d\psi_L^B$ are directed along the y′ axis. Rotations ϕ_L^T, ψ_L^T, ϕ_L^B and ψ_L^B are approximated quadratically within the consistent laminated shell element using the nodal degrees of freedom $(\phi^T_{i,L},\psi^T_{i,L},\phi^B_{i,L},\psi^B_{i,L})$ at the corner and mid-side nodes. Displacements $d\phi_L^T$, $d\psi_L^T$, $d\phi_L^B$ and $d\psi_L^B$ are interpolated quadratically within the element in a similar manner. For the same degrees of freedom $(u_i,v_i,w_i,\alpha_i,\beta_i,\phi^T_{i,L},\psi^T_{i,L},d\phi^T_{i,L},$ $d\psi^T_{i,L},\phi^B_{i,L},\psi^B_{i,L},d\phi^B_{i,L},d\psi^B_{i,L}$, . . . ,$d\psi^B_{i,NL}$) at each node there are 65+104*NL degrees of freedom per element, where NL is the total number of layers. However, only 42+48*NL of these are active.

The global displacements (u,v,w) are written in terms of the nodal degrees of freedom as

$$\begin{Bmatrix} u \\ v \\ w \end{Bmatrix} = \Sigma \bar{N}_i \begin{Bmatrix} u_i \\ v_i \\ w_i \end{Bmatrix} + \Sigma N_i M_1 [\hat{V}_i] \begin{Bmatrix} \alpha_i \\ \beta_i \end{Bmatrix} + \Sigma N_i [\hat{V}_i] \sum_L^{NL} \left[M_3 \begin{Bmatrix} \phi^T_{i,L} \\ \psi^T_{i,L} \end{Bmatrix} \right.$$

$$\left. + M_4 \begin{Bmatrix} d\phi^T_{i,L} \\ d\psi^T_{i,L} \end{Bmatrix} + M_5 \begin{Bmatrix} \phi^B_{i,L} \\ \psi^B_{i,L} \end{Bmatrix} + M_6 \begin{Bmatrix} d\phi^B_{i,L} \\ d\psi^B_{i,L} \end{Bmatrix} \right] \qquad (5.12)$$

where $\bar{N}_i$ and N_i are the cubic and quadratic interpolation functions, respectively, and are given in Appendix A2. Matrix $[\hat{V}_i] = [\hat{V}_{1,i}, -\hat{V}_{2,i}]$

where unit vectors $\hat{V}_{1,i}$ and $\hat{V}_{2,i}$ are directed along the local x′ and y′ axes, respectively. The procedure for calculation of $\hat{V}_{1,i}$ and $\hat{V}_{2,i}$ is presented in Appendix C. Interpolation function M_1 approximates the displacement through the shell thickness due to rotations α and β and is given by

$$M_1 = \frac{H_i t}{2} \tag{5.13}$$

where H_i is the shell thickness at the i^{th} node. Functions M_3, M_4, M_5 and M_6 which approximate the nonlinear displacement field through the thickness of each layer are the same as those given previously in section 5.2.2 by Equation 5.3. It should be emphasized that degrees of freedom ϕ_L^T, ψ_L^T, $d\phi_L^T$, $d\psi_L^T$, ϕ_L^B, ψ_L^B, $d\phi_L^B$ and $d\psi_L^B$ approximate the cubic variation of the global displacements only within the L^{th} layer of the laminate. Also, the laminas can have different thicknesses and need not be symmetric about the middle surface of the shell.

Transforming the global displacements in Equation 5.12 by employing transformation matrix $[\theta]$ given in Equation 3.6 of Chapter Three gives the local displacements u′, v′ and w′ in terms of the nodal degrees of freedom as

$$\begin{Bmatrix} u' \\ v' \\ w' \end{Bmatrix} = \Sigma \bar{N}_i [\theta] \begin{Bmatrix} u_i \\ v_i \\ w_i \end{Bmatrix} + \Sigma N_i M_1 [C_i] \begin{Bmatrix} \alpha_i \\ \beta_i \end{Bmatrix} + \Sigma N_i [C_i] \sum_{L}^{NL} \left[M_3 \begin{Bmatrix} \phi^T_{i,L} \\ \psi^T_{i,L} \end{Bmatrix} \right.$$

$$\left. + M_4 \begin{Bmatrix} d\phi^T_{i,L} \\ d\psi^T_{i,L} \end{Bmatrix} + M_5 \begin{Bmatrix} \phi^B_{i,L} \\ \psi^B_{i,L} \end{Bmatrix} + M_6 \begin{Bmatrix} d\phi^B_{i,L} \\ d\psi^B_{i,L} \end{Bmatrix} \right] \tag{5.14}$$

where

$$[C_i] = [\theta]\,[\hat{V}_i] = \begin{bmatrix} C_i^{11} & C_i^{12} \\ C_i^{21} & C_i^{22} \\ C_i^{31} & C_i^{32} \end{bmatrix} = \begin{bmatrix} (l_1l_{1i}+m_1m_{1i}+n_1n_{1i}) & (-l_1l_{2i}-m_1m_{2i}-n_1n_{2i}) \\ (l_2l_{1i}+m_2m_{1i}+n_2n_{1i}) & (-l_2l_{2i}-m_2m_{2i}-n_2n_{2i}) \\ (l_3l_{1i}+m_3m_{1i}+n_3n_{1i}) & (-l_3l_{2i}-m_3m_{2i}-n_3n_{2i}) \end{bmatrix}.$$

5.3.3 Strain-Displacement and Stress-Strain Relationships

The local strains ($\epsilon_{x'x'}, \epsilon_{y'y'}, \gamma_{x'y'}, \gamma_{x'z'}, \gamma_{y'z'}$) are expressed in terms of the local displacements (u', v', w') in Equation 3.5 of Chapter Three. Substituting the expression for the local displacements, Equation 5.14, into the strain displacement relation, Equation 3.5, and multiplying yields

$$\{\epsilon'\} = [B']\,\{d\} \tag{5.15}$$

where matrix [B'] relates the nodal degrees of freedom to the local strains and is given in Appendix I.

The stress-strain relationship employs the typical orthotropic elasticity matrix. It is derived by substituting $\sigma_{zz} = 0$ into the three dimensional orthotropic material matrix and then eliminating ϵ_{zz}. This yields (Jones 1975)

$$[D^{12}] = \begin{bmatrix} Q_{11} & Q_{12} & 0 & 0 & 0 \\ Q_{12} & Q_{22} & 0 & 0 & 0 \\ 0 & 0 & G_{12} & 0 & 0 \\ 0 & 0 & 0 & G_{13} & 0 \\ 0 & 0 & 0 & 0 & G_{23} \end{bmatrix} \tag{5.16}$$

where $$Q_{11} = C_{11} - \frac{C_{13}C_{13}}{C_{33}}$$

$$Q_{12} = C_{12} - \frac{C_{13}C_{23}}{C_{33}}$$

$$Q_{22} = C_{22} - \frac{C_{23}C_{23}}{C_{33}}$$

G_{12}, G_{13}, G_{23} = shear moduli in the 1-2, 1-3 and 2-3 material planes, respectively.

Constants C_{ij} are defined in terms of the elastic moduli and Poisson's ratios as follows

$$C_{11} = \frac{1 - \nu_{23}\nu_{32}}{E_2E_3\Delta} \qquad C_{12} = \frac{\nu_{21} + \nu_{31}\nu_{23}}{E_2E_3\Delta}$$

$$C_{22} = \frac{1 - \nu_{13}\nu_{31}}{E_1E_3\Delta} \qquad C_{13} = \frac{\nu_{31} + \nu_{21}\nu_{32}}{E_2E_3\Delta} \qquad (5.17,a\text{-}g)$$

$$C_{33} = \frac{1 - \nu_{12}\nu_{21}}{E_1E_2\Delta} \qquad C_{23} = \frac{\nu_{32} + \nu_{12}\nu_{31}}{E_1E_3\Delta}$$

$$\Delta = \frac{1 - \nu_{12}\nu_{21} - \nu_{23}\nu_{32} - \nu_{31}\nu_{13} - 2\nu_{21}\nu_{32}\nu_{13}}{E_1E_2E_3}$$

where

E_1, E_2, E_3 = elastic moduli in principal material directions 1, 2 and 3, respectively.

ν_{ij} = Poisson's ratio for transverse strain in the j^{th} direction when stressed in the i^{th} direction.

The selection of the material parameters should be done carefully to not violate the laws of thermodynamics.

As mentioned previously the fiber orientation typically varies from layer to layer. In order to analyse such a structure the fiber orientation for each layer must be referenced to some common geometric axis. The local x′ axis has been chosen as the reference axis. The fiber orientation with respect to the x′ axis is defined by the angle θ as shown in Figure 5.5. Since the strains are referred to the local axes the elasticity matrix $[D^{12}]$, Equation 5.16, must also be referred to the local co-ordinate system. This is accomplished through the following transformation

$$[D'] = [T_\epsilon]^T [D^{12}] [T_\epsilon] \tag{5.18}$$

where transformation matrix $[T_\epsilon]$ relates strains ($\epsilon_{x'x'}, \epsilon_{y'y'}, \gamma_{x'y'}, \gamma_{x'z'}, \gamma_{y'z'}$) in the local co-ordinate system to strains ($\epsilon_1, \epsilon_2, \gamma_{12}, \gamma_{13}, \gamma_{23}$) in the material co-ordinates and is given (Cook et al. 1989) as

$$[T_\epsilon] = \begin{bmatrix} \cos^2\theta & \sin^2\theta & \cos\theta\sin\theta & 0 & 0 \\ \sin^2\theta & \cos^2\theta & -\sin\theta\cos\theta & 0 & 0 \\ -2\cos\theta\sin\theta & 2\sin\theta\cos\theta & (\cos^2\theta - \sin^2\theta) & 0 & 0 \\ 0 & 0 & 0 & \cos\theta & -\sin\theta \\ 0 & 0 & 0 & \sin\theta & \cos\theta \end{bmatrix} \tag{5.19}$$

It should be noted that local axis z′ and material co-ordinate 3 are coincident. Therefore, the above transformation represents a rotation of the material axes 1 and 2 in the local x′-y′ plane.

5.3.4 Element Stiffness Matrix

The element stiffness matrix is calculated as

$$[k] = \int_V [B']^T [D'] [B'] \, dV \tag{5.20}$$

which is integrated numerically using the Gaussian-Quadrature scheme. The integration is performed along co-ordinates r, s and t_L instead of along r, s and t as was done for the consistent shell element. This then gives the element stiffness matrix [k] as

$$[k] = \int_0^{+1} \int_0^{+1} \sum_L^{NL} \left[\int_{+1}^{+1} [B_L']^T [D_L'] [B_L'] \frac{h_L}{H} \, dt_L \right] \det|J| \, drds \tag{5.21}$$

where $\det|J|$ is the determinant of the Jacobian matrix given by Equation 3.16 of Chapter Three. The constant h_L/H relates differentials dt and dt_L and is calculated using Equation 5.4. The elasticity matrix $[D_L']$ for the L^{th} layer is given by Equation 5.18. The partial derivatives of the shape functions $\tilde{N}_i$, N_i and M_i in the strain-displacement matrix $[B_L']$ with respect to the local co-ordinates (x',y',z') are written in terms of derivatives in the curvilinear co-ordinate system (r,s,t) as described in section 3.2.4 of Chapter Three. However, interpolation functions M_3, M_4, M_5 and M_6 are functions of t_L. Derivatives of these functions can be written in terms of derivatives with respect t_L using the chain rule as follows

$$\frac{\partial}{\partial x'} = \frac{\partial t}{\partial x'} \frac{\partial}{\partial t} = \frac{\partial t}{\partial x'} \frac{\partial t_L}{\partial t} \frac{\partial}{\partial t_L} = \frac{\partial t}{\partial x'} \frac{H}{h_L} \frac{\partial}{\partial t_L}$$

$$\frac{\partial}{\partial y'} = \frac{\partial t}{\partial y'}\frac{\partial}{\partial t} = \frac{\partial t}{\partial y'}\frac{\partial t_L}{\partial t}\frac{\partial}{\partial t_L} = \frac{\partial t}{\partial y'}\frac{H}{h_L}\frac{\partial}{\partial t_L}$$

$$\frac{\partial}{\partial z'} = \frac{\partial t}{\partial z'}\frac{\partial}{\partial t} = \frac{\partial t}{\partial z'}\frac{\partial t_L}{\partial t}\frac{\partial}{\partial t_L} = \frac{\partial t}{\partial z'}\frac{H}{h_L}\frac{\partial}{\partial t_L}. \qquad (5.22,a\text{-}c)$$

Integration of Equation 5.21 is performed using seven integration points in the r-s plane and five integration points through each layer along t_L. One can use three integration points through a layer to save on computation time. Calculation of the element stiffness matrix in this manner requires that columns of matrix $[B_L']$ associated with degrees of freedom which do not approximate strains in the current layer be zeroed.

5.4 Kinematic Constraints

In order to maintain displacement continuity through the thickness of the consistent laminated beam element and the consistent laminated shell element certain kinematic constraints must be imposed. In the case of the consistent laminated beam element these constraints can be written as

$$d\phi^B_{i,1} = 0$$

$$d\phi^B_{i,L} = d\phi^T_{i,L-1} \qquad (5.23,a\text{-}c)$$

$$d\phi^T_{i,NL} = 0.$$

The above constraints specify that displacement $d\phi$ is equated at the interface of

two plys to maintain continuity of u and w through the beam depth. In addition, since the shear strain at the top and bottom of the beam is known to be zero, displacement $d\phi$ which is the displacement due to shearing is equated to zero at these points. The kinematic constraints imposed on the consistent laminated shell element nodal degrees of freedom are as follows

$$d\phi^{B}_{i,1} = d\psi^{B}_{i,1} = 0$$

$$d\phi^{B}_{i,L} = d\phi^{T}_{i,L-1}$$

$$d\psi^{B}_{i,L} = d\psi^{T}_{i,L-1} \qquad (5.24,a\text{-}d)$$

$$d\phi^{T}_{i,NL} = d\psi^{T}_{i,NL} = 0$$

which are required to maintain continuity of the displacements u, v and w through the shell thickness and also to satisfy the zero shear strain condition on the top and bottom surfaces of the shell.

These constraints lead to a reduction in the number of active degrees of freedom per element. The number of active degrees of freedom for the beam element is reduced from 11+12*NL to 10+11*NL and for the shell element the active degrees of freedom are reduced from 42+48*NL to 40+46*NL. These constraints have been imposed internally in the consistent laminated beam element and the consistent laminated shell element programs.

5.5 Numerical Examples

5.5.1 Deep Laminated Composite Beam

Two thick laminated composite beams have been analysed using the consistent laminated beam element in order to verify its formulation and also to assess its accuracy. Both beams are composed of layers of a unidirectional fibrous composite material which simulates a high modulus graphite/epoxy composite. The first beam is a two ply laminate with the fibers parallel to the centroidal axis in the bottom layer and transverse to it in the top layer. Both layers are of equal thickness. The second beam is a three ply laminate with the fibers aligned with the centroidal axis in the top and bottom layers and transverse to it in the middle layer. Again all layers have the same thickness. Both beams are simply supported, have the same geometry and are subjected to a sinusoidal load. The dimensions and material properties for the beams are shown in Figure 5.6. The results predicted by the finite element models are compared with the elasticity solutions given by Pagano (1969).

Four consistent laminated beam elements have been used to model one half of each of the beams due to symmetry. The predicted normal stress variation through the thickness of both beams at the mid-span is plotted in Figure 5.7. It can be seen that the predicted variations are in excellent agreement with the elasticity solutions. The predicted shear stress variation through the depth of both beams at $x = 0$ is plotted in Figure 5.8. Again the consistent laminated beam element predictions are in excellent agreement with the elasticity solutions. Especially noteworthy is the excellent agreement

between the predicted stresses at the interface of two layers. The stresses are seen to be very nearly continuous. In addition, the predicted stresses at the top and bottom surfaces are very nearly zero as required. The predicted deformation of the normal to the centroidal axis for both of the beams at $x = 0$ is plotted in Figure 5.9. Again there is excellent agreement between the elasticity solutions and the finite element predictions, even for the three ply laminate whose cross-sectional deformation is very nonlinear. The predicted mid-span deflections for both beams are compared to the deflections given by the elasticity solutions in Table 5.1. They are seen to be in excellent agreement. This example verifies the formulation of the consistent laminated

Table 5.1: Mid-span deflections for laminated composite beams.

	Consistent Laminated Beam Element (in.)	Elasticity (in.)
2 ply	-0.00613	-0.00606
3 ply	-0.00373	-0.00364

beam element and also demonstrates that it is capable of providing accurate predictions of stresses and displacements in thick laminated beams. This is true even when the laminas are not symmetrically distributed about the centroidal axis.

5.5.2 Laminated Composite Plate

To verify the formulation of the consistent laminated shell element and also to assess its accuracy two laminated composite plates have been analysed.

Both plates contain nine plys of a unidirectional fiber reinforced composite material arranged symmetrically about the mid-surface. In both plates the fiber orientation alternates between 0° and 90° with respect to the x axis. The 0° layers are at the outer surfaces of the laminates. The total thickness of the 0° and 90° layers within a laminate is the same, while layers which have the same orientation have equal thicknesses. Both plates are square and have the same in plane dimensions. However, they have different width to thickness ratios. The first is a moderately thick plate with a width to thickness ratio of 10 and the second is a thick plate with a width to thickness ratio of 4. The material properties of the plys are representative of a high modulus graphite/epoxy composite and are given in Figure 5.10 along with the dimensions of the laminates. Both plates are simply supported along their boundaries. The results predicted by the finite element models are compared with the elasticity solutions given by Pagano and Hatfield (1972).

Only one quarter of each laminate has been modelled due to the double symmetry. Each model is composed of 32 consistent laminated shell elements. The predicted normal stress variation through the thickness of both laminates at the center of the plates is given in Figure 5.11. It can be seen that the predicted stresses are in excellent agreement with the elasticity solutions. The predicted variations of the transverse shear stress τ_{xz} at $x = 0$ and $y = L/2$ through the depth of the plates is depicted in Figure 5.12. The stresses predicted by the consistent laminated shell element models are again seen to be in excellent agreement with the elasticity solutions. It is important to mention that the stress plotted at the interface of two plys is not an average value. The finite element models predict stresses at the interface which are very nearly

continuous. Also, the stresses predicted at the top and bottom surfaces of the plates are seen to be negligible. The cross-sectional deformation of the plates at $x = 0$ and $y = L/2$ is plotted in Figure 5.13. The variation of the inplane displacement through the thickness of the moderately thick laminate is seen to be almost linear while the variation through the depth of the thick laminate is highly nonlinear. The displacements predicted by the consistent laminated shell element models are in very good agreement with those given by the elasticity solution for both the moderately thick and thick laminates. The center plate deflection and the maximum inplane shear stress τ_{xy} at $x = y = 0$ for both of the plates are given Table 5.2 along with the values given by the elasticity solutions. Both the deflections and the inplane shear stresses are seen to be in excellent agreement with the elasticity solutions. This example verifies the

Table 5.2: Deflections and inplane shear stresses for laminated composite plates.

L/H		Consistent Laminated Plate Element	Elasticity
4	w_c (in.)	-0.001142	-0.001126
	τ_{xy} (psi)	56.0	52.48
10	w_c (in.)	-0.006543	-0.006520
	τ_{xy} (psi)	244	234

consistent laminated shell element formulation and also demonstrates that it is able to predict very accurately the stresses and displacements through the thickness of laminated fiber reinforced composite plates.

5.5.3 Thin Laminated Composite Cylindrical Shell

A thin fibrous composite cylindrical shell has been analysed using the consistent laminated shell element. The shell is subjected to a uniform internal pressure and is composed of two layers of orthotropic material. The fiber orientation in the inner layer is in the longitudinal direction and in the outer layer in the circumfrential direction. Both layers are of equal thickness. The shell is supported at both ends in such a way that the radial deflection is restrained but the longitudinal displacement and the rotation about the longitudinal axis are free to occur. The dimensions and material properties for the shell are shown in Figure 5.14.

Due to the symmetry of the problem only one-eighth of the shell has been modelled using sixty-four consistent laminated shell elements. A closed-form solution for this problem has been obtained by Chaudhuri et al. (1986) using classical lamination theory (CLT). The variation of the shear stress $\tau_{y\theta}$ through the thickness of the shell at its end (i.e. y = 0) is plotted in Figure 5.15. The stress distribution predicted by the finite element model is seen to be in very good agreement with the stresses given by the CLT solution. The radial displacement at the mid-span of the cylinder predicted by the consistent laminated shell element model is 0.002505 in. which agrees very well with the value given by CLT of 0.002565 in. This example verifies the formulation and accuracy of the consistent laminated shell element when it is distorted to model curved surfaces.

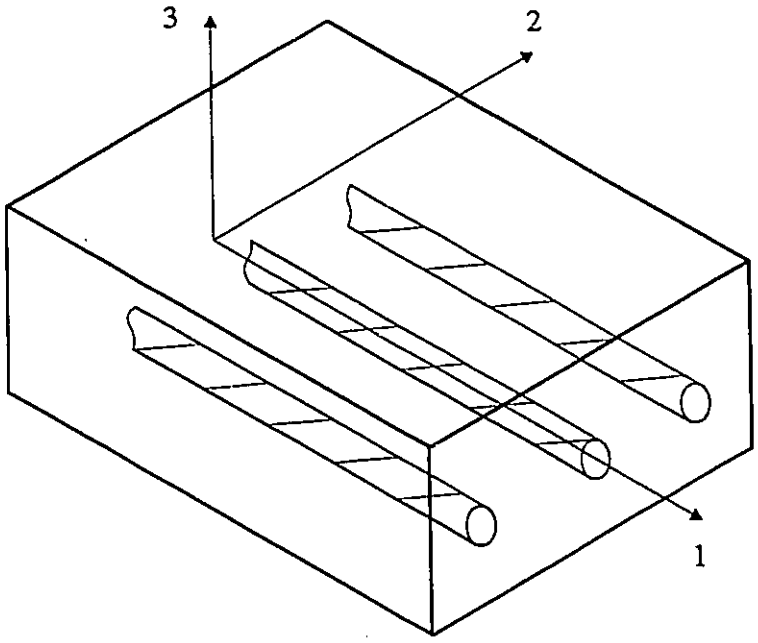

Figure 5.1: Definition of principal material directions for fiber reinforced composite lamina.

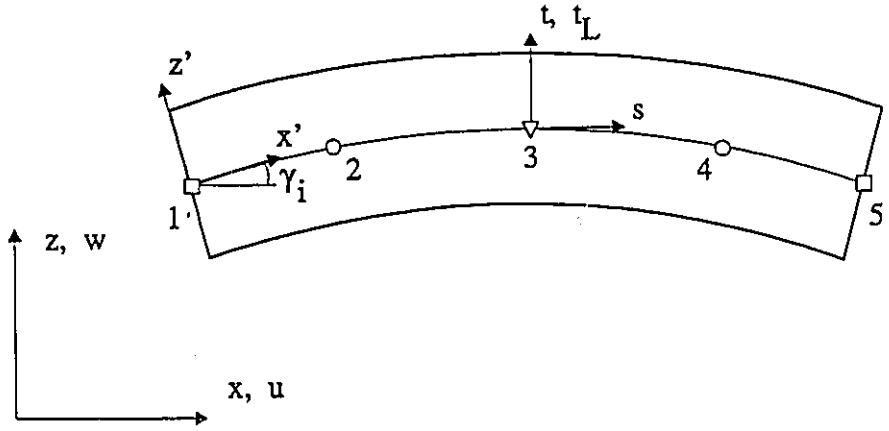

□ u_i, w_i, α_i, $\phi^T_{i,L}$, $d\phi^T_{i,L}$, $\phi^B_{i,L}$, $d\phi^B_{i,L}$, . . . , $d\phi^B_{i,NL}$

○ ui, wi

▽ α_i, ϕ_i, $d\phi^T_{i,L}$, $\phi^B_{i,L}$, $d\phi^B_{i,L}$, . . . , $d\phi^B_{i,NL}$

Figure 5.2: Consistent laminated beam element co-ordinate systems and degrees of freedom.

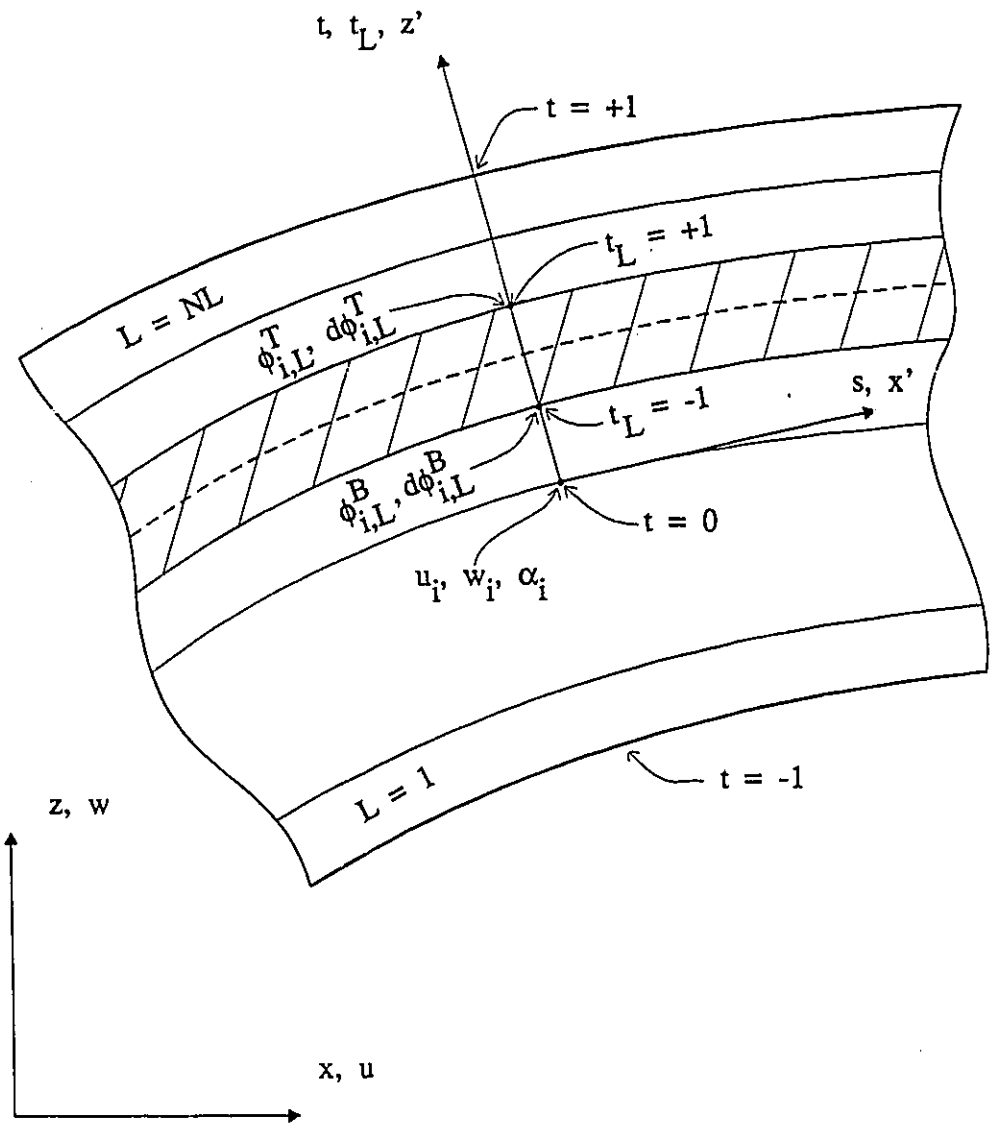

Figure 5.3: Laminae degrees of freedom and co-ordinate t_L at the i^{th} node.

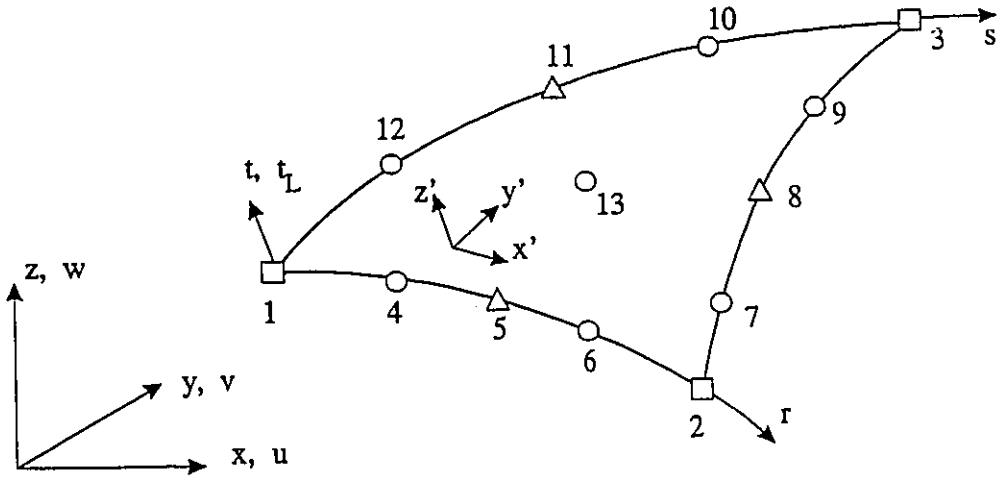

□ $u_i\ v_i\ w_i\ \alpha_i\ \beta_i\ \phi^T_{iL}\ \psi^T_{iL}\ d\phi^T_{iL}\ d\psi^T_{iL}\ \phi^B_{iL}\ \psi^B_{iL}\ d\phi^B_{iL}\ d\psi^B_{iL}\ \ldots\ d\psi^B_{iNL}$

△ $\alpha_i\ \beta_i\ \phi^T_{iL}\ \psi^T_{iL}\ d\phi^T_{iL}\ d\psi^T_{iL}\ \phi^B_{iL}\ \psi^B_{iL}\ d\phi^B_{iL}\ d\psi^B_{iL}\ \ldots\ d\psi^B_{iNL}$

○ $u_i\ v_i\ w_i$

Figure 5.4: Consistent laminated shell element co-ordinate systems and nodal degrees of freedom.

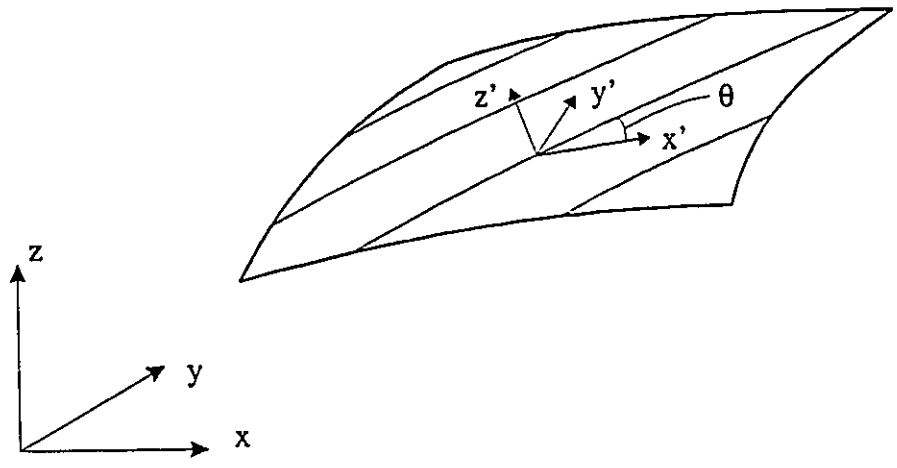

Figure 5.5: Definition of fiber orientation with respect to the local x' axis.

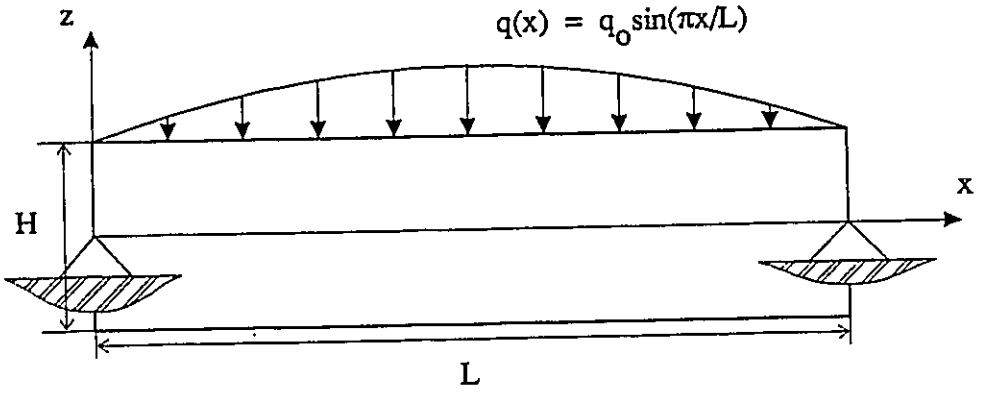

H = 5 in. L = 20 in. unit width qo = 100 lbs.

$E_1 = 25 \times 10^6$ psi $G_{13} = 0.5 \times 10^6$ psi

$E_2 = 1 \times 10^6$ psi $G_{23} = 0.2 \times 10^6$ psi

$\nu_{12} = 0.25$

2 Ply Laminate

3 Ply Laminate

L denotes layers in which the fibers are parallel to the x axis and T denotes layers where the fibers are transverse to the x-z plane.

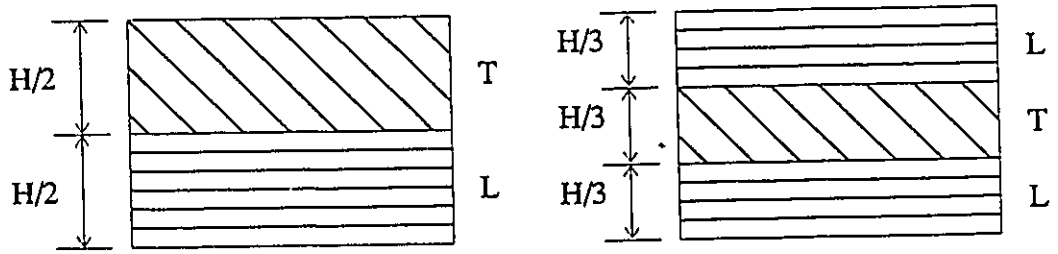

Figure 5.6: Dimensions and material properties of laminated fiber reinforced composite beams.

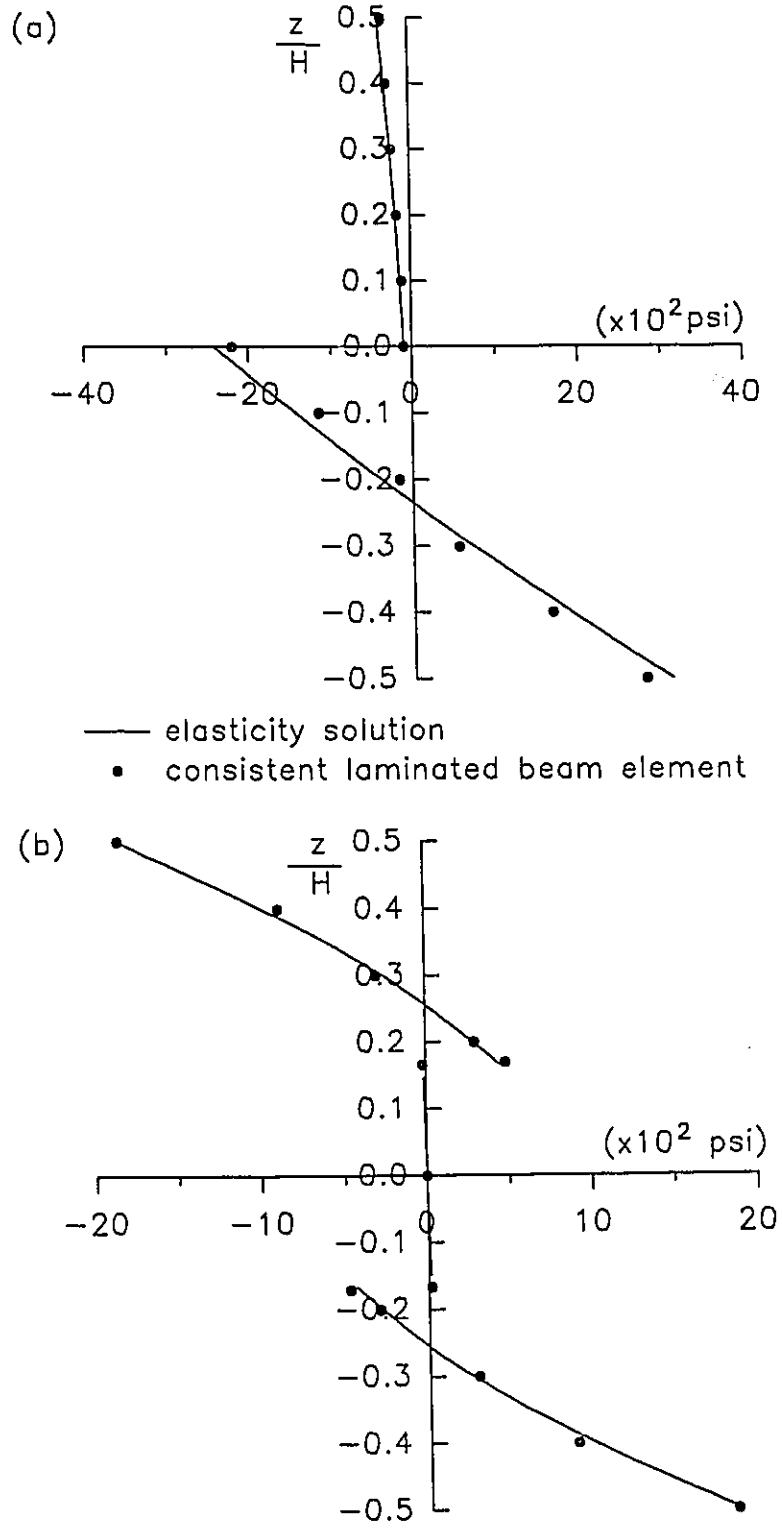

Figure 5.7: Normal stress distribution at the mid-span of the (a) 2 ply laminate (b) 3 ply laminate.

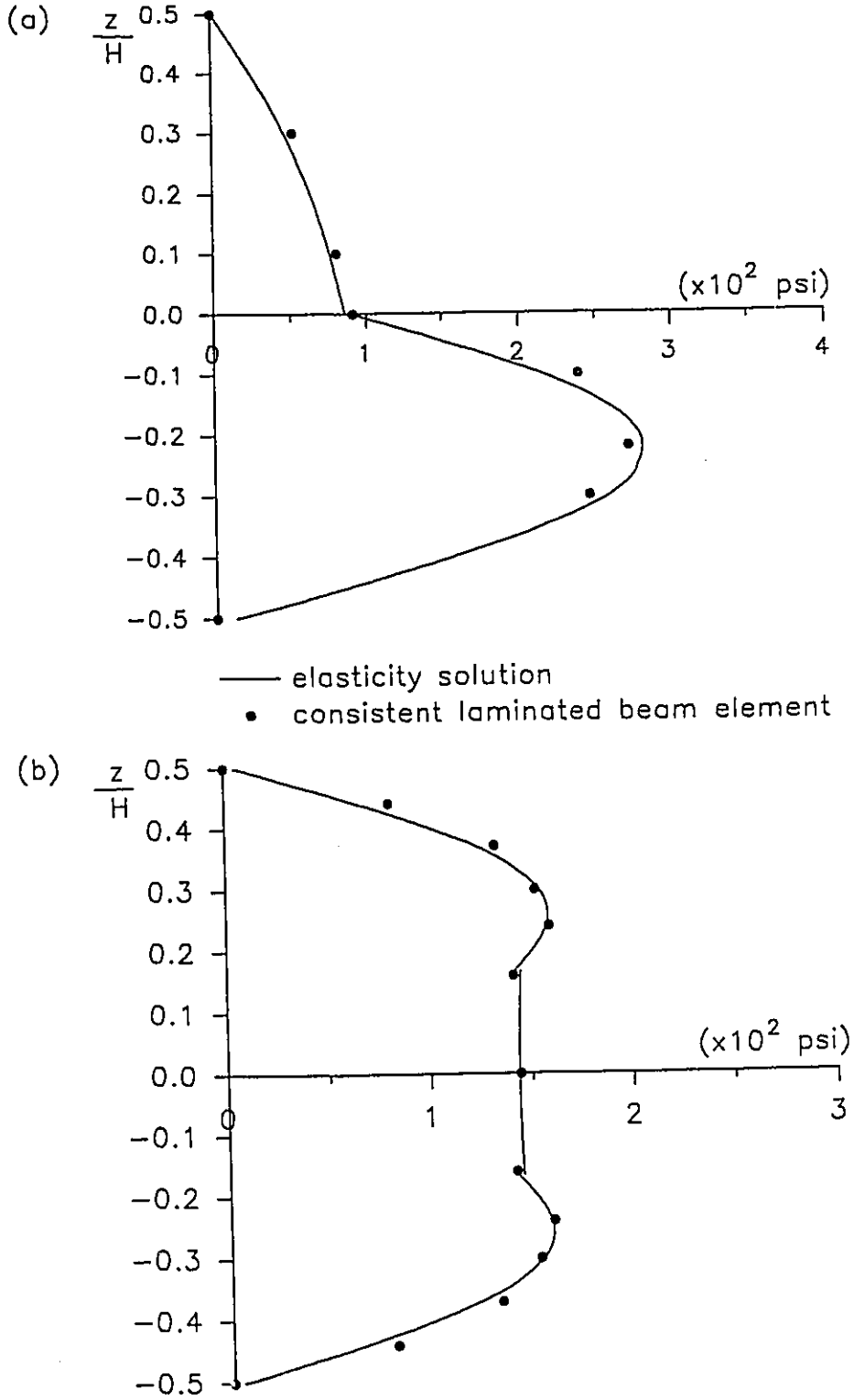

Figure 5.8: Shear stress distribution at x = 0 for the (a) 2 ply laminate (b) 3 ply laminate.

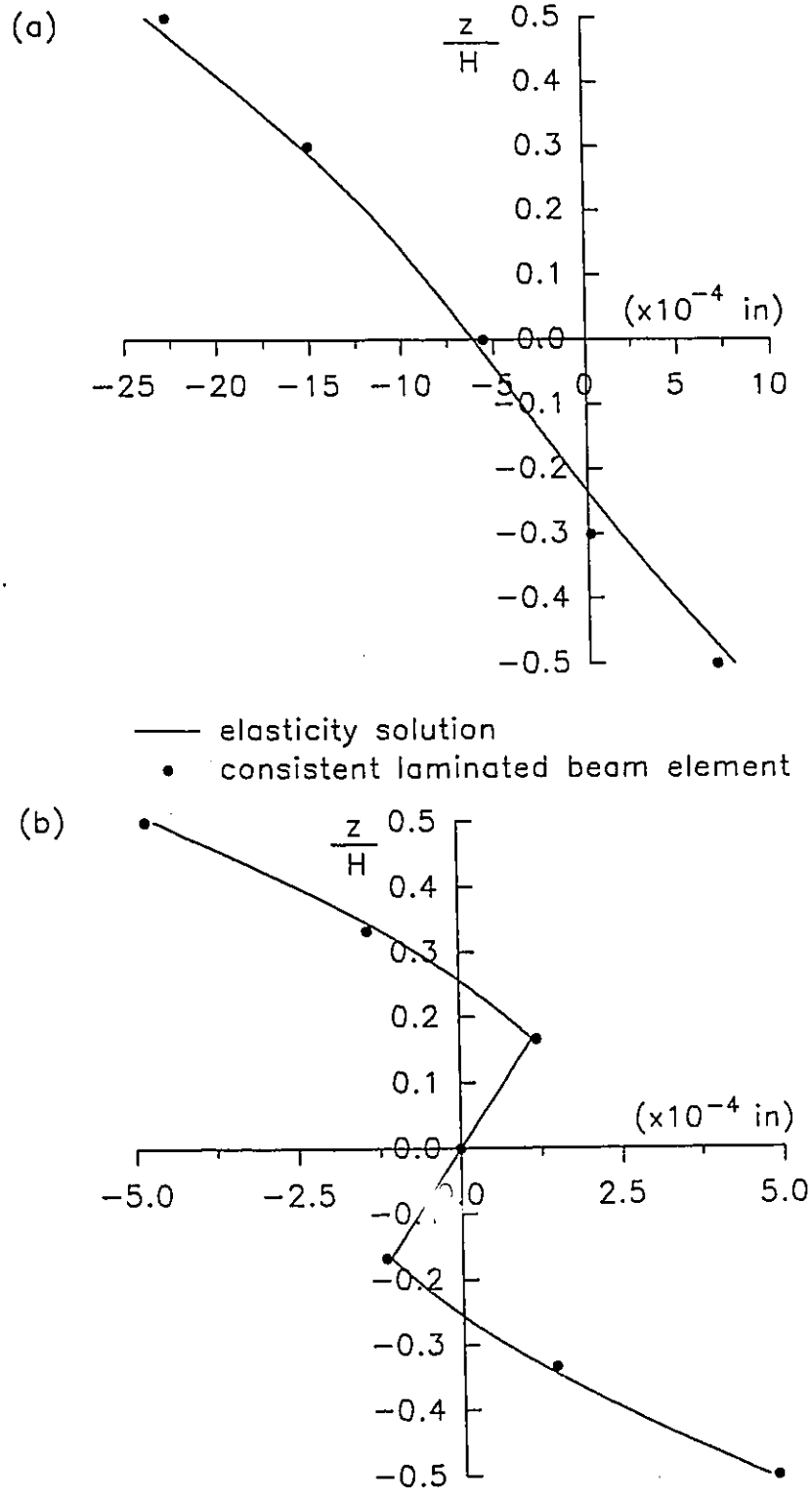

Figure 5.9: Cross–sectional deformation at x = 0 for the (a) 2 ply laminate (b) 3 ply laminate.

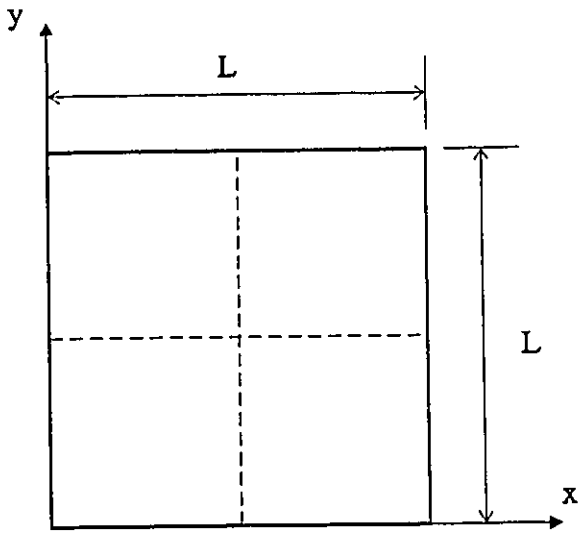

L = 10.0 in
Sinusoidal transverse load
$q = 100\sin(\pi x/L)\sin(\pi y/L)$ psi
Simply supported

$E_1 = 25 \times 10^6$ psi $\qquad E_2 = 1 \times 10^6$ psi

$G_{12} = G_{13} = 0.5 \times 10^6$ psi $\qquad G_{23} = 0.2 \times 10^6$ psi

$\nu_{12} = \nu_{13} = \nu_{23} = 0.25$

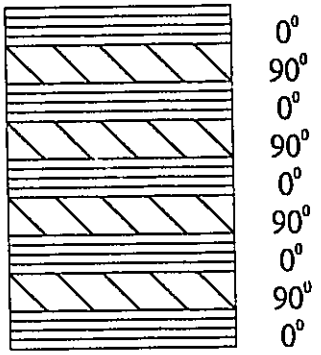

0^o and 90^o denote the fiber orientation with respect to the x axis

L/H = 4	L/H =10
$t^0 = 0.25$ in	$t^0 = 0.1$ in
$t^{90} = 0.3125$ in	$t^{90} = 0.125$ in

Figure 5.10: Dimensions and material properties for laminated fiber reinforced composite plates.

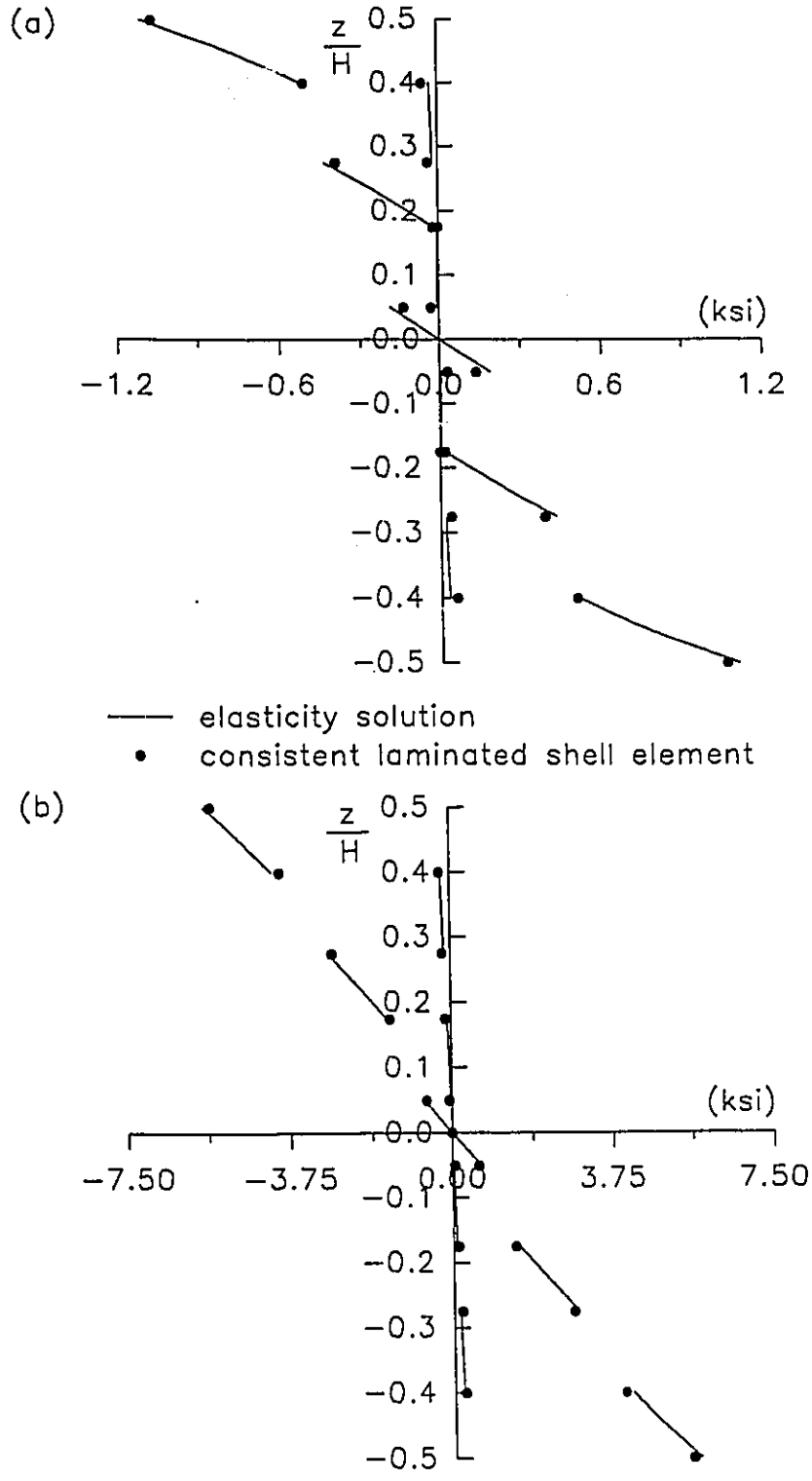

Figure 5.11: Normal stress σ_{xx} through thickness of 9 ply laminate; (a) L/H = 4 (b) L/H = 10.

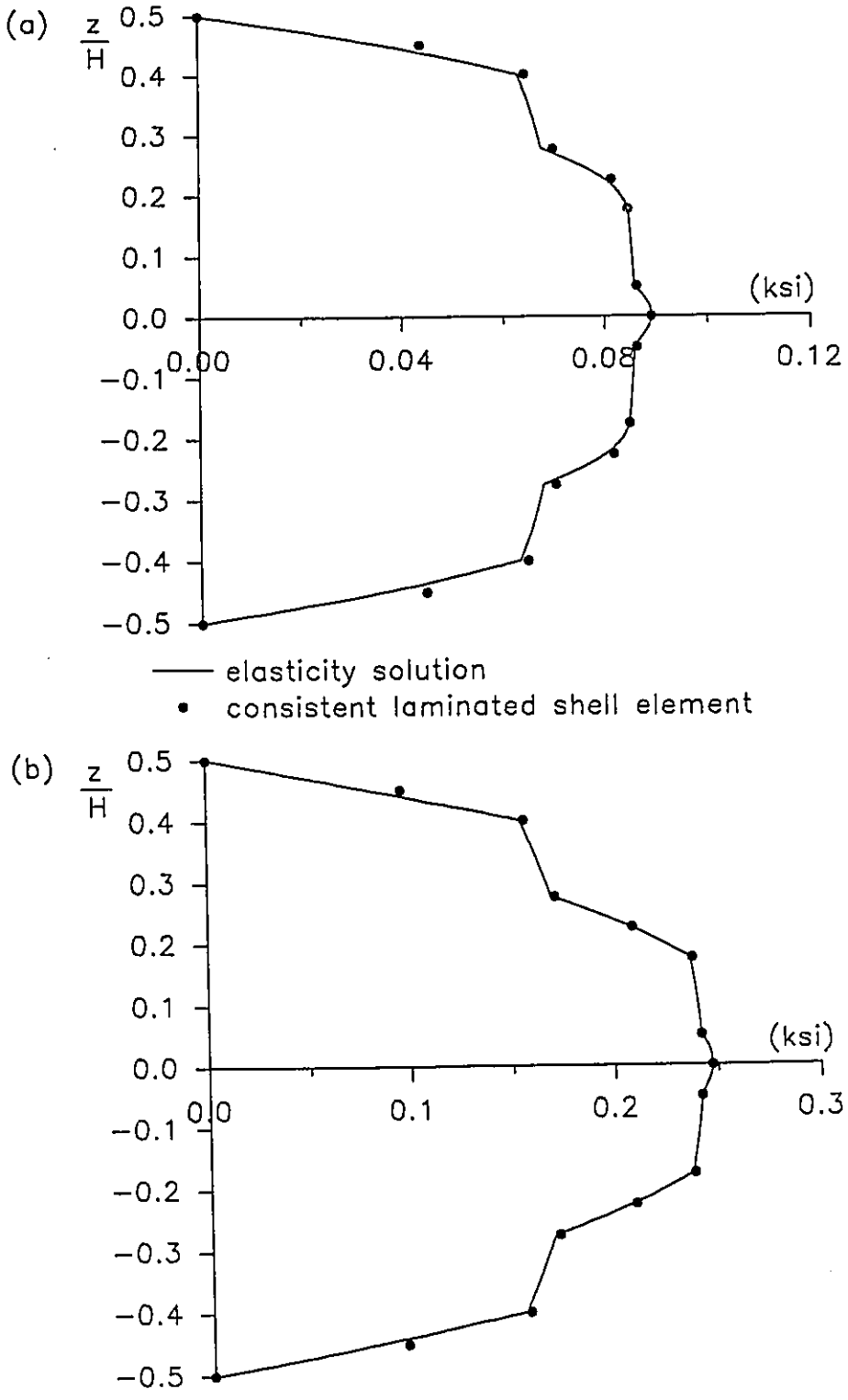

Figure 5.12: Shear stress τ_{xz} through thickness of 9 ply laminate; (a) L/H = 4 (b) L/H = 10.

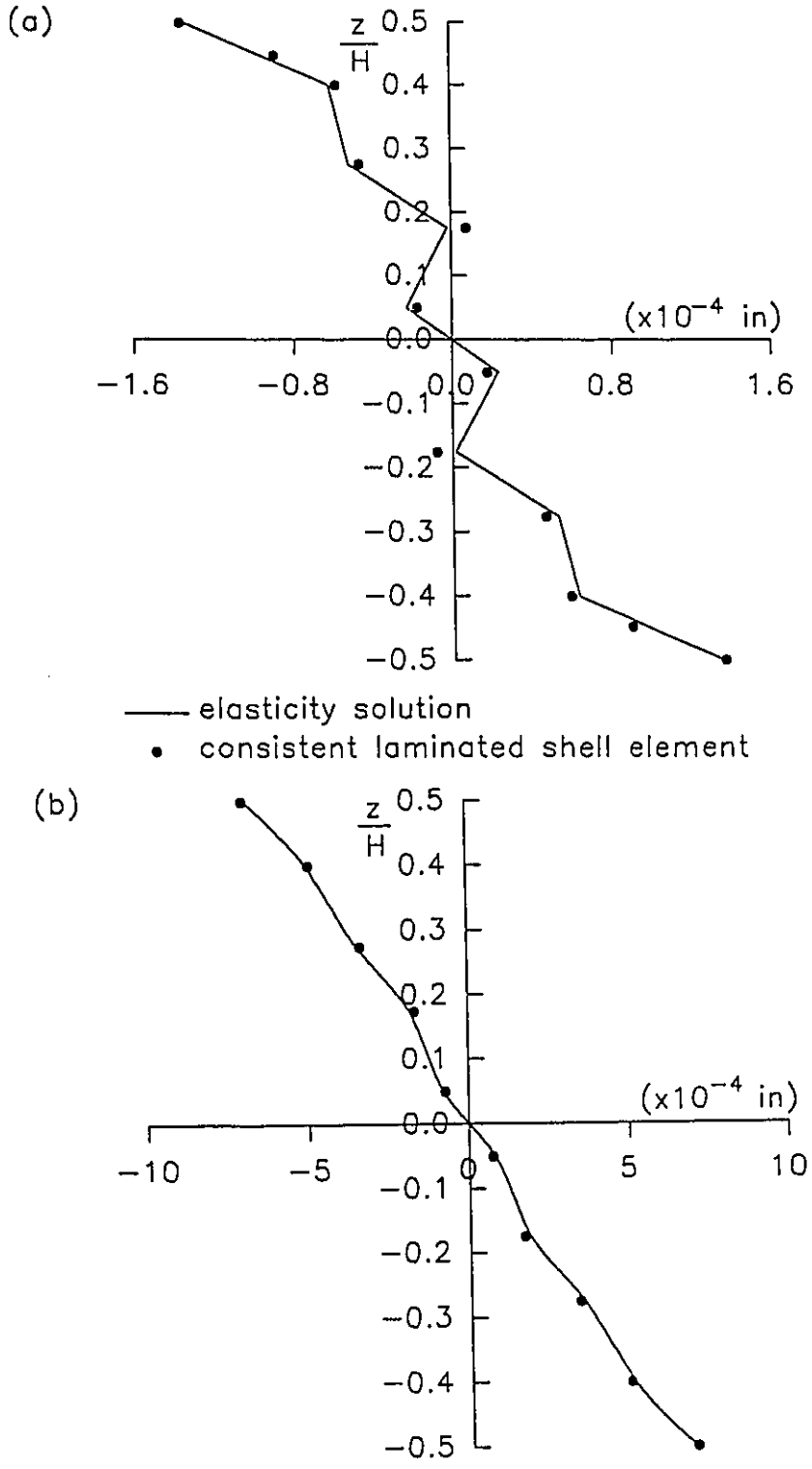

Figure 5.13: Variation of inplane displacement u through thickness of 9 ply laminate; (a) L/H = 4 (b) L/H = 10.

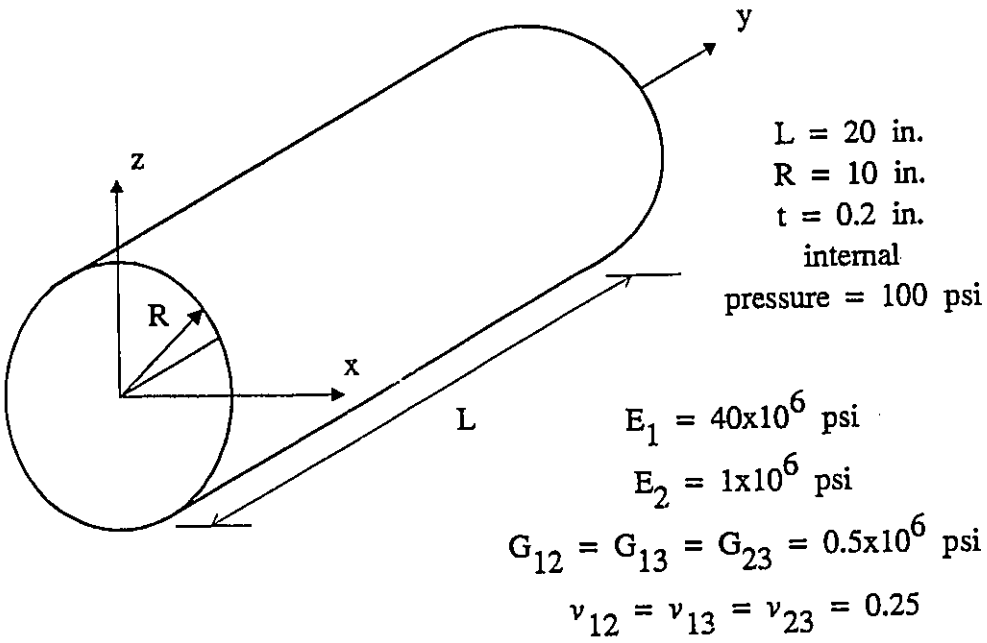

Figure 5.14: Dimensions and material properties of thin laminated fiber reinforced cylindrical shell.

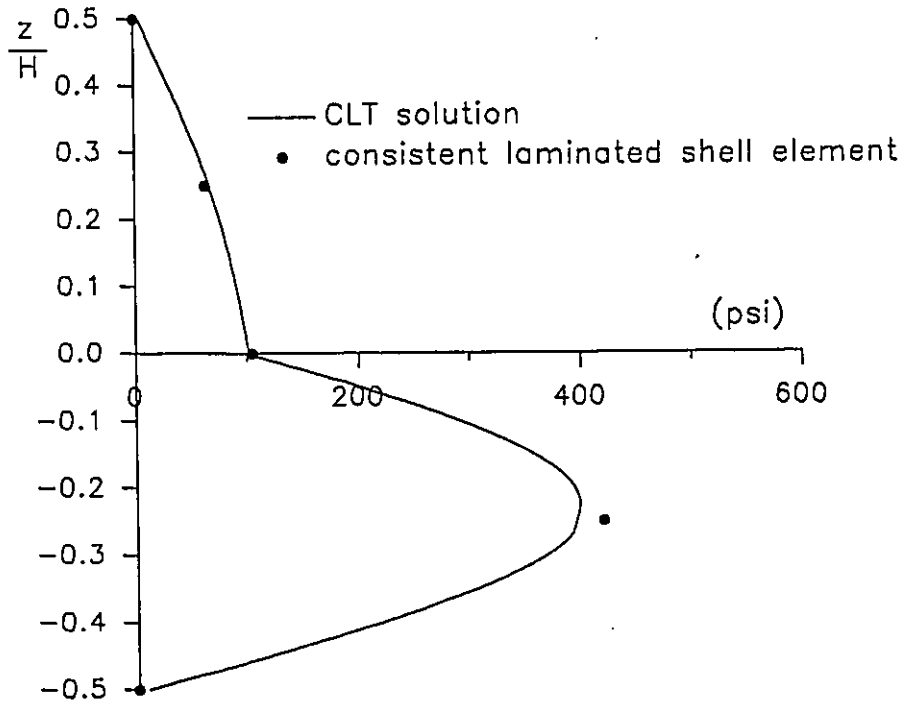

Figure 5.15: Composite cylindrical shell shear stress $\tau_{y\theta}$ distribution at y = 0.

CHAPTER SIX

CONCLUSIONS AND RECOMMENDATIONS

6.1 Conclusions

It has been shown that the spurious transverse shear modes result from an inconsistency in the order of the polynomials used for approximation of the displacements and the total rotations in the formulation of the beam and shell finite elements which approximate the transverse shear strain as the difference between the total rotation and the flexural rotation (i.e. according to Timoshenko beam theory or Mindlin plate theory). Specifically, the use of quadratic polynomials for approximation of both displacements and total rotations yields a linear expression for the flexural rotation and a quadratic expression for the total rotation. Consequently, there is no quadratic term in the flexural rotation to match the quadratic term in the total rotation. Therefore, the quadratic term of the total rotation remains undetermined in the expression for the transverse shear strain. This leads to the so called spurious transverse shear strain mode(s). Even though the inconsistency in the approximation of the transverse shear strain has been illustrated using the quadratic isoparametric beam element it can be generalized to all elements (beam or shell) in which the transverse shear strain(s) is/are calculated as the difference between the total rotation(s) and the flexural rotation(s). Therefore, spurious variations of the transverse shear strain(s) will exist whenever polynomials of the same order are used to approximate the displacements and the total rotations. This fact leads to

the following assertion.

"A consistent formulation is achieved when the displacements are approximated by a polynomial which is one order higher than that used for approximation of the total rotations. This ensures that the flexural rotations and the total rotations are approximated by the same order polynomial. Hence, all polynomial coefficients in the transverse shear stain expression are uniquely determined and the element will be free of spurious mode(s)."

The newly formulated consistent beam element and consistent shell element have been shown to be free of spurious variations of the transverse shear strain(s). Hence, the reduced integration technique is not required to provide improved responses for thin beams or shells. This has been achieved by providing cubic polynomials for approximations of displacements and quadratic polynomials for approximation of rotations, thereby ensuring a consistent formulation. Patch tests and eigenvalue analyses of the consistent beam element and the consistent shell element confirmed the existence of the required rigid body modes and the absence of any spurious zero-energy deformation modes. The numerical results show that the elements provide excellent predictions of the responses of thin and thick beams and shells. Both elements provide a quadratic variation of the transverse shear strain(s) through their thicknesses. This eliminates the need for use of the shear correction factor κ normally required by Timoshenko beam theory and Mindlin plate theory to account for the assumption of constant shear strain across the depth. Also, a cubic variation of the global displacements through the thicknesses of the consistent beam and shell elements accounts for cross-sectional distortion and hence takes care of

warping. The numerical results show that the elements provide excellent predictions of the normal stress(es) and shear stress(es) across the thickness for thin and thick beams and shells. Material non-linearity has also been included in both elements and comparisons with the available solutions show that the elements predict accurately the progression of plasticity through the thickness. The consistent shell element contains a relatively large number of degrees of freedom per element. Many of these however are inactive. By employing a sub-matrix formulation in conjunction with a modified frontal solution scheme, the computational efficiency of the element improves considerably. "The sub-matrix formulation reduces the computational time by forty to fifty percent." Overall, the consistent beam element and the consistent shell element have been shown to be highly accurate elements for the prediction of displacements and stresses, easy to use and computationally efficient. "The consistent shell element meets all of the requirements of the so called 'ideal' shell element (Hinton and Owen 1984), listed in section 1.1.1."

The comparison of the numerical results with the experimental data shows that the finite element model formulated for the analysis of reinforced concrete structures is capable of providing very good predictions of the overall reinforced concrete structural behaviour. In the case of point loads it has been found that the model is capable of predicting punching shear failure in reinforced concrete slabs. The finite element results were obtained using a load control scheme whereas the experimental data has been obtained using the displacement control test. This discrepancy is most likely responsible for the differences in the predicted and experimental responses of the structure in the cracking range. Displacement control analyses of a plain concrete tension

specimen were carried out using three different finite element meshes which contained 6, 16 and 36 elements, respectively. "The adopted constitutive model is found to be reasonably objective with respect to refinement of the finite element mesh, irrespective of the rate of softening in the post peak load region." The sensitivity of the post peak load behaviour to variation of the strain softening parameters H and μ for the concrete specimen was examined. The values of H and μ, as employed in the analysis of the reinforced concrete slab and the multigirder prestressed concrete slab, were found to simulate a brittle response in the post peak load region for the concrete specimen. This suggests that the fracture of concrete in the slabs is essentially a linear elastic phenomenon.

The laminated composite beam element and the laminated composite shell element are capable of providing excellent predictions of laminate displacements and stresses. The predicted variation of the transverse shear stresses through the laminate thickness have been shown to be very nearly continuous across the interface of two layers and also very nearly zero at the top and bottom surfaces of the laminate as required. No post-analysis of the stresses is required, unlike other currently popular methods such as the Equilibrium Method. This has been achieved by allowing the transverse shear strains to be discontinuous across an interface while maintaining continuity of the displacements by allowing additional rotation and displacement degrees of freedom for each layer. In addition, the elements perform equally well regardless of whether the laminate is symmetric or unsymmetric. Comparisons of the predicted results with the available elasticity solutions show that the elements are capable of providing excellent predictions of the cross-sectional

deformation and transverse displacement for both thin and thick laminates. The accuracy of the consistent laminated shell element has been shown to be unaffected by distortion of the element. Overall, the consistent laminated beam element and the consistent laminated shell element have been found to predict with a high degree of accuracy the displacements and stresses of laminated fiber reinforced composites.

6.2 Recommendations for Future Research

The consistent beam element and the consistent shell element are applicable only to small displacement analyses with material non-linearity. It would be desirable to extend the formulation of these elements to include the effects of geometric non-linearities so that the range of problems to which they can be applied is broadened. It is expected that they will prove to be efficient and accurate elements for the large displacement analyses of beam or shell structures. In the analysis of an actual shell structure it may be necessary to model shell intersections, and shell to solid intersections. Thus, the formulation of a finite element which would act as a transition element between the consistent shell element and a three dimensional solid element would also be desirable.

For the analysis of complex reinforced concrete structures such as nuclear containment vessels the reinforced concrete finite element model should be extended to include temperature dependent strains and cyclic loading. This will require further development of the adopted constitutive model. The development of analytical models for the interaction between concrete and

reinforcement, and the interaction between concrete and girders would allow more rational modelling of bond slip and shear connection in the finite element model. Most experimental data for reinforced concrete structures is obtained using displacement control. Therefore, extension of the incremental finite element solution procedure to include a displacement control scheme would enable more realistic comparisons to be made between the predicted and the experimental results. This could possibly be achieved using the arc length method. Further investigation is required into strain softening parameters H and μ. The effects of concrete prestress and reinforcement should be investigated so that H and μ can be determined more rationally. This may require further experimental investigation into the softening behaviour of concrete under these conditions. Also, more experimental data for reinforced concrete shell structures is required for calibration and verification of the finite element model.

The consistent laminated beam element and the consistent laminated shell element are capable of predicting deformations and stresses through a laminate thickness with good accuracy. It is recommended that they be applied to the study of failure mechanisms in laminated composite materials. This will require the introduction of some type of damage progression model so that the laminate failure could be followed.

APPENDIX A

FINITE ELEMENT INTERPOLATION FUNCTIONS

Appendix A1: Consistent Beam Element

Appendix A2: Consistent Shell Element

Appendix A3: Reinforcement Element

Appendix A4: Girder Element

Appendix A1

Consistent Beam Element

Quadratic Interpolation Functions:

$$N_1(s) = -\frac{1}{2}s(1-s) \qquad N_2(s) = 0$$

$$N_3(s) = (1-s)(1+s) \qquad N_4(s) = 0) \qquad \text{(A1.1,a-e)}$$

$$N_5(s) = \frac{1}{2}s(1+s).$$

Cubic Interpolation Functions:

$$\bar{N}_1(s) = -\frac{9}{16}(1-s)(\frac{1}{3}+s)(\frac{1}{3}-s)$$

$$\bar{N}_2(s) = \frac{27}{16}(1+s)(1-s)(\frac{1}{3}-s)$$

$$\bar{N}_3(s) = 0 \qquad \text{(A1.2,a-e)}$$

$$\bar{N}_4(s) = \frac{27}{16}(1+s)(1-s)(\frac{1}{3}+s)$$

$$\bar{N}_5(s) = -\frac{9}{16}(1+s)(\frac{1}{3}+s)(\frac{1}{3}-s)$$

Appendix A2

Consistent Shell Element

Quadratic Interpolation Functions:

$$N_1(L_1,L_2,L_3) = L_1(2L_1-1) \qquad N_2(L_1,L_2,L_3) = L_2(2L_2-1)$$

$$N_3(L_1,L_2,L_3) = L_3(2L_3-1) \qquad N_4(L_1,L_2,L_3) = 0$$

$$N_5(L_1,L_2,L_3) = 4L_1L_2 \qquad N_6(L_1,L_2,L_3) = 0$$

$$N_7(L_1,L_2,L_3) = 0 \qquad N_8(L_1,L_2,L_3) = 4L_2L_3 \qquad \text{(A2.1,a-m)}$$

$$N_9(L_1,L_2,L_3) = 0 \qquad N_{10}(L_1,L_2,L_3) = 0$$

$$N_{11}(L_1,L_2,L_3) = 4L_1L_3 \qquad N_{12}(L_1,L_2,L_3) = 0$$

$$N_{13}(L_1,L_2,L_3) = 0.$$

Cubic Interpolation Functions:

$$\bar{N}_1(L_1,L_2,L_3) = \frac{1}{2}L_1(3L_1-1)(3L_1-2) \qquad \bar{N}_2(L_1,L_2,L_3) = \frac{1}{2}L_2(3L_2-1)(3L_2-2)$$

$$\bar{N}_3(L_1,L_2,L_3) = \frac{1}{3}L_3(3L_3-1)(3L_3-2) \qquad \bar{N}_4(L_1,L_2,L_3) = \frac{9}{2}L_1L_2(3L_1-1)$$

$$\bar{N}_5(L_1,L_2,L_3) = 0 \qquad \bar{N}_6(L_1,L_2,L_3) = \frac{9}{2}L_1L_2(3L_2-1)$$

$$\bar{N}_7(L_1,L_2,L_3) = \frac{9}{2}L_2L_3(3L_2-1) \qquad \bar{N}_8(L_1,L_2,L_3) = 0 \qquad \text{(A2.2,a-m)}$$

$$\bar{N}_9(L_1,L_2,L_3) = \frac{9}{2}L_2L_3(3L_3-1) \qquad \bar{N}_{10}(L_1,L_2,L_3) = \frac{9}{2}L_3L_1(3L_3-1)$$

$$\bar{N}_{11}(L_1,L_2,L_3) = 0 \qquad \bar{N}_{12}(L_1,L_2,L_3) = \frac{9}{2}L_3L_1(3L_1-1)$$

$$\bar{N}_{13}(L_1,L_2,L_3) = 27L_1L_2L_3.$$

Note that area co-ordinates (L_1,L_2,L_3) are not independent. Only two co-ordinates need to be specified to uniquely locate a point. Let these two co-ordinates be denoted by r and s. Area co-ordinates L_1, L_2 and L_3 are defined in terms of r and s as follows

$$L_1 = r \qquad L_2 = s \qquad L_3 = 1 - r - s. \qquad \text{(A2.3,a-c)}$$

Appendix A3

Reinforcement Element

Cubic Interpolation Functions:

$$N_1^r(\varsigma) = -\frac{9}{16}(1-\varsigma)(\frac{1}{3}+\varsigma)(\frac{1}{3}-\varsigma)$$

$$N_2^r(\varsigma) = \frac{27}{16}(1+\varsigma)(1-\varsigma)(\frac{1}{3}-\varsigma)$$

$$N_3^r(\varsigma) = \frac{27}{16}(1+\varsigma)(1-\varsigma)(\frac{1}{3}+\varsigma) \qquad \text{(A3.1,a-d)}$$

$$N_4^r(\varsigma) = -\frac{9}{16}(1+\varsigma)(\frac{1}{3}+\varsigma)(\frac{1}{3}-\varsigma)$$

Appendix A4

Girder Element

Quadratic Interpolation Functions:

$$N^g_1(\zeta) = -\frac{1}{2}\zeta(1-\zeta) \qquad N^g_2(\zeta) = 0$$

$$N^g_3(\zeta) = (1-\zeta)(1+\zeta) \qquad N^g_4(\zeta) = 0 \qquad \text{(A4.1,a-e)}$$

$$N^g_5(\zeta) = \frac{1}{2}\zeta(1+\zeta)$$

Cubic Interpolation Functions:

$$\bar{N}^g_1(\zeta) = -\frac{9}{16}(1-\zeta)(\frac{1}{3}+\zeta)(\frac{1}{3}-\zeta)$$

$$\bar{N}^g_2(\zeta) = \frac{27}{16}(1+\zeta)(1-\zeta)(\frac{1}{3}-\zeta)$$

$$\bar{N}^g_3(\zeta) = 0 \qquad \text{(A4.2,a-e)}$$

$$\bar{N}^g_4(\zeta) = \frac{27}{16}(1+\zeta)(1-\zeta)(\frac{1}{3}+\zeta)$$

$$\bar{N}^g_5(\zeta) = -\frac{9}{16}(1+\zeta)(\frac{1}{3}+\zeta)(\frac{1}{3}-\zeta)$$

APPENDIX B

DERIVATION OF THROUGH THICKNESS INTERPOLATION FUNCTION M2

Let rotation ϕ vary quadratically through the thickness and be approximated by

$$\phi(\bar{z}) = a + b\bar{z} + c\bar{z}^2 \tag{B.1}$$

where $\bar{z}$ is the dimensional co-ordinate in the thickness direction and a, b and c are unknown constants. The displacement u_ϕ due to ϕ is calculated as

$$u_\phi(\bar{z}) = \int \phi(\bar{z})\, d\bar{z}. \tag{B.2}$$

Substituting the expression for ϕ given by Equation B.1, into the above equation and integrating gives

$$u_\phi(\bar{z}) = a\bar{z} + \frac{b\bar{z}^2}{2} + \frac{c\bar{z}^3}{3} + d \tag{B.3}$$

where d is an additional unknown constant. The following boundary conditions are imposed

$$u_\phi(\tfrac{h}{2}) = 0 \qquad u_\phi(\tfrac{h}{2}) = 0 \qquad u_\phi(0) = 0 \qquad \phi(0) = \phi_i. \tag{B.4,a-d}$$

where ϕ_i is the allowed rotational degree of freedom. Substitution of the above boundary conditions into the approximations for ϕ and u_ϕ, i.e. equations B.1 and B.3, respectively gives four equations for the unknowns as

$$a\frac{h}{2} + b\frac{h^2}{8} + c\frac{h^3}{24} + d = 0$$

$$-a\frac{h}{2} + b\frac{h^2}{8} - c\frac{h^3}{24} + d = 0 \qquad \text{(B.5,a-d)}$$

$$d = 0 \qquad a = \phi_i.$$

Solving equations B.5 for the unknown constants yields

$$a = \phi_i \qquad b = 0 \qquad c = -\frac{12}{h^2} \qquad d = 0 \qquad \text{(B.6,a-d)}$$

which are substituted into the approximations for ϕ and u_ϕ given by Equation B.1 and Equation B.3, respectively, to give

$$\phi(\bar{z}) = \left[1 - \frac{12}{h^2}\bar{z}^2 \right] \phi_i$$

$$u_\phi(\bar{z}) = \left[\bar{z} - \frac{4}{h^2}\bar{z}^3 \right] \phi_i. \qquad \text{(B.7,a-b)}$$

The relationship between the non-dimensional co-ordinate t and the dimensional co-ordinate $\bar{z}$ is given as

$$\bar{z} = \frac{ht}{2} \tag{B.8}$$

which is used to re-write equations B.7 in terms of t as

$$\phi(t) = (1 - 3t^2) \phi_i$$

$$u_\phi(t) = \frac{ht}{2} (1 - t^2) \phi_i = M_2 \phi_i. \tag{B.9,a-b}$$

Interpolation function M_2 defines the displacement variation through the thickness due to rotation ϕ.

APPENDIX C

CONSTRUCTION OF ORTHOGONAL BASIS

The Jacobian matrix can be written as

$$[J] = \begin{Bmatrix} \mathbf{R} \\ \mathbf{S} \\ \mathbf{T} \end{Bmatrix} \tag{C.1}$$

where vectors **R** and **S** are tangent to the surface defined by t = constant. A vector $\mathbf{V}_3$ normal to this surface is found as

$$\mathbf{V}_3 = \mathbf{R} \times \mathbf{S}. \tag{C.2}$$

The remaining vectors $\mathbf{V}_2$ and $\mathbf{V}_1$ of the orthogonal basis are given by

$$\mathbf{V}_2 = \mathbf{V}_3 \times \mathbf{R}$$

$$\mathbf{V}_1 = \mathbf{V}_2 \times \mathbf{V}_3. \tag{C.3,a-b}$$

Normalizing $\mathbf{V}_1$, $\mathbf{V}_2$, and $\mathbf{V}_3$ gives the set of unit vectors $\hat{\mathbf{V}}_1$, $\hat{\mathbf{V}}_2$, and $\hat{\mathbf{V}}_3$ from which the transformation matrix of direction cosines is constructed as

$$[\theta] = \begin{Bmatrix} \hat{V}_1 \\ \hat{V}_2 \\ \hat{V}_3 \end{Bmatrix} \begin{matrix} \\ x' \\ y' \\ z' \end{matrix} \begin{bmatrix} \overset{x}{l_1} & \overset{y}{m_1} & \overset{z}{n_1} \\ l_2 & m_2 & n_2 \\ l_3 & m_3 & n_3 \end{bmatrix}. \qquad \text{(C.4)}$$

APPENDIX D

CONSISTENT SHELL ELEMENT STIFFNESS SUB-MATRICES

$$[k^S]_{11} = \frac{E}{(1-\nu^2)}\int_V \Bigg[\left[l_1^2+\frac{1-\nu}{2}(l_2^2+l_3^2)\right][A]+\left[l_2^2+\frac{1-\nu}{2}(l_1^2+l_3^2)\right][C] + \left[l_1l_2\frac{\nu+1}{2}\right]([E]+[E]^T)+\frac{1-\nu}{2}\Big[(l_1l_3)([J]+[J]^T)+(l_1^2+l_2^2)[O] + (l_2l_3)([Q]+[Q]^T)\Big]\Bigg]dV$$

$$[k^S]_{12} = \frac{E}{(1-\nu^2)}\int_V \Bigg[\left[l_1m_1+\frac{1-\nu}{2}(l_2m_2+l_3m_3)\right][A]+\left[l_2m_2+\frac{1-\nu}{2}(l_1m_1+l_3m_3)\right][C] \left[\nu l_1m_2+\frac{1-\nu}{2}m_1l_2\right][E]+\left[\nu m_1l_2+\frac{1-\nu}{2}l_1m_2\right][E]^T+\frac{1-\nu}{2}\Big[(l_1m_3)[J]+ (l_3m_1)[J]^T+(l_1m_1+l_2m_2)[O]+(l_2m_3)[Q]+(l_3m_2)[Q]^T\Big]\Bigg]dV$$

$$[k^S]_{13} = \frac{E}{(1-\nu^2)}\int_V \Bigg[\left[l_1n_1+\frac{1-\nu}{2}(l_2n_2+l_3n_3)\right][A]+\left[l_2n_2+\frac{1-\nu}{2}(l_1n_1+l_3n_3)\right][C] \left[\nu l_1n_2+\frac{1-\nu}{2}n_1l_2\right][E]+\left[\nu n_1l_2+\frac{1-\nu}{2}l_1n_2\right][E]^T+\frac{1-\nu}{2}\Big[(l_1n_3)[J] +(l_3n_1)[J]^T+(l_1n_1+l_2n_2)[O]+(l_2n_3)[Q]+(l_3n_2)[Q]^T\Big]\Bigg]dV$$

$$[k^S]_{14} = \frac{E}{(1-\nu^2)}\int_V \Bigg[l_1\frac{\partial M_1}{\partial x'}[H^{11}]^T+l_2\frac{\partial M_1}{\partial y'}[I^{21}]^T+\nu l_1\frac{\partial M_1}{\partial y'}[H^{21}]^T+\frac{1-\nu}{2}\Big[l_1\frac{\partial M_1}{\partial y'} [I^{11}]^T+l_1\frac{\partial M_1}{\partial x'}[I^{21}]^T+\left[l_2\frac{\partial M_1}{\partial y'}+l_3\frac{\partial M_1}{\partial z'}\right][H^{11}]^T+\left[l_2\frac{\partial M_1}{\partial x'}+ l_3\frac{\partial M_1}{\partial z'}\right][H^{21}]^T+\left[l_1\frac{\partial M_1}{\partial x'}+l_2\frac{\partial M_1}{\partial y'}\right][L^{31}]+\left[l_3\frac{\partial M_1}{\partial x'}+ l_3\frac{\partial M_1}{\partial y'}\right][H^{31}]^T+l_2\frac{\partial M_1}{\partial z'}[L^{21}]\Big]\Bigg]dV$$

$$[k^S]_{15} = \frac{E}{(1-\nu^2)}\int_V \Bigg[l_2\frac{\partial M_1}{\partial y'}[I^{22}]^T + l_1\frac{\partial M_1}{\partial x'}[H^{12}]^T + \nu l_1\frac{\partial M_1}{\partial y'}[H^{22}]^T + \frac{1-\nu}{2}\Bigg(l_1\frac{\partial M_1}{\partial y'}[I^{12}]^T + l_1\frac{\partial M_1}{\partial x'}[I^{22}]^T + \Bigg(l_2\frac{\partial M_1}{\partial y'} + l_3\frac{\partial M_1}{\partial z'}\Bigg)[H^{12}]^T + \Bigg(l_2\frac{\partial M_1}{\partial x'} + l_3\frac{\partial M_1}{\partial z'}\Bigg)[H^{22}]^T + l_1\frac{\partial M_1}{\partial z'}[L^{21}] + \Bigg(l_1\frac{\partial M_1}{\partial x'} + l_2\frac{\partial M_1}{\partial y'}\Bigg)[L^{32}] + \Bigg(l_3\frac{\partial M_1}{\partial x'} + l_3\frac{\partial M_1}{\partial y'}\Bigg)[H^{32}]^T + l_2\frac{\partial M_1}{\partial z'}[L^{22}]\Bigg)\Bigg]dV$$

$$[k^S]_{16} = \frac{E}{(1-\nu^2)}\int_V \Bigg[l_1\frac{\partial M_2}{\partial x'}[H^{11}]^T + l_2\frac{\partial M_2}{\partial y'}[I^{21}]^T + \nu l_1\frac{\partial M_2}{\partial y'}[H^{21}]^T + \frac{1-\nu}{2}\Bigg(l_1\frac{\partial M_2}{\partial y'}[I^{11}]^T + l_1\frac{\partial M_2}{\partial x'}[I^{21}]^T + \Bigg(l_2\frac{\partial M_2}{\partial y'} + l_3\frac{\partial M_2}{\partial z'}\Bigg)[H^{11}]^T + \Bigg(l_2\frac{\partial M_2}{\partial x'} + l_3\frac{\partial M_2}{\partial z'}\Bigg)[H^{21}]^T + l_1\frac{\partial M_2}{\partial z'}[L^{11}] + \Bigg(l_1\frac{\partial M_2}{\partial x'} + l_2\frac{\partial M_2}{\partial y'}\Bigg)[L^{31}] + \Bigg(l_3\frac{\partial M_2}{\partial x'} + l_3\frac{\partial M_2}{\partial y'}\Bigg)[H^{31}]^T + l_2\frac{\partial M_2}{\partial z'}[L^{21}]\Bigg)\Bigg]dV$$

$$[k^S]_{17} = \frac{E}{(1-\nu^2)}\int_V \Bigg[l_2\frac{\partial M_2}{\partial y'}[I^{22}]^T + l1\frac{\partial M_2}{\partial x'}[H^{12}]^T + \nu l_1\frac{\partial M_2}{\partial y'}[H^{22}]^T + \frac{1-\nu}{2}\Bigg(l_1\frac{\partial M_2}{\partial y'}[I^{12}]^T + l_1\frac{\partial M_2}{\partial x'}[I^{22}]^T + \Bigg(l_2\frac{\partial M_2}{\partial y'} + l_3\frac{\partial M_2}{\partial z'}\Bigg)[H^{12}]^T + \Bigg(l_2\frac{\partial M_2}{\partial x'} + l_3\frac{\partial M_2}{\partial z'}\Bigg)[H^{22}]^T + l_1\frac{\partial M_2}{\partial z'}[L^{12}] + \Bigg(l_1\frac{\partial M_2}{\partial x'} + l_2\frac{\partial M_2}{\partial y'}\Bigg)[L^{32}] + \Bigg(l_3\frac{\partial M_2}{\partial x'} + l_3\frac{\partial M_2}{\partial y'}\Bigg)[H^{32}]^T + l_2\frac{\partial M_2}{\partial z'}[L^{22}]\Bigg)\Bigg]dV$$

$$[k^S]_{22} = \frac{E}{(1-\nu^2)}\int_V \Bigg[\Bigg(m_1^2 + \frac{1-\nu}{2}(m_2^2+m_3^2)\Bigg)[A] + \Bigg(m_2^2 + \frac{1-\nu}{2}(m_1^2+m_3^2)\Bigg)[C] + \Bigg(m_1m_2\frac{\nu+1}{2}\Bigg)([E]+[E]^T) + \frac{1-\nu}{2}\Bigg((m_1m_3)([J]+[J]^T) + (m_1^2+m_2^2)[O] + (m_2m_3)([Q]+[Q]^T)\Bigg)\Bigg]dV$$

$$[k^S]_{23} = \frac{E}{(1-\nu^2)}\int_V \Bigg[\Bigg(m_1n_1 + \frac{1-\nu}{2}(m_2n_2+m_3n_3)\Bigg)[A] + \Bigg(\nu n_1m_2 + \frac{1-\nu}{2}m_1n_2\Bigg)[E]^T + \Bigg(m_2n_2 + \frac{1-\nu}{2}(m_1n_1+m_3n_3)\Bigg)[C] + \Bigg(\nu m_1n_2 + \frac{1-\nu}{2}n_1m_2\Bigg)[E] +$$

$$\frac{1-\nu}{2}\Big[(m_1n_3)[J]+(m_3n_1)[J]^T+(m_1n_1+m_2n_2)[O]+(m_2n_3)[Q]+(m_3n_2)[Q]^T\Big]\Big]dV$$

$$[k^S]_{24}=\frac{E}{(1-\nu^2)}\int_V\Bigg[\Bigg[m_1\frac{\partial M_1}{\partial x'}+\frac{1-\nu}{2}\Bigg[m_3\frac{\partial M_1}{\partial z'}+m_2\frac{\partial M_1}{\partial y'}\Bigg]\Bigg][H^{11}]^T+m_2\frac{\partial M_1}{\partial y'}[I^{21}]^T+\Bigg[\nu m_1\frac{\partial M_1}{\partial y'}+\frac{1-\nu}{2}\Bigg[m_3\frac{\partial M_1}{\partial z'}+m_2\frac{\partial M_1}{\partial x'}\Bigg]\Bigg][H^{21}]^T+\frac{1-\nu}{2}\Bigg[m_1\frac{\partial M_1}{\partial y'}[I^{11}]^T+m_1\frac{\partial M_1}{\partial x'}[I^{21}]^T+m_1\frac{\partial M_1}{\partial z'}[L^{11}]+\Bigg[m_1\frac{\partial M_1}{\partial x'}+m_2\frac{\partial M_1}{\partial y'}\Bigg][L^{31}]+\Bigg[m_3\frac{\partial M_1}{\partial x'}+m_3\frac{\partial M_1}{\partial y'}\Bigg][H^{31}]^T+m_2\frac{\partial M_1}{\partial z'}[L^{21}]\Bigg]\Bigg]dV$$

$$[k^S]_{25}=\frac{E}{(1-\nu^2)}\int_V\Bigg[m_2\frac{\partial M_1}{\partial y'}[I^{22}]^T+m_1\frac{\partial M_1}{\partial x'}[H^{12}]^T+\nu m_1\frac{\partial M_1}{\partial y'}[H^{22}]^T+\frac{1-\nu}{2}\Bigg[m_1\frac{\partial M_1}{\partial y'}[I^{12}]^T+m_1\frac{\partial M_1}{\partial x'}[I^{22}]^T+\Bigg[m_2\frac{\partial M_1}{\partial y'}+m_3\frac{\partial M_1}{\partial z'}\Bigg][H^{12}]^T+\Bigg[m_2\frac{\partial M_1}{\partial x'}+m_3\frac{\partial M_1}{\partial z'}\Bigg][H^{22}]^T+m_1\frac{\partial M_1}{\partial z'}[L^{12}]+\Bigg[m_1\frac{\partial M_1}{\partial x'}+m_2\frac{\partial M_1}{\partial y'}\Bigg][L^{32}]+\Bigg[m_3\frac{\partial M_1}{\partial x'}+m_3\frac{\partial M_1}{\partial y'}\Bigg][H^{32}]^T+m_2\frac{\partial M_1}{\partial z'}[L^{22}]\Bigg]\Bigg]dV$$

$$[k^S]_{26}=\frac{E}{(1-\nu^2)}\int_V\Bigg[\Bigg[m_1\frac{\partial M_2}{\partial x'}+\frac{1-\nu}{2}\Bigg[m_3\frac{\partial M_2}{\partial z'}+m_2\frac{\partial M_2}{\partial y'}\Bigg]\Bigg][H^{11}]^T+m_2\frac{\partial M_2}{\partial y'}[I^{21}]^T+\Bigg[\nu m_1\frac{\partial M_2}{\partial y'}+\frac{1-\nu}{2}\Bigg[m_3\frac{\partial M_2}{\partial z'}+m_2\frac{\partial M_2}{\partial x'}\Bigg]\Bigg][H^{21}]^T+\frac{1-\nu}{2}\Bigg[m_1\frac{\partial M_2}{\partial y'}[I^{11}]^T+m_1\frac{\partial M_2}{\partial x'}[I^{21}]^T+m_1\frac{\partial M_2}{\partial z'}[L^{11}]+\Bigg[m_1\frac{\partial M_2}{\partial x'}+m_2\frac{\partial M_2}{\partial y'}\Bigg][L^{31}]+\Bigg[m_3\frac{\partial M_2}{\partial x'}+m_3\frac{\partial M_2}{\partial y'}\Bigg][H^{31}]^T+m_2\frac{\partial M_2}{\partial z'}[L^{21}]\Bigg]\Bigg]dV$$

$$[k^S]_{27}=\frac{E}{(1-\nu^2)}\int_V\Bigg[m_2\frac{\partial M_2}{\partial y'}[I^{22}]^T+m_1\frac{\partial M_2}{\partial x'}[H^{12}]^T+\nu m_1\frac{\partial M_2}{\partial y'}[H^{22}]^T+\frac{1-\nu}{2}\Bigg[m_1\frac{\partial M_2}{\partial y'}[I^{12}]^T+m_1\frac{\partial M_2}{\partial x'}[I^{22}]^T+\Bigg[m_2\frac{\partial M_2}{\partial y'}+m_3\frac{\partial M_2}{\partial z'}\Bigg][H^{12}]^T+\Bigg[m_2\frac{\partial M_2}{\partial x'}+m_3\frac{\partial M_2}{\partial z'}\Bigg][H^{22}]^T+m_1\frac{\partial M_2}{\partial z'}[L^{12}]+\Bigg[m_1\frac{\partial M_2}{\partial x'}+m_2\frac{\partial M_2}{\partial y'}\Bigg][L^{32}]+\Bigg[m_3\frac{\partial M_2}{\partial x'}+m_3\frac{\partial M_2}{\partial y'}\Bigg][H^{32}]^T+m_2\frac{\partial M_2}{\partial z'}[L^{22}]\Bigg]\Bigg]dV$$

$$[k^S]_{33} = \frac{E}{(1-\nu^2)}\int_V \Bigg[\left[n_1^2+\frac{1-\nu}{2}(n_2^2+n_3^2)\right][A]+\left[n_2^2+\frac{1-\nu}{2}(n_1^2+n_3^2)\right][C] + \left[n_1n_2\frac{\nu+1}{2}\right]([E]+[E]^T)+\frac{1-\nu}{2}\Big[(n_1n_3)([J]+[J]^T)+(n_1^2+n_2^2)[O] + (n_2n_3)([Q]+[Q]^T)\Big]\Bigg]dV$$

$$[k^S]_{34} = \frac{E}{(1-\nu^2)}\int_V \Bigg[\left[n_1\frac{\partial M_1}{\partial x'}+\frac{1-\nu}{2}\left[n_3\frac{\partial M_1}{\partial z'}+n_2\frac{\partial M_1}{\partial y'}\right]\right][H^{11}]^T+n_2\frac{\partial M_1}{\partial y'}[I^{21}]^T+ \left[\nu n_1\frac{\partial M_1}{\partial y'}+\frac{1-\nu}{2}\left[n_3\frac{\partial M_1}{\partial z'}+n_2\frac{\partial M_1}{\partial x'}\right]\right][H^{21}]^T+\frac{1-\nu}{2}\left[n_1\frac{\partial M_1}{\partial y'}[I^{11}]^T+ n_1\frac{\partial M_1}{\partial x'}[I^{21}]^T+n_1\frac{\partial M_1}{\partial z'}[L^{11}]+\left[n_1\frac{\partial M_1}{\partial x'}+n_2\frac{\partial M_1}{\partial y'}\right][L^{31}]+ \left[n_3\frac{\partial M_1}{\partial x'}+n_3\frac{\partial M_1}{\partial y'}\right][H^{31}]^T+n_2\frac{\partial M_1}{\partial z'}[L^{21}]\right]\Bigg]dV$$

$$[k^S]_{35} = \frac{E}{(1-\nu^2)}\int_V \Bigg[n_2\frac{\partial M_1}{\partial y'}[I^{22}]^T+n_1\frac{\partial M_1}{\partial x'}[H^{12}]^T+\nu n_1\frac{\partial M_1}{\partial y'}[H^{22}]^T+ \frac{1-\nu}{2}\left[n_1\frac{\partial M_1}{\partial y'}[I^{12}]^T+n_1\frac{\partial M_1}{\partial x'}[I^{22}]^T+\left[n_2\frac{\partial M_1}{\partial y'}+n_3\frac{\partial M_1}{\partial z'}\right][H^{12}]^T+ \left[n_2\frac{\partial M_1}{\partial x'}+n_3\frac{\partial M_1}{\partial z'}\right][H^{22}]^T+n_1\frac{\partial M_1}{\partial z'}[L^{12}]+\left[n_1\frac{\partial M_1}{\partial x'}+n_2\frac{\partial M_1}{\partial y'}\right][L^{32}]+ \left[n_3\frac{\partial M_1}{\partial x'}+n_3\frac{\partial M_1}{\partial y'}\right][H^{32}]^T+n_2\frac{\partial M_1}{\partial z'}[L^{22}]\right]\Bigg]dV$$

$$[k^S]_{36} = \frac{E}{(1-\nu^2)}\int_V \Bigg[\left[n_1\frac{\partial M_2}{\partial x'}+\frac{1-\nu}{2}\left[n_3\frac{\partial M_2}{\partial z'}+n_2\frac{\partial M_2}{\partial y'}\right]\right][H^{11}]^T+n_2\frac{\partial M_2}{\partial y'}[I^{21}]^T+ \left[\nu n_1\frac{\partial M_2}{\partial y'}+\frac{1-\nu}{2}\left[n_3\frac{\partial M_2}{\partial z'}+n_2\frac{\partial M_2}{\partial x'}\right]\right][H^{21}]^T+\frac{1-\nu}{2}\left[n_1\frac{\partial M_2}{\partial y'}[I^{11}]^T+ n_1\frac{\partial M_2}{\partial x'}[I^{21}]^T+n_1\frac{\partial M_2}{\partial z'}[L^{11}]+\left[n_1\frac{\partial M_2}{\partial x'}+n_2\frac{\partial M_2}{\partial y'}\right][L^{31}]+\left[n_3\frac{\partial M_2}{\partial x'}+ n_3\frac{\partial M_2}{\partial y'}\right][H^{31}]^T+n_2\frac{\partial M_2}{\partial z'}[L^{21}]\right]\Bigg]dV$$

$$[k^S]_{37} = \frac{E}{(1-\nu^2)}\int_V \Bigg[n_2\frac{\partial M_2}{\partial y'}[I^{22}]^T+n_1\frac{\partial M_2}{\partial x'}[H^{12}]^T+\nu n_1\frac{\partial M_2}{\partial y'}[H^{22}]^T+ \frac{1-\nu}{2}\left[n_1\frac{\partial M_2}{\partial y'}[I^{12}]^T+n_1\frac{\partial M_2}{\partial x'}[I^{22}]^T+\left[n_2\frac{\partial M_2}{\partial y'}+n_3\frac{\partial M_2}{\partial z'}\right][H^{12}]^T+ \left[n_2\frac{\partial M_2}{\partial x'}+n_3\frac{\partial M_2}{\partial z'}\right][H^{22}]^T+n_1\frac{\partial M_2}{\partial z'}[L^{12}]+\left[n_1\frac{\partial M_2}{\partial x'}+n_2\frac{\partial M_2}{\partial y'}\right][L^{32}]+$$

$$\left[n_3\frac{\partial M_2}{\partial x'}+n_3\frac{\partial M_2}{\partial y'}\right][H^{32}]^T+n_2\frac{\partial M_2}{\partial z'}[L^{22}]\Big]\Big]dV$$

$$[k^S]_{44}=\frac{E}{(1-\nu^2)}\int_V\Big[M_1^2\Big[[P^{1111}]+[R^{2121}]\Big]+\frac{\partial M_1^2}{\partial x'}[G^{1111}]+\frac{\partial M_1^2}{\partial y'}[G^{2121}]+$$
$$\nu M_1^2[F^{1121}]+\nu\frac{\partial M_1\partial M_1}{\partial y'\partial x'}[G^{1121}]+\frac{1-\nu}{2}\Big[\Big[\frac{\partial M_1^2}{\partial y'}+\frac{\partial M_1^2}{\partial z'}\Big][G^{1111}]+$$
$$\frac{\partial M_1\partial M_1}{\partial y'\partial x'}[G^{1121}]+M_1^2\Big[[R^{1111}]+[F^{1121}]^T+[P^{2121}]+[M^{1111}]+$$
$$[K^{1131}]+[P^{3131}]+[M^{2121}]+[S^{2131}]+[R^{3131}]\Big]+\Big[\frac{\partial M_1^2}{\partial x'}+$$
$$\frac{\partial M_1^2}{\partial z'}\Big][G^{2121}]+\frac{\partial M_1\partial M_1}{\partial z'\partial x'}[G^{1131}]+\Big[\frac{\partial M_1^2}{\partial x'}+\frac{\partial M_1^2}{\partial y'}\Big][G^{3131}]+$$
$$\frac{\partial M_1\partial M_1}{\partial z'\partial y'}[G^{2131}]\Big]\Big]dV$$

$$[k^S]_{45}=\frac{E}{(1-\nu^2)}\int_V\Big[M_1^2\Big[[P^{1112}]+[R^{2122}]\Big]+\frac{\partial M_1^2}{\partial x'}[G^{1112}]+\frac{\partial M_1^2}{\partial y'}[G^{2122}]+$$
$$\nu M_1^2[F^{1122}]+\nu\frac{\partial M_1\partial M_1}{\partial y'\partial x'}[G^{1122}]+\frac{1-\nu}{2}\Big[\Big[\frac{\partial M_1^2}{\partial y'}+\frac{\partial M_1^2}{\partial z'}\Big][G^{1112}]+$$
$$\frac{\partial M_1\partial M_1}{\partial y'\partial x'}[G^{1122}]+M_1^2\Big[[R^{1112}]+[F^{1122}]^T+[P^{2122}]+[F^{2112}]+[M^{1112}]$$
$$+[K^{1132}]+[P^{3132}]+[M^{2122}]+[S^{2132}]+[S^{3132}]\Big]+\frac{\partial M_1\partial M_1}{\partial z'\partial x'}[G^{1132}]$$
$$+\frac{\partial M_1\partial M_1}{\partial z'\partial y'}[G^{2132}]+\frac{\partial M_1\partial M_1}{\partial z'\partial y'}[G^{3122}]+\frac{\partial M_1\partial M_1}{\partial z'\partial x'}[G^{3112}]+\Big[\frac{\partial M_1^2}{\partial x'}$$
$$+\frac{\partial M_1^2}{\partial y'}\Big][G^{3132}]+\Big[\frac{\partial M_1^2}{\partial x'}+\frac{\partial M_1^2}{\partial z'}\Big][G^{2122}]+\frac{\partial M_1\partial M_1}{\partial x'\partial y'}[G^{2112}]\Big]\Big]dV$$

$$[k^S]_{46}=\frac{E}{(1-\nu^2)}\int_V\Big[M_1M_2\Big[[P^{1111}]+[R^{2121}]\Big]+\frac{\partial M_1\partial M_2}{\partial x'\partial x'}[G^{1111}]+$$
$$\frac{\partial M_1\partial M_2}{\partial y'\partial y'}[G^{2121}]+\nu M_1M_2[F^{1121}]+\nu\frac{\partial M_2\partial M_1}{\partial y'\partial x'}[G^{1121}]+$$
$$\frac{1-\nu}{2}\Big[\Big[\frac{\partial M_1\partial M_2}{\partial y'\partial y'}+\frac{\partial M_1\partial M_2}{\partial z'\partial z'}\Big][G^{1111}]+\frac{\partial M_2\partial M_2}{\partial y'\partial x'}[G^{1121}]+$$
$$M_1M_2\Big[[R^{1111}]+[F^{1121}]^T+[P^{2121}]+[F^{2111}]+[M^{1111}]+[K^{1131}]$$

$$+[S^{2131}]+[M^{2121}]+[R^{3131}]+[S^{3121}]\Big]+\frac{\partial M_1\partial M_2}{\partial z'\partial x'}[G^{1131}]+$$
$$\frac{\partial M_1\partial M_2}{\partial z'\partial y'}[G^{2131}]+\frac{\partial M_2\partial M_1}{\partial z'\partial y'}[G^{3121}]+\frac{\partial M_2\partial M_1}{\partial z'\partial x'}[G^{3111}]+$$
$$\left[\frac{\partial M_1\partial M_2}{\partial x'\partial x'}+\frac{\partial M_1\partial M_2}{\partial y'\partial y'}\right][G^{3131}]+\left[\frac{\partial M_1\partial M_2}{\partial x'\partial x'}+\frac{\partial M_1\partial M_2}{\partial z'\partial z'}\right][G^{2121}]+$$
$$\frac{\partial M_1\partial M_2}{\partial x'\partial y'}[G^{2111}]\Big]\Big]dV$$

$$[k^S]_{47}=\frac{E}{(1-\nu^2)}\int_V\Big[M_1M_2\Big[[P^{1112}]+[R^{2122}]\Big]+\frac{\partial M_1\partial M_2}{\partial x'\partial x'}[G^{1112}]+$$
$$\frac{\partial M_1\partial M_2}{\partial y'\partial y'}[G^{2122}]+\nu M_1M_2[F^{1122}]+\nu\frac{\partial M_2\partial M_1}{\partial y'\partial x'}[G^{1122}]+$$
$$\frac{1-\nu}{2}\Big[\left[\frac{\partial M_1\partial M_2}{\partial y'\partial y'}+\frac{\partial M_1\partial M_2}{\partial z'\partial z'}\right][G^{1112}]+\frac{\partial M_2\partial M_2}{\partial y'\partial x'}[G^{1122}]+$$
$$M_1M_2\Big[[R^{1112}]+[F^{1122}]^T+[P^{2122}]+[F^{2112}]+[M^{1112}]+[K^{1132}]+$$
$$[S^{2132}]+[M^{2122}]+[R^{3132}]+[S^{3122}]\Big]+\frac{\partial M_1\partial M_2}{\partial z'\partial x'}[G^{1132}]+$$
$$\frac{\partial M_1\partial M_2}{\partial z'\partial y'}[G^{2132}]+\frac{\partial M_2\partial M_1}{\partial z'\partial y'}[G^{3122}]+\frac{\partial M_2\partial M_1}{\partial z'\partial x'}[G^{3112}]+$$
$$\left[\frac{\partial M_1\partial M_2}{\partial x'\partial x'}+\frac{\partial M_1\partial M_2}{\partial y'\partial y'}\right][G^{3132}]+\left[\frac{\partial M_1\partial M_2}{\partial x'\partial x'}+\frac{\partial M_1\partial M_2}{\partial z'\partial z'}\right][G^{2122}]+$$
$$\frac{\partial M_1\partial M_2}{\partial x'\partial y'}[G^{2112}]\Big]\Big]dV$$

$$[k^S]_{55}=\frac{E}{(1-\nu^2)}\int_V\Big[{M_1}^2\Big[[P^{1212}]+[R^{2222}]\Big]+\frac{\partial {M_1}^2}{\partial x'}[G^{1212}]+\frac{\partial {M_1}^2}{\partial y'}[G^{2222}]+$$
$$\nu{M_1}^2[F^{1222}]+\nu\frac{\partial M_1\partial M_1}{\partial y'\partial x'}[G^{1222}]+\frac{1-\nu}{2}\Big[\left[\frac{\partial {M_1}^2}{\partial y'}+\frac{\partial {M_1}^2}{\partial z'}\right][G^{1212}]+$$
$$\frac{\partial M_1\partial M_1}{\partial y'\partial x'}[G^{1222}]+{M_1}^2\Big[[R^{1212}]+[F^{1222}]^T+[P^{2222}]+[M^{1212}]+$$
$$[K^{1232}]+[P^{3232}]+[M^{2222}]+[S^{2232}]+[R^{3232}]\Big]+\left[\frac{\partial {M_1}^2}{\partial x'}+\right.$$
$$\left.\frac{\partial {M_1}^2}{\partial z'}\right][G^{2222}]+\frac{\partial M_1\partial M_1}{\partial z'\partial x'}[G^{1232}]+\left[\frac{\partial {M_1}^2}{\partial x'}+\frac{\partial {M_1}^2}{\partial y'}\right][G^{3232}]+$$
$$\frac{\partial M_1\partial M_1}{\partial z'\partial y'}[G^{2232}]\Big]\Big]dV$$

$$[k^S]_{56} = \frac{E}{(1-\nu^2)}\int_V \Bigg[M_1M_2\Big[[P^{1211}]+[R^{2221}]\Big]+\frac{\partial M_1\partial M_2}{\partial x'\partial x'}+[G^{1211}]+ \frac{\partial M_1\partial M_2}{\partial y'\partial y'}[G^{2221}]+\nu M_1M_2[F^{1221}]+\nu\frac{\partial M_2\partial M_1}{\partial y'\partial x'}[G^{1221}]+ \frac{1-\nu}{2}\Bigg[\Big[\frac{\partial M_1\partial M_2}{\partial y'\partial y'}+\frac{\partial M_1\partial M_2}{\partial z'\partial z'}\Big][G^{1211}]+\frac{\partial M_2\partial M_2}{\partial y'\partial x'}[G^{1221}]+ M_1M_2\Big[[R^{1211}]+[F^{1221}]^T+[P^{2221}]+[F^{2211}]+[M^{1211}]+[K^{1231}]+ [S^{2231}]+[M^{2221}]+[R^{3231}]+[S^{3221}]^T+[P^{3231}]+ [K^{3211}]^T\Big]+\frac{\partial M_1\partial M_2}{\partial z'\partial x'}[G^{1231}]+\frac{\partial M_1\partial M_2}{\partial z'\partial y'}[G^{2231}]+\frac{\partial M_2\partial M_1}{\partial z'\partial y'}[G^{3221}]+ \frac{\partial M_2\partial M_1}{\partial z'\partial x'}[G^{3211}]+\Big[\frac{\partial M_1\partial M_2}{\partial x'\partial x'}+\frac{\partial M_1\partial M_2}{\partial y'\partial y'}\Big][G^{3131}]+\Big[\frac{\partial M_1\partial M_2}{\partial x'\partial x'}+ \frac{\partial M_1\partial M_2}{\partial z'\partial z'}\Big][G^{2221}]+\frac{\partial M_1\partial M_2}{\partial x'\partial y'}[G^{2211}]\Big]\Bigg]dV$$

$$[k^S]_{57} = \frac{E}{(1-\nu^2)}\int_V \Bigg[M_1M_2\Big[[P^{1212}]+[R^{2222}]\Big]+\frac{\partial M_1\partial M_2}{\partial x'\partial x'}[G^{1212}]+ \frac{\partial M_1\partial M_2}{\partial y'\partial y'}[G^{2222}]+\nu M_1M_2[F^{1222}]+\nu\frac{\partial M_2\partial M_1}{\partial y'\partial x'}[G^{1222}]+ \frac{1-\nu}{2}\Bigg[\Big[\frac{\partial M_1\partial M_2}{\partial y'\partial y'}+\frac{\partial M_1\partial M_2}{\partial z'\partial z'}\Big][G^{1212}]+\frac{\partial M_2\partial M_2}{\partial y'\partial x'}[G^{1222}]+ M_1M_2\Big[[R^{1212}][F^{1222}]^T+[P^{2222}]+[F^{2212}]+[M^{1212}]+[K^{1232}]+ [S^{2232}]+[M^{2222}]+[R^{3232}]+[S^{3222}]^T+[P^{3232}]+[K^{3212}]^T\Big]+ \frac{\partial M_1\partial M_2}{\partial z'\partial x'}[G^{1232}]+\frac{\partial M_1\partial M_2}{\partial z'\partial y'}[G^{2232}]+\frac{\partial M_2\partial M_1}{\partial z'\partial y'}[G^{3222}]+ \frac{\partial M_2\partial M_1}{\partial z'\partial x'}[G^{3212}]+\Big[\frac{\partial M_1\partial M_2}{\partial x'\partial x'}+\frac{\partial M_1\partial M_2}{\partial y'\partial y'}\Big][G^{3232}]+\Big[\frac{\partial M_1\partial M_2}{\partial x'\partial x'}+ \frac{\partial M_1\partial M_2}{\partial z'\partial z'}\Big][G^{2222}]+\frac{\partial M_1\partial M_2}{\partial x'\partial y'}[G^{2212}]\Big]\Bigg]dV$$

$$[k^S]_{66} = \frac{E}{(1-\nu^2)}\int_V \Bigg[M_2{}^2\Big[[P^{1111}]+[R^{2121}]\Big]+\frac{\partial M_2{}^2}{\partial x'}[G^{1111}]+\frac{\partial M_2{}^2}{\partial y'}[G^{2121}]+ \nu M_2{}^2[F^{1121}]+\nu\frac{\partial M_2\partial M_2}{\partial y'\partial x'}[G^{1121}]+\frac{1-\nu}{2}\Bigg[\Big[\frac{\partial M_2{}^2}{\partial y'}+\frac{\partial M_2{}^2}{\partial z'}\Big][G^{1111}]+ \frac{\partial M_2\partial M_2}{\partial y'\partial x'}[G^{1121}]+M_2{}^2\Big[[R^{1111}]+[F^{1121}]^T+[P^{2121}]+[M^{1111}]$$

$$+[K^{1131}]+[P^{3131}]+[M^{2121}]+[S^{2131}]+[R^{3131}]\Big]+\Big[\frac{\partial M_2}{\partial x'}^2+$$
$$\frac{\partial M_2}{\partial z'}^2\Big][G^{2121}]+\frac{\partial M_2}{\partial z'}\frac{\partial M_2}{\partial x'}[G^{1131}]+\Big[\frac{\partial M_2}{\partial x'}^2+\frac{\partial M_2}{\partial y'}^2\Big][G^{3131}]+$$
$$\frac{\partial M_2}{\partial z'}\frac{\partial M_2}{\partial y'}[G^{2131}]\Big]\Big]dV$$

$$[k^S]_{67}=\frac{E}{(1-\nu^2)}\int_V\Big[M_2{}^2\Big[[P^{1112}]+[R^{2122}]\Big]+\frac{\partial M_2}{\partial x'}^2[G^{1112}]+\frac{\partial M_2}{\partial y'}^2[G^{2122}]+$$
$$\nu M_2{}^2[F^{1122}]+\nu\frac{\partial M_2}{\partial y'}\frac{\partial M_2}{\partial x'}[G^{1122}]+\frac{1-\nu}{2}\Big[\Big[\frac{\partial M_2}{\partial y'}^2+\frac{\partial M_2}{\partial z'}^2\Big][G^{1112}]+$$
$$\frac{\partial M_2}{\partial y'}\frac{\partial M_2}{\partial x'}[G^{1122}]+M_2{}^2\Big[[R^{1112}]+[F^{1122}]^T+[P^{2122}]+[F^{2112}]+$$
$$[M^{1112}]+[K^{1132}]+[S^{2132}]+[M^{2122}]+[R^{3132}]+[S^{3122}]^T+[K^{3112}]^T$$
$$+[P^{3132}]\Big]+\frac{\partial M_2}{\partial z'}\frac{\partial M_2}{\partial x'}[G^{1132}]+\frac{\partial M_2}{\partial z'}\frac{\partial M_2}{\partial y'}[G^{2132}]+\frac{\partial M_2}{\partial z'}\frac{\partial M_2}{\partial y'}[G^{3122}]$$
$$+\frac{\partial M_2}{\partial z'}\frac{\partial M_2}{\partial x'}[G^{3112}]+\Big[\frac{\partial M_2}{\partial x'}^2+\frac{\partial M_2}{\partial y'}^2\Big][G^{3132}]+\Big[\frac{\partial M_2}{\partial x'}^2+$$
$$\frac{\partial M_2}{\partial z'}^2\Big][G^{2122}]+\frac{\partial M_2}{\partial x'}\frac{\partial M_2}{\partial y'}[G^{2112}]\Big]\Big]dV$$

$$[k^S]_{77}=\frac{E}{(1-\nu^2)}\int_V\Big[M_2{}^2\Big[[P^{1212}]+[R^{2222}]\Big]+\frac{\partial M_2}{\partial x'}^2[G^{1212}]+\frac{\partial M_2}{\partial y'}^2[G^{2222}]+$$
$$\nu M_2{}^2[F^{1222}]+\nu\frac{\partial M_2}{\partial y'}\frac{\partial M_2}{\partial x'}[G^{1222}]+\frac{1-\nu}{2}\Big[\Big[\frac{\partial M_2}{\partial y'}^2+\frac{\partial M_2}{\partial z'}^2\Big][G^{1212}]+$$
$$\frac{\partial M_2}{\partial y'}\frac{\partial M_2}{\partial x'}[G^{1222}]+M_2{}^2\Big[[R^{1212}]+[F^{1222}]^T+[P^{2222}]+[M^{1212}]$$
$$+[K^{1232}]+[P^{3232}]+[M^{2222}]+[S^{2232}]+[R^{3232}]\Big]+$$
$$\Big[\frac{\partial M_2}{\partial x'}^2+\frac{\partial M_2}{\partial z'}^2\Big][G^{2222}]+\frac{\partial M_2}{\partial z'}\frac{\partial M_2}{\partial x'}[G^{1232}]+\Big[\frac{\partial M_2}{\partial x'}^2+$$
$$\frac{\partial M_2}{\partial y'}^2\Big][G^{3232}]+\frac{\partial M_2}{\partial z'}\frac{\partial M_2}{\partial y'}[G^{2232}]\Big]\Big]dV$$

and $[k^S]_{ij}=[k^S]^T_{ji}$ where i = 2,7 and j = 1,(i-1). The shape function matrices

are given by

$$A_{ij} = \frac{\partial \bar{N}_i}{\partial x'} \frac{\partial \bar{N}_j}{\partial x'} \qquad C_{ij} = \frac{\partial \bar{N}_i}{\partial y'} \frac{\partial \bar{N}_j}{\partial y'}$$

$$E_{ij} = \frac{\partial \bar{N}_i}{\partial x'} \frac{\partial \bar{N}_j}{\partial y'} \qquad F_{ij}^{klmn} = C_i^{kl} C_j^{mn} \frac{\partial N_i}{\partial x'} \frac{\partial N_i}{\partial y'}$$

$$G_{ij}^{klmn} = C_i^{kl} C_j^{mn} N_i N_j \qquad H_{ij}^{kl} = C_i^{kl} N_i \frac{\partial \bar{N}_j}{\partial x'}$$

$$I_{ij}^{kl} = C_i^{kl} N_i \frac{\partial \bar{N}_j}{\partial y'} \qquad J_{ij} = \frac{\partial \bar{N}_i}{\partial z'} \frac{\partial \bar{N}_j}{\partial x'}$$

$$K_{ij}^{klmn} = C_i^{kl} C_j^{mn} \frac{\partial N_i}{\partial z'} \frac{\partial N_i}{\partial x'} \qquad L_{ij}^{kl} = C_j^{kl} \frac{\partial \bar{N}_i}{\partial z'} N_j$$

$$M_{ij}^{klmn} = C_i^{kl} C_j^{mn} \frac{\partial N_i}{\partial z'} \frac{\partial N_i}{\partial z'} \qquad O_{ij} = \frac{\partial \bar{N}_i}{\partial z'} \frac{\partial \bar{N}_j}{\partial z'}$$

$$P_{ij}^{klmn} = C_i^{kl} C_j^{mn} \frac{\partial N_i}{\partial x'} \frac{\partial N_i}{\partial x'} \qquad Q_{ij} = \frac{\partial \bar{N}_i}{\partial z'} \frac{\partial \bar{N}_j}{\partial y'}$$

$$R_{ij}^{klmn} = C_i^{kl} C_j^{mn} \frac{\partial N_i}{\partial y'} \frac{\partial N_i}{\partial y'} \qquad S_{ij}^{klmn} = C_i^{kl} C_j^{mn} \frac{\partial N_i}{\partial z'} \frac{\partial N_i}{\partial y'}$$

APPENDIX E

CONSISTENT SHELL ELEMENT

STRAIN-DISPLACEMENT MATRIX [B′]

$$[B'] = \sum_{1}^{13} \begin{bmatrix} l_1\frac{\partial \bar{N}_i}{\partial x'} & m_1\frac{\partial \bar{N}_i}{\partial x'} & n_1\frac{\partial \bar{N}_i}{\partial x'} \\ l_2\frac{\partial \bar{N}_i}{\partial y'} & m_2\frac{\partial \bar{N}_i}{\partial y'} & n_2\frac{\partial \bar{N}_i}{\partial y'} \\ l_1\frac{\partial \bar{N}_i}{\partial y'} + l_2\frac{\partial \bar{N}_i}{\partial x'} & m_1\frac{\partial \bar{N}_i}{\partial y'} + m_2\frac{\partial \bar{N}_i}{\partial x'} & n_1\frac{\partial \bar{N}_i}{\partial y'} + n_2\frac{\partial \bar{N}_i}{\partial x'} \\ l_1\frac{\partial \bar{N}_i}{\partial z'} + l_3\frac{\partial \bar{N}_i}{\partial x'} & m_1\frac{\partial \bar{N}_i}{\partial z'} + m_3\frac{\partial \bar{N}_i}{\partial x'} & n_1\frac{\partial \bar{N}_i}{\partial z'} + n_3\frac{\partial \bar{N}_i}{\partial x'} \\ l_2\frac{\partial \bar{N}_i}{\partial z'} + l_3\frac{\partial \bar{N}_i}{\partial y'} & m_2\frac{\partial \bar{N}_i}{\partial z'} + m_3\frac{\partial \bar{N}_i}{\partial y'} & n_2\frac{\partial \bar{N}_i}{\partial z'} + n_3\frac{\partial \bar{N}_i}{\partial y'} \end{bmatrix}$$

$$\begin{bmatrix} C_i^{11}\left[M_1\frac{\partial N_i}{\partial x'} + \frac{\partial M_1}{\partial x'}N_i\right] & \\ C_i^{21}\left[M_1\frac{\partial N_i}{\partial y'} + \frac{\partial M_1}{\partial y'}N_i\right] & \\ C_i^{11}\left[M_1\frac{\partial N_i}{\partial y'} + \frac{\partial M_1}{\partial y'}N_i\right] & + C_i^{21}\left[M_1\frac{\partial N_i}{\partial x'} + \frac{\partial M_1}{\partial x'}N_i\right] \\ C_i^{11}\left[M_1\frac{\partial N_i}{\partial z'} + \frac{\partial M_1}{\partial z'}N_i\right] & + C_i^{31}\left[M_1\frac{\partial N_i}{\partial x'} + \frac{\partial M_1}{\partial x'}N_i\right] \\ C_i^{21}\left[M_1\frac{\partial N_i}{\partial z'} + \frac{\partial M_1}{\partial z'}N_i\right] & + C_i^{31}\left[M_1\frac{\partial N_i}{\partial y'} + \frac{\partial M_1}{\partial y'}N_i\right] \end{bmatrix}$$

$$
\begin{vmatrix}
C_i^{12}\left[M_1\frac{\partial N_i}{\partial x'}+\frac{\partial M_1}{\partial x'}N_i\right] & \\
C_i^{22}\left[M_1\frac{\partial N_i}{\partial y'}+\frac{\partial M_1}{\partial y'}N_i\right] & \\
C_i^{12}\left[M_1\frac{\partial N_i}{\partial y'}+\frac{\partial M_1}{\partial y'}N_i\right]+C_i^{22}\left[M_1\frac{\partial N_i}{\partial x'}+\frac{\partial M_1}{\partial x'}N_i\right] & \\
C_i^{12}\left[M_1\frac{\partial N_i}{\partial z'}+\frac{\partial M_1}{\partial z'}N_i\right]+C_i^{32}\left[M_1\frac{\partial N_i}{\partial x'}+\frac{\partial M_1}{\partial x'}N_i\right] & \\
C_i^{22}\left[M_1\frac{\partial N_i}{\partial z'}+\frac{\partial M_1}{\partial z'}N_i\right]+C_i^{32}\left[M_1\frac{\partial N_i}{\partial y'}+\frac{\partial M_1}{\partial y'}N_i\right] &
\end{vmatrix}
$$

$$
\begin{vmatrix}
C_i^{11}\left[M_2\frac{\partial N_i}{\partial x'}+\frac{\partial M_2}{\partial x'}N_i\right] & \\
C_i^{21}\left[M_2\frac{\partial N_i}{\partial y'}+\frac{\partial M_2}{\partial y'}N_i\right] & \\
C_i^{11}\left[M_2\frac{\partial N_i}{\partial y'}+\frac{\partial M_2}{\partial y'}N_i\right]+C_i^{21}\left[M_2\frac{\partial N_i}{\partial x'}+\frac{\partial M_2}{\partial x'}N_i\right] & \\
C_i^{11}\left[M_2\frac{\partial N_i}{\partial z'}+\frac{\partial M_2}{\partial z'}N_i\right]+C_i^{31}\left[M_2\frac{\partial N_i}{\partial x'}+\frac{\partial M_2}{\partial x'}N_i\right] & \\
C_i^{21}\left[M_2\frac{\partial N_i}{\partial z'}+\frac{\partial M_2}{\partial z'}N_i\right]+C_i^{31}\left[M_2\frac{\partial N_i}{\partial y'}+\frac{\partial M_2}{\partial y'}N_i\right] &
\end{vmatrix}
$$

$$
\begin{vmatrix}
C_i^{12}\left[M_2\frac{\partial N_i}{\partial x'}+\frac{\partial M_2}{\partial x'}N_i\right] & \\
C_i^{22}\left[M_2\frac{\partial N_i}{\partial y'}+\frac{\partial M_2}{\partial y'}N_i\right] & \\
C_i^{12}\left[M_2\frac{\partial N_i}{\partial y'}+\frac{\partial M_2}{\partial y'}N_i\right]+C_i^{22}\left[M_2\frac{\partial N_i}{\partial x'}+\frac{\partial M_2}{\partial x'}N_i\right] & \\
C_i^{12}\left[M_2\frac{\partial N_i}{\partial z'}+\frac{\partial M_2}{\partial z'}N_i\right]+C_i^{32}\left[M_2\frac{\partial N_i}{\partial x'}+\frac{\partial M_2}{\partial x'}N_i\right] & \\
C_i^{22}\left[M_2\frac{\partial N_i}{\partial z'}+\frac{\partial M_2}{\partial z'}N_i\right]+C_i^{32}\left[M_2\frac{\partial N_i}{\partial y'}+\frac{\partial M_2}{\partial y'}N_i\right] &
\end{vmatrix}
$$

APPENDIX F

JOINT ELEMENT AND REINFORCEMENT ELEMENT BOUNDARY NODE TRANSFORMATION MATRICES

1. Transformation matrix $[T_4]$ to be used when node four of reinforcement element is on the boundary:

$$\begin{bmatrix} & [0]_{9\times 9\ 1} & [I]_{9\times 9} \\ \sum_{i}^{13} \begin{bmatrix} \bar{N}_i & 0 & 0 & N_iM_1l_{1i} & -N_iM_1l_{2i} & N_iM_2l_{1i} & -N_iM_2l_{2i} \\ 0 & \bar{N}_i & 0 & N_iM_1m_{1i} & -N_iM_1m_{2i} & N_iM_2m_{1i} & -N_iM_2m_{2i} \\ 0 & 0 & \bar{N}_i & N_iM_1n_{1i} & -N_iM_1n_{2i} & N_iM_2n_{1i} & -N_iM_2n_{2i} \end{bmatrix} & [0]_{3\times 9} \end{bmatrix} \qquad \text{(F.1)}$$

12x100

2. Transformation matrix $[T_1^{joint}]$ to be used when node one of a joint element is on the boundary:

$$\begin{bmatrix} & [I]_{9\ 1\times 9\ 1} & [0]_{9\ 1\times 9} \\ \sum_{i}^{13} \begin{bmatrix} \bar{N}_i & 0 & 0 & N_iM_1l_{1i} & -N_iM_1l_{2i} & N_iM_2l_{1i} & -N_iM_2l_{2i} \\ 0 & \bar{N}_i & 0 & N_iM_1m_{1i} & -N_iM_1m_{2i} & N_iM_2m_{1i} & -N_iM_2m_{2i} \\ 0 & 0 & \bar{N}_i & N_iM_1n_{1i} & -N_iM_1n_{2i} & N_iM_2n_{1i} & -N_iM_2n_{2i} \end{bmatrix} & [0]_{3\times 9} \\ & [0]_{9\times 9\ 1} & [I]_{9\times 9} \end{bmatrix} \qquad \text{(F.2)}$$

103x100

3. Transformation matrix $[T_4^{joint}]$ to be used when node four of a joint element is on the boundary:

$$\begin{bmatrix} & & & & & & & [I] & [0] \\ & & & & & & & {\scriptstyle 91\times 91} & {\scriptstyle 91\times 9} \\ & & & & & & & [0] & [I] \\ & & & & & & & {\scriptstyle 9\times 91} & {\scriptstyle 9\times 9} \\ \sum_{i}^{13} & \begin{bmatrix} \bar{N}_i & 0 & 0 & N_iM_1l_{1i} & -N_iM_1l_{2i} & N_iM_2l_{1i} & -N_iM_2l_{2i} \\ 0 & \bar{N}_i & 0 & N_iM_1m_{1i} & -N_iM_1m_{2i} & N_iM_2m_{1i} & -N_iM_2m_{2i} \\ 0 & 0 & \bar{N}_i & N_iM_1n_{1i} & -N_iM_1n_{2i} & N_iM_2n_{1i} & -N_iM_2n_{2i} \end{bmatrix} & \begin{matrix} \\ [0] \\ {\scriptstyle 3\times 9} \end{matrix} \end{bmatrix} \qquad (F.3)$$

$$103\text{x}100$$

APPENDIX G

DERIVATION OF LAMINA THROUGH THICKNESS INTERPOLATION FUNCTIONS M3, M4, M5 AND M6

Let rotation ϕ_L vary quadratically through the thickness of the lamina and be approximated by

$$\phi_L(\bar{z}) = a + b\bar{z} + c\bar{z}^2 \tag{G.1}$$

where $\bar{z}$ is the dimensional co-ordinate in the lamina thickness direction and a, b and c are unknown constants. The displacement $d\phi_L$ due to rotation ϕ_L is calculated as

$$d\phi_L(\bar{z}) = \int \phi_L(\bar{z})\, d\bar{z}. \tag{G.2}$$

Substituting the expression for ϕ_L, Equation G.1, into the above equation and integrating gives

$$d\phi_L(\bar{z}) = a\bar{z} + \frac{b\bar{z}^2}{2} + \frac{c\bar{z}^3}{3} + d \tag{G.3}$$

where d is an additional unknown constant. The displacements and rotations at the top and bottom of the layer are taken as degrees of freedom i.e.

$$d\phi(\frac{h_L}{2}) = d\phi_L^T \qquad \phi_L(\frac{h_L}{2}) = \phi_L^T$$

$$d\phi(-\frac{h_L}{2}) = d\phi_L^B \qquad \phi_L(-\frac{h_L}{2}) = \phi_L^B \qquad \text{(G.4,a-d)}$$

where subscripts T and B designate the top and bottom of the layer respectively and h_L is the thickness of the lamina. Substituting the expressions for ϕ_L and $d\phi_L$, Equations G.1 and Equation G.3, respectively into the above equations gives the degrees of freedom in terms of the unknown constants as

$$\begin{Bmatrix} d\phi_L^T \\ d\phi_L^B \\ \phi_L^T \\ \phi_L^B \end{Bmatrix} = \begin{bmatrix} h_L/2 & h_L^2/8 & h_L^3/24 & 1 \\ -h_L/2 & h_L^2/8 & -h_L^3/24 & 1 \\ 1 & h_L/2 & h_L^2/4 & 0 \\ 1 & -h_L/2 & h_L/2 & 0 \end{bmatrix} \begin{Bmatrix} a \\ b \\ c \\ d \end{Bmatrix}. \qquad \text{(G.5)}$$

Since there are four equations and four unknowns the above equation can be solved to give the unknown constants a, b, c and d in terms of the degrees of freedom as

$$\begin{Bmatrix} a \\ b \\ c \\ d \end{Bmatrix} = \begin{bmatrix} 3/(2h_L) & -3/(2h_L) & -1/4 & -1/4 \\ 0 & 0 & 1/h_L & -1/h_L \\ -6/h_L^3 & 6/h_L^3 & 3/h_L^2 & 3/h_L^2 \\ 1/2 & 1/2 & -h_L/8 & h_L/8 \end{bmatrix} \begin{Bmatrix} d\phi_L^T \\ d\phi_L^B \\ \phi_L^T \\ \phi_L^B \end{Bmatrix}. \qquad \text{(G.6)}$$

The above expressions for the constants are now substituted into the expression for ϕ_L and $d\phi_L$ equations G.1 and G.3, respectively, and the terms having like

degrees of freedom are grouped. This yields

$$\phi_L(\bar{z}) = \left(\frac{-1}{4} + \frac{1}{h_L}\bar{z} + \frac{3}{h_L^2}\bar{z}^2\right)\phi_L^T + \left(\frac{3}{2h_L} - \frac{6}{h_L^3}\bar{z}^2\right)d\phi_L^T$$

$$+ \left(\frac{-1}{4} - \frac{1}{h_L}\bar{z} + \frac{3}{h_L^2}\bar{z}^2\right)\phi_L^B + \left(\frac{-3}{2h_L} + \frac{6}{h_L^3}\bar{z}^2\right)d\phi_L^B$$

(G.7,a-b)

$$d\phi_L(\bar{z}) = \left(\frac{-1}{4}\bar{z} + \frac{1}{2h_L}\bar{z}^2 + \frac{1}{h_L^2}\bar{z}^3 - \frac{h_L}{8}\right)\phi_L^T + \left(\frac{3}{2h_L}\bar{z} - \frac{2}{h_L^3}\bar{z}^3 + \frac{1}{2}\right)d\phi_L^T$$

$$+ \left(\frac{-1}{4}\bar{z} - \frac{1}{2h_L}\bar{z}^2 + \frac{1}{h_L^2}\bar{z}^3 + \frac{h_L}{8}\right)\phi_L^B + \left(\frac{-3}{2h_L}\bar{z} + \frac{2}{h_L^3}\bar{z}^3 + \frac{1}{2}\right)d\phi_L^B.$$

The relationship between the dimensional co-ordinate $\bar{z}$ and the non-dimensional co-ordinate t_L is given by

$$\bar{z} = \frac{h_L t_L}{2} \qquad \text{(G.8)}$$

which is used to re-write equations G.7 in terms of t_L as

$$\phi_L(t_L) = \left(\frac{-1}{4} + \frac{t_L}{2} + \frac{3t_L^2}{4}\right)\phi_L^T + \left(\frac{3}{2h_L} - \frac{3t^2}{2h_L}\right)d\phi_L^T$$

$$+ \left(\frac{-1}{4} - \frac{t_L}{2} + \frac{3t_L^2}{4}\right)\phi_L^B + \left(\frac{-3}{2h_L} + \frac{3t^2}{2h_L}\right)d\phi_L^B$$

(G.9,a-b)

$$d\phi_L(t_L) = \frac{h_L}{8}\left(-t_L + t_L^2 + t_L^3 - 1\right)\phi_L^T + \frac{1}{4}\left(3t_L - t_L^3 + 2\right)d\phi_L^T$$

$$+ \frac{h_L}{8}(-t_L - t_L^2 + t_L^3 + 1)\phi_L^B + \frac{1}{4}(-3t_L + t_L^3 + 2)d\phi_L^B.$$

Equation G.9(b) can also be written as

$$d\phi_L(t_L) = M_3\phi_L^T + M_4 d\phi_L^T + M_5\phi_L^B + M_6 d\phi_L^B \qquad (G.10)$$

where interpolation functions M_3, M_4, M_5 and M_6 define the displacement variation through the thickness of the lamina due to degrees of freedom ϕ_L^T, $d\phi_L^T$, ϕ_L^B and $d\phi_L^B$.

APPENDIX H

CONSISTENT LAMINATED BEAM ELEMENT

STRAIN-DISPLACEMENT MATRIX [B′]

$$
[B'] = \sum_{i}^{5} \left[\begin{array}{c|c|c} \dfrac{\partial \bar{N}_i}{\partial x'} \cos\gamma & \dfrac{\partial \bar{N}_i}{\partial x'} \sin\gamma & -M_1\ CU_i\ \dfrac{\partial N_i}{\partial x'} \\ -\dfrac{\partial \bar{N}_i}{\partial x'} \sin\gamma & \dfrac{\partial \bar{N}_i}{\partial x'} \cos\gamma & -N_i CU_i \dfrac{\partial M_1}{\partial z'} - M_1\ CW_i \dfrac{\partial N_i}{\partial x'} \end{array} \right] +
$$

$$
\sum_{1}^{NL} \left[\begin{array}{c|c} -M_3\ CU_i\ \dfrac{\partial N_i}{\partial x'} & -M_4\ CU_i\ \dfrac{\partial N_i}{\partial x'} \\ -N_i CU_i \dfrac{\partial M_3}{\partial z'} - M_3\ CW_i \dfrac{\partial N_i}{\partial x'} & -N_i CU_i \dfrac{\partial M_4}{\partial z'} - M_4\ CW_i \dfrac{\partial N_i}{\partial x'} \end{array} \right.
$$

$$
\left. \begin{array}{c|c} -M_5\ CU_i\ \dfrac{\partial N_i}{\partial x'} & -M_6\ CU_i\ \dfrac{\partial N_i}{\partial x'} \\ -N_i CU_i \dfrac{\partial M_5}{\partial z'} - M_5\ CW_i \dfrac{\partial N_i}{\partial x'} & -N_i CU_i \dfrac{\partial M_6}{\partial z'} - M_6\ CW_i \dfrac{\partial N_i}{\partial x'} \end{array} \right]
$$

APPENDIX I

CONSISTENT LAMINATED SHELL ELEMENT

STRAIN-DISPLACEMENT MATRIX [B′]

$$[B'] = \sum_{1}^{13} \begin{bmatrix} l_1\frac{\partial \bar{N}_i}{\partial x'} & m_1\frac{\partial \bar{N}_i}{\partial x'} & n_1\frac{\partial \bar{N}_i}{\partial x'} \\ l_2\frac{\partial \bar{N}_i}{\partial y'} & m_2\frac{\partial \bar{N}_i}{\partial y'} & n_2\frac{\partial \bar{N}_i}{\partial y'} \\ l_1\frac{\partial \bar{N}_i}{\partial y'} + l_2\frac{\partial \bar{N}_i}{\partial x'} & m_1\frac{\partial \bar{N}_i}{\partial y'} + m_2\frac{\partial \bar{N}_i}{\partial x'} & n_1\frac{\partial \bar{N}_i}{\partial y'} + n_2\frac{\partial \bar{N}_i}{\partial x'} \\ l_1\frac{\partial \bar{N}_i}{\partial z'} + l_3\frac{\partial \bar{N}_i}{\partial x'} & m_1\frac{\partial \bar{N}_i}{\partial z'} + m_3\frac{\partial \bar{N}_i}{\partial x'} & n_1\frac{\partial \bar{N}_i}{\partial z'} + n_3\frac{\partial \bar{N}_i}{\partial x'} \\ l_2\frac{\partial \bar{N}_i}{\partial z'} + l_3\frac{\partial \bar{N}_i}{\partial y'} & m_2\frac{\partial \bar{N}_i}{\partial z'} + m_3\frac{\partial \bar{N}_i}{\partial y'} & n_2\frac{\partial \bar{N}_i}{\partial z'} + n_3\frac{\partial \bar{N}_i}{\partial y'} \end{bmatrix}$$

$$\begin{bmatrix} C_i^{11}\left[M_1\frac{\partial N_i}{\partial x'} + \frac{\partial M_1}{\partial x'}N_i\right] \\ C_i^{21}\left[M_1\frac{\partial N_i}{\partial y'} + \frac{\partial M_1}{\partial y'}N_i\right] \\ C_i^{11}\left[M_1\frac{\partial N_i}{\partial y'} + \frac{\partial M_1}{\partial y'}N_i\right] + C_i^{21}\left[M_1\frac{\partial N_i}{\partial x'} + \frac{\partial M_1}{\partial x'}N_i\right] \\ C_i^{11}\left[M_1\frac{\partial N_i}{\partial z'} + \frac{\partial M_1}{\partial z'}N_i\right] + C_i^{31}\left[M_1\frac{\partial N_i}{\partial x'} + \frac{\partial M_1}{\partial x'}N_i\right] \\ C_i^{21}\left[M_1\frac{\partial N_i}{\partial z'} + \frac{\partial M_1}{\partial z'}N_i\right] + C_i^{31}\left[M_1\frac{\partial N_i}{\partial y'} + \frac{\partial M_1}{\partial y'}N_i\right] \end{bmatrix}$$

$$
\begin{bmatrix}
C_i^{12}\left[M_1\frac{\partial N_i}{\partial x'}+\frac{\partial M_1}{\partial x'}N_i\right] & \\
C_i^{22}\left[M_1\frac{\partial N_i}{\partial y'}+\frac{\partial M_1}{\partial y'}N_i\right] & \\
C_i^{12}\left[M_1\frac{\partial N_i}{\partial y'}+\frac{\partial M_1}{\partial y'}N_i\right]+C_i^{22}\left[M_1\frac{\partial N_i}{\partial x'}+\frac{\partial M_1}{\partial x'}N_i\right] & \\
C_i^{12}\left[M_1\frac{\partial N_i}{\partial z'}+\frac{\partial M_1}{\partial z'}N_i\right]+C_i^{32}\left[M_1\frac{\partial N_i}{\partial x'}+\frac{\partial M_1}{\partial x'}N_i\right] & \\
C_i^{22}\left[M_1\frac{\partial N_i}{\partial z'}+\frac{\partial M_1}{\partial z'}N_i\right]+C_i^{32}\left[M_1\frac{\partial N_i}{\partial y'}+\frac{\partial M_1}{\partial y'}N_i\right] &
\end{bmatrix}
+
$$

$$
\sum_1^{NL}
\begin{bmatrix}
C_i^{11}\left[M_3\frac{\partial N_i}{\partial x'}+\frac{\partial M_3}{\partial x'}N_i\right] & \\
C_i^{21}\left[M_3\frac{\partial N_i}{\partial y'}+\frac{\partial M_3}{\partial y'}N_i\right] & \\
C_i^{11}\left[M_3\frac{\partial N_i}{\partial y'}+\frac{\partial M_3}{\partial y'}N_i\right]+C_i^{21}\left[M_3\frac{\partial N_i}{\partial x'}+\frac{\partial M_3}{\partial x'}N_i\right] & \\
C_i^{11}\left[M_3\frac{\partial N_i}{\partial z'}+\frac{\partial M_3}{\partial z'}N_i\right]+C_i^{31}\left[M_3\frac{\partial N_i}{\partial x'}+\frac{\partial M_3}{\partial x'}N_i\right] & \\
C_i^{21}\left[M_3\frac{\partial N_i}{\partial z'}+\frac{\partial M_3}{\partial z'}N_i\right]+C_i^{31}\left[M_3\frac{\partial N_i}{\partial y'}+\frac{\partial M_3}{\partial y'}N_i\right] &
\end{bmatrix}
$$

$$
\begin{bmatrix}
C_i^{12}\left[M_3\frac{\partial N_i}{\partial x'}+\frac{\partial M_3}{\partial x'}N_i\right] & \\
C_i^{22}\left[M_3\frac{\partial N_i}{\partial y'}+\frac{\partial M_3}{\partial y'}N_i\right] & \\
C_i^{12}\left[M_3\frac{\partial N_i}{\partial y'}+\frac{\partial M_3}{\partial y'}N_i\right]+C_i^{22}\left[M_3\frac{\partial N_i}{\partial x'}+\frac{\partial M_3}{\partial x'}N_i\right] & \\
C_i^{12}\left[M_3\frac{\partial N_i}{\partial z'}+\frac{\partial M_3}{\partial z'}N_i\right]+C_i^{32}\left[M_3\frac{\partial N_i}{\partial x'}+\frac{\partial M_3}{\partial x'}N_i\right] & \\
C_i^{22}\left[M_3\frac{\partial N_i}{\partial z'}+\frac{\partial M_3}{\partial z'}N_i\right]+C_i^{32}\left[M_3\frac{\partial N_i}{\partial y'}+\frac{\partial M_3}{\partial y'}N_i\right] &
\end{bmatrix}
$$

$$
\begin{vmatrix}
C_i^{11}\left[M_4\frac{\partial N_i}{\partial x'}+\frac{\partial M_4}{\partial x'}N_i\right] & \\
C_i^{21}\left[M_4\frac{\partial N_i}{\partial y'}+\frac{\partial M_4}{\partial y'}N_i\right] & \\
C_i^{11}\left[M_4\frac{\partial N_i}{\partial y'}+\frac{\partial M_4}{\partial y'}N_i\right]+C_i^{21}\left[M_4\frac{\partial N_i}{\partial x'}+\frac{\partial M_4}{\partial x'}N_i\right] & \\
C_i^{11}\left[M_4\frac{\partial N_i}{\partial z'}+\frac{\partial M_4}{\partial z'}N_i\right]+C_i^{31}\left[M_4\frac{\partial N_i}{\partial x'}+\frac{\partial M_4}{\partial x'}N_i\right] & \\
C_i^{21}\left[M_4\frac{\partial N_i}{\partial z'}+\frac{\partial M_4}{\partial z'}N_i\right]+C_i^{31}\left[M_4\frac{\partial N_i}{\partial y'}+\frac{\partial M_4}{\partial y'}N_i\right] &
\end{vmatrix}
$$

$$
\begin{vmatrix}
C_i^{12}\left[M_4\frac{\partial N_i}{\partial x'}+\frac{\partial M_4}{\partial x'}N_i\right] & \\
C_i^{22}\left[M_4\frac{\partial N_i}{\partial y'}+\frac{\partial M_4}{\partial y'}N_i\right] & \\
C_i^{12}\left[M_4\frac{\partial N_i}{\partial y'}+\frac{\partial M_4}{\partial y'}N_i\right]+C_i^{22}\left[M_4\frac{\partial N_i}{\partial x'}+\frac{\partial M_4}{\partial x'}N_i\right] & \\
C_i^{12}\left[M_4\frac{\partial N_i}{\partial z'}+\frac{\partial M_4}{\partial z'}N_i\right]+C_i^{32}\left[M_4\frac{\partial N_i}{\partial x'}+\frac{\partial M_4}{\partial x'}N_i\right] & \\
C_i^{22}\left[M_4\frac{\partial N_i}{\partial z'}+\frac{\partial M_4}{\partial z'}N_i\right]+C_i^{32}\left[M_4\frac{\partial N_i}{\partial y'}+\frac{\partial M_4}{\partial y'}N_i\right] &
\end{vmatrix}
$$

$$
\begin{vmatrix}
C_i^{11}\left[M_5\frac{\partial N_i}{\partial x'}+\frac{\partial M_5}{\partial x'}N_i\right] & \\
C_i^{21}\left[M_5\frac{\partial N_i}{\partial y'}+\frac{\partial M_5}{\partial y'}N_i\right] & \\
C_i^{11}\left[M_5\frac{\partial N_i}{\partial y'}+\frac{\partial M_5}{\partial y'}N_i\right]+C_i^{21}\left[M_5\frac{\partial N_i}{\partial x'}+\frac{\partial M_5}{\partial x'}N_i\right] & \\
C_i^{11}\left[M_5\frac{\partial N_i}{\partial z'}+\frac{\partial M_5}{\partial z'}N_i\right]+C_i^{31}\left[M_5\frac{\partial N_i}{\partial x'}+\frac{\partial M_5}{\partial x'}N_i\right] & \\
C_i^{21}\left[M_5\frac{\partial N_i}{\partial z'}+\frac{\partial M_5}{\partial z'}N_i\right]+C_i^{31}\left[M_5\frac{\partial N_i}{\partial y'}+\frac{\partial M_5}{\partial y'}N_i\right] &
\end{vmatrix}
$$

$$
\begin{vmatrix}
C_i^{12}\left[M_5\frac{\partial N_i}{\partial x'}+\frac{\partial M_5}{\partial x'}N_i\right] & \\
C_i^{22}\left[M_5\frac{\partial N_i}{\partial y'}+\frac{\partial M_5}{\partial y'}N_i\right] & \\
C_i^{12}\left[M_5\frac{\partial N_i}{\partial y'}+\frac{\partial M_5}{\partial y'}N_i\right]+C_i^{22}\left[M_5\frac{\partial N_i}{\partial x'}+\frac{\partial M_5}{\partial x'}N_i\right] & \\
C_i^{12}\left[M_5\frac{\partial N_i}{\partial z'}+\frac{\partial M_5}{\partial z'}N_i\right]+C_i^{32}\left[M_5\frac{\partial N_i}{\partial x'}+\frac{\partial M_5}{\partial x'}N_i\right] & \\
C_i^{22}\left[M_5\frac{\partial N_i}{\partial z'}+\frac{\partial M_5}{\partial z'}N_i\right]+C_i^{32}\left[M_5\frac{\partial N_i}{\partial y'}+\frac{\partial M_5}{\partial y'}N_i\right] &
\end{vmatrix}
$$

$$
\begin{vmatrix}
C_i^{11}\left[M_6\frac{\partial N_i}{\partial x'}+\frac{\partial M_6}{\partial x'}N_i\right] & \\
C_i^{21}\left[M_6\frac{\partial N_i}{\partial y'}+\frac{\partial M_6}{\partial y'}N_i\right] & \\
C_i^{11}\left[M_6\frac{\partial N_i}{\partial y'}+\frac{\partial M_6}{\partial y'}N_i\right]+C_i^{21}\left[M_6\frac{\partial N_i}{\partial x'}+\frac{\partial M_6}{\partial x'}N_i\right] & \\
C_i^{11}\left[M_6\frac{\partial N_i}{\partial z'}+\frac{\partial M_6}{\partial z'}N_i\right]+C_i^{31}\left[M_6\frac{\partial N_i}{\partial x'}+\frac{\partial M_6}{\partial x'}N_i\right] & \\
C_i^{21}\left[M_6\frac{\partial N_i}{\partial z'}+\frac{\partial M_6}{\partial z'}N_i\right]+C_i^{31}\left[M_6\frac{\partial N_i}{\partial y'}+\frac{\partial M_6}{\partial y'}N_i\right] &
\end{vmatrix}
$$

$$
\begin{vmatrix}
C_i^{12}\left[M_6\frac{\partial N_i}{\partial x'}+\frac{\partial M_6}{\partial x'}N_i\right] & \\
C_i^{22}\left[M_6\frac{\partial N_i}{\partial y'}+\frac{\partial M_6}{\partial y'}N_i\right] & \\
C_i^{12}\left[M_6\frac{\partial N_i}{\partial y'}+\frac{\partial M_6}{\partial y'}N_i\right]+C_i^{22}\left[M_6\frac{\partial N_i}{\partial x'}+\frac{\partial M_6}{\partial x'}N_i\right] & \\
C_i^{12}\left[M_6\frac{\partial N_i}{\partial z'}+\frac{\partial M_6}{\partial z'}N_i\right]+C_i^{32}\left[M_6\frac{\partial N_i}{\partial x'}+\frac{\partial M_6}{\partial x'}N_i\right] & \\
C_i^{22}\left[M_6\frac{\partial N_i}{\partial z'}+\frac{\partial M_6}{\partial z'}N_i\right]+C_i^{32}\left[M_6\frac{\partial N_i}{\partial y'}+\frac{\partial M_6}{\partial y'}N_i\right] &
\end{vmatrix}
$$

REFERENCES

AHMED, S., IRONS, B. M., and ZIENKIEWICZ, O. C. 1970. Analysis of thick and thin shell structures by curved finite elements. International Journal for Numerical Methods in Engineering, 2 : 419-451.

BARKER, R. M., DANA, J. R., and PRYOR, C. W. 1974. Stress concentrations near holes in laminates. Journal of Engineering Mechanics Division, ASCE, 100 : 477-488.

BATCHELOR, D. V. 1990. Private communication from Dr. Batchelor. Queen's University, Kingston, Canada.

BATHE, K. J. 1982. Finite Element Procedures in Engineering Analysis. Prentice-Hall Inc., Englewood Cliffs, NJ.

BATHE, K. J., WALCZAK, J., WELCH, A., and MISTRY, N. 1989. Nonlinear analysis of concrete structures. Computers and Structures, 32 : 563-590.

BAZANT, Z. P., and CEDOLIN, L. 1979. Blunt crack band propogation in finite element analysis. Journal of Engineering Mechanics Division, ASCE, 105 : 297-315.

BAZANT, Z. P., and OH, B. H. 1983. Crack band theory for fracture of concrete. Materials and Structures, 16 : 155-176.

BAZANT, Z. P., and SHIEH, C. L. 1978. Endochronic model for nonlinear triaxial behaviour of concrete. Nuclear Division, ASCE, 102 : 305-315.

BELYTSCHKO, T., WONG LEONG, B., and STOLARSKI, H. 1989. Assumed strain stabilization procedure for the 9-node lagrange shell element. International Journal for Numerical Methods in Engineering, 28 : 385-414.

BRIASSOULIS, D. 1988. The zero-energy modes problem of the nine-node lagrangian degenerated shell element. Computers and Structures, 30 : 1389-1402.

CEDOLIN, L., CRUTZEN, Y. R. J., and POLI, S. D. 1977. Triaxial stress-strain relationships for concrete. Journal of Engineering Mechanics Division, ASCE, 103 : 423-439.

CHAUDHURI, R. A. 1986. An equilibrium method for predicition of transverse shear stresses in a thick laminated plate. Computers and Structures, 23 : 139-146.

CHAUDHURI, R. A., BALARAMAN, K., and KUNUKKASSERIL, V. X. 1986. Arbitrarily laminated, anisotropic cylindrical shell under internal pressure. AIAA Journal, 24 : 1851-1858.

CHEN, W. F. 1982. Plasticity in Reinforced Concrete. McGraw-Hill, New York, NY.

CHEN, W. F., and HAN, D. J. 1988. Plasticity for Structural Engineers. Springer-Verlag Inc., New York, NY.

CHOI, C. K., and KWAK, H.G. 1990. The effect of finite element mesh size in nonlinear analysis of reinforced concrete structures. Computers and Structures, 36 : 807-815.

CHOW, W. K. M. 1984. Finite Element Modelling of Prestressed Concrete Slabs. M.Eng Thesis, McMaster University, Hamilton, Canada.

COOK, R. D., MALKUS, D. S. and PLESHA, M. E. 1989. Concepts and Applications of Finite Element Analysis, 3rd edition. John Wiley & Sons Inc., New York, NY.

ENGBLOM, J. J., and OCHOA, O. O. 1985. Through-the-thickness stress predictions for laminated plates of advanced composite materials. International Journal for Numerical Methods in Engineering, 21 : 1759-1776.

ERGATOUDIS, J. G., IRONS, B. M., and ZIENKIEWICZ, O. C. 1968. Curved isoparamteric, quadrilateral elements for finite element analysis. International Journal of Solids and Structures, 4 : 31–42.

GAJER, G. and DUX, P. F. 1989. Strain-softening analysis of concrete structures. Computers and Structures, 33 : 575-582.

HAND, F. R., PECKNOLD, D. A., and SCHNOBRICH, W. C. 1973. Nonlinear layered analysis of RC plates and shells. Journal of Structural Division, ASCE, 99 : 1491-1505.

HARMON, T. G., and ZHANGYUAN, N. 1989. Shear strength of reinforced concrete plates and shells determined by finite element analysis using layered elements. Journal of Structural Division, ASCE, 115 : 1141-1157.

HINTON, E., and OWEN, D. R. J. 1977. Finite Element Programming. Academic Press Inc., London.

HINTON, E., and OWEN, D. R. J. 1984. Finite Element Software for Plates and Shells. Pineridge Press Ltd., Swansea, UK.

HUGHES, T. J. R., and COHEN, M. 1978. The 'Heterosis' finite element for plate bending. Computers and Structures, 9 : 445–450.

IRONS, B. M. 1970. A frontal solution program. International Journal for Numerical Methods in Engineering, 2 : 5–32.

JIANG, J. 1985. Analysis of Reinforced and Prestressed Concrete Slabs by Finite Element Method. M.Eng Thesis, McMaster University, Hamilton, Canada.

JIANG, J. 1988. Modelling of Mechanical Behaviour of Concrete Structures. Ph.D Thesis, McMaster University, Hamilton, Canada.

JONES, R. M. 1975. Mechanics of Composite Materials. McGraw-Hill Book Company, New York, NY.

KAMOULAKOS, A. 1988. Understanding and improving the reduced integration of Mindlin shell elements. International Journal of Numerical Methods in Engineering, 26 : 2009-2029.

KANT, T. 1982. Numerical analysis of thick plates. Computer Methods in Applied Mechanics and Engineering, 31 : 1-18.

KANT, T, and MANJUNATHA, B. S. 1990. Higher-order theories for symmetric and unsymmetric fiber reinforced composite beams with C^0 finite elements. Finite Elements in Analysis and Design, 6 : 303-320.

KANT, T., OWEN, D. R. J., and ZIENKIEWICZ, O. C. 1982. A refined higher-order C^0 plate bending element. Computers and Structures, 15 : 177-183.

KREJA, I. and CYWINSKI, Z. 1988. Is reduced integration just a numerical trick. Computers and Structures, 29 : 491-496.

LIN, S. C., and SCORDELIS, A. C. 1975. Nonlinear analysis of RC shells of general form. Journal of Structural Division, ASCE, 101 : 523-538.

LITTLE, R. W. 1973. Elasticity. Prentice–Hall Inc., Englewood Cliffs, NJ.

LO, K. H., CHRISTENSEN, R. M., and WU, E. M. 1977. A high-order theory of plate deformation. Journal of Applied Mechanics, ASME, 663-676.

MACNEAL, R. H. and HARDER, R. L. 1985. A proposed standrad set of problems to test finite element accuracy. Finite Element Analysis and Design, 11 : 3–20.

MARCHERTAS, A. H., KENNEDY, J. M., and PFEIFFER, P. A. 1988. Reinforced flexural elements for temp-stress program. Nuclear Engineering and Design, 106 : 87-102.

MAU, S. T., TONG, P., and PIAN, H. H. 1972. Finite element solutions for laminated thick plates. Journal of Composite Materials, 6 : 304-311.

MENDELSON, A. 1970. Plasticity: Theory and Application. Collier–MacMillan Canada Ltd., Toronto, ONT.

MINDLIN, R. D. 1951. Influence of rotary inertia and shear deformation on flexural motions of isotropic elastic plates. ASME Journal of Applied Mechanics, 18 : 31–38.

MIRZA, F. A. and KOROL, R. M. 1983. Double chord RHS trusses analytical model. Journal of Structural Engineering, 12.

MORLEY, L. S. D., and MORRIS, A. J. 1978. Conflict between finite elements and shell theory. Royal Aircraft Establishment Report, London, UK.

NGO, D., and SCORDELIS, A. C. 1967. Finite element analysis of reinforced concrete beams. Journal of ACI, 64 : 152-163.

NILSON, A. H. 1968. Nonlinear analysis of reinforced concrete by finite element method. Journal of ACI, 65 : 757-766.

OWEN, D. R. J. and HINTON, E. 1980. Finite Elements in Plasticity: Theory and Practice. Pineridge Press Ltd., Swansea, UK.

PAGANO, N. J. 1969. Exact solutions for composite laminates in cylindrical bending. Journal of Composite Materials, 3 : 398-410.

PAGANO, N. J., and HATFIELD, S. J. 1972. Elastic behaviour of multilayered bidirectional composites. AIAA Journal, 10 : 931-933.

PANDA, S. C., and NATARAJAN, R. 1979. Finite element analysis of laminated composite plates. International Journal for Numerical Methods in Engineering, 14 : 69-79.

PANDYA, B. N., and KANT, T. 1988. Flexural analysis of laminated composites using refined higher-order C^o plate bending elements. Computer Methods in Applied Mechanics and Engineering, 66 : 173-198.

PARISCH, H. 1979. A critical survey of the 9-node degenerated shell element with special emphasis on thin shell application and reduced integration. Computer Methods in Applied Mechanics and Engineering, 20 : 323-350.

PHAN, N. D., and REDDY, J. N. 1985. Analysis of laminated composite plates using a higher-order shear deformation theory. International Journal for Numerical Methods in Engineering, 21 : 2201-2219.

PIETRUSZCZAK, S., JIANG, J. and MIRZA, F. A. 1988. An elastoplastic constitutive model for concrete. International Journal of Solids and Structures, 7 : 705-722.

PRAHTHAP, G., and BABU, C. R. 1986. An isoparametric quadratic thick curved beam element. International Journal for Numerical Methods in Engineering, 23 : 1583–1600.

PRYOR, C. W., and BARKER, R. M. 1971. A finite element analysis

including transverse shear effects for applications to laminated plates. AIAA, 9 : 912-917.

RANJBARAN, A. 1991. Embedding of reinforcements in reinforced concrete elements implemented in DENA. Computers and Structures, 40 : 925-930.

RASHID,Y. R. 1968. Analysis of prestressed concrete pressure vessels. Nuclear Engineering and Design, 7 : 334-344.

SATHURAPPAN, G., RAJAGOPALAN, N., and KRISHNAMOORTHY, C. S. 1992. Nonlinear finite element analysis of reinforced and prestressed concrete slabs with reinforcement (inclusive of prestressing steel) modelled as discrete integral components. Computers and Strutures, 44 : 575-584.

SPILKER, R. L. 1982. Hybrid-stress eight-node elements for thin and thick multilayer laminated plates. International Journal for Numerical Methods in Engineering, 18 : 801-828.

TAYLOR, R., MAHER, D. R. H. and HAYES, B. 1966. Effect of the arrangement of reinforcement on the behaviour of reinforced concrete slabs. Magazine of Concrete Research, 18 : 85-94.

TIMOSHENKO, S. 1955. Strength of Materials: Part 1 Elementary Theory and Problems, 3rd edition. Robert E. Krieger Publishing Company, Huntington, NY.

TIMOSHENKO, S. 1959. Theory of Plates and Shells. McGraw–Hill Book Company Inc., New York, NY.

TSAI, S. W., and HAHN, H. T. 1980. Introduction to Composite Materials. Technomic Publishing Company.

VU–QUOC, L., and MORA, J. A. 1989. A class of simple and efficient degenerated shell elements–analysis of global spurious–mode filtering. Computer Methods in Applied Mechanics and Engineering, 74 : 117–175.

WHITENEY, J. M. 1972. Stress analysis of thick laminated composite and sandwhich plates. Journal of Composite Materials, 6 : 426-441.

YOUNG, W. C. 1989. Roark's Formulas for Stress and Strain, 6th edition. McGraw–Hill Book Company Inc., New York, NY.

ZHOU, Y. 1991. Development of a Finite Element Model for Composite Structures of Concrete and Steel. M.Eng Thesis, McMaster University, Hamilton, Canada.

ZIENKIEWICZ, O. C., TAYLOR, R. L., and TOO, J. M. 1971. Reduced integration technique in general analysis of plates and shells. International Journal for Numerical Methods in Engineering, 3 : 275–290.

ZIENKIEWICZ, O. C. 1977. The Finite Element Method, 3rd edition. McGraw-Hill Book Company (UK) Ltd.